Title

Qubit Control and Applications to Quantum Computation and Open Quantum Systems

Permalink

https://escholarship.org/uc/item/1013q1cj

Author

Yang, Zhibo

Publication Date

2024

Peer reviewed|Thesis/dissertation

Qubit Control and Applications to Quantum Computation and Open Quantum Systems

by

Zhibo Yang

A dissertation submitted in partial satisfaction of the

requirements for the degree of

Doctor of Philosophy

in

Chemistry

in the

Graduate Division

of the

University of California, Berkeley

Committee in charge:

Professor K. Birgitta Whaley, Chair
Associate Professor David T. Limmer
Associate Professor Lin Lin

Spring 2024

Qubit Control and Applications to Quantum Computation and Open Quantum Systems

Abstract

Qubit Control and Applications to Quantum Computation and Open Quantum Systems

by

Zhibo Yang

Doctor of Philosophy in Chemistry

University of California, Berkeley

Professor K. Birgitta Whaley, Chair

Quantum computing has the potential to solve problems that are intractable for classical computers. In practice, physical qubits are coupled to their environments and are open quantum systems. To mitigate and correct environmental noises or utilize environmental degrees of freedom, one needs to carefully study the qubit properties in a open quantum system setting. In this thesis, we will first provide an overview of environmental couplings that are relevant to the quantum hardware of interest in the following chapters.

We begin the main body of this thesis by introducing a robust control method for the implementation of quantum logic gates in superconducting devices. By switching between two time-constant Hamiltonians, single and two-qubit gates can be implemented with fidelity exceeding the threshold of most quantum error corrections codes in the presence of TLS bath and Markovian bath. This method is inspired by variational quantum algorithms (VQA), and we continue to study quantum machine learning (QML), which is a specific type of VQA, in the following chapter. We investigate the impact of dephasing on QML and show dephasing significantly lower image classification accuracy of QML models. However, we also reveal that increasing virtual bond dimension of QML networks by adding ancilla can improve the accuracy and adding two ancilla can mostly compensate for the accuracy loss due to dephasing.

We then investigate qubits in open quantum system for quantum emulation. Specifically, we focus on the emulation of energy transfer between chromosomes in natural light-harvesting complexes using ion-trap quantum devices. This uphill energy transfer is assisted by vibrational modes in the molecules and is named vibration assisted energy transfer (VAET). We start with the study of VAET between two sites (qubits) coupled to one vibrational mode in the presence of classical white noise, which has the effect of dephasing. We show that in the weak noise regime, energy transfer is enhanced by VAET and harmed by the classical noise. In strong noise regime, the VAET signature is wiped out and the energy transfer efficiency will first increase with noise strength and then decrease to a quantum Zeno regime, a

phenomenon termed as environment-assisted quantum transport (ENAQT). This is followed by the study of an expanded system with three sites coupled to two vibrational modes. We present a rich array of energy transfer processes. Among them, two phonon process associated to the mode coupled to the bridging site is found to have the greatest contribution to the energy transfer process. We also investigate the model in different scenarios, including varying coupling strength and temperature, presence of dephasing and coupled nodes, finding similar patterns but different relative energy transfer efficiencies. We then conclude with the impact of these studies on the application of near-term quantum devices.

To my parents, Chunli Zhao and Hongwei Yang, and my partner Trista Feng.

Graduate School has been the most challenging journey in my life and I'm so lucky to have your supports.

Contents

List of Figures

List of Tables

Acknowledgments

I would like to begin by thanking my advisor, Professor K. Birgitta Whaley. Her compelling seminar on quantum computation captivated me and led me to this field. I am deeply grateful for her decision to take a chance on me despite my limited background in physics and mathematics. Throughout my PhD studies, Professor Whaley has been a source of inspiration, providing profound insights into quantum computing and open quantum systems. She has exemplified the essence of scientific research and communication within the scientific community.

The VAET project was my first one in Ph.D. research, where I gained invaluable knowledge on modeling open quantum systems thanks to Dr. Zhengzhao Li, Dr. Mohan Sarovar and Liwen Ko. This foundation was crucial for my subsequent projects. Our experimental collaborators, including Professor Hartmut Häffner, Joseph Broz, and Ryan Shaffer, offered vital perspectives on trapped-ion quantum computing.

I was fortunate to collaborate with experts in machine learning, optimization and quantum algorithms. Working with Haoran Liao and Ian Convy opened up new areas of machine learning for me, inspired innovative ideas of William Huggins. Jiahao Yao introduced me to the potential of reinforcement learning algorithms in quantum control. The insightful lectures by Professor Lin Lin on quantum algorithms proved to be a substantial source of knowledge and inspiration. I extend my gratitude to Dr. Robert L. Kosut for his valuable insights on control theory and optimization, which have significantly contributed to the depth and breadth of our quantum control project.

I extend my thanks to the faculty members who guided me through graduate school. Professors Daniel Neumark, David T. Limmer, Eric Neuscamman, and Hartmut Häffner rigorously tested my knowledge during my qualification exam. Moreover, I am grateful to Professors Limmer and Lin Lin for their support as members of my thesis committee.

Additionally, I appreciate the guidance received from industry professionals. My internships, although not directly related to my thesis, provided high-level insights into quantum computing. I thank Ryan Shaffer for introducing me to Amazon Braket, where my direct manager Dr. Peter Komar showed me how to effectively deliver research results in the industry setting. My mentors Dr. Matthew Beach and Dr. Mao Lin taught me a lot on industrial coding practices and neutral atom quantum computers. My skip-level manager Dr. Eric Kessler presented broad application potentials of analogue Hamiltonian simulations. My time at Riverlane under Dr. Hari Krovi and Dr. Setiawan offered a glimpse into superconducting hardware and circuit QED improvements. These industrial experiences were invaluable, influencing the writing of this thesis.

My family and friends have supported me throughout this incredible journey, and words cannot express my gratitude. My parents, Chunli Zhao and Hongwei Yang, have always supported my dream of becoming a scholar, sustaining their belief in me through my darkest moments. Without their love and inspiration, I would not be the person I am today. My girlfriend, Trista Feng, joined me in the US during the most challenging phases of the COVID pandemic, exemplifying her immense support and dedication throughout our decade-long

relationship. I am also profoundly grateful to my aunt, Xueying Zhao, and her family for their care and concern when I was separated from my family in China. Although I am an only child, my best friend, Chongrui Li, has been like a brother to me, offering his consistent support throughout my endeavors. At Berkeley, I was lucky to meet friends like Jerry Li, Daisong Pan, Xingzhi Wang and the Datong Society of China Studies, who have enriched my life with unforgettable memories.

Finally, I would like to express my profound appreciation for the creativity inherent in our species, Homo sapiens. This creativity is not only the foundation of the entire scientific research community but also enriches many aspects of my life outside my career. My fascination with movies, books, games, arts of all forms, manga, and more, all stem from their demonstrations of human creativity. It was my passion for innovation and exploration that initially propelled me into research. Many consider the existence of life to be a thermodynamic miracle; I believe that the vibrant civilization we have crafted through creativity, is another.

Chapter 1

Introduction

Quantum computing holds the potential to revolutionize various fields, including computational chemistry [1], condensed matter physics [2], cryptography [3], machine learning [4], and finance [5], among others. A substantial portion of research in this domain is dedicated to a digital approach, which involves translating problems into discrete gate sequences for quantum computers. This method boasts the benefit of universality [6]. In addition, the analogue approach—mapping a target system onto the qubit Hamiltonian with fewer parameters, known as *analogue quantum simulation* or *quantum emulation*—holds promising prospects for near-term advancements and has gained significant research interest [7, 8]. This thesis will explore both methodologies.

Despite the potential advantages, currently available near-term quantum devices have limited coherence time, circuit depth and gate fidelity, which limits their applications [9]. A class of heuristic algorithms, variational quantum algorithms (VQA) including variational quantum eigensolver (VQE) [10], quantum approximation optimization algorithm (QAOA) [11] and quantum machine learning (QML) [12], have attracted significant interest on their application to near term devices due to their feasibility on near-term devices. The key idea of VQA is to encode the problem onto the quantum computer through a certain ansatz, evaluate a cost function with the quantum computer and optimize the parameters of the ansatz with a classical computer [12]. Chapter 3 introduces a control method that is inspired by QAOA and Chapter 4 studies QML in the presence of environmental noise.

To achieve quantum advantage, much efforts in the field is directed to Quantum Error Correction (QEC) [13], in which multiple physical qubits are used to encode fewer logical qubits to protect the information from being destroyed by errors. To realize quantum error correction, high-precision control on physical qubits are needed as the physical gate fidelity should be higher than the threshold of the QEC code of interest[14–16]. In Chapter 3, a high-fidleity control method is introduced for the implementation of quantum logic gates with fidelity higher than most contemporary QEC codes.

As other quantum systems in nature, quantum devices are coupled to their environments. The dynamics of the qubits can be modeled with various open quantum system frameworks. Chapter 2 briefly introduces these interactions with environmental degrees of freedom. The

environmental effect can either beneficial or detrimental to quantum computing. In Chapters 3 and 4, environmental effects are viewed as harmful and need to be mitigated. In Chapters 5 and 6, environmental degrees of freedom are employed to emulate the environment of light harvesting complexes and their interactions with qubit states result in rich physical phenomenon.

1.1   Outline

The remaining of this thesis is organized as follows. In Chapter 2, we introduce the open quantum system descriptions of the qubit dynamics that are used in the rest of the chapters. The remaining chapters, except for the conclusion in Chapter 7, are derived from a series of published papers and constitute the main contributions of the thesis.

In Chapter 3, we shall introduce a Hamiltonian switching control method inspired by QAOA to mitigate environmental noises including Two level system (TLS) coupling and Lindblad bath on qubit systems. The key idea is switching between two time-constant control Hamiltonians as the control ansatz for the implementation of high-fidelity quantum logic gates. We shall show that this method can implement gates with fidelity 0.9999 to 0.999999 in the majority of test cases. We shall also present the dependence of fidelity on gate time, control depth and coupling properties.

In Chapter 4, we shall study two tensor network QML networks in the presence of dephasing and explore the benefit of adding ancillas. The task for benchmarking the networks' performance is a binary classification task on image data sets and the performance of the quantum networks shall be compared with a state-of-the-art classical residual network. We shall show that the impact of different degrees of decoherence on the classification performance and adding at least two ancillas can give performance similar to non-decohered networks with no ancilla.

In Chapter 5 and 6, we switch the focus to analog quantum simulation (quantum emulation). A initial work [17] demonstrated both numerically and experimentally the emulation of vibrationally assisted energy transfer (VAET) between two chromophores in light-harvesting complexes with a ion-trap quantum device. Inspired by this work, we shall further explore the quantum emulations of energy transfer in the presence of environmental impact. In Chapter 5, we shall study the properties of energy transfer affected by both vibration mode and classical white noise, corresponding to VAET [17] and environment-assisted quantum transport (ENAQT) [18, 19] respectively. We shall demonstrate that VAET is damaged by weak classical noise and insignificant in strong classical noise, and the ENAQT dependence on classical noise strength is not affected by vibrational modes. In Chapter 6, we shall study VAET in an extended system with three sites coupled to two vibrational modes. We shall reveal single- to multi-phonon processes in such systems and their dependence on various factors like site-vibration coupling strenghths, temperature and dissipation. All the simulations in Chapter 5 and 6 are done with parameters and Hamiltonians that are both feasible

for experiments on ion-trap quantum devices and comparable to light-harvesting complexes up to some scaling factor.

In Chapter 7, we conclude with a summary of major findings of this thesis, emphasizing their significance on near-term applications.

Chapter 2

Qubits in Open Quantum Systems

Real-world quantum systems are all open quantum systems, so as qubit systems. An open quantum system is a system coupled to a environment whose states are usually unknown and uncontrollable. There are a variety of different types of quantum hardware and they each have different environmental coupling. In this chapter, we will focus on the environmental couplings in to superconducting and trapped-ion devices, which are relevant to other chapters of this thesis.

In quantum computing, a commonly used basis for qubit states is the computational basis, in which the ± 1 eigenstates of σ_z operator are enumerated as $|0\rangle$ and $|1\rangle$ respectively. Unless specified, the quantum states in this chapter are all in the computational basis.

2.1 Environmental Noises

Environmental coupling is a major source of noise in quantum computing. These couplings can cause decoherence in the qubits and make the final results useless. Among various types of quantum hardware, the most commonly studied decoherence processes are relaxation and dephasing, corresponding to qubit parameters T_1 and T_2, which are frequently used to characterize qubit quality.

2.1.1 Relaxation

Relaxation refers to the non-unitary transition between the $|0\rangle$ and $|1\rangle$ states. The relaxation results from coupling to environmental electromagnetic and thermal degrees of freedom is generally present in various types of quantum devices [20–24]. A simplified picture where thermal excitation is assumed to be minimum and spontaneous relaxation from the excited $|1\rangle$ being the dominate relaxation process due to low temperature compared to qubit transition frequency is usually adapted [20, 21]. This spontaneous emission refers to solely the decay from $|1\rangle$ to $|0\rangle$ state. For a single qubit, using Born-Markov approximation, it can be

modeled by the Lindblad master equation [20, 25] with the dissipator

$$\gamma_1 \mathcal{D}[\sigma_-]\rho = \gamma_1 \left(\sigma_- \rho \sigma_+ - \frac{1}{2}\{\sigma_+\sigma_-, \rho\} \right) \tag{2.1}$$

The relaxation rate is usually defined by the reciprocal of the time required for the population of $|1\rangle$ to decay to its $1/e$, which is denoted as T_1 (i.e. $\gamma_1 \equiv 1/T_1$). The spontaneous emission is thus also referred to as T_1 decay.

2.1.2   Dephasing

Dephasing refers to the decay of the off-diagonal elements of the density matrix. It has two contributions, one is from T_1 decay as a consequence of relaxation from the $|1\rangle$ state and the other is pure decay of the off-diagonal elements, called *pure dephasing*. Pure dephasing is caused by the fluctuation of qubit transition frequency, which results in uncertainties in the transverse direction of the Bloch sphere [20, 21, 24]. For a single qubit, under Born-Markov approximation, it can be modeled by the Lindblad master equation [20, 25] with the dissipator

$$2\gamma_\varphi \mathcal{D}[|1\rangle \langle 1|]\rho = 2\gamma_\varphi \left(|1\rangle \langle 1| \rho |1\rangle \langle 1| - \frac{1}{2}\{|1\rangle \langle 1|, \rho\} \right) \tag{2.2}$$

Combining the dissipators for spontaneous emission and pure dephasing together, we have the Lindblad equation for a single qubit as

$$\frac{d}{dt}\rho = -i[H_S, \rho] + \gamma_1 \mathcal{D}[\sigma_-]\rho + 2\gamma_\varphi \mathcal{D}[|1\rangle \langle 1|]\rho, \tag{2.3}$$

where H_S is the qubit Hamiltonian. For a single qubit evolving from a general state $|\psi\rangle = \alpha |0\rangle + \beta |1\rangle$ in the rotating frame of the H_S at time $t = 0$, the state after time τ becomes [6, 21, 25]

$$\rho(t) = \begin{pmatrix} 1 + (|\alpha|^2 - 1)e^{-\gamma_1\tau} & \alpha\beta^* e^{-\frac{\gamma_1}{2}\tau} e^{-\gamma_\varphi\tau} \\ \alpha^*\beta e^{-\frac{\gamma_1}{2}\tau} e^{-\gamma_\varphi\tau} & |\beta|^2 e^{-\gamma_1\tau} \end{pmatrix} \tag{2.4}$$

The overall decay rate of the off-diagonal terms is $\gamma_2 = \frac{\gamma_1}{2} + \gamma_\varphi$ and its corresponding timescale is $T_2 = \frac{1}{\gamma_2}$.

Although this Markovian model presented above is simplified and cannot capture the complex physics behind each type of quantum devices, it is relatively easy to simulate and does a fairly good job capturing most of the decoherence phenomenon in different types of devices and T_1 and T_2 are used as standard parameters characterizing qubit quality. In this thesis, this Markovian model is used to simulate relaxation in Chapter 3 and dephasing in Chapters 4, 5 and 6 with different numerical methods.

2.1.3   Non-Markovian Models

As stated in the above sections, the T_1 and T_2 decays are simplified models for more complicated processes. Generally in superconducting devices, the Markov approximation is valid for relaxation but the pure dephasing exhibits more complex behavior due to broadband noises [21]. A common model for the dephasing in superconducting devices is $1/f$ noise, in which the noisy Hamiltonian term is assumed to be constant in each evolution (i.e. quasistatic) [21, 26].

Moreover, in superconducting systems, the qubit couple to two *two-level-systems* (TLS) which are produced by defects in the device [27–29] and the corresponding noise is highly non-Markovian [30]. We shall discuss this type of coupling in detail in Chapter 3 and propose a control method robust to this type of noise.

2.2   Vibrations in Ion Trap Systems

For ion trap devices, the coupling between electronic qubit states and environmental vibrations is crucial for their controls and applications. The most common form of vibrational coupling is coupling to global harmonic vibration modes determined by the trapping potential [22]. This type of interaction is necessary for the implementation of two-qubits gates like Cirac-Zoller gate [31] and Mølmer-Sørensen gate [32], which made universal quantum computing possible on ion trap devices. The key idea of these gates is to generate entanglement between qubits with the aid of global vibrational states.

In addition to the coupling to global vibration models, one can locally couple a single qubit to a vibration mode by applying a local laser beam. This engineered system is analogues to biological light-harvesting systems and was used to emulate the latter in [17]. In Chapters 5 and 6, we shall study the energy transfer dynamics of this type of systems in the context of quantum emulation of light-harvesting complexes using ion trap quantum devices.

Chapter 3

Hamiltonian Switching Control of Qubits in Open Quantum Systems

3.1 Preface

Except for Sec. 3.13 and 3.17, which were written specifically for this thesis, this chapter is taken from the previously published Ref. [33], originally appearing in New Journal of Physics. It was co-authored by the author of this thesis, Dr. Robert L. Kosut, and Professor K. Birgitta Whaley. The numerical simulations and most of analysis of this work is done by the the author of this thesis. Professor Whaley provided significant portions of insights in analysis and research directions. Dr. Kosut provided optimization and control theory expertise. The majority of the writing was completed by the author of this thesis, with substantial input from all of the co-authors.

3.2 Introduction

Quantum computation has a number of promising potential applications. However, currently available noisy intermediate scale quantum (NISQ) devices suffer from various sources of noise, which limit their performance [34, 35]. Error mitigation methods are needed to improve the fidelity of quantum circuits in order to obtain meaningful results from the computations. To generate unitary controls that mitigate against qubit noise due to unwanted interactions with external qubit or spin systems, we introduce here a Hamiltonian switching technique inspired by the Quantum Approximate Optimization Algorithm (QAOA). First studied in the context of the combinatorial optimization problems [11], QAOA employs a set of piece-wise constant Hamiltonians to parameterize quantum circuits with a relatively small set of parameters. The QAOA methodology has also received interest as an ansatz for quantum control and error mitigation. Several recent works have investigated robust control under classical noise using QAOA with reinforcement learning [36, 37], sequential convex programming (SCP) [38, 39] and policy gradient (PG) [40–42]. These methods were shown

to outperform prevalent gradient-based control algorithms for the majority of test-cases on both a single qubit and a coupled spin chain having classical Hamiltonian uncertainties, suggesting an intrinsic robustness of QAOA-based controls.

A typical control Hamiltonian $H_c(t)$ is dependent on a set of control variables $\{v_j(t), j = 1\dots, m\}$, where often $H_c(t)$ is linear in these variables: $H_c(t) = \sum_{j=1}^{m} v_j(t)H_j$. In our Hamiltonian switching ansatz, the operational time of the gate is divided into m variable length intervals that we refer to as "hold times" and $H_c(t)$ is held constant during each hold time at one of the m Hamiltonians in a predefined set, $\{H_j, j = 1\dots, m\}$. During each hold time only one control is active and is set to its maximum value; the remaining controls are set to zero.

In this work we apply the Hamiltonian switching ansatz to control of the *central spin* (CS) model. Sometimes referred to as the *spin star* model, the CS model is relevant to various types of solid-state quantum devices [30, 43–46]. Extensive work has been done on different aspects of CS models for quantum information processing, such as reduced spin dynamics [30, 47–49], coherence times[50–52] and bipartite control [46, 53–56]. In the CS model, the central spin, which can be used as a qubit for quantum computation, is coupled to a collection of bath spins through isotropic Heisenberg [57] or dipole-dipole [58] spin-spin interactions. The CS model is also relevant to coherent noise in superconducting transmon qubits. In these devices, multiple *two-level-systems* (TLS) couple coherently to the qubit through dipole-dipole couplings due to the defects introduced by device fabrication [59]. The relevant Hamiltonian then takes the same form as a CS model with dipole-dipole couplings. The transmon qubit has been one of the most promising candidates for near-term applications and has been notably used for Google's quantum supremacy experiment [60]. The energy splittings, coupling strengths, and mechanism of TLS coupling have been experimentally characterized in several works [27–29]. Bipartite control of a single transmon qudit coupled to both a TLS bath and a Lindblad bath, which provides a more realistic model for real physical devices, has also been studied [61].

Despite this activity, relatively little work has been done on controlling central spin systems to implement target gates with sufficiently high fidelity for fault-tolerant quantum computation. Specifically, it is highly desirable to implement elementary quantum gates with fidelity higher than the thresholds of practically relevant quantum error correction codes. Since the error thresholds for non-local concatenation codes and practical surface codes are of order 10^{-4} [14–16], a gate fidelity higher than $1 - 10^{-4} = 0.9999$ (we refer to this as "four nines") is a reasonable target for successful control of quantum computers. In this work, we will test the performance of bipartite Hamiltonian switching control to enable implementation of high-quality quantum logic gates with fidelity higher than $1 - 10^{-4}$ on CS systems containing one or two system qubits under the effect of coupling to both a primary bath of a small number of spins with or without a secondary Lindblad bath representing coupling to an extended environment. The hold times of the switching Hamiltonians will be optimized for maximum fidelity of specific target gates, using policy gradient (PG) algorithms for this classical optimization step.

Our results show that the bipartite Hamiltonian switching control can readily implement

single qubit gates on a qubit isotropically coupled to bath spins with fidelity over six nines, and single and two qubit gates on qubits coupled to TLS through dipole-dipole couplings with fidelity over four nines. The fidelity of single qubit gates with dipole-dipole coupled TLS can be further improved to nine nines by adding a secondary optimization using GRadient Ascent Pulse Engineering (GRAPE [62]). For systems with a secondary Lindblad bath, the fidelity achieved lies generally between two to four nines. We also reveal the trends of fidelity dependence on total time, control depth and the number of bath spins/TLS. The fidelity of different gates on the same system have similar fidelity level and control properties.

The remainder of the paper is structured as follows. We will first introduce our physical models in Sec. 3.3, followed by presentation of the bipartite Hamiltonian switching control ansatz and secondary optimization by GRAPE in Sec. 3.4. We then present the fidelity measure and the classical algorithms used for optimization in Sec. 3.5. Numerical results and analysis are presented in Sec. 3.6 and the features of the results discussed in Sec. 3.7. We then discuss the fidelity differences for different test cases and present possible improvements in Sec. 3.7. Sec. 3.8 concludes with a summary and outlook.

3.3   Physical Models

We set $\hbar = 1$ throughout this work. σ_q^i, $i \in \{z, y, z, +, -\}$ are Pauli operators. The number of bath spins/TLS is n. We focus primarily on the central spin models with dipole-dipole couplings to the bath spins, but also make some comparisons with behavior of the well-known CS model with isotropic Heisenberg couplings is also studied and the results are in Appendix 3.9. We also consider additional Lindblad decoherence due to a secondary bath acting on both the qubits and the primary bath of spins.

A general Hamiltonian for the controlled dynamics is

$$H(t) = H_S + H_c(t) + H_{\text{env}} + H_I, \tag{3.1}$$

where H_S and H_{env} describes the intrinsic dynamics of the system (qubits) and primary bath (bath spins/TLS) respectively, and H_I describes the coupling between system and primary spin bath. These terms are all time-independent. $H_c(t)$ describes the time-dependent control applied to the system qubits, which will be discussed in detail in the next section.

We study the control problem on single and two-qubit systems. The system Hamiltonian H_S for the one-qubit system is just the energy splitting

$$H_S^{1\text{qubit}} = -\frac{E}{2}\sigma_0^z. \tag{3.2}$$

For the 2-qubit system, H_S contains an extra coupling term between the two qubits to enable implementation of 2-qubit gates:

$$H_S^{2\text{qubit}} = -\frac{E_0}{2}\sigma_0^z - \frac{E_1}{2}\sigma_1^z + \gamma\sigma_0^z\sigma_1^z. \tag{3.3}$$

Note that neither H_S^{1qubit} nor H_S^{2qubit} allow implementation of arbitrary 1-qubit or 2-qubit quantum gates, respectively. This capability will be added by the control Hamiltonians $H_c(t)$. Note that the enumeration of qubits is different in the 1-qubit and 2-qubit systems. For the 1-qubit system, the system qubit is indexed as 0 and the bath spins start from index 1. For the 2-qubit system, the system qubits are indexed as 0 and 1 and the bath spin index starts at 2.

3.3.1 Isotropic Heisenberg Couplings

To showcase the approach and calibrate its capabilities, we first apply it to a reference CS model in which all spins in the primary bath are coupled to the central spin through a $\sigma^x\sigma^x + \sigma^y\sigma^y + \sigma^z\sigma^z$ type of interaction. The coupling Hamiltonian is then

$$H_I^{\text{iso}} = \sum_{q=1}^{n} A_q \sum_{s=x,y,z} \sigma_0^s \sigma_q^s. \tag{3.4}$$

Using the notation of [46], we set the energy splitting of the system qubit to be $E = 1$. The coupling strengths A_q are set to be equal to 1 when they are all equal ($A_q = 1$), and to be uniformly distributed between 1 and 2 ($A_q \sim \mathcal{U}[1, 2]$) when they are not equal. We employ a coupling strength that is strong relative to the system energy to provide a challenging control problem. Note that this relative coupling strength is much larger than that used for the physically relevant dipole-dipole coupling model in the next subsection. For this strongly coupled reference system, we employ arbitrary units of energy, with corresponding time units. Conventionally, analysis of this reference CS model has not included finite Hamiltonians for the bath spins [46, 56, 57] which can be rationalized as analysis within an interaction picture or rotating frame with respect to the Hamiltonian of the bath spins [48, 49]. We shall also add bath Hamiltonian terms with the same form as Eq. (3.2), i.e.,

$$H_{\text{env}}^{\text{iso}} = -\sum_{q=1}^{n} \frac{\Delta_q}{2} \sigma_q^z \tag{3.5}$$

with $\Delta_q = (1 + 0.1(q - 1))E$, and compare the performance when Hamiltonian switching control is implemented in the lab frame and in a frame rotating with $H_{\text{env}}^{\text{iso}}$.

3.3.2 Dipole-dipole Couplings

In this model, environmental TLS are coupled to the system through a $\sigma^+\sigma^- + \sigma^-\sigma^+ \equiv 1/2(\sigma^x\sigma^x + \sigma^y\sigma^y)$ type dipole-dipole Heisenberg interaction. This model is relevant to decoherence in superconducting transmon qubits, one important component of which is caused by the qubit coupling to TLS that are associated with device defects [59]. Among several possible mechanisms for qubit-TLS coupling, we focus on one that is induced by charge

fluctuations, resulting in a dipole-dipole coupling. The interaction Hamiltonian takes the form

$$H_I^{\text{dipole}} = \sum_{q=1}^{n} \frac{A_q}{2}(\sigma_0^+ \sigma_q^- + \sigma_0^- \sigma_q^+) \equiv \sum_{q=1}^{n} \frac{A_q}{4}(\sigma_0^x \sigma_q^x + \sigma_0^y \sigma_q^y) \tag{3.6}$$

and the TLS bath Hamiltonian is

$$H_{\text{env}}^{\text{dipole}} = -\sum_{q=1}^{n} \frac{\Delta_q}{2}\sigma_q^z. \tag{3.7}$$

For superconducting qubit systems, the TLS energy splittings Δ_q typically have a similar magnitude as the qubit energy splitting E (i.e., $\Delta_q \approx E$) and the coupling strength A_q is normally 2 to 3 orders of magnitude smaller [27–29]. The coupling constants in real devices are usually not homogeneous, so we focus here on the variable coupling situation. We use $E = 8\,\text{GHz}$, $\Delta_q = 8 + 0.8(q-1)\,\text{GHz}$, and assign A_q to a variable value uniformly distributed in the range $4 - 40\,\text{MHz}$ [27–29]. The system energy splitting E is equivalent to an angular frequency $\omega = 8 \times 2\pi \cdot 10^9\,\text{rad} \cdot s^{-1}$, corresponding to a unit time of $\frac{1}{16\pi} \approx 0.02\,\text{ns}$. For this model, the qubit-environmental TLS coupling is significantly smaller than the qubit energies, but even small dipolar couplings are known to generate non-trivial dissipative dynamics of a central spin [50, 63].

In the two-qubit system with dipolar coupling to TLS, the bath and interaction Hamiltonians take the form

$$
\begin{aligned}
H_{\text{env}}^{\text{dipole-2qubit}} &= -\sum_{i=0}^{1}\sum_{q_i=1}^{n_i} \frac{\Delta_{q_i}}{2}\sigma_{q_i}^z \\
H_I^{\text{dipole-2qubit}} &= \sum_{i=0}^{1}\sum_{q_i=1}^{n_i} \frac{A_{q_i}}{2}(\sigma_i^+ \sigma_{q_i}^- + \sigma_i^- \sigma_{q_i}^+) \equiv \sum_{i=0}^{1}\sum_{q_i=1}^{n_i} \frac{A_{q_i}}{4}(\sigma_i^x \sigma_{q_i}^x + \sigma_i^y \sigma_{q_i}^y).
\end{aligned}
\tag{3.8}
$$

Here the index i enumerates the system qubits and n_i is the number of TLS coupling to the system qubit i. We set $E_0 = 8.0$ GHz and $E_1 = 8.4$ GHz. All other parameter values are the same as for the single qubit.

Since the classical simulation cost scales exponentially with system size, the largest system simulated here is of six bath spins/TLS. However, as shown in Sec. 3.3.3, within the time-frame of our simulations and in the absence of control, several bath TLS can effectively represent a larger and even infinite spin bath. Fig. 3.1b shows that the dynamics of a single qubit coupled to a different finite number of TLS or an infinite TLS bath are in very good agreement up to 2 ns, which is beyond the maximal time of most simulations in this work.

3.3.3 Reduced Dynamics of Different Bath Sizes

The dynamics of central spin systems with specific system Hamiltonians have been solved analytically in [30] for dipole-dipole couplings and in [47] for isotropic couplings. These

solutions cannot be directly applied to our simulations as they require conservation of the z-component of total angular momentum, which is not the case in our control ansatz. However, we can utilize these solutions in the absence of control to compare the dynamics of our simulated smaller systems with larger systems and even an infinite spin bath.

The dynamics of central spin systems of different sizes with no control fields are plotted in Fig. 3.1. The initial state of the qubit is $|0\rangle$, and the initial state of the bath is an infinite temperature mixed state for both plots.
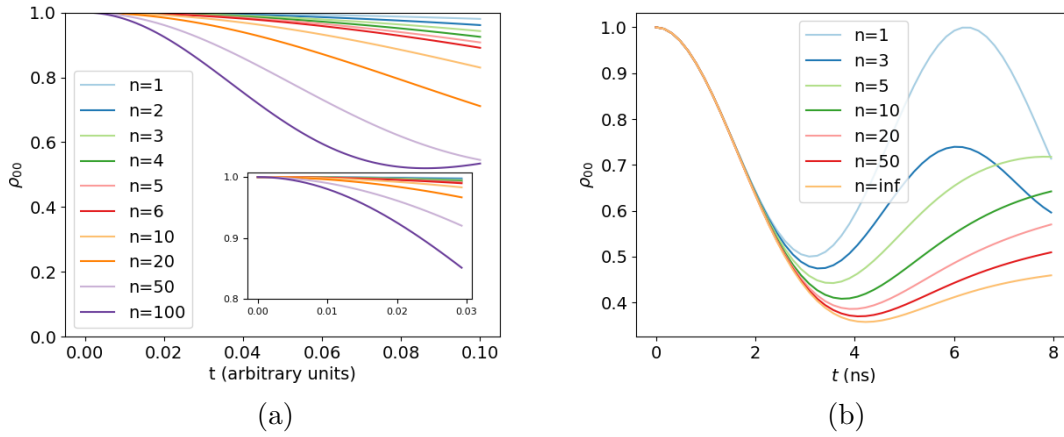
Figure 3.1: Time dependence of the $|0\rangle$ state population of a qubit coupled to different numbers of bath spins with 2 different models of qubit-bath spin coupling. (a) Isotropic Heisenberg coupling, with a non-zero qubit energy splitting of strength 1 (in arbitrary energy units). (b) Dipole-dipole coupling of strength 40 MHz, with a qubit energy splitting of 8 GHz. The initial state of the qubit is $|0\rangle$ and the initial state of the bath is an infinite temperature mixed state.

Panel (a) of Fig. 3.1 shows that the dynamics of systems with less than 10 bath spins agree well only within $t = 0.02$ time units. However, as will be presented in the next section, the typical timescale of a working control protocol for the isotropic coupling is well above 1 time unit, which means that the simulated central spin systems cannot represent a larger bath. Panel (b) shows that, for a superconducting qubit coupled to TLS through dipole-dipole couplings, the dynamics agree well up to 2 ns for different number of TLS, even for a infinite number of TLS. In comparison, the protocols in this work typically take less than 0.2 ns, which is well below this timescale. Therefore, the optimized protocols for smaller dipolar TLS coupled systems should be applicable to a larger or even infinite TLS bath.

3.3.4 Secondary Bath

We refer to the finite number of environmental spins as the *primary bath*. To better simulate real physical systems, in some calculations we further also consider a *secondary bath*, described by Lindblad dynamics, that acts on both the system qubits and the environmental spins (TLS). For this we choose a model modified from that in [61], which is a superconducting device coupled to TLS with dipole-dipole coupling under the effect of spontaneous emission (T_1 decay). This model is an extension to our model in Sec. 3.3.2. The overall dynamics for this model can be described by

$$\frac{d\rho}{dt} = -i\left[H(t), \rho\right] + \sum_k \left(L_k \rho L_k^\dagger - \frac{1}{2}\left\{L_k^\dagger L_k, \rho\right\}\right). \tag{3.9}$$

Here the Lindblad operators for spontaneous emission are $L_0 = 1/\sqrt{T_1^S}\sigma_0^-$ for the system and $L_q = 1/\sqrt{T_1^{\text{dipole}}}\sigma_q^-$ for each of the TLS, where T_1^S and T_1^{dipole} are the T_1 time of the qubit and TLS respectively.

3.4 Bipartite Control with Hamiltonian Switching

The idea of QAOA is to switch between two time-constant Hamiltonians according to an ansatz designed for a specific computational task [11]. In the current implementation of the Hamiltonian switching method, we also employ two control Hamiltonians H_A and H_B. The parameters are then the time duration over which each piece-wise constant Hamiltonian is applied. In the i-th round out of p total rounds, we denote the time applying H_A to be α_i and the time applying H_B to be β_i. p is called the *control depth*,i.e. the number of switching times is $2p$ and it is the total number of parameters. The control sequence $\boldsymbol{\theta} \equiv \{\alpha_i, \beta_i\}_{i=1}^p$ is then optimized classically. The unitary evolution of the full system can then be written as

$$U(\boldsymbol{\theta}) = e^{-iH_B\beta_p}e^{-iH_A\alpha_p}\dots e^{-iH_B\beta_1}e^{-iH_A\alpha_1}, \tag{3.10}$$

with the *total duration* of the controls given by $T = \sum_{i=1}^p(\alpha_i + \beta_i)$. We define a fidelity measure $F(\boldsymbol{\theta})$ in the next section that serves as the performance merit of the control. We then use classical optimization methods to find the optimal control sequence $\boldsymbol{\theta}^*$, defined as

$$\boldsymbol{\theta}^* \equiv \{\alpha_i^*, \beta_i^*\}_{i=1}^p = \underset{\{\alpha_i,\beta_i\}_{i=1}^p, \sum_{i=1}^p(\alpha_i+\beta_i)=T}{\arg\max} F\left(\{\alpha_i, \beta_i\}_{i=1}^p\right). \tag{3.11}$$

The classical optimizer employed in this work is reinforcement learning with policy gradient (PG), which will be introduced in Sec. 3.5.2.1.

This Hamiltonian switching approach to quantum control shares some features with the well-known method of "bang-bang" control [64–66]. Both methods employ constant strengths of the control Hamiltonians and variable control durations. However, the Hamiltonian switching approach is a more general method. Bang-bang control specifically considers

switching between on and off of a single control Hamiltonian[64–66], while the Hamiltonian switching method employs two or more distinct and non-trivial switching Hamiltonians and is thus significantly more flexible.

3.4.1 Control Ansatz

The specific goal of the Hamiltonian switching control in this work is to implement arbitrary quantum logic gates on the system qubits, which requires that the control ansatz be universal on the logical subspace. Thus, the alternating terms of the Hamiltonian switching ansatz should be able to generate arbitrary unitary transformations on the system Hilbert space in the absence of coupling to the environment.

3.4.1.1 Single-qubit

For single-qubit control, the ansatz we choose is derived from an experimentally relevant form of the Landau–Zener Hamiltonian [67, 68]. We apply a piece-wise constant control pulse with constant strength and alternating direction in the form of σ^x on the system qubit, with an always-on system σ^z term representing the system energy splitting [36]. The ansatz is then expanded by turning on coupling to environmental degrees of freedom as described in the previous section. The control is only on the system part, which makes the control problem bipartite.

For the system with dipolar coupling to TLS, the corresponding piece-wise constant Hamiltonians are

$$
\begin{aligned}
H_A^{\text{dipole}} &= -\frac{E}{2}\sigma_0^z + 2E\sigma_0^x - \sum_{q=1}^{n}\frac{\Delta_q}{2}\sigma_q^z + \sum_{q=1}^{n}\frac{A_q}{2}(\sigma_0^+\sigma_q^- + \sigma_0^-\sigma_q^+) \\
&= H_S^{\text{1qubit}} + 2E\sigma_0^x + H_I^{\text{dipole}} + H_{\text{env}}^{\text{dipole}} \\
H_B^{\text{dipole}} &= -\frac{E}{2}\sigma_0^z - 2E\sigma_0^x - \sum_{q=1}^{n}\frac{\Delta_q}{2}\sigma_q^z + \sum_{q=1}^{n}\frac{A_q}{2}(\sigma_0^+\sigma_q^- + \sigma_0^-\sigma_q^+) \\
&= H_S^{\text{1qubit}} - 2E\sigma_0^x + H_I^{\text{dipole}} + H_{\text{env}}^{\text{dipole}}.
\end{aligned}
\tag{3.12}
$$

The corresponding switching Hamiltonians for the reference isotropic Heisenberg coupling model are given in Appendix 3.9.

To further improve the fidelity for this model, we considered application of a 4-Hamiltonian switching scheme by adding a σ^y control term, as detailed in Appendix 3.10. The combination of alternating signs of σ^x and σ^y control terms then gives 4 switching Hamiltonians. We also further tested a secondary optimization with GRadient Ascent Pulse Engineering (GRAPE) [62] on the optimization results of the 2-Hamiltonian switching control. With this additional secondary optimization, the unitary evolution operator becomes

$$
U(\mathbf{c}, \boldsymbol{\theta}) = \prod_{i=1}^{p} \exp(-i(H_d^{\text{dipole}} + c_{b_i}H_c)\beta_i) \exp(-i(H_d^{\text{dipole}} + c_{a_i}H_c)\alpha_i),
\tag{3.13}
$$

where $H_d^{\text{dipole}} = H_S^{\text{1qubit}} + H_I^{\text{dipole}} + H_{\text{env}}^{\text{dipole}}$ and $H_c = 2E\sigma_0^x$, the time-duration protocol $\boldsymbol{\theta} \equiv \{\alpha_i, \beta_i\}_{i=1}^p$ is the optimized result for Hamiltonian switching, and the piecewise-constant pulse-strength protocol $\mathbf{c} \equiv \{c_{a_i}, c_{b_i}\}_{i=1}^p$ is optimized using GRAPE. The strengths $\mathbf{c}$ are initialized as alternating ± 1, which are the strengths in the Hamiltonian switching protocol.

3.4.1.2 Two-qubits

For a universal ansatz on the SU(4) group for two-qubit gates, the control ansatz we use is based on that proposed in [69]. The idea is to alternate 2-local $\sigma^z\sigma^z$ terms and single-qubit σ^x terms. For a control ansatz, we treat the σ^z terms as the drift part and alternate the sign of σ^x terms, which will not change the generated Lie algebra. This results in the following QAOA Hamiltonians

$$
\begin{aligned}
H_A^{\text{dipole-2qubit}} &= -\frac{E_0}{2}\sigma_0^z - \frac{E_1}{2}\sigma_1^z + \gamma\sigma_0^z\sigma_1^z + E_0(\sigma_0^x + \sigma_1^x) + H_{\text{env}}^{\text{dipole-2qubit}} + H_I^{\text{dipole-2qubit}} \\
H_B^{\text{dipole-2qubit}} &= -\frac{E_0}{2}\sigma_0^z - \frac{E_1}{2}\sigma_1^z + \gamma\sigma_0^z\sigma_1^z - E_0(\sigma_0^x + \sigma_1^x) + H_{\text{env}}^{\text{dipole-2qubit}} + H_I^{\text{dipole-2qubit}},
\end{aligned}
$$

(3.14)

with $H_{\text{env}}^{\text{dipole-2qubit}}$ and $H_I^{\text{dipole-2qubit}}$ defined in Eq. (3.8). We focus on the dipole-dipole coupled TLS for two qubit controls. We have set $E_0 \neq E_1$ here since this is required for the ansatz to be universal according to [70]. The σ^z terms resemble the Hamiltonian of a CPHASE gate, practically relevant to superconducting devices. [21]

We note that for three or more qubits, this ansatz is only universal for an odd number of qubits [70], due to the symmetry of the coupling constants when the number of qubits is even. However, this is not true when there are only two qubits, since there is only one qubit-qubit coupling parameter, and the two-qubit ansatz is actually universal in this special case. A detailed proof is given in Appendix 3.11. This is also validated by our numerical experiments, where we find that a fidelity of seven nines can be achieved by this control ansatz for 2 qubits alone, i.e., in the absence of coupling to TLS.

3.5 Methods

3.5.1 Theoretical Methods

3.5.1.1 Unitary Fidelity

An intuitive fidelity measure is the overlap between the final state, as the result of control, and the target state. However, the states of the bath spins, i.e., the TLS, are not of interest, so a fidelity measure assuming an optimal bath condition has been proposed in [55, 56].

Ref. [55] first defines a distance between the unitary evolution of Eq. (3.10) and the tensor product between the target gate on the qubits W and an arbitrary unitary Φ on

the bath spins, by taking the Frobenius norm of the difference matrix. Assuming that the
optimal unitary factorizes, this yields

$$D(\boldsymbol{\theta}, \Phi) = \|U(\boldsymbol{\theta}) - W \otimes \Phi\|_{\text{fro}}^2. \tag{3.15}$$

The optimal control will minimize this distance. However, the choice of the bath unitary
Φ will still affect the distance $D(\boldsymbol{\theta})$. To eliminate this bath dependence, a fidelity measure
$F(\boldsymbol{\theta})$ is defined in terms of the value of $D(\boldsymbol{\theta})$ that is optimized with respect to Φ [55, 56].
For one or two system qubits interacting with the bath spins, $F(\boldsymbol{\theta})$ is given implicitly by

$$\min_{\Phi \in U(N_B)} D(\boldsymbol{\theta}, \Phi) = 2N(1 - \sqrt{F(\boldsymbol{\theta})}). \tag{3.16}$$

Here $N_B = 2^n$ is the total number of degrees of freedom of the bath, and $N = 2^{n+1}$ or
$N = 2^{n+2}$ is the total number of degrees of freedom of the system and bath. This optimization
can be done analytically [55, 56] to obtain an optimal bath unitary Φ that is characterized
by fidelity

$$F(\boldsymbol{\theta}) = (\text{tr}\{\sqrt{Q^\dagger Q}\}/N)^2, \tag{3.17}$$

where $Q(\boldsymbol{\theta}) = \text{tr}_S \left\{ (W \otimes I_{\text{bath}})^\dagger U(\boldsymbol{\theta}) \right\}$. In this work we classically optimize the fidelity
measure in Eq. (3.17) to obtain high-fidelity gate implementations for specific one- and
two-qubit gates W.

The fidelity of Eq. (3.17) is state-independent, with the target being a system unitary.
Eq. (3.18) presents the target unitary gate matrices W which we use here for benchmarking
the bipartite control method on the CS systems in this work. Together these unitaries
generate the Clifford + T universal set of gates [71].

$$Z \equiv \sigma^z = \begin{pmatrix} 1 & 0 \\ 0 & -1 \end{pmatrix} \quad \text{Hadamard} \equiv \frac{1}{\sqrt{2}} \begin{pmatrix} 1 & 1 \\ 1 & -1 \end{pmatrix}$$

$$\text{T} \equiv \begin{pmatrix} 1 & 0 \\ 0 & e^{i\pi/4} \end{pmatrix} \quad \text{CNOT} \equiv \begin{pmatrix} 1 & 0 & 0 & 0 \\ 0 & 1 & 0 & 0 \\ 0 & 0 & 0 & 1 \\ 0 & 0 & 1 & 0 \end{pmatrix} \tag{3.18}$$

3.5.1.2 Average State Fidelity

While the fidelity measure from Eq. (3.17) is state-independent, it is often practically rel-
evant to check how the controlled final state and the target state overlap for a given gate
implementation. For this purpose, we compared the values of $F(\boldsymbol{\theta})$ obtained from the above
optimization, with an averaged state fidelity $F_S(\boldsymbol{\theta})$ defined as the average over M randomly
and uniformly sampled initial states, i.e.,

$$F_S(\boldsymbol{\theta}) = \frac{1}{M} \sum_m^M \langle \psi_T | \rho_{Sm}(\boldsymbol{\theta}) | \psi_T \rangle, \tag{3.19}$$

with the time-evolved reduced density matrix at time T defined as

$$\rho_{Sm}(\boldsymbol{\theta}) = \text{tr}_B(U(\boldsymbol{\theta}) \ket{\psi_{im}} \bra{\psi_{im}} U(\boldsymbol{\theta})^\dagger), \tag{3.20}$$

where $\ket{\psi_{im}} = \ket{m_S} \otimes \ket{m_B}$, $\ket{m_S}$ and $\ket{m_B}$ are Haar-random states of the system and the bath respectively, and $\ket{\psi_T} = W \ket{m_S}$ is the target state. The Haar-random states are generated using the Python software qutip [72].

3.5.1.3 Fidelity with respect to a set of reference states

In the case of Lindblad evolution, the unitary fidelity of Eq. (3.17) is not applicable, since the Lindblad evolution provides a quantum channel instead of a unitary over the qubits and coupled spins that constitute the primary bath. Instead, we use the fidelity measure proposed in [73] for optimizations with Lindblad dynamics. This fidelity is the average of the Hilbert–Schmidt product between the target state and the evolved density matrix with respect to a set of reference states [35, 73],

$$F(\boldsymbol{\theta}) = \sum_{i=0}^{d} \frac{w_i}{\text{Tr}\left[\rho_i^2\right]} \Re e \left\{ \text{Tr}\left[W\rho_i W^\dagger \mathcal{D}[\rho_i]\right] \right\}. \tag{3.21}$$

Here $d+1$ is the number of reference states in the set, ρ_i is the i-th reference state, w_i is a weight for each reference state with $\sum_i w_i = 1$ and

$$\mathcal{D}[\rho_i] = \text{tr}_B\left(\mathcal{L}[\rho_i]\right) \tag{3.22}$$

is the quantum channel governing the evolution. $\mathcal{L}[\cdot]$ is the Lindblad evolution of Eq. (3.9) for the qubits and primary TLS bath.

Following [73], for efficiency and accuracy we choose $d = 2$ for a single qubit and $d = 4$ for two qubits, corresponding to the dimension of the system Hilbert space in each case. The reference states are $\rho_i = \ket{\varphi_i} \bra{\varphi_i}$ for $i = 0, \ldots, d-1$, with $\ket{\varphi_i} \bra{\varphi_i}$ being computational basis states and $(\rho_d)_{ij} = \frac{1}{d}$. All weights are set equal to $w_i = \frac{1}{d+1}$. The TLS initial state is the zero temperature state.

3.5.2 Numerical Methods

3.5.2.1 Optimization Algorithms

Optimization of the bipartite control problem is a numerically challenging task and requires careful design of the optimization algorithm [46, 56]. In this work, we employ reinforcement learning with *policy gradient* (PG), which have been shown to be effective for optimizing QAOA protocols on systems with classical noise. [40–42]. We also applied the sequential convex programming (SCP) method of [38, 39] which showed outcomes similar to those obtained with PG. To keep the focus on the Hamiltonian switching protocol rather than on the algorithmic implementations, we present only the PG results here.

The PG method used in this work was developed in [40–42]. The key idea is to treat the values each parameter as a probability distribution and to then optimize over the mean and standard deviation of the distribution, instead of over the parameter themselves. This has the advantage of not requiring any information about the derivatives of the fidelity function. The final result is expected to converge to a delta distribution with the mean value being the optimal value of the parameter [40]. The original PG method developed in [40] has the disadvantages of unbounded protocol durations and possibility of negative time intervals, which limits its application to Hamiltonian switching control. These issues were fixed in subsequent work [41, 42] and we use here the improved versions of the PG methods from Refs. [41, 42].

Although we can set constraints on the time duration of the protocols and avoid the occurrence of negative entries (i.e., non-physical negative time intervals), small negative values are nevertheless still observed in optimizations. This issue is resolved by taking the absolute value of the negative entries in the protocol when evaluating the fidelity. The number of PG iterations is set to 2000 to ensure convergence (see Sec. 3.5.3). All simulations are carried out with several optimizations running in parallel. To achieve the best result within a reasonable simulation time, each simulation is run 3 to 5 times with different initial interval sets. In all cases we show the best results from all of the parallel simulations.

When the accuracy reached with PG optimization of Hamiltonian switching is not sufficient, we conduct a secondary optimization using the GRAPE method [62] on the outcomes of Hamiltonian switching control. Instead of optimizing the hold times as in the Hamiltonian switching control, we now optimize the amplitude of each control pulse in GRAPE with their time durations fixed at the values obtained from the Hamiltonian switching optimization. The numerical optimization in GRAPE is carried out using gradient-based methods.

3.5.2.2   Numerical Details

The unitary dynamics are implemented using NumPy [74]. The unitary evolution operator Eq. (3.10) is generated by directly multiplying $-iH_A$ and $-iH_B$ in computational basis with time durations α_i, β_i, exponentiating the resultant matrix, then multiplying all $2p$ matrices together. Simulation of Lindblad dynamics is carried out with the superoperator approach implemented using NumPy [74] for three or less total number of spins and TLS (system plus primary bath), and by numerical integration of the ordinary differential equation implemented with qutip [72] for larger models. All of the Pauli operators in the computational basis are generated using Python package quspin [75].

The GRAPE optimizations are done using qutip [72] with modifications. The gradient of fidelity measure Eq. (3.17) used in GRAPE optimization is given in [76]. The optimization method is the BFGS algorithm implemented by scipy [77]. The control amplitudes are constrained to lie within the range $[-1.2, 1.2]$, while the control amplitudes in Hamiltonian switching control are held at ± 1.

In all of the plots shown in this work, the fidelity is presented as *minus log infidelity*

(MLI), i.e., the vertical axis of the displayed plots

$$-\log_{10}(1 - F(\theta^*)). \tag{3.23}$$

This allows the fidelity differences between different simulations to be better assessed, since most of the fidelities are close to 1. The integer part of the MLI gives the number of nines in the actual fidelity.

In numerical experiments for a certain physical model, we focus on characterizing the change of the fidelity with the control depth p and the total evolution time T. The control depth p corresponds to the number of parameters for the circuit parameterization: larger p gives added flexibility to the protocol, which is expected to give more powerful protocols and thus higher fidelity. However, larger control depth adds to the effort of optimization and is experimentally harder to implement. It is also desirable for the total evolution time T to be short for fast gate implementation. However, for an ansatz with fixed control strength there is a theoretical lower bound for the required gate time [36, 68]. Since any protocol with shorter gate time would give lower fidelity, we therefore simultaneously probe the effect of both p and T on the fidelity of the Hamiltonian switching control, and look for low-depth and short-time protocols that give fidelity values larger than 0.9999, corresponding to infidelities, i.e., gate errors, below the threshold of most contemporary quantum error correction codes. [14–16]

3.5.3   Trial Simulations

To find the number of iterations required to achieve optimal fidelity with reasonable resources in a PG optimization, we first carried out a series of test optimizations for the reference CS system with isotropic Heisenberg couplings to the primary bath of spins. Additional calculations with this model are presented in Appendix 3.9. We set the energy splitting of the system qubit to be $E = 1$ and take the system-primary bath coupling strengths to be $A_q = 1$ when these are all equal, and to be uniformly distributed between 1 and 2 ($A_q \sim \mathcal{U}[1,2]$) when they are not equal. The energy unit is chosen to be arbitrary for simplicity and generality in this demonstration example. A very strong coupling strength was chosen here in order to test the capabilities of the control approach.

Fig. 3.2a shows the MLI dependence on the number of PG iterations for a Z gate on a single qubit isotropically coupled (see Eq. (3.4)) to n environmental spins. These calculations were carried out in the rotating frame (Section 3.3.1). We find that 2000 iterations are enough for the optimizer to converge. The vertical axis here is the best fidelity reached in any single run. The uncertainties are due to averaging over several (3 or 5) simulations with different initial protocols. It is evident that the fidelity is not significantly improving after 1000 iterations, so 2000 is enough to exploit the power of the optimizer. The fidelity change over the number of iterations for other simulations are also checked and show a similar trend, confirming that 2000 iterations is a valid choice.

(a)   (b)
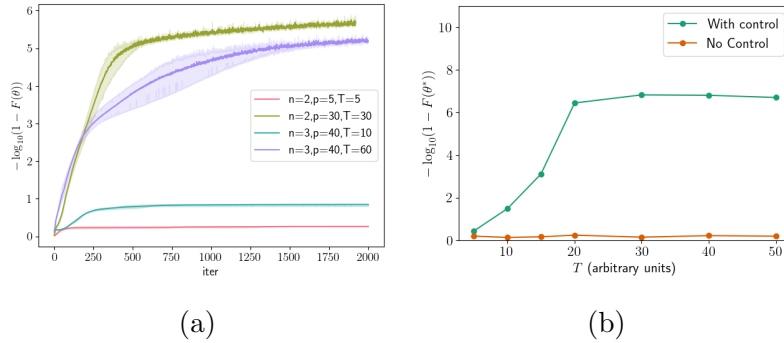
Figure 3.2: (a) Dependence of MLI of fidelity (Eqs. (3.17) and (3.23)) on the number
of iterations with PG, for a Z gate on a single qubit with isotropic Heisenberg coupling
to n environmental spins (Eq. (3.4)), with equal coupling strengths $A_q = 1$ and system
qubit splitting $E = 1$ (arbitrary units). Run parameters are displayed in the legend. (b)
Comparison of the unitary fidelity (Eq. (3.17)) for a Z gate on a single qubit isotropically
coupled to $n = 2$ bath spins under evolution with (green curve)or without (orange curve)
Hamiltonian switching. The horizontal T axis is the total duration of evolution for the
bipartite protocol. The control depth for the green curve is $p = 20$ and the optimization
method used is PG. The fidelities of the orange points without Hamiltonian switching are
calculated with the same total duration of the corresponding control protocol and would be
equal to 1 if there were no decoherence due to coupling to the primary bath of spins. Lines
connecting the points are shown to guide the eye.

We also compare with the fidelity for evolution without any control. Fig. 3.2b) shows
the MLI as a function of the control protocol time T for a Z gate on a single qubit isotrop-
ically coupled to $n = 2$ bath spins under evolution with (green curve) or without (orange
curve) Hamiltonian switching. This comparison is made with a state evolved with the same
number of bath spins under the Hamiltonian that directly produces the unitary within the
total duration of the protocol T. For example, for the target gate Z, the system part of the
Hamiltonian is $H'_s = -\frac{\pi}{2T}\sigma^z$, which gives $\exp(-iH'_sT) = \sigma^z$ up to a phase. Then the unitary
under decoherence due to the primary bath is given by $U_n = \exp(-i(H'_s + H_I)T)$, and the
fidelity under this evolution is given by the fidelity measure in Eq. (3.17). In the absence of
coupling to the bath ($H_I = 0$), both of these evolutions would give unit fidelity. However, it
is evident from Fig. 3.2b) that the fidelity is significantly lower in the presence of coupling
to the bath (red points). Implementing the Hamiltonian switching bipartite control leads
to a considerable improvement in fidelity (green points), showing the effectiveness of the
Hamiltonian switching bipartite control.

3.6 Results for qubits coupled to TLS

In this section we present the simulation results for the qubit systems with dipolar couplings to TLS. All simulations are carried out in the lab frame.

3.6.1 Single qubit

Here we apply bipartite Hamiltonian switching control to a single qubit coupled to TLS through dipole-dipole couplings as described in Eq. (3.6). In this model we focus on the variable coupling case (A_q sampled uniformly on $[4, 40]$ MHz) for practical relevance, since in superconducting qubits the coupling strengths between the qubit and individual TLS are generally variable [27–29]. The results of fidelity dependence on time with PG optimization are shown in Fig. 3.3a, 3.3b for $n = 2, 3$ bath spins. Notice that the horizontal axis is in units of nanoseconds. One time unit in these simulations is $\frac{1}{16\pi} \approx 0.02$ ns. The fidelity dependence on T for $n = 1, 4, 5$ is also simulated and shows very similar behavior. Trial simulations with all coupling constants equal to 40MHz yield results very similar to those shown in Fig. 3.3.

The fidelity dependence on T and p for all simulations are rather similar. We refer to the minimal depth required for significant fidelity improvement with time as the *critical depth* p^*. Beyond the critical depth p^*, the fidelity generally first increases with total evolution time T and then reaches a plateau. We refer to the transition time between the increasing and plateau regions for given number of spins n as the *critical time* T^*. The critical time T^* for all the Z gate simulations is $\frac{4}{16\pi}$ ns ≈ 0.08 ns (4 time units), which is significantly shorter than the corresponding value obtained for the reference isotropically coupled model calculations presented in Appendix 3.9. The critical depth p^* is also much lower than for the isotropically coupled model. Here all simulations for $n = 2 - 5$ show an increase to a plateau value for $p = 20$ that does not change significantly for larger p values. Additional simulations suggest that the value of the critical depth for all $n = 2 - 5$ test cases with target gate Z is $p^* = 5$. The significantly lower critical time and critical depth values relative to those for the isotropically coupled model is likely the result of the much weaker coupling strength for the dipolar coupling model. This is confirmed by trial simulations carried out with dipole-dipole coupled qubits having the same coupling strengths as those employed in the isotropic model (i.e., of the same order of magnitude as the system energy splitting). Such simulations give larger T^* and p^* values, similar to those found for the reference isotropic coupling model in Appendix 3.9.

The results for Hadamard and T gates are shown in Fig. 3.3d. The critical time of the Hadamard gate is $T^* = \frac{2}{16\pi}$ ns ≈ 0.04 ns (2 time units) and of the T gate is $T^* = \frac{3}{16\pi}$ ns ≈ 0.06 ns (3 time units), which are both shorter than the Z gate. The critical depths are also lower. The highest fidelity achieved is also around four nines. In general, the control properties of different target gates are quite similar, but the Hadamard and T gates are expected to be

(a) $n = 2$, fixed p, Z gate

(b) $n = 3$, fixed p, Z gate

(c) $n = 2 - 5$, fixed $T = \frac{4}{16\pi}$ ns, Z gate

(d) $n = 2, p = 20$, Hadamard and T gates
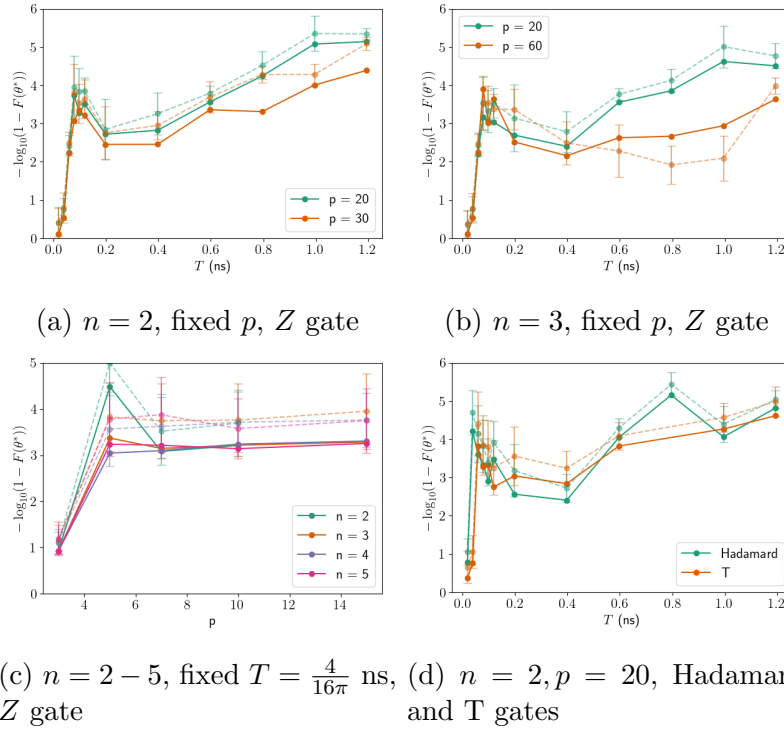
Figure 3.3: Single qubit gate fidelity dependence on (a),(b) and (d): total evolution time and (c) control depth for dipole-dipole coupled systems optimized with PG. The target gate is Z for panels (a)-(c) and Hadamard and T for panel (d). The coupling constants are unequal and evenly distributed over the range 4-40 MHz, which is in the relevant strength range for superconducting devices. Each point is the best result of 3 or 5 parallel simulations with different initialization. For each pair of lines with the same color and T value, the solid one is the actual optimization result and the pale dashed one with error bar is the average state fidelity over $M = 100$ Haar-random states. All fidelities are plotted as MLI, Eq. (3.23).

easier to implement because the critical depths are lower and the critical times are shorter compared to the Z gate.

In general, all of the curves for the TLS coupling model show a rather similar pattern, with a short critical time T^* and a low critical depth p^*, and with final gate fidelity limited at around four nines. The results are summarized in Table. 3.1. The similarity of critical time and depth among different numbers of TLS agree with the characteristic feature of the reduced dynamics of the control-free system shown in Fig. 3.1b, namely, that the dynamics of a single qubit coupled to different number of TLS appear almost identical within the timescale of the simulations.

In these calculations the optimization was carried out with the unitary fidelity of Eq. (3.17). The corresponding state fidelities of Eq. (3.19) are also plotted in Fig. 3.3, as

Target gate	# of bath spins (n)	Critical depth $(p^*, T = T^*)$	Highest MLI
	2	5	5.14 $(9.48)^a$
Z	3	5	4.62
	4	5	3.66
	5	5	3.66
Hadamard	2	≤ 3	5.15
T	2	≤ 3	4.61

^{a} Highest MLI obtained with secondary GRAPE optimization.

Table 3.1: The estimated critical depth p^* and highest log fidelity reached in the single qubit gate simulations of dipole-dipole couplings.

dashed pale lines of the same color. The size of the Haar-random sampling of states is set to $M = 100$: this value produces an almost identical mean and standard deviation as the larger values $M = 1000$ and $M = 10000$. In all the cases, the standard deviation of the state fidelities are very low, showing only a weak dependence on the initial states. We note that the state fidelity of the protocols for the TLS model is somewhat higher than the gate fidelity. The standard deviation of the state fidelity is also larger than that for the isotropic coupling model, but are still generally small, indicating weak fidelity dependence on initial states.

It is apparent that for qubits with dipolar coupling to the primary bath spins, Hamiltonian switching alone does not always reliably increase the fidelity significantly above the desired fidelity. To further improve the fidelity, we applied GRAPE to undertake a secondary optimization of the piecewise constant control amplitudes with the duration of each piece fixed to the optimal protocol derived from the optimal Hamiltonian switching control. This was carried out on the results for $n = 2$ bath spins with $T = 20, 30, 40, 50, 60$ time units (approximately 0.4, 0.6, 0.8, 1.0 and 1.2 ns) and $p = 20$ that are presented in Fig. 3.3a. The MLI after PG optimization are 2.83, 3.56, 4.24, 5.08 and 5.14. After GRAPE optimization, the MLI are improved to 7.65, 8.16, 8.44, 9.48 and 8.45 respectively. These values are now well above our target of four nines.

In Appendix 3.12 we show additional results obtained with a non-universal control ansatz, motivated by [61], where it was shown that coupling a 4-level qudit to a TLS could allow a non-universal control Hamiltonian to become universal. Appendix 3.12 demonstrates a counter-example for which a non-Clifford gate is achieved with very high fidelity yet the coupling to the TLS does not provide universality.

We also studied the effect of T_1 decay on both the qubit and TLS, as described in Eq. (3.9). The decay rates of the qubit and all TLS are set to be equal. Results are shown in Fig. 3.4 for a target T gate on a single qubit, with zero TLS (panel (a)) and with $n = 3$ TLS (panel (b)). Simulation costs restricted the PG iterations to 250 in the latter case, but the fidelities were well converged at this point. Calculations for other gates show similar performance. The fidelity measure used here is given by Eq. (3.21). Note that this fidelity

measure is defined on a set of reference states that effectively represents an average over all states in the qubit Hilbert space [73], so we do not additionally present an average state fidelity over Haar-random states.

(a) $n = 0$ with T_1 decay

(b) $n = 3$ with T_1 decay
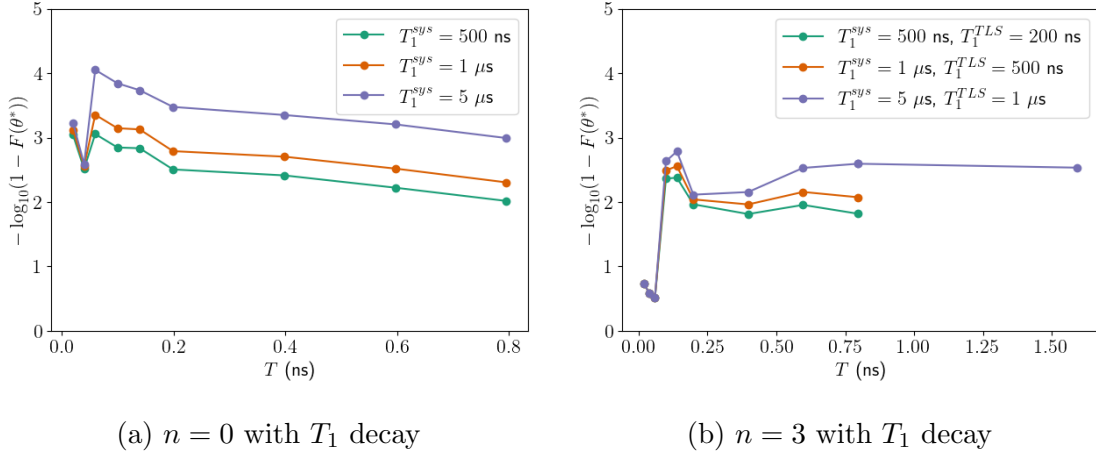
Figure 3.4: T gate fidelity dependence on total evolution time for a single qubit coupled to n TLS and optimized with PG. In addition to coupling to the TLS, both the system and TLS are under T_1 decay. The coupling constants are unequal and evenly distributed over 4-40 MHz, which is in the relevant strength range for superconducting devices. Each point is the best result of 3 or 5 parallel simulations with different protocol parameter initialization. The fidelity, Eq. (3.21), is plotted as MLI, Eq. (3.23).

Fig. 3.4a shows that spontaneous emission severely reduces the gate fidelity of an isolated qubit ($n = 0$), lowering this from a value above ten nines in the absence of both TLS and spontaneous emission, to a value of only three to four nines. The critical behavior with respect to time is still apparent but there is now no real plateau and instead the fidelity (MLI) shows a slow decay over duration of the protocol which is consistent with the dissipative nature of spontaneous emission. Fig. 3.4b shows that after adding the additional coupling to the TLS, the fidelity further drops, as expected because of the increased overall noise strength with coupling to both the TLS and Lindblad bath, but the critical time is not changed.

3.6.2   Two Qubits

So far we have shown the results of bipartite Hamiltonian switching control on a single qubit. In this section we present the results of applying the method to two system qubits to implement the entangling CNOT gate. The two-qubit model studied here is two superconducting qubits coupled to a primary bath of TLS, as described by Eq. (3.8), with or without a secondary Lindblad bath. The control ansatz is given in Eq. (3.14).

(a) 2 qubit, $p = 30$ (b) 2 qubit, $T = \frac{30}{16\pi}$ ns≈ 0.6 ns
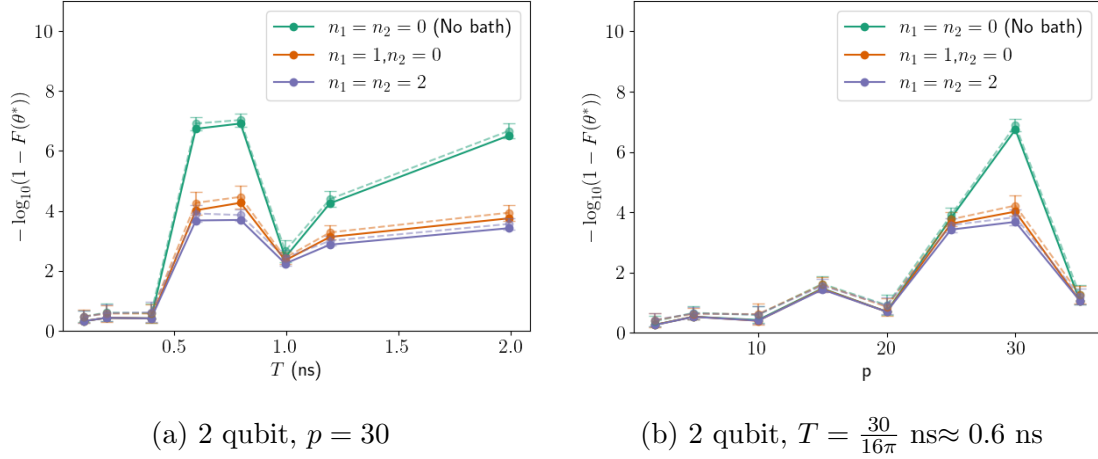
Figure 3.5: CNOT gate fidelity dependence on (a) total evolution time and (b) control depth for 2-qubit system coupled to n TLS and optimized with PG. The coupling constants are unequal and evenly distributed in the relevant strength of superconducting devices. Each point is the best result of 5 parallel simulations with different initialization. For each pair of points with the same color and T value, the solid line is the actual optimization result and the pale line with error bar is the average state fidelity over $M = 100$ Haar-random states. The fidelity, Eq. (3.17), is plotted as MLI, Eq. (3.23).

The results of 2-qubit control with only the primary TLS bath are plotted in Fig. 3.5. Results for the case with no TLS are also plotted for comparison. The 2-qubit gate fidelity in the absence of TLS can reach seven nines, which shows that the ansatz is effective. After turning on the couplings, the fidelity drops but the dependence on total time and protocol depth has the same pattern as that with no couplings. The fidelity generally increases to about four nines after the critical time and critical depth, and is lower for smaller values of T and p. The state fidelity of each protocol is also plotted in Fig. 3.5 (points with error bars, connected by pale dashed lines), showing good agreement with the optimization results.

The results of 2-qubit control with both a primary TLS bath and a secondary Lindblad bath are plotted in Fig. 3.6. As expected, the fidelity is lowered compared to that without Lindblad decoherence in Fig. 3.6. In general, the effect of the Lindblad bath in decreasing the gate fidelity is seen to be more significant than the effect of the TLS bath. In addition, given a fixed level of Lindblad noise, the fidelity with different numbers of TLS is very similar. The lowest MLI under the strongest Lindblad noise ($T_1^{sys} = 500$ ns, $T_1^{TLS} = 200$ ns) and one TLS is about 1.36. The critical time is not significantly affected by either the Lindblad noise strength or the coupling strength to the TLS.

Comparing Fig. 3.3 and Fig. 3.5, we can see that the two-qubit gate fidelities are similar to one-qubit when the qubits are coupled only to the primary TLS bath. But when the

(a) $n_1 = n_2 = 0$ (No TLS)   (b) $n_1 = 1, n_2 = 0$
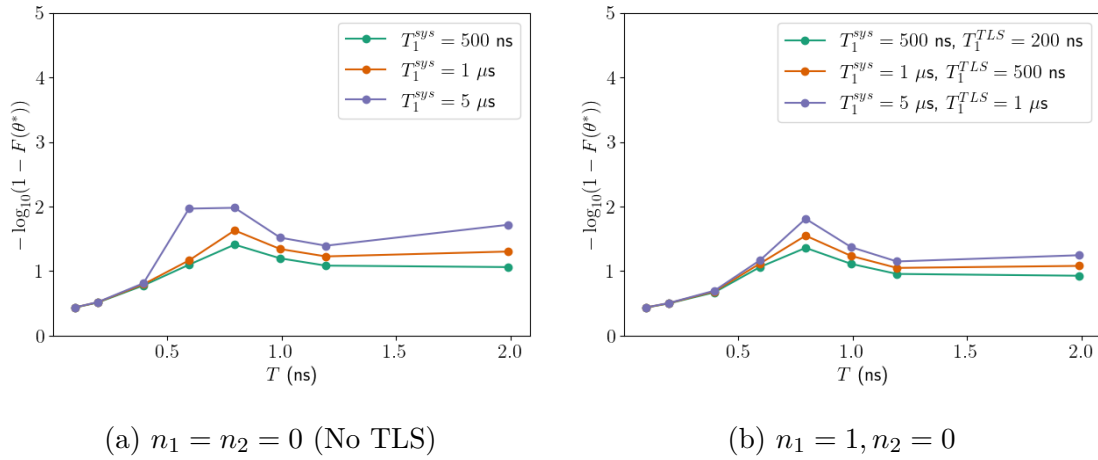
Figure 3.6: CNOT gate fidelity dependence on total evolution time for 2-qubit system coupled to n TLS under the effect of both TLS couplings and Lindblad decoherence optimized with PG. Each point is the best result of 3 parallel simulations with different initialization. The control depth is $p = 30$. The fidelity, Eq. (3.21), is plotted as MLI, Eq. (3.23).

qubits are also coupled to the secondary Lindblad bath, the fidelity of two-qubit control is lower than the one-qubit case. It is apparent that the Hamiltonian switching control of a two-qubit system is less robust to Lindblad noise. In both cases (i.e. with or without T_1 decay), the critical time T^* and depth p^* of two-qubit control are both larger than one-qubit control.

3.7   Discussion

Table 3.2 summarizes all simulations carried out for qubits coupled to a primary bath of spins via dipole-dipole coupling, with or without a secondary Lindblad bath.

The fidelity at the plateau region for primary bath size $n = 1 - 5$ TLS is around four nines. Beyond the critical depth p^*, further increasing the protocol depth p does not appear to improve the fidelity. Adjusting other protocol parameters is found to be ineffective in increasing the fidelity level. To explore the factors affecting the highest achievable fidelity level, we have performed additional simulations described in Appendix 3.14. These results show that different performance levels can be obtained by implementing the control in the rotating frame. The highest fidelity level is found for calculations performed in a rotating frame on a qubit system with strong system-bath couplings, achieving fidelities of six to eight nines. Moving from this implementation frame and parameter regime to either the lab frame and/or the weak coupling regime is found to lower the fidelity to around four nines.

To analyze these observations, we first computed the gradient and Hessian of several simulations, as described in Appendix 3.14. The largest components of the gradients for all four

Primary bath	Coupling strength relative to qubit energy	Ansatz	# of qubits	Secondary bath	Highest MLI
Dipole-dipole coupling, lab frame	$5 * 10^{-4} - 5 * 10^{-3}$	universal	1	No	5.15
				Lindblad	2.79
			2	No	4.27 $(9.48)^a$
				Lindblad	1.81
		non-universal	1	No	7.18^b
				Lindblad	2.48^b

^{a} Highest MLI obtained with secondary GRAPE optimization.
^{b} Only applicable to Z-rotation gates.

Table 3.2: Summary of simulations carried out for the dipolar coupling model. The results for the universal ansatz are presented in Sec. 3.6 and the non-universal ansatz results are presented in Appendix 3.12.

selected simulations were found to be approximately 10^{-3}, which are relatively small, indicating proximity to critical points of the control landscape. The majority of the eigenvalues of the Hessian matrices were negative, indicative of locations that are local, or even global, maxima in most directions (see Appendix 3.14). Furthermore, in the weak coupling case, most of the eigenvalues have small magnitudes, suggesting possible control modifications to enhance robustness of the control without sacrificing fidelity [78].

We also conducted a controllability analysis in Appendix 3.16 for the case of 2 bath spins, to understand whether the differences in precision achieved in different frames could be assigned to different extent of controllability. The results are summarized in Table 3.3.

Frame	Equal coupling strength?	Qubit controllable?	Spin bath controllable?
Rotating	N	Y	N
	Y	N	N
Lab	N	Y	N
	Y	Y	N

Table 3.3: Summary of controllability of systems with 1 qubit coupled to 2 bath spins through dipole-dipole couplings. See Appendix 3.16 for full details.

It is evident that controllablity analysis is not able to explain the fidelity differences observed between rotating and lab frames, nor of course, the differences due to the change of coupling strength. Controllability of the qubit and bath spins does not necessarily depend on whether they are described in the rotating or the lab frame, nor on the strength of the couplings relative to the system energy. Instead, it depends only on whether the coupling

strengths are all equal or not. Furthermore, as shown in Appendix 3.9, the critical depth p^* depends on controllability of the system.

We explored several options to improve the fidelity for the dipolar coupling case for the realistic weak coupling situation. One is to add an additional σ^y control term, which ensures controllability of the system qubit regardless of the type and relative strength of the couplings to the bath spins. These calculations require extension of the two-Hamiltonian switching protocol to a four-Hamiltonian protocol and are summarized in Appendix. 3.10. The resulting simulation results show that the fidelity in the lab frame and strong coupling regime is now improved above six nines, but the fidelity in the other test cases is not significantly improved.

A more successful strategy derives from noting that for the specific choice of Hamiltonians H_A and H_B used in the switching Hamiltonian protocol in this work, Eq. (12), the effective control Hamiltonian reduces to alternating between $-2E\sigma_x$ and $+2E\sigma_x$. This suggests that we may further refine the strength of the effective control pulses obtained from the Hamiltonian switching method to allow variable strength of the σ_x term during each variable time interval determined by optimization of the Hamiltonian switching protocol. We carried this out by applying the GRAPE method as described in Sec. IV.B. The results for the dipole-dipole coupled systems in the lab frame and in the weak coupling regime were presented in Sec. 3.6.1, where we saw that the fidelity is now significantly improved by such secondary optimization of the pulse strength. Note that this secondary optimization may also be understood as a generalization of the Hamiltonian switching protocol to allow variation of an additional parameter in each instance of H_A and H_B, i.e., varying both the strength of each Hamiltonian in addition to its duration.

In general, our results indicate that the fidelities that can be achieved by the basic form of Hamiltonian switching given in Eq. (12) are primarily affected by the presence of the bath σ^z terms arising in lab frame implementations and by the relative strength of the qubit system-bath spin couplings and the system energies. The fact that the fidelities are lower in the weak coupling regime indicates that it is hard for a symmetric switching between fixed Hamiltonians to cancel the effect of weak qubit-spin couplings, so that the fidelities can reach only four or five nines. However, the additional flexibility offered by a secondary optimization of the effective control strength from pulse to pulse using the GRAPE method allows this to be further improved to nine nines.

We note that the duration of gates studied in this work are well below the typical duration of single qubit gates on superconducting qubits [79–82]. This is a result of optimizing the gates without imposing experimental constraints such as current limits on gate times, minimal Hamiltonian pulse times, or the finite time required to implement a switch between two Hamiltonians. These unconstrained calculations reveal the key features of a critical depth p^* and a critical time T^*. For single qubit gates, the critical depth values are remarkably low, equal or less than 5 (see Table 3.1). We expect that the feature of critical depth will be maintained for switching protocols carried out under realistic experimental constraints. To verify this we have carried out additional simulations (not shown) for single-qubit gates carried out over a total evolution time $T \sim 20$ ns with $p = 5$, corresponding to a single

Hamiltonian duration of 2ns, consistent with minimal pulse times (see below). These calculations on realistic gate timescales attain a fidelity level similar to that shown in Fig. 3.3, achieving MLI of 4.12.

The other experimental constraints derive from minimal time constraints on the physical control pulses implementing a Hamiltonian, e.g., ~ 2 ns for superconducting qubits [83], and also the requirement of finite time for switching between two Hamiltonians, typically by gradually ramping up and down the corresponding control pulses. We can expect these to be relatively minor constraints in practice, since one may add such constraints and then re-optimize the sequence of Hamiltonian switches to recover a similar level of fidelity as the original protocol [83]. Such an extension of the Hamiltonian switching protocol to incorporate constraints provides a potential constructive approach to implement the switching protocols.

3.8   Summary and Outlook

In this work, we have developed a bipartite Hamiltonian switching control protocol for qubits coupled to a primary bath of two level systems and a Lindblad bath describing an extended environment. We applied this approach to systems of one and two qubits coupled to a primary bath of spins/TLS via either an isotropic interaction or a dipole-dipole interaction, and analysed the control of the system in this setting, as well as with a secondary Lindblad bath. The simulations for systems coupled only to the primary bath (spin or TLS bath) are optimized using a unitary gate fidelity measure, while the simulations for systems coupled to both a primary bath and a secondary Lindblad bath are optimized using a reference state fidelity measure. The Hamiltonian control optimizes the time duration for application of each Hamiltonian, with constant amplitude in all time intervals. In cases where the fidelity obtained with this basic Hamiltonian switching control was too low, we boosted the fidelity using a secondary optimization with GRAPE that also allows the amplitude of the Hamiltonian controls to be adjusted for each time interval.

Our numerical results demonstrated the effectiveness of bipartite Hamiltonian switching control. In the presence of coupling to the primary bath, the fidelity of direct implementation of gates would drop below 0.9. However, with Hamiltonian switching, the fidelity in most of the test cases were improved to between $1 - 10^{-4}$ and $1 - 10^{-8}$. Further refinement with a secondary GRAPE optimization brought the fidelity in all cases to $1 - 10^{-8}$ or higher, which is well within the thresholds of most contemporary quantum error correction codes. Applying the resulting protocols to specific states gives state fidelities of similar magnitude to the corresponding gate fidelities.

Analysis of the change of fidelity over the protocol evolution time reveals a general pattern that the fidelity first increases with time, then reaches a plateau region that is approximately constant as the protocol time increases further. A similar trend holds for the fidelity change as the control depth p, i.e., the number of Hamiltonian switching intervals, is increased. However, only with sufficient control depth p can the behavior of an increase to a plateau value over total evolution time be observed, and the plateau value does not change signifi-

cantly when the control depth is further increased. We refer to the turning points between
the region of increasing fidelity and the subsequent plateau region as the critical time T^*
and critical depth p^*, for the dependence on protocol time T and depth p respectively. The
most desirable protocol for implementation of a gate is obtained using the critical depth p^*,
which is the smallest value at which the time dependence of fidelity reaches a plateau value.

The parameters used for qubits coupled to TLS through dipole-dipole interactions, emu-
late typical superconducting qubit systems. With a Z gate target, simulations with different
TLS count n and control depth p were found to yield almost identical highest fidelity values,
as well as identical dependence on the total protocol evolution time T. The critical time
and depth are $T^* = \frac{4}{16\pi}$ ns ≈ 0.08 ns (4 time units) and $p^* = 5$, suggesting relatively easy
implementation in experimental systems. These values are independent of the number of
TLS. This is consistent with the weaker coupling and also with the simulated reduced dy-
namics, since the reduced dynamics of a qubit with no control fields but coupled by dipolar
interactions to different numbers of TLS are almost the same up to 2 ns (see Fig. 3.1b), a
considerably longer time than most simulations in this work. The critical time and critical
depth are found to be similar for Hadamard and T gate targets. The highest fidelity reached
by Hamiltonian switching alone for qubits with dipolar coupling to a bath of TLS is around
$1 - 10^{-4}$, but was shown to be improved to $1 - 10^{-9}$ by a secondary optimization by GRAPE
that modulates the amplitudes of the switching Hamiltonians in addition to their duration.
Introducing additional couplings to a secondary Lindblad bath causing T_1 decay of the sys-
tem qubits lowers the fidelity, as expected. Nevertheless, a fidelity of approximately $1 - 10^{-3}$
on a single qubit can still be reached when the T_1 time of the qubit is 500 ns.

This work demonstrated that bipartite Hamiltonian switching control for high-fidelity
quantum gates can very effectively mitigate environmental noise, particularly when the op-
timization of the switching Hamiltonian pulse durations is supplemented by secondary opti-
mization of the switching Hamiltonian amplitudes. Our analysis revealed several interesting
features of this method. One notable feature is that with a universal ansatz, the control
properties depend only weakly on the target gate, suggesting a generic robustness of the op-
timal bipartite control. Additional simulations not shown here also demonstrated that the
Hamiltonian switching method is robust to at least 1% uncertainty in the magnitude of the
coupling strengths. It will be interesting in the future to further explore the robustness of
this bipartite control scheme in a more systematic manner, e.g., examining its performance
under diverse uncertainties using the recently developed classical averaging method [78]. For
example, one can ask whether there are classes of imperfections for which control of switching
time intervals and the fine-tuning their amplitudes is naturally more robust than standard
pulse shaping. Many robustness issues are related to the topology of the quantum control
landscape, i.e., the fidelity as a function of the control variables. In particular, at the top
of the landscape where the fidelity is near one and the gradient is near zero, there is a large
null space which allows for considerable design freedom, e.g., for a significant robustness in
the choice of control parameters. An interesting question here is to compare the null space
for Hamiltonian switching with that for standard pulse control. For example, if the key
variable is the area under the pulse, for the standard case this is simply amplitude times a

fixed time interval, whereas for Hamiltonian switching it is a fixed amplitude times a varying time-interval. The robustness properties will also depend on the accuracy of setting the pulse intervals and/or the pulse amplitudes. In some cases larger pulse amplitudes induce other phenomena, e.g., if too much energy is pumped into the system. In such situations, Hamiltonian switching by intrinsically fixing the pulse amplitudes may avoid disruptions or unwanted side effects. In general, we conclude that Hamiltonian switching bipartite control is a promising practical candidate for the implementation of high-fidelity quantum gates on NISQ devices.

In the following sections, we present results that are supplementary to the main contents in this chapter, including additional simulation results and detailed derivations.

3.9 Isotropic Couplings

3.9.1 Control Ansatz

For the reference CS model with isotropic coupling, we evolve the system under the following two piece-wise constant Hamiltonians:

$$
\begin{aligned}
H_A^{\text{iso}} &= -\frac{E}{2}\sigma_0^z + 2E\sigma_0^x + \sum_{q=1}^{n} A_q \sum_{s=x,y,z} \sigma_0^s\sigma_q^s = H_S^{\text{1qubit}} + 2E\sigma_0^x + H_I^{\text{iso}} \\
H_B^{\text{iso}} &= -\frac{E}{2}\sigma_0^z - 2E\sigma_0^x + \sum_{q=1}^{n} A_q \sum_{s=x,y,z} \sigma_0^s\sigma_q^s = H_S^{\text{1qubit}} - 2E\sigma_0^x + H_I^{\text{iso}}.
\end{aligned}
\tag{3.24}
$$

For this reference model, unless otherwise specified, we evolve the systems in the rotating frame with respect to the bath Hamiltonian. This eliminates the bath σ^z terms, which simplifies the dynamics. The difference in control performance between rotating frame and lab frame implementations will be analyzed in Appendix 3.14.

3.9.2 Simulation Results

We first study control of the isotropically coupled central spin system with all the coupling constants set equal to $A = 1$. We start with the target gate Z. The optimization results for $n = 2, 3$ bath spins are displayed in Fig. 3.7.

In all of the test-cases, the highest fidelity reached is above $1 - 10^{-6}$, given sufficient control depth p and evolution time T. A notable feature is that the protocol depth p needs to be large enough to achieve a significant fidelity change with gate duration T. For instance, in Fig. 3.7a, for $p < 20$ the fidelity shows no significant change with T, but for $p \geq 20$, the fidelity increases significantly when T changes from 10 to 20 ns. Panel (a) for $n = 2$ shows that in the plateau region, the fidelity may not improve much, as the depth p further increases. To better reveal the fidelity dependence on protocol depth p, Fig. 3.7c shows the fidelity plotted as a function of p, for fixed time T. For $n = 2$ we see a significant

(a) $n = 2$, fixed p (b) $n = 3$, fixed p (c) $n = 2, 3$, fixed T
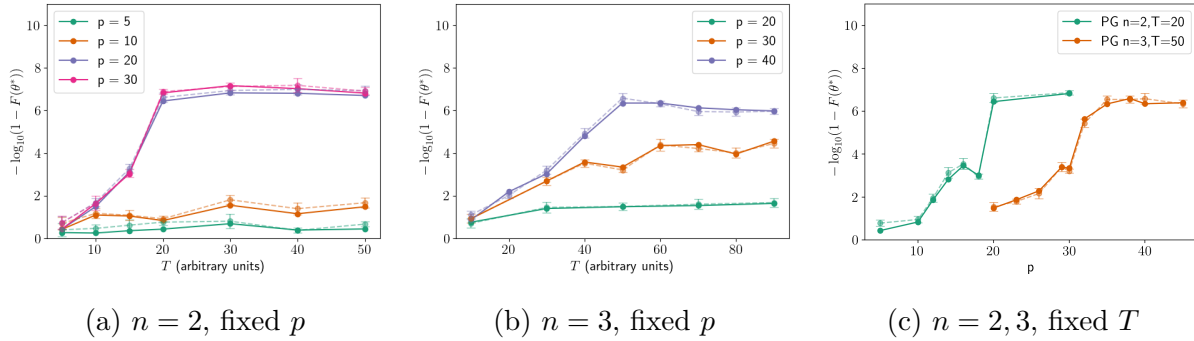
Figure 3.7: Z gate fidelity dependence on total evolution time T (panels (a),(b)) and control depth p (panel (c)) for isotropically coupled systems optimized with PG. All coupling constants are equal to $A_q = 1.0$. Each point is the best result of 3 or 5 parallel simulations with different protocol parameter initialization. For each pair of points with the same color and T value, the solid line is the actual optimization result and the dashed pale line with error bar is the average state fidelity over $M = 100$ Haar-random states. The fidelity, Eq. (3.17), is plotted as MLI, Eq. (3.23).

improvement in fidelity as p increases to 20, and we can infer that $p^* = 20$. For $n = 3$ the corresponding jump is not so drastic, but we can still see the appearance of a critical depth at $p^* = 32$. In general, the fidelity changes with time and with control depth display similar behaviors, with both increasing to a plateau value. The critical points represent the onset of plateau for each parameter. We note that only when one parameter is located beyond its critical value, can the other parameter show this pattern of increase to a plateau value. In all other situations the fidelity is restricted to low values.

The MLI differences between mean state fidelity (Eq. (3.19)) and unitary fidelity (Eq. (3.17)) are all within 0.5, corresponding to fidelity differences less than 10^{-7} in the plateau region, and the two fidelities display almost identical behavior. We thus find that the unitary fidelity is an effective generalized fidelity measure for optimization.

With knowledge of the critical depth p^* for the target gate Z, we can now choose parameters that give high fidelity with a relatively low depth and use these to test the critical depth for Hadamard and T gates. Fig. 8 summarizes results for these gates with $n = 2$ bath spins. Panels (a) and (b) show simulations with equal coupling constants, using depth values $p = 20, 30$ that are just above the critical depth $p^* = 20$. These results show similar trends to the results for the Z gate in Fig. 3.7. The fidelities reached for each of these target gates are of similar magnitude at sufficiently large T and p, with more than six nines in most cases. The critical depth and critical time are about $p^* = 20$ and $T^* = 20$ in all cases, which are the same values as for the Z gate. Thus, we can conclude that the control properties for different 1-qubit target unitaries are similar.

The results for the isotropic coupling model with equal coupling constants, i.e., all $A_q = 1$, are summarized in Table 3.4. Note that the results for $n = 1, 4$ are not plotted but the

(a) Hadamard Gate

(b) T gate

(c)   Different   Coupling
Strengths, Z gate
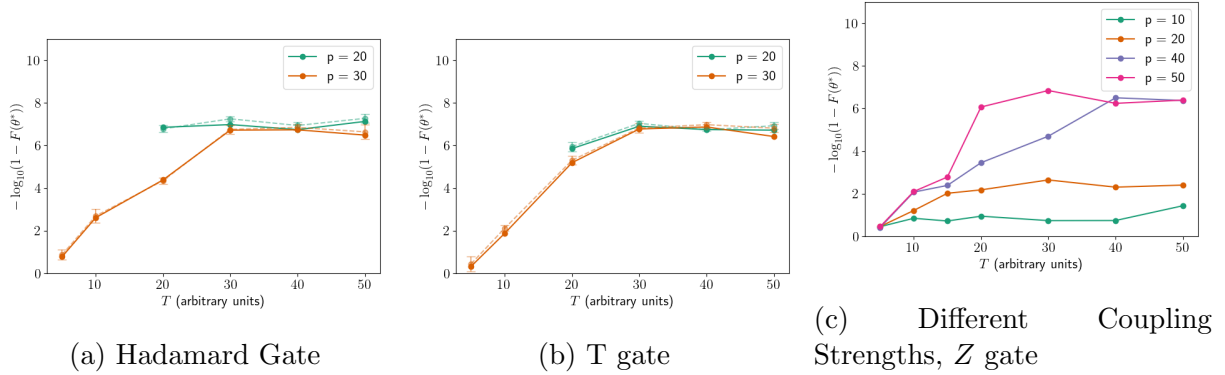
Figure 3.8: Single qubit gate fidelity dependence on total evolution time for isotropically coupled central spin systems with $n = 2$ bath spins optimized with PG. The target gates are (a) Hadamard gate, (b) T gate and (c) Z gate. In panels (a), (b), the coupling constants are all equal to $A_q = 1.0$. In panel (c), the coupling strengths are unequal and evenly distributed in the range $[1, 2]$. Each point in (a) and (b) is the best result of 3 or 5 parallel simulations with different initialization. For each pair of points with the same color and T value, the solid line is the actual optimization result and the pale dashed line with error bar is the average state fidelity over $M = 100$ Haar-random states. All fidelities are plotted as MLI, Eq. (3.23).

patterns are similar to those found in Figs. 3.7 and 3.8.

Target gate	# of bath spins (n)	Critical depth (p^*)	Critical time (T^*)	Highest MLI
Z	1	~ 10	~ 10	8.14
	2	~ 20	~ 20	7.17
	3	~ 32	~ 40	6.35
	4	~ 60	~ 70	5.38
Hadamard	2	≤ 20	~ 20	6.63
T	2	≤ 20	~ 20	6.91

Table 3.4: The estimated critical depth p^* and critical time T^* values, together with the highest MLI reached in single-qubit gate simulations of the reference isotropic coupling model with equal coupling strengths set equal to the energy of the single system qubit.

While not exact, the critical value assignments in Table 3.4 already show rich features of the control. A general trend with increasing bath spin count n is that the critical time T^* and critical depth p^* increase, while the highest fidelity drops. This trend is reasonable, since an increased bath size increases the noise strength and adds to the difficulty of the

control task. This result is consistent with the reduced dynamics shown in Fig. 3.1a in the absence of the control Hamiltonian, in which the dynamics of systems with different bath spin count n behave very differently within the timescale of the protocols.

As shown in [46], controllability is rather different when the coupling constants between the system and bath spins A_q vary with q. Specifically, when the coupling constants are different, the bath spins of the central spin model with isotropic couplings become controllable through bipartite control. However, the additional controllable degree of freedom adds difficulty to the control problem, and was found in [46] to result in lower fidelity than the equal coupling case. Fig. 3.8c shows the result of applying Hamiltonian switching on a single qubit system with coupling strengths uniformly distributed between 1 and 2, as employed in the controllability study of [46]. We can see from the plots that the difficulty of control is significantly greater when the couplings are different. The critical depth for 2 qubits increases to 40 or 50. In the case of $n = 2, p = 50$, we see the typical behavior of an initial increase in the MLI, and hence the fidelity, which is followed by a plateau above a critical depth p^*. Note that the critical time is still around 20, which is the same as the case of $n = 2$ for equal couplings in Fig. 3.7a. Changing to the variable coupling strengths A_q increases the critical depth p^* but appears to keep the critical time T^* the same. Notably, the fidelity above critical time and depth can still reach six nines.

We conducted a controllability analysis (described in Appendix 3.15) for the case of two bath spins, to understand whether the differences in precision achieved with Hamiltonian switching, as shown in Appendix 3.14, could be assigned to different extents of controllability. In general, controllability and fidelity are affected by different factors and controllablity analysis is not able to explain the fidelity differences observed between rotating and lab frames, nor of course, the differences due to the change of coupling strength. However, the controllability does affect the critical depth p^*, as shown above.

3.10 Four-Hamiltonian Switching

To improve the fidelity in the lab frame and weak coupling regime, we tested an ansatz containing an additional σ^y term, which results in switching between the following four

Hamiltonians for the dipole-dipole coupling model:

$$H_A^{\text{dipole}} = -\frac{E}{2}\sigma_0^z + 2E\sigma_0^x + \frac{3}{2}E\sigma_0^y - \sum_{q=1}^n \frac{\Delta_q}{2}\sigma_q^z + \sum_{q=1}^n \frac{A_q}{2}(\sigma_0^+\sigma_q^- + \sigma_0^-\sigma_q^+)$$

$$H_B^{\text{dipole}} = -\frac{E}{2}\sigma_0^z + 2E\sigma_0^x - \frac{3}{2}E\sigma_0^y - \sum_{q=1}^n \frac{\Delta_q}{2}\sigma_q^z + \sum_{q=1}^n \frac{A_q}{2}(\sigma_0^+\sigma_q^- + \sigma_0^-\sigma_q^+)$$

$$H_C^{\text{dipole}} = -\frac{E}{2}\sigma_0^z - 2E\sigma_0^x + \frac{3}{2}E\sigma_0^y - \sum_{q=1}^n \frac{\Delta_q}{2}\sigma_q^z + \sum_{q=1}^n \frac{A_q}{2}(\sigma_0^+\sigma_q^- + \sigma_0^-\sigma_q^+)$$

$$H_D^{\text{dipole}} = -\frac{E}{2}\sigma_0^z - 2E\sigma_0^x - \frac{3}{2}E\sigma_0^y - \sum_{q=1}^n \frac{\Delta_q}{2}\sigma_q^z + \sum_{q=1}^n \frac{A_q}{2}(\sigma_0^+\sigma_q^- + \sigma_0^-\sigma_q^+).$$

$$(3.25)$$

It can be readily shown that this ansatz is universal on the qubit. The fidelity dependence on evolution time T is plotted in Fig. 3.9.
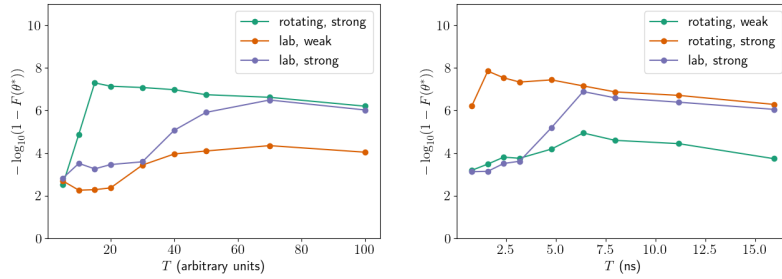
(a) Equal isotropic couplings   (b) Equal dipolar couplings

Figure 3.9: Fidelity dependence on evolution time T for a Z gate on a single qubit systems coupled to a bath of $n = 2$ spins, with (a) isotropic Heisenberg system-bath coupling, and (b) dipole-dipole coupling, and all equal coupling constants in both cases. Optimization of the control protocol is performed with PG, using 4-Hamiltonian switching, and control depth $p = 20$. For each set of plotted points, "lab" refers to lab frame (i.e., the Hamiltonian includes bath σ^Z terms), "rotating" refers to rotating frame (i.e., no bath σ^z terms), "strong" means strong coupling strength (i.e., of the same order of magnitude as the system energy splitting), and "weak", means weak coupling strength (i.e. about 10^{-3} relative to the system energy splitting). Each point is the best result of 5 parallel simulations with different initialization. The fidelity, Eq. (3.17), is plotted as MLI, Eq. (3.23).

3.11 Universality of 2-qubit Ansatz

The Lie algebra generated by the two-qubit ansatz Eq. (3.14), $\mathcal{L}_{2\text{qb}}$, without coupling to the bath is the same as that derived from

$$H_Z = \sigma_0^z + \omega\sigma_1^z + \gamma\sigma_0^z\sigma_1^z$$
$$H_X = \sigma_0^x + \sigma_1^x. \tag{3.26}$$

We note that to make this ansatz universal, one needs to set $\omega \neq 1$ (see [70]). From $[iH_Z, iH_X]$, we then get, up to a constant factor,

$$H_{\text{YZ}} = \sigma_0^y + \omega\sigma_1^y + \gamma(\sigma_0^y\sigma_1^z + \sigma_0^z\sigma_1^y) \tag{3.27}$$

From $[iH_{\text{YZ}}, iH_X]$ and linear combination with H_Z, we get, up to a constant factor,

$$H^{(1)} = 2\sigma_0^y\sigma_1^y - \sigma_0^z\sigma_1^z. \tag{3.28}$$

From $[iH^{(1)}, iH_X]$ and linear combination with H_{YZ}, we get, up to a constant factor,

$$H_Y = \sigma_0^y + \omega\sigma_1^y \tag{3.29}$$

From $[[iH_Y, iH_X], iH_Y]$, we get, up to a constant factor,

$$H_{X1} = \sigma_0^x + \omega^2\sigma_1^x \tag{3.30}$$

By evaluating the commutator and taking linear combinations between H_X, H_{X1}, H_Y, we can readily show that

$$i\sigma_0^x, i\sigma_0^y, i\sigma_0^z, i\sigma_1^x, i\sigma_1^y, i\sigma_1^z \in \mathcal{L}_{2\text{qb}}, \tag{3.31}$$

which means that arbitrary single-qubit rotations on either qubit can be generated. Additionally, arbitrary single-qubit unitaries combined with any entangling two-qubit operator can generate any $SU(4)$ unitary [70, 84]. Furthermore, we can readily show that the entangling $\sigma_0^z\sigma_1^z$ operator is in the Lie algebra by subtracting the single-qubit σ^z terms from H_Z. Therefore, this ansatz is universal when there are two qubits.

3.12 Non-universal Control

We also tested a model that is a single-qubit analog of the 4-level qudit model in [61] by changing the control term to $\pm 2E\sigma_0^z$ in Eq. (3.12), resulting in the following switching Hamiltonians

$$H_A^{\text{NonUni}} = -\frac{E}{2}\sigma_0^z + 2E\sigma_0^z - \sum_{q=1}^{n}\frac{\Delta_q}{2}\sigma_q^z + \sum_{q=1}^{n}\frac{A_q}{2}(\sigma_0^+\sigma_q^- + \sigma_0^-\sigma_q^+)$$
$$= H_S^{\text{1qubit}} + 2E\sigma_0^z + H_I^{\text{dipole}} + H_{\text{env}}^{\text{dipole}}$$
$$H_B^{\text{NonUni}} = -\frac{E}{2}\sigma_0^z - 2E\sigma_0^z - \sum_{q=1}^{n}\frac{\Delta_q}{2}\sigma_q^z + \sum_{q=1}^{n}\frac{A_q}{2}(\sigma_0^+\sigma_q^- + \sigma_0^-\sigma_q^+)$$
$$= H_S^{\text{1qubit}} - 2E\sigma_0^z + H_I^{\text{dipole}} + H_{\text{env}}^{\text{dipole}}. \tag{3.32}$$

Without the TLS bath this Hamiltonian can only generate Z-rotations and is thus not universal in SU(2). However, as noted in [61], the dipole-dipole coupling between the 4-level qudit and TLS introduces transversal terms to the Hamiltonian and thereby changes the algebraic structure of this ansatz, enabling it to generate transformations in a larger subspace of the corresponding unitary group. It is expected that the same argument might also hold for the model of Eq. (3.32), since the Lie algebra generated by the σ^z terms in Eq. (3.32) and the dipolar coupling terms of Eq. (3.6) has higher rank than the trivial Lie algebra generated by the drift and control term in Eq. (3.32) alone. This motivates a test of Hamiltonian switching with the non-universal ansatz Eq. (3.32).

We first analyzed the performance of Eq. (3.32) for implementation of a T gate without coupling to bath qubits. Since the gate itself is a Z-rotation, the ansatz can generate the gate with high fidelity, as shown in Fig. 3.10. Fig. 3.10a shows results for a T gate implemented on an isolated qubit by both the universal ansatz (Eq. (3.12)) and the non-universal ansatz (Eq. (3.32)). The universal ansatz shows the increase to a plateau value seen in the previous sections, whereas the non-universal ansatz gives a very high fidelity (over ten nines) for the shortest total durations, and does not show a plateau behavior. Estimates of the minimum time duration for the T gate realized under each ansatz using the Margolus–Levitin (ML) bound for driven quantum systems [85, 86] shows that the lower bound for the gate time using the non-universal ansatz ($\simeq 3.125$ ps) is shorter than that for the universal ansatz ($\simeq 3.790$ ps), which is consistent with this observation. Details of this analysis are in Sec. 3.13 All the simulations are carried out with T values well beyond the ML bounds. The fact that the critical times T^* are also larger than the minimum gate times is likely due to the constraint of a finite number of switches, i.e., to finite p values.

After turning on the coupling to $n > 0$ TLS, the fidelity is still above six nines and is weakly dependent on TLS count, as shown in Fig. 3.10b. Compared to the similar case for the universal ansatz in Fig. 3.3, which is also plotted in Fig. 3.10b, with highest fidelity around four nines, the fidelity of non-universal control ansatz is still higher. After tuning on Lindblad T_1 decay (purple points in Fig. 3.10b), the fidelity drops to around two nines, which is now similar to the performance of universal ansatz in Fig. 3.4. Lindblad results for $n = 0, 1$ (not shown) are virtually identical to the result shown here for $n = 2$, indicating that the fidelity dependence on the number of TLS n is even weaker in the presence of T_1 decay.

In the case of the Hadamard gate target (not shown), the straight fidelity without T_1 decay is about 0.5 for any number n of TLS (including $n = 0$). After turning on the T_1 decay, the straight fidelity drops with the protocol duration T but generally stays above 0.4. The straight fidelity for the same protocol duration with different numbers of TLS is almost the same and is well below 0.9 (i.e. a MLI less than 1).

In general, the non-universal control shows better performance when applied to Z-rotation gates like the T gate. For these gates, the fidelity obtained with the non-universal control is higher than can be obtained with the universal control ansatz and the critical times are shorter for $n = 0$. However, when applied to other gates such as the Hadamard gate, the non-universal control ansatz is not effective and gives fidelities well below 0.9. We note

(a) One isolated qubit

(b) One qubit with TLS and spontaneous emission
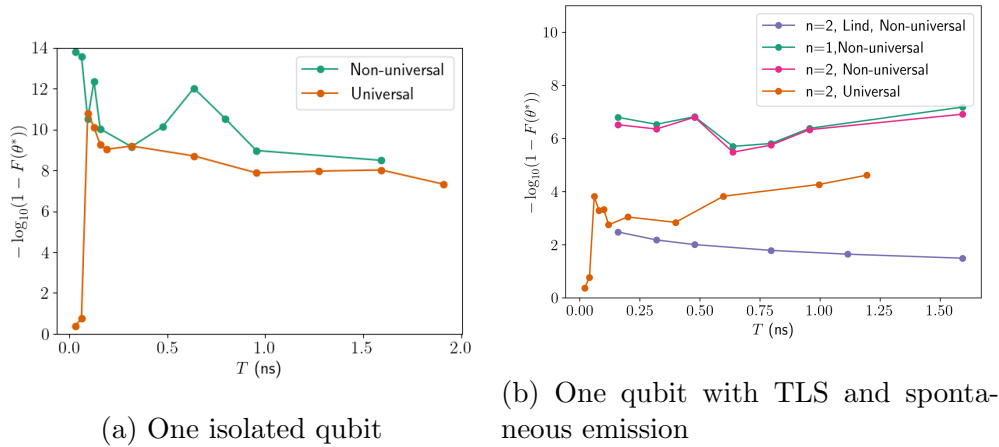
Figure 3.10: T gate fidelity dependence on total evolution time for (a) 1 isolated qubit (b) 1 qubit dipole coupled to n TLS. Optimizations were performed with PG, using a control depth $p = 20$ for calculations without Lindblad decoherence and $p = 30$ for calculations with Lindblad decoherence. The control ansatzes are Eq. (3.12) (universal) and Eq. (3.32) (non-universal). In panel (b), the purple line shows results for a system where both the qubit and TLS are subject to T_1 decay, with $T_1^{sys} = 500$ ns and $T_1^{TLS} = 200$ ns. All other lines show results with no Lindblad decoherence. The dipolar coupling constants are unequal and evenly distributed over $4 - 40$ MHz. Each point is the best result of 3 parallel simulations with different initialization. The fidelity, Eq. (3.21), is plotted as MLI, Eq. (3.23).

that the fidelity achieved for the T gate here is higher than that obtained for quantum gates on a 4-level qudit similarly experiencing spontaneous decay while also undergoing dipolar interaction with n TLS spins [61].

The non-universal ansatz is not capable of implementing arbitrary single-qubit gates. While it can reach higher fidelities when implementing Z-rotations including the T gate, also with lower critical time than the universal ansatz when $n = 0$, the fidelity is however very low when implementing other gates. Our analysis shows that while coupling to TLS changes the Lie algebraic structure of the coupled system-primary bath, it does not increase the fidelity per se when implementing either Z-rotation or Hadamard gates. This is because in this case, unlike the qudit case in [61], coupling the qubit system to TLS does not enable generation of high-fidelity transformations in a larger fraction of the corresponding unitary group. In general, this non-universal ansatz is better suited for implementing Z-rotation gates like the T gate, but is not as capable for other gates like the Hadamard gate.

3.13 Quantum Speed Limit for T Gate

In Fig. 3.10a, we observed the presence of increase to plateau behavior for the universal ansatz but not for the non-universal ansatz. In this section, we will apply the two versions of quantum speed limit (QSL) that are summarized in [86] to the implementation of a T gate, as an attempt to explain the differences in critical time T^* between the universal ansatz and the non-universal ansatz when $n = 0$ (i.e. 0.06 ns compared to < 0.02 ns). The QSL is one interpretation of the energy-time uncertainty principle, which defines the minimal time to drive between quantum states [86, 87]. Specifically, we focus on two theoretical lower bounds, Mandelstam–Tamm bound and Margolus–Levitin bound, for the time T to drive a state $|\psi_i\rangle$ to $|\psi_f\rangle$.

3.13.1 Mandelstam–Tamm bound

This bound is also referred to as Fleming-Bhattacharyya bound. Its idea originate from the bound derived in [88] and in [87], the author gave the bound

$$T \geq \frac{\hbar \arccos |\langle \psi_f | \psi_i \rangle|}{\Delta E} \equiv T_{\text{MT}} \tag{3.33}$$

where ΔE is the time-averaged energy variance and is defined as [86]

$$\Delta E_T = (1/T) \int_0^T dt \left(\langle H^2(t) \rangle - \langle H(t) \rangle^2 \right)^{1/2} \tag{3.34}$$

A Landau-Zener Hamiltonian is [67, 68, 89]

$$H(t) = \Gamma(t)\sigma^z + \omega(t)\sigma^x \tag{3.35}$$

for this Hamiltonian, we have

$$-\sqrt{\Gamma^2(t) + \omega^2(t)} \leq \langle H(t) \rangle \leq \sqrt{\Gamma^2(t) + \omega^2(t)}$$
$$0 \leq \langle H(t) \rangle^2 \leq \Gamma^2(t) + \omega^2(t), \tag{3.36}$$

where the lower and upper bounds of the first inequality are the two eigenvalues of the Hamiltonian. And for its square, we have

$$H^2(t) = (\Gamma^2(t) + \omega^2(t))I$$
$$\langle H^2(t) \rangle = \Gamma^2(t) + \omega^2(t). \tag{3.37}$$

We can't use Eq. 3.36 to give a meaningful bound for ΔE as the bounds are too loose. One needs to find a better bound for the energy fluctuations to use the Mandelstam–Tamm bound. Ref. [67] used a constant ω in place of ΔE and [89] used a expression for ΔE relevant to their control method.

The non-universal ansatz can be mapped to a Landau-Zener Hamiltonian with $\omega(t) = 0$. So the formula in [67] cannot be used for comparision, although it may be applicable to the universal ansatz. One very loose upper bound of ΔE can be gained by simply setting $\langle H(t) \rangle^2 = 0$, equal to its lower bound, then we have

$$\Delta E \leq \sqrt{\langle H^2(t) \rangle} = \sqrt{\Gamma^2(t) + \omega^2(t)} \tag{3.38}$$

3.13.2 Margolus–Levitin bound

This version of QSL was proposed in [85]. We also refer to the formulation in [86]. The bound is

$$T \geq \frac{\hbar \arccos | \langle \psi_f | \psi_i \rangle |}{E_T} \equiv T_{\text{ML}} \tag{3.39}$$

where $E_T = 1/T \int_0^T dt |\langle \psi_0 | H_t | \psi_0 \rangle|$, the time-averaged energy with repect to the initial state $|\psi_0\rangle$. Note that this average energy should be calibrated such that the ground state energy of the Hamiltonian is zero.

For the Hamiltonian switching problem, the Hamiltonian is piecewise constant and the average energy can be written as

$$
\begin{aligned}
E_T &= \frac{1}{T} T |\langle \psi_0 | H_A | \psi_0 \rangle f_A^T + \langle \psi_0 | H_B | \psi_0 \rangle f_B^T | - E_g \\
&= |\langle \psi_0 | H_A | \psi_0 \rangle f_A^T + \langle \psi_0 | H_B | \psi_0 \rangle f_B^T | - E_g
\end{aligned}
\tag{3.40}
$$

where f_A^T, f_B^T are the fraction of duration applying each Hamiltonian respectively and E_g is the ground state energy.

According to observations on the simulations results, we can approximately have $f_A^T = f_B^T = 1/2$. Then the average energy can be further simplified to

$$E_T \approx \frac{1}{2} |\langle \psi_0 | H_A | \psi_0 \rangle + \langle \psi_0 | H_B | \psi_0 \rangle| - E_g \tag{3.41}$$

This approximation will be used in the rest of this section.

3.13.3 T Gate on an Arbitrary State

Starting from an arbitrary state $|\psi_i\rangle = \cos(\theta/2)|0\rangle + e^{i\phi}\sin(\theta/2)|1\rangle$, a T gate will give a final state $|\psi_f\rangle = \cos(\theta/2)|0\rangle + e^{i(\phi+\pi/4)}\sin(\theta/2)|1\rangle$. Substituting in Eqs. 3.33 or 3.39 and after simplification, one gets

$$T_{\text{QSL}} = \frac{\arccos \sqrt{\left(1 + \frac{\sqrt{2}-2}{4}\sin^2\theta\right)}}{\text{Energy Factor}} \tag{3.42}$$

The numerator has a range $[0, \pi/8]$ and takes value $\pi/8$ when $\theta = \pi/2$ (i.e. a state on the equator of the Bloch Sphere).

We then focus on a initial state $|\psi_0\rangle = |+\rangle \equiv 1/\sqrt{2}\,|0\rangle + 1/\sqrt{2}\,|1\rangle$ and implement a T gate on it, resulting in a state $|\psi_T\rangle = 1/\sqrt{2}\,|0\rangle + (1/2 + i/2)\,|1\rangle$. The overlap angle for the numerator is $\arccos|\langle\psi_f|\psi_i\rangle| = \pi/8$.

3.13.3.1 Universal Ansatz

For the universal ansatz, the switching Hamiltonians are

$$
\begin{aligned}
H_A^{\text{uni}} &= -\frac{E}{2}\sigma_0^z + 2E\sigma_0^x \\
H_B^{\text{uni}} &= -\frac{E}{2}\sigma_0^z - 2E\sigma_0^x.
\end{aligned}
\tag{3.43}
$$

The ground state energy of both Hamiltonians is $-\sqrt{17}E/2$. We then have

$$
\begin{aligned}
\langle\psi_0|H_A|\psi_0\rangle &= 2E \\
\langle\psi_0|H_B|\psi_0\rangle &= -2E
\end{aligned}
\tag{3.44}
$$

Taking into account the ground state energy $-\sqrt{17}E/2$, we get $E_T = \sqrt{17}E/2$. That gives us a ML bound of

$$
T_{\text{ML}}^{\text{uni}} = \frac{h}{2\pi}\frac{\pi}{8}\frac{1}{\frac{\sqrt{17}E}{2}} = \frac{h}{8\sqrt{17}E}
\tag{3.45}
$$

choosing $E = h * 8$ GHz, we get $T_{\text{ML}}^{\text{uni}} \approx 3.790$ ps

3.13.3.2 Non-universal Ansatz

For the non-universal ansatz, the switching Hamiltonians are

$$
\begin{aligned}
H_A^{\text{nu}} &= -\frac{E}{2}\sigma_0^z + 2E\sigma_0^z = \frac{3E}{2}\sigma_0^z \\
H_B^{\text{nu}} &= -\frac{E}{2}\sigma_0^z - 2E\sigma_0^z = -\frac{5E}{2}\sigma_0^z.
\end{aligned}
\tag{3.46}
$$

The ground state energy of the Hamiltonians are $-3E/2, -5E/2$ respectively. We then have

$$
\begin{aligned}
\langle\psi_0|H_A|\psi_0\rangle &= 0 \\
\langle\psi_0|H_B|\psi_0\rangle &= 0
\end{aligned}
\tag{3.47}
$$

If we chose the ground state energy being $-5E/2$, we get $E_T = 5E/2$. That gives us a ML bound of

$$
T_{\text{ML}}^{\text{nu}} = \frac{h}{2\pi}\frac{\pi}{8}\frac{1}{\frac{5E}{2}} = \frac{h}{40E}
\tag{3.48}
$$

choosing $E = h * 8$ GHz, we get $T_{\text{ML}}^{\text{nu}} \approx 3.125$ ps.

As for the Mandelstam–Tamm bound, the loose bound for ΔE Eq. 3.38 actually gives the same value as the Margolus–Levitin presented above for both ansatz if one further upper bound $\sqrt{\Gamma^2(t) + \omega^2(t)}$ by the highest energy of the switching Hamiltonians. This consistency is the result of the loose bounds of the energy terms and the assumption of 'zero' average energy in both cases. The resultant numerical values of QSL are likely too small but they already reveal that the non-universal ansatz has a lower minimal bound for the duration of a T gate.

To get better bounds for the minimal gate times, there are two potential ways. The first is to evaluate the average energy during evolution numerically. It can be self-contradictory as each evolution has its own gate time but the general statistics of different evolutions may give insights into the common values of the energy average and variation. The second is to add the effect of coupling to the environment, as outlined in [90]. This may be rather involved for the spin bath model.

3.14 Factors Impacting Fidelity

To ascertain which system parameters determine the highest fidelity that can be achieved in the simulations, further single-qubit simulations were carried out for both types of CS couplings. In addition to different coupling strengths, we also compare the performance of the control when implemented in the rotating frame that simplifies the switching Hamiltonians, with the performance when implemented in the lab frame. We set $E = 1$ for the reference isotropic coupling model and $E = 8$ GHz for the physical dipolar coupling model. In the strong coupling regime for the isotropic model, we have $A_q = E = 1$ when the couplings are equal and A_q uniformly distributed in $[1, 2]$ when they are variable. In the weak coupling regime for isotropic couplings, we have $A_q = E = 0.005$ when the couplings are equal and A_q uniformly distributed in $[5, 10] \times 10^{-3}$ when they are variable. In the strong coupling regime for the dipole-dipole couplings, we have $A_q = E = 8$ GHz when the couplings are equal. In the weak coupling regime for dipole-dipole couplings, we have $A_q = 40$ MHz when the couplings are equal. For the $n = 2$ bath spin simulations shown below, we set $\Delta_q = 0$ for rotating frame implementation and $\Delta_q = 1.0, 1.1$ for lab frame implementation. The results are shown in Fig. 3.11. The parameters for the two models have the same numerical values in these simulations, which enables us to make comparisons across models. Note that the parameters for the dipole-dipole model are the same as those in Sec. 3.3.2.

The three plots in Fig. 3.11 show a very similar trend. Notably, we can only get a fidelity larger than $1 - 10^{-6}$ when we use both a rotating frame implementation and strong system-primary bath coupling. If the couplings are weak and/or we use a lab frame implementation, the highest fidelity we can reach will be around $1 - 10^{-4}$. The simulations do not include all possible combinations of the parameter choices since the presented plot already reveals this pattern.

To better understand the impact of coupling strength on fidelity, we carried out simulations for coupling strength of variable magnitude relative to the qubit energy. These results
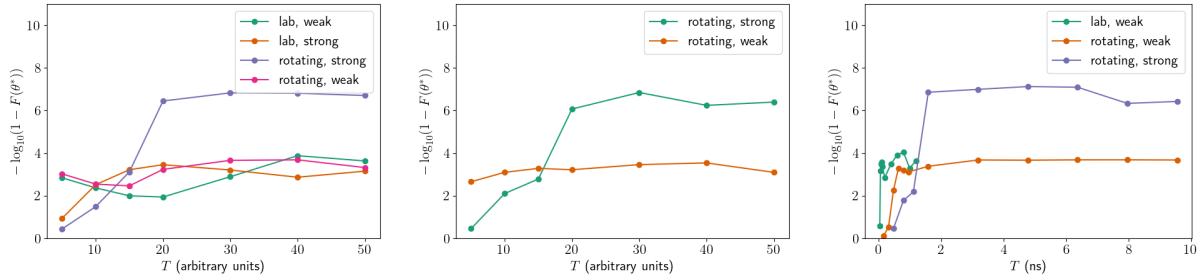
(a) Equal isotropic couplings   (b) Variable isotropic couplings   (c) Equal dipolar couplings

Figure 3.11: Fidelity dependence on evolution time for (a) and (b) isotropically and (c) dipole-dipole coupled systems optimized with PG. The target gate is Z. The coupling constants are equal in panels (a) and (c), and unequal in panel (b). The number of bath spins for all plots is $n = 2$. In the legend, 'lab' means lab frame (i.e. the Hamiltonian includes bath σ^z terms), 'rotating' means rotating frame (i.e. no bath σ^z terms), 'strong' means coupling strength of the same order of magnitude as the system energy splitting, and 'weak' means coupling strength about 10^{-3} relative to the system energy splitting. Each point is the best result of 3 or 5 parallel simulations with different initialization. The fidelity, Eq. (3.17), is plotted as MLI, Eq. (3.23).

are shown in Fig. 3.12, where the results at coupling strengths 1×8 GHz and $10^{-4} \times 8$ GHz correspond to points shown in Fig. 3.11. While the fidelity in the weak coupling limit is the highest, as expected since the noise induced by the coupling is weaker, the small rise in fidelity as the coupling strength becomes equal to the qubit energy is somewhat surprising and deserves further study. Over the entire range of coupling strength, the lowest fidelities obtained are between $10^{-1} \times 8$ GHz and $10^{-2} \times 8$ GHz.

To further understand the numerical properties of the optimal protocols, we evaluated the gradient and Hessian of the simulation results with $T = 30$ units in Fig. 3.11a. The l-infinity norm (i.e. largest absolute value of the components) of the gradients and the eigenvalues of Hessian matrices are summarized in Table 3.5. The gradients are all very small and the associated Hessians have a few large negative eigenvalues, the rest being relatively small. This indicates that the control solution is very near a global fidelity maximum. The large number of small Hessian eigenvalues suggests interesting possibilities for modifications to the control which operate primarily in the null space defined by the eigenvectors corresponding to these small eigenvalues. These changes will not affect fidelity thereby enabling other desirable properties such as robustness of control to be achieved [78].

(a) Rotating Frame   (b) Lab Frame
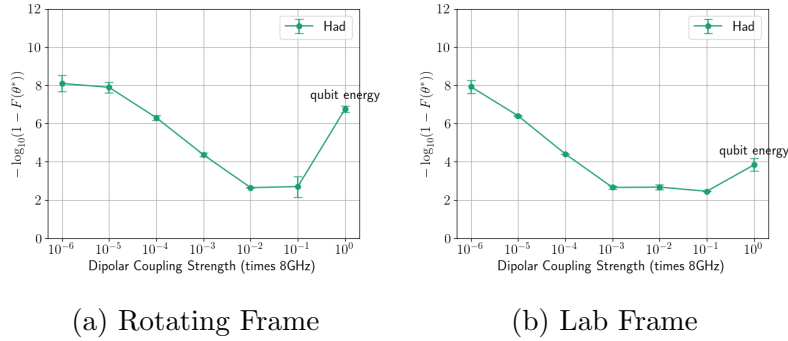
Figure 3.12: Fidelity dependence on coupling strength relative to qubit energy for dipole-dipole coupled systems optimized with PG. The target gate is Hadamard. The coupling constants are equal. The number of bath spins for both plots is $n = 2$. Each point is the best result of 3 or 5 parallel simulations with different initialization. The fidelity, Eq. (3.17), is plotted as MLI, Eq. (3.23).

3.15 Controllability Analysis: Isotropic Couplings

The analysis in this section focus on the case of $n = 2$ bath spins. For each model in this section and Appendix. 3.16, we will explore the single and two-spin Pauli terms that are in the Lie algebra that are generated by the corresponding Hamiltonians. A spin is fully controllable if all three single-spin Pauli terms are in the Lie algebra, as the corresponding Lie group is equal to the special unitary group [46]. For one qubit coupled to two bath spins, all the single and two spin terms are

$$
\begin{aligned}
&i\sigma_\alpha^x, i\sigma_\alpha^y, i\sigma_\alpha^z, \\
&i\sigma_\alpha^x\sigma_\beta^x, i\sigma_\alpha^x\sigma_\beta^y, i\sigma_\alpha^x\sigma_\beta^z, \\
&i\sigma_\alpha^y\sigma_\beta^x, i\sigma_\alpha^y\sigma_\beta^y, i\sigma_\alpha^y\sigma_\beta^z, \\
&i\sigma_\alpha^z\sigma_\beta^x, i\sigma_\alpha^z\sigma_\beta^y, i\sigma_\alpha^z\sigma_\beta^z,
\end{aligned}
\tag{3.49}
$$

where $\alpha, \beta \in \{0, 1, 2\}$.

The results of the analysis in this section are summarized in Table 3.6.

3.15.1 Rotating Frame

According to the controllability analysis for isotropically coupled systems in [46], when the coupling strengths are equal, the qubit is controllable and the CS bath is controllable in each subspace conserving total angular momentum, while when the coupling strengths are variable, the qubit and the full CS bath are both controllable, using a control ansatz with identical Lie algebra to that in this work.
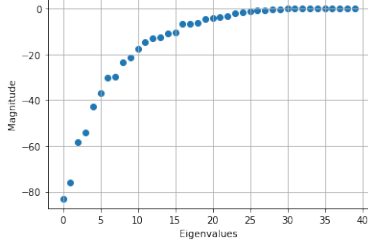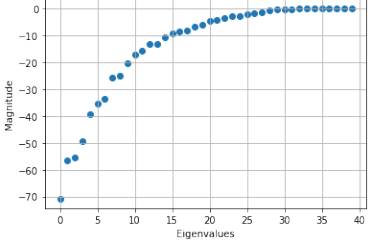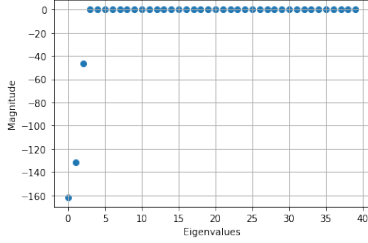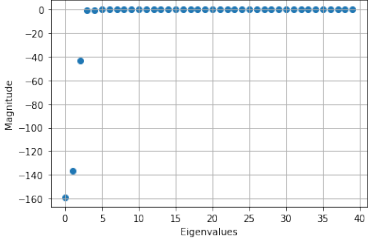
Model	Rotating Frame, Strong Couplings	Lab Frame, Strong Couplings
MLI	6.83	3.21
$|\nabla F(\theta)|_{\theta=\theta^*}|_\infty$	1.48×10^{-3}	1.46×10^{-3}
Hessian Eigenvalues		
Model	Rotating Frame, Weak Couplings	Lab Frame, Weak Couplings
MLI	3.66	2.89
$|\nabla F(\theta)|_{\theta=\theta^*}|_\infty$	0.91×10^{-3}	2.25×10^{-3}
Hessian Eigenvalues		

Table 3.5: *l*-infinity norm (i.e. largest absolute value of the components) of the gradients and plots of the eigenvalues of Hessian matrices for selected simulations for the isotropic models plotted in Fig. 3.11a

Frame	Equal coupling strength?	Qubit controllable?	Spin bath controllable?
Rotating	N	Y	Y
	Y	Y	N
Lab	N	Y	Y
	Y	Y	Y

Table 3.6: Summary of controllability of systems with 1 qubit coupled to 2 bath spins through isotropic couplings analyzed in this section.

3.15.2 Lab Frame

The Lie algebra generated by the two switching Hamiltonians is identical to that generated by

$$H_0^A = \sigma_0^z + g(\sigma_0^x\sigma_1^x + \sigma_0^y\sigma_1^y + \sigma_0^z\sigma_1^z) + h(\sigma_0^x\sigma_2^x + \sigma_0^y\sigma_2^y + \sigma_0^z\sigma_2^z) + \sigma_1^z + \epsilon\sigma_2^z$$
$$H_c^A = \sigma_0^x, \tag{3.50}$$

where g, h are the coupling constants and can be equal or not, and the bath energy splittings
are $1, \epsilon$ ($\epsilon \neq 1$). We define $A_1 = iH_0^A$ and $A_2 = iH_c^A$. With the commutator $[A_1, A_2]$, we
have, up to a constant

$$A_3 = i(\sigma_0^y + g(\sigma_0^y \sigma_1^z - \sigma_0^z \sigma_1^y) + h(\sigma_0^y \sigma_2^z - \sigma_0^z \sigma_2^y)). \tag{3.51}$$

From $[A_3, A_2]$, we get, up to a constant

$$A_4 = i(\sigma_0^z + g(\sigma_0^y \sigma_1^y + \sigma_0^z \sigma_1^z) + h(\sigma_0^y \sigma_2^y + \sigma_0^z \sigma_2^z)). \tag{3.52}$$

Then
$$A_5 = i(A_1 - A_4) = i(g\sigma_0^x \sigma_1^x + h\sigma_0^x \sigma_2^x + \sigma_1^z + \epsilon\sigma_2^z). \tag{3.53}$$

The nested commutator $[[A_3, A_4], A_5]$ yields up to a constant

$$A_6 = i(2g^2\sigma_1^y + h^2(1+\epsilon)\sigma_2^y + gh(h-g)\sigma_1^z\sigma_2^y + gh(g-h)\sigma_1^y\sigma_2^z + gh\sigma_0^x\sigma_1^x\sigma_2^y + gh\epsilon\sigma_0^x\sigma_1^y\sigma_2^x). \tag{3.54}$$

We then define

$$A^{(s)} = i(k_1^{(s)}\sigma_1^y + k_2^{(s)}\sigma_2^y + k_3^{(s)}\sigma_1^z\sigma_2^y + k_4^{(s)}\sigma_1^y\sigma_2^z + k_5^{(s)}\sigma_0^x\sigma_1^x\sigma_2^y + k_6^{(s)}\sigma_0^x\sigma_1^y\sigma_2^x),$$
$$A^{(s)} = [[A^{(s-1)}, A_5], A_5] \tag{3.55}$$
$$A^{(1)} = A_6,$$

and by evaluating the nested commutator with A_5, i.e., $[[\cdot, A_5], A_5]$, we then get the recursive
formulae

$$\begin{aligned}
k_1^{(s)} &= -k_1^{(s-1)}(g^2 + 1) \\
k_2^{(s)} &= -k_2^{(s-1)}(h^2 + \epsilon^2) \\
k_3^{(s)} &= -(h^2 + g^2 + \epsilon^2)k_3^{(s-1)} - 2ghk_4^{(s-1)} + gk_5^{(s-1)} + 2g\epsilon k_6^{(s-1)} \\
k_4^{(s)} &= -2ghk_3^{(s-1)} - (h^2 + g^2 + 1)k_4^{(s-1)} + 2hk_5^{(s-1)} + h\epsilon k_6^{(s-1)} \\
k_5^{(s)} &= gk_3^{(s-1)} + 2hk_4^{(s-1)} - (1 + \epsilon^2 + h^2)k_5^{(s-1)} - 2\epsilon k_6^{(s-1)} \\
k_6^{(s)} &= 2g\epsilon k_3^{(s-1)} + h\epsilon k_4^{(s-1)} - 2\epsilon k_5^{(s-1)} - (1 + \epsilon^2 + g^2)k_6^{(s-1)}
\end{aligned} \tag{3.56}$$

Inspired by the method in [46], we try to isolate the single spin terms $i\sigma_1^y, i\sigma_2^y$ by taking linear
combinations between $A^{(s)}$ formulae. If there exists six such coefficients, $s_1, s_2, s_3, s_4, s_5, s_6$,
such that the determinant of the following matrix

$$\begin{pmatrix}
k_1^{(s_1)} & k_2^{(s_1)} & k_3^{(s_1)} & k_4^{(s_1)} & k_5^{(s_1)} & k_6^{(s_1)} \\
k_1^{(s_2)} & k_2^{(s_2)} & k_3^{(s_2)} & k_4^{(s_2)} & k_5^{(s_2)} & k_6^{(s_2)} \\
k_1^{(s_3)} & k_2^{(s_3)} & k_3^{(s_3)} & k_4^{(s_3)} & k_5^{(s_3)} & k_6^{(s_3)} \\
k_1^{(s_4)} & k_2^{(s_4)} & k_3^{(s_4)} & k_4^{(s_4)} & k_5^{(s_4)} & k_6^{(s_4)} \\
k_1^{(s_5)} & k_2^{(s_5)} & k_3^{(s_5)} & k_4^{(s_5)} & k_5^{(s_5)} & k_6^{(s_5)} \\
k_1^{(s_6)} & k_2^{(s_6)} & k_3^{(s_6)} & k_4^{(s_6)} & k_5^{(s_6)} & k_6^{(s_6)}
\end{pmatrix} \tag{3.57}$$

is non-zero, then one can get $i\sigma_1^y, i\sigma_2^y$ from the linear combination between $A^{(s_1)}, A^{(s_2)}, A^{(s_3)}, A^{(s_4)}, A^{(s_5)}, A^{(s_6)}$ Numerical tests for $s_1, s_2, s_3, s_4, s_5, s_6 = 1, 2, 3, 4, 5, 6$ show that the determinant of the matrix Eq. (3.57) is generally non-zero for both $g = h$ and $g \neq h$. This implies that $i\sigma_1^y, i\sigma_2^y \in \mathcal{L}$. Other single and two-spin terms in Eq. (3.49) can be obtained by the following steps:

- from $[i\sigma_1^y, A_4]$, we get, up to a constant, $i\sigma_0^z\sigma_1^x$ and similarly $i\sigma_0^z\sigma_2^x$

- from $[i\sigma_1^y, i\sigma_0^z\sigma_1^x]$, we get, up to a constant,, $i\sigma_0^z\sigma_1^z$ and similarly $i\sigma_0^z\sigma_2^z$

- from $[i\sigma_0^x, i\sigma_0^z\sigma_1^x]$, we get up, to a constant $i\sigma_0^y\sigma_1^x$, and similarly $i\sigma_0^y\sigma_1^x, i\sigma_0^y\sigma_2^x, i\sigma_0^y\sigma_1^z, i\sigma_0^y\sigma_2^z$

- from $[[\sigma_1^y, A_5], i\sigma_0^z\sigma_1^z]$, we get up, to a constant, $i(g\sigma_0^y - \sigma_0^z\sigma_1^y)$. Similarly, we obtain $i(h\sigma_0^y - \epsilon\sigma_0^z\sigma_2^y)$. Taking linear combinations of these terms with $A_3, \sigma_0^y\sigma_1^z, \sigma_0^y\sigma_2^z$, we get,, up to a constant $i\sigma_0^y$

- other terms in Eq. (3.49) can be readily generated

These steps hold for both $g = h$ and $g \neq h$. The Lie algebra generated in this way guarantees that the qubit and bath spins are all controllable as all the single and two-spin terms are in the Lie algebra. [46, 91].

3.16 Controllability Analysis: Dipole-dipole Couplings

The analysis in this section focuses on the case of $n = 2$ bath spins. The results of the analysis in this section are summarized in Table 3.3.

3.16.1 Rotating Frame

The Lie algebra generated by the two switching Hamiltonians is identical to that generated by

$$
\begin{aligned}
H_0^B &= \sigma_0^z + g(\sigma_0^x\sigma_1^x + \sigma_0^y\sigma_1^y) + h(\sigma_0^x\sigma_2^x + \sigma_0^y\sigma_2^y) \\
H_c^B &= \sigma_0^x
\end{aligned}
\tag{3.58}
$$

where g, h are the coupling constants and can be equal or not. Similarly, we define $B_1 = iH_0^B$ and $B_2 = iH_c^B$. With the commutator $[B_1, B_2]$, we have, up to a constant,

$$
B_3 = i(\sigma_0^y - g\sigma_0^z\sigma_1^y - h\sigma_0^z\sigma_2^y).
\tag{3.59}
$$

From $[B_3, B_2]$, we get, up to a constant

$$
B_4 = i(\sigma_0^z + g\sigma_0^y\sigma_1^y + h\sigma_0^y\sigma_2^y).
\tag{3.60}
$$

Then

$$
B_5 = i(B_1 - B_4) = i(g\sigma_0^x\sigma_1^x + h\sigma_0^x\sigma_2^x).
\tag{3.61}
$$

From $[[B_5, B_3], B_3]$, we get, up to a constant

$$B_6 = i(g^2 \sigma_1^z + h^2 \sigma_2^z + g(h^2 + 1)\sigma_0^x \sigma_1^x + h(g^2 + 1)\sigma_0^x \sigma_2^x). \tag{3.62}$$

We can similarly define

$$\begin{aligned}
B^{(s)} &= i(l_1^{(s)} \sigma_1^z + l_2^{(s)} \sigma_2^z + l_3^{(s)} \sigma_0^x \sigma_1^x + l_4^{(s)} \sigma_0^x \sigma_2^x), \\
B^{(s)} &= [[B^{(s-1)}, B_3], B_3] \\
B^{(1)} &= B_6,
\end{aligned} \tag{3.63}$$

and by evaluating the nested commutators with B_3, i.e., $[[\cdot, B_3], B_3]$, we then get the recursive formulae

$$\begin{aligned}
l_1^{(s)} &= l_1^{(s-1)} g^2 + l_3^{(s-1)} g \\
l_2^{(s)} &= l_2^{(s-1)} h^2 + l_4^{(s-1)} h \\
l_3^{(s)} &= l_1^{(s-1)} g + l_3^{(s-1)} (h^2 + 1) \\
l_4^{(s)} &= l_2^{(s-1)} h + l_4^{(s-1)} (g^2 + 1).
\end{aligned} \tag{3.64}$$

3.16.1.1 Variable Couplings

Inspired by the method in [46], we try to isolate the single spin terms $i\sigma_1^z, i\sigma_2^z$ by taking linear combinations between $B^{(s)}$ formulae. If there exists four such coefficients, s_1, s_2, s_3, s_4, such that the determinant of the following matrix

$$\begin{pmatrix}
l_1^{(s_1)} & l_2^{(s_1)} & l_3^{(s_1)} & l_4^{(s_1)} \\
l_1^{(s_2)} & l_2^{(s_2)} & l_3^{(s_2)} & l_4^{(s_2)} \\
l_1^{(s_3)} & l_2^{(s_3)} & l_3^{(s_3)} & l_4^{(s_3)} \\
l_1^{(s_4)} & l_2^{(s_4)} & l_3^{(s_4)} & l_4^{(s_4)}
\end{pmatrix} \tag{3.65}$$

is non-zero, then one can get $i\sigma_1^z, i\sigma_2^z$ from the linear combination between $B^{(s_1)}, B^{(s_2)}, B^{(s_3)}, B^{(s_4)}$. Numerical tests for $s_1, s_2, s_3, s_4 = 1, 2, 3, 4$ show that the determinant of the matrix Eq. (3.65) is generally non-zero for $g \neq h$. This implies $i\sigma_1^z, i\sigma_2^z \in \mathcal{L}$. With commutators and linear combinations between $i\sigma_1^z, i\sigma_2^z$ and B_3, B_4, B_5, the following single and two-qubit/spin terms can be generated.

$$i\sigma_0^\alpha, i\sigma_a^z, i\sigma_0^\alpha \sigma_a^\beta \tag{3.66}$$

Where $\alpha = x, y, z$, $\beta = x, y$ and $a = 1, 2$. The qubit is controllable but the full system is not.

3.16.1.2 Equal Couplings

When $g = h$, the determinant 3.65 is always zero. We then attempted to get $i\sigma_1^z, i\sigma_2^z$ from other commutators but were not successful. Therefore, the only single spin term that we have found to be in the Lie algebra generated by the Hamiltonians Eq. (3.58) is σ^x on the qubit, and thus it appears that neither the qubit nor the bath spins are controllable.

3.16.2 Lab Frame

The Lie algebra generated by the two switching Hamiltonians is identical to that generated
by

$$H_0^C = \sigma_0^z + g(\sigma_0^x\sigma_1^x + \sigma_0^y\sigma_1^y) + h(\sigma_0^x\sigma_2^x + \sigma_0^y\sigma_2^y) + \sigma_1^z + \epsilon\sigma_2^z$$
$$H_c^C = \sigma_0^x,$$

$$(3.67)$$

where g, h are the coupling constants and can be equal or not, and the bath energy splittings
are $1, \epsilon$ ($\epsilon \neq 1$). We define $C_1 = iH_0^C$ and $C_2 = iH_c^C$. With the commutator $[C_1, C_2]$, we
have, up to a constant,

$$C_3 = i(\sigma_0^y - g\sigma_0^z\sigma_1^y - h\sigma_0^z\sigma_2^y). \qquad (3.68)$$

From $[C_3, C_2]$, we get, up to a constant,

$$C_4 = i(\sigma_0^z + g\sigma_0^y\sigma_1^y + h\sigma_0^y\sigma_2^y). \qquad (3.69)$$

Then

$$C_5 = i(C_1 - C_4) = i(g\sigma_0^x\sigma_1^x + h\sigma_0^x\sigma_2^x + \sigma_1^z + \epsilon\sigma_2^z) \qquad (3.70)$$

From $[[C_5, C_3], C_3]$, we get, up to a constant,

$$C_6 = i(2g^2\sigma_1^z + h^2(1+\epsilon)\sigma_2^z + g(h^2+2)\sigma_0^x\sigma_1^x + h(g^2+1+\epsilon)\sigma_0^x\sigma_2^x). \qquad (3.71)$$

We can similarly define

$$C^{(s)} = i(m_1^{(s)}\sigma_1^z + m_2^{(s)}\sigma_2^z + m_3^{(s)}\sigma_0^x\sigma_1^x + m_4^{(s)}\sigma_0^x\sigma_2^x),$$
$$C^{(s)} = [[C^{(s-1)}, C_3], C_3] \qquad (3.72)$$
$$C^{(1)} = C_6,$$

and by evaluation of the nested commutators with C_3, i.e., $[[\cdot, C_3], C_3]$, we get the recursive
formulae

$$m_1^{(s)} = m_1^{(s-1)}g^2 + m_3^{(s-1)}g$$
$$m_2^{(s)} = m_2^{(s-1)}h^2 + m_4^{(s-1)}h$$
$$m_3^{(s)} = m_1^{(s-1)}g + m_3^{(s-1)}(h^2+1) \qquad (3.73)$$
$$m_4^{(s)} = m_2^{(s-1)}h + m_4^{(s-1)}(g^2+1).$$

Inspired by the method in [46], we try to isolate the single spin terms $i\sigma_1^z, i\sigma_2^z$ by taking
linear combinations between $C^{(s)}$ formulae. If there exists six such coefficients, s_1, s_2, s_3, s_4,
such that the determinant of the following matrix

$$\begin{pmatrix} m_1^{(s_1)} & m_2^{(s_1)} & m_3^{(s_1)} & m_4^{(s_1)} \\ m_1^{(s_2)} & m_2^{(s_2)} & m_3^{(s_2)} & m_4^{(s_2)} \\ m_1^{(s_3)} & m_2^{(s_3)} & m_3^{(s_3)} & m_4^{(s_3)} \\ m_1^{(s_4)} & m_2^{(s_4)} & m_3^{(s_4)} & m_4^{(s_4)} \end{pmatrix} \qquad (3.74)$$

is non-zero, then one can get $i\sigma_1^z, i\sigma_2^z$ from the linear combination between $C^{(s_1)}, C^{(s_2)}, C^{(s_3)}, C^{(s_4)}$. Numerical tests for $s_1, s_2, s_3, s_4 = 1, 2, 3, 4$ show that the determinant of the matrix Eq. (3.74) is generally non-zero for both $g = h$ and $g \neq h$. This implies $i\sigma_1^z, i\sigma_2^z \in \mathcal{L}$. With commutators and linear combinations between $i\sigma_1^z, i\sigma_2^z$ and C_3, C_4, C_5, the following single and two-qubit/spin terms can be generated.

$$i\sigma_0^\alpha, i\sigma_a^z, i\sigma_0^\alpha \sigma_a^\beta \tag{3.75}$$

Where $\alpha = x, y, z$, $\beta = x, y$ and $a = 1, 2$. These steps hold for both $g = h$ and $g \neq h$. The qubit is controllable but the full system is not.

3.17 Future Works

The following extensions of this work have either been tested or discussed, but are not published in [33].

3.17.1 Beyond Bang-bang Control

In [92], the authors showed that in traverse field Ising model, a bang-anneal-bang control can give better results than QAOA. They used a gradient based optimization method with Lagrange multiplier. This method can be potentially applied to the control problem in this work to further enhance the gate fidelity.

As the optimization formalism in [92] works on state vectors, applying it to the fidelity measure Eq. 3.17 is non-trivial. However, by converting the density matrix in fidelity measure Eq. 3.21 to its vectorized form, the optimization method in [92] can be conveniently applied.

3.17.2 Ancillary Qubits

As shown in [93] and Chapter 4, adding ancillary qubits to quantum machine learning (QML) models can partially mitigate the effect of decoherence and enhance robustness. Due to the shared varational nature of QML and QAOA, it is reasonable to contemplate that using ancillary qubits for the control problem in this paper can improve gate fidelity.

In the case of adding one controlled ancillary qubit to the implementation of single-qubit gates, the two-qubit ansatz Eq. 3.14 can be employed for the control and the final fidelity is computed by treating the ancillary qubit as a bath spin/TLS. Initial results are shown in Fig. 3.13

The fidelity without any TLS is only four 9s, which is lower than the case without ancillary qubit. No significant improvement is seen in the simulations with TLS couplings. This result shows no significant benefit from introducing ancillary qubits.

However, this result does not prove that the noise-resilience in [93] can't be realized in this control problem. As the QML ansatz in [93] is much more flexible than the ansatz
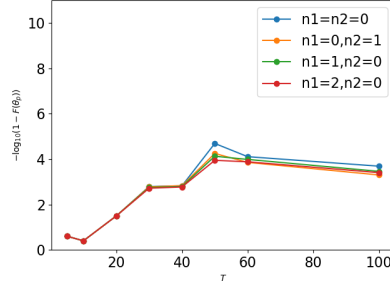
Figure 3.13: Single qubit gate fidelity dependence on total evolution time for dipole-dipole coupled systems with one ancillary qubit optimized with PG. The target gate is Z. The number of TLS coupled to the main qubit and ancilla are n_1, n_2 respectively. The coupling constants are unequal and evenly distributed over 4-40 MHz, which is in the relevant strength range for superconducting devices. Each point is the best result of 3 or 5 parallel simulations with different initialization. All fidelities are plotted as MLI, Eq. 3.23.

Eq. 3.14 in this work and the optimization methods are different, it is possible that higher fidelity with ancillary qubits can be achieved with a different ansatz and better optimization algorithms.

3.17.3 Robustness to parameter Fluctuations

It is of desirable to have controls that are robust to parameter fluctuations. The worst-case fidelity is taken to be the reward function of the optimizer, as the case in [39, 40].

$$F_{\mathrm{w}}(\boldsymbol{\theta}) = \min_{\delta \in \Delta} F(\boldsymbol{\theta}, \delta) \tag{3.76}$$

For each realization of noise δ, the dynamics of the systems are changed accordingly as

$$
\begin{aligned}
H_{\mathrm{A,ns}} &= -\frac{1}{2}\sigma_0^z + 2\sigma_0^x + \sum_{q=1}^{n}(A_q + \delta_q)\sum_s \sigma_0^s \sigma_q^s \\
H_{\mathrm{B,ns}} &= -\frac{1}{2}\sigma_0^z - 2\sigma_0^x + \sum_{q=1}^{n}(A_q + \delta_q)\sum_s \sigma_0^s \sigma_q^s
\end{aligned}
\tag{3.77}
$$

In the case of Lindblad dynamics, we can introduce uncertainty on the decoherence rate

$$\frac{\partial \rho}{\partial t} = -i[H(t), \rho] + \sum_i (\gamma_i + \delta_i)\left(L_i \rho L_i^\dagger - \frac{1}{2}\{L_i^\dagger L_i, \rho\}\right) \tag{3.78}$$

The noise parameters are sampled from a uniform distribution with $\delta \sim \mathcal{U}(-\Delta, \Delta)$.

Trial simulations in this scenario have been done and the fidelity level is similar to the case without parameter uncertainties.

Chapter 4

Quantum Machine Learning in Open Quantum Systems

4.1 Preface

This chapter is taken from the previously published Ref. [93], originally appearing in Quantum Machine Intelligence. It was co-authored by Haoran Liao, Ian Convy, the author of this thesis, and Professor K. Birgitta Whaley. The numerical simulations were done by Haoran Liao and the author of this thesis. Haoran Liao and Ian Convy did analysis on machine learning framework and the author of this thesis contributed to the analysis on open quantum system. The majority of the writing was completed by Haoran Liao.

4.2 Introduction

Tensor networks (TNs) are compact data structures engineered to efficiently approximate certain classes of quantum states used in the study of quantum many-body systems. Many tensor network topologies are designed to represent the low-energy states of physically realistic systems by capturing certain entanglement entropy and correlation scalings of the state generated by the network [94–97]. Some tensor networks allow for interpretations of coarse-grained states at increasing levels of the network as a renormalization group or scale transformation that retains information necessary to understand the physics on longer length scales [98, 99]. This motivates the usage of such networks to perform discriminative tasks, in a manner similar to classical machine learning (ML) using neural networks with layers like convolution and pooling that perform sequential feature abstraction to reduce the dimension and to obtain a hierarchical representation of the data [100, 101]. In addition to applying TNs such as the tree tensor network (TTN) [102] and the multiscale entanglement renormalization ansatz (MERA) [103] for quantum-inspired tensor network ML algorithms [104–106], there have been efforts to variationally train the generic unitary nodes in TNs to perform quantum machine learning (QML) on data-encoded qubits. The unitary TTN [107, 108] and

MERA [107] have been explored for this purpose mindful of feasible implementations, such as normalized input states, on a quantum computer.

Tensor network QML models are linear classifiers on a feature space whose dimension grows exponentially in the number of data qubits and where the feature map is non-linear. Such models employ fully-parametrized unitary tensor nodes that form a rich subset of larger unitaries with respect to all input and output qubits upon tensor contractions. They provide circuit variational ansatze more general than those with common parametrized gate sets [109–111], although their compilations into hardware-dependent native gates are more costly because of the need to compile generic unitaries.

In this work, we focus on discriminative QML. We investigate and numerically quantify the competing effect between decoherence and increasing bond dimension of two common tensor network QML models, namely the unitary TTN and the MERA. By removing the off-diagonal elements, i.e., the coherence, from the density matrix of a quantum state, we reduce its representation down to a classical probability distribution over a given basis. The evolution through the unitary matrices at every layer of the model, together with the full de-phasing of the density matrix at input and output, then becomes successive Bayesian updates of classical probability distributions, thus removing the quantumness of the model. This process can occur between any two layers of the unitary TTN or the MERA, and should in principle reduce the amount of information or representative flexibility available to the classification algorithm. However, as we add and increase the number of ancillas and accordingly increase the virtual bond dimension of the tensor networks, this diminished expressiveness may be compensated by the increased dimension of the classical probability distributions and their conditionals, manifested in the increasing number of diagonals intermediate within the network, as well as by the increased sized of the stochastic matrices encapsulated by the corresponding Bayesian networks in the fully-dephased limit. The possibility that an increased bond dimension fully compensates for the decoherence of the network would indicate that the role of coherence in QML is not essential and it offers no unique advantage, whereas a partial compensation provides insights into the trade-off between adding ancillas and increasing the level of decoherence in affecting the network performance, and therefore offers guidance in determining the number of noisy ancillas to be included in NISQ-era [9] implementations.

The remainder of the paper is structured as follows. Sec. 4.3 explains two tensor network QML models, the unitary TTN and the MERA. Sec. 4.4 reviews the dephasing effect on quantum states and shows its effect on the models from the perspective of regression. In Sec. 4.5 we explain the scheme in which ancillas are added to the networks and the growth of the virtual bond dimensions of the networks. Sec. 4.6 summarizes related work to unify fully-dephased tensor networks into probabilistic graphical models. In Sec. 4.7 we numerically experiment on natural images to show the competing effect between decoherence and adding ancillas while accordingly increasing the virtual bond dimension of the network. Sec. 4.8 summarizes and discusses the conclusions. In App. 4.10, a formal mathematical treatment to connect the fully-dephased tensor networks to classical Bayesian networks is presented.
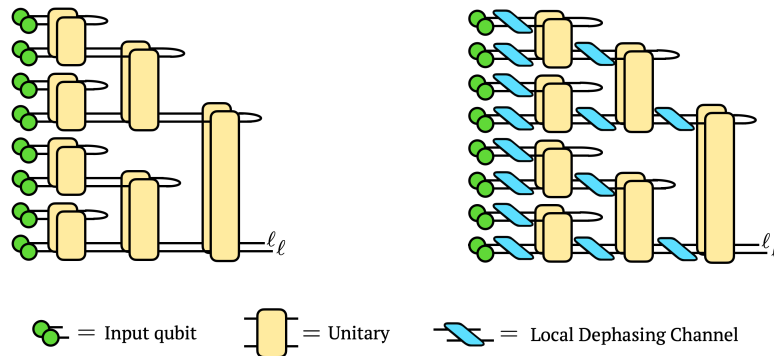
Figure 4.1: Left: A unitary TTN on eight input features encoded in the density matrices ρ_{in}'s forming the data layer, where the basis state ℓ is measured at the output of the root node. Right: Dephasing the unitary TTN is to insert dephasing channels with a dephasing rate p, assumed to be uniform across all, into the network between every layer.

4.3 Preliminary

4.3.1 Tensor Network QML Models

4.3.1.1 Unitary TTN

Unitary TTN is a classically tractable realization of tensor network QML models, with a topology that can be interpreted as a local coarse-graining transformation that keeps the most relevant degrees of freedom, in a sense that the information contained within each subtree is separated from those contained outside of the subtree. We focus on 1D binary trees. A generic binary TTN consists of $\log(m)$ layers of nodes where m is the number of input features, plus a layer of data qubits appended to the leaf level of the tree. A diagram of the unitary TTN is shown in Fig. 4.1 (left). Every node in a unitary TTN is forced to be a unitary matrix with respect to its input and output Hilbert spaces. Each unitary tensor entangles a pair of inputs from the previous layer. At each layer, one of the two output qubits is unobserved and also not further operated on, while the other output qubit is evolved by a node at the next layer. If the classification is binary, at the output of the last layer, namely the root node, only one qubit is measured. Accumulation of measurement statistics then reveals the confidence in predicting the binary labels associated with the measurement basis. After variationally learning the weights in the unitary nodes, we recover a quantum channel such that the information contained in the output qubits of each layer can be viewed as a coarse-grained representation of that in the input qubits, which sequentially extracts useful features of the data encoded in the data qubits. A dephased unitary TTN has local *dephasing channels* inserted between any two layers of the network, as depicted in Fig. 4.1 (right).

4.3.1.2   MERA

In tensor network QML, the MERA topology overcomes the drawback of local coarse-graining in unitary TTN by adding disentanglers U, which are unitaries, to connect neighboring subtrees. Its subsequent decimation of the Hilbert space by a MERA is achieved by isometries V that obey the isometric condition only in the reverse coarse-graining direction, i.e., $V^\dagger V = I'$ but $VV^\dagger \neq I$. From the perspective of discriminative QML, these unitaries correlate information from states in neighboring subtrees. We thus refer to these unitaries as entanglers.

By the design of MERA [103], the adjoint of an isometry, namely an isometry viewed in the coarse-graining direction in QML, can be naively achieved by measuring one of the two output qubits in the computational basis and post-selecting runs with measurements yielding $|0\rangle$. However, this way of decimating the Hilbert space is generally prohibitive, given the vanishing probability of sampling a bit string of all output qubits with most of them in $|0\rangle$. Hence, operationally an isometry is replaced by a unitary node, half of whose output qubits are partially traced over, which is the same as a unitary node in the TTN. The MERA can now be understood as a unitary TTN with extra entanglers inserted before every tree layer except the root layer, such that they entangle states in neighboring subtrees, as shown in Fig. 4.2 (left). Its dephased version is similar to the dephased unitary TTN, as depicted in Fig. 4.2 (right).

4.4   Dephasing

4.4.1   Dephasing Qubits after Unitary Evolution

A dephasing channel with a rate $p \in (0, 1]$ on a qubit is obtained by tracing out the environment after the environment scatters off of the qubit with some probability p. We denote the dephasing channel on a qubit with a dephasing rate p as $\mathcal{E}$, such that

$$
\begin{aligned}
\mathcal{E}[\rho] &= (1 - \frac{1}{2}p)\rho + \frac{1}{2}p\sigma_3\rho\sigma_3 \\
&= \sum_{ij}(1-p)^{1-\delta_{ij}} \langle i|\rho|j\rangle |i\rangle \langle j| = \sum_{ij}(1-p)^{1-\delta_{ij}} \rho_{ij} |i\rangle \langle j|,
\end{aligned}
\tag{4.1}
$$

where the summation goes from 0 to 1 for every index hereafter unless specified otherwise, whose effect is to damp the off-diagonal entries of the density matrix by $(1 - p)$. The operator-sum representation of $\mathcal{E}[\rho]$ can be written as with the two Kraus operators[1],

$$
K_0 = \sqrt{1 - \frac{p}{2}}I, \quad K_1 = \sqrt{\frac{p}{2}}\sigma_3,
\tag{4.2}
$$

---

[1]A more commonly-used, but less computationally efficient in terms of Eq. (4.3), representation uses three Kraus operators: $K_0 = \sqrt{1-p}I$ and $K_{1/2} = \frac{\sqrt{p}}{2}(I \pm \sigma_3)$ such that $\mathcal{E}[\rho] = \sum_{i=0}^{2} K_i\rho K_i^\dagger$ and $\sum_{i=0}^{2} K_i^\dagger K_i = I$.
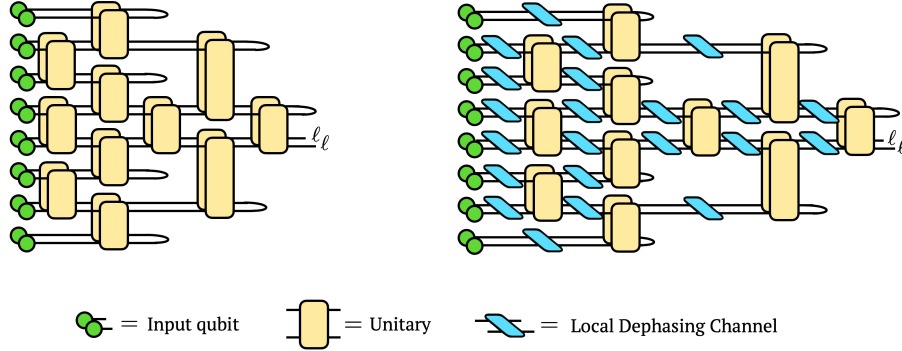
Figure 4.2: Left: A MERA on eight input features encoded in the ρ_{in}'s forming the data layer, where the basis state ℓ is measured at the output of the root node. Right: Dephasing the MERA is to insert dephasing channels with a dephasing rate p, assumed to be uniform across all, into the network between every layer.

defined such that $\mathcal{E}[\rho] = \sum_i K_i \rho K_i^\dagger$ and $\sum_i K_i^\dagger K_i = I$. Assuming local dephasing on each qubit, the dephasing channel on the density matrix ρ of m qubits, entangled or not, is given by

$$\mathcal{E}[\rho] = \sum_{i_1,\ldots,i_m} \left(\bigotimes_{n=1}^{m} K_{i_n} \right) \rho \left(\bigotimes_{n=1}^{m} K_{i_n}^\dagger \right). \tag{4.3}$$

If we allow a generic unitary U to act on $\mathcal{E}[\rho]$ for a single qubit, we have the purity of the resultant state given by

$$\begin{aligned}
\text{Tr}\left[\left(U\mathcal{E}[\rho]U^\dagger \right)^2 \right] &= \text{Tr}\left[\left(\left(1 - \frac{p}{2} \right) \rho + \frac{p}{2} \sigma_3 \rho \sigma_3 \right)^2 \right] \\
&= \left(1 - p + \frac{p^2}{2} \right) \text{Tr}\left(\rho^2 \right) + \left(p - \frac{p^2}{2} \right) \text{Tr}\left(\rho \sigma_3 \rho \sigma_3 \right) \\
&= \text{Tr}\left(\rho^2 \right) - 4p\rho_{01}^2 \left(1 - \frac{p}{2} \right) \leq \text{Tr}\left(\rho^2 \right),
\end{aligned} \tag{4.4}$$

where we used Eq. (4.1) in the first line. Therefore, in a given basis, successive applications of a dephasing channel and generic unitary evolution decrease the purity of any input quantum state, until the state becomes maximally mixed[2]. Successively applying the dephasing channel alone decreases the purity of the state until it becomes fully decohered, namely diagonal in its density operator in a given basis. It is thus a process in which quantum information of the input is irreversibly and gradually (for $p < 1$) lost to the environment until the state becomes completely describable by a discrete classical probability distribution.

---

[2]Unitary evolution on the d-dimensional maximally mixed states, which are the only rotationally invariant states, does not produce coherence.

4.4.2 Dephasing Product-state Encoded Input Qubits

When inputting data into a tensor network, it is common to featurize each sample into a product state, or a rank-one tensor. The density matrix of such a state with m features is given by $\rho = \bigotimes_{n=1}^{m} |f^{(n)}\rangle \langle f^{(n)}| = \bigotimes_{n=1}^{m} \rho^{(n)}$,

In the context of our tensor network classifier, the effect of dephasing can be seen by considering just a single feature. If we normalize this feature such that its value is $x^{(n)} \in [0,1]$, then we can utilize the commonly-used qubit encoding [112–114] to encode this classical feature into a qubit as

$$|f^{(n)}\rangle = \begin{bmatrix} \sin\left(\frac{\pi}{2}x^{(n)}\right) \\ \cos\left(\frac{\pi}{2}x^{(n)}\right) \end{bmatrix}, \tag{4.5}$$

respectively. A notable property of these encodings is that the elements of $|f^{(n)}\rangle$ are always positive, so there is a one-to-one mapping between $|\langle i^{(n)}|f^{(n)}\rangle|^2$ and $\langle i^{(n)}|f^{(n)}\rangle$ for all $i^{(n)}$. This means that every element of $\rho^{(n)} = |f^{(n)}\rangle \langle f^{(n)}| \equiv \rho$ can be written as a function of probabilities $\lambda_0^{(n)} \equiv \lambda_0$ and $\lambda_1^{(n)} \equiv \lambda_1$, where

$$\rho_{00} = \lambda_0, \quad \rho_{01} = \rho_{10} = \sqrt{\lambda_0 \lambda_1}, \quad \rho_{11} = \lambda_1. \tag{4.6}$$

Using Eq. (4.14), we get

$$\lambda_0' = |U_{00}|^2 \lambda_0 + |U_{01}|^2 \lambda_1 + 2\sqrt{\lambda_0 \lambda_1} \Re(U_{00} U_{01}) \tag{4.7}$$

$$\lambda_1' = |U_{11}|^2 \lambda_1 + |U_{10}|^2 \lambda_0 + 2\sqrt{\lambda_0 \lambda_1} \Re(U_{10} U_{11}), \tag{4.8}$$

where it is clear that the new probabilities λ_i' are non-linear functions of the old probabilities λ_j. Specifically, there is a dependence on $\sqrt{\lambda_0 \lambda_1}$. Such non-linear functions cannot be generated by a stochastic matrix acting on $\text{diag}(\rho^{(n)})$, since the off-diagonal $\sqrt{\lambda_0 \lambda_1}$ terms will be set to zero. By fully dephasing the input state before acting the unitary, the fully-dephased output is less expressive in the sense that we lose the regressor $\sqrt{\lambda_0 \lambda_1}$. But knowing the relative phase of the encoding, this lost regressor does not contain any extra information than the regressors λ_0 and λ_1, so in that sense the information content of the encoding is unaffected by the dephasing.

4.4.3 Impact on Regressors by Dephasing

To understand the dephasing effect on the linear regression induced by the unitary TTN network topology, it is illuminating to study the evolution of $\text{Tr}_A(U\mathcal{E}[\rho]U^\dagger)$ which is undertaken by a unitary node acting on a pair of dephased input qubits followed by a partial tracing over one of the output qubits. The diagonals of the output density matrix before partial

tracing, i.e., the diagonals of $U\mathcal{E}[\rho]U^\dagger$, are

$$
\begin{aligned}
\rho'_{ii} = &|U_{i0}|^2\rho_{00} + |U_{i1}|^2\rho_{11} + |U_{i2}|^2\rho_{22} + |U_{i3}|^2\rho_{33}+ \\
&2(1-p)\left[\Re(U_{i1}U^*_{i0}\rho_{10}) + \Re(U_{i2}U^*_{i0}\rho_{20})+\right. \\
&\qquad \left.\Re(U_{i3}U^*_{i1}\rho_{31}) + \Re(U_{i3}U^*_{i2}\rho_{32})\right] + \\
&2(1-p)^2\left[\Re(U_{i3}U^*_{i0}\rho_{30}) + \Re(U_{i2}U^*_{i1}\rho_{21})\right],
\end{aligned}
\tag{4.9}
$$

for $i \in \{0,1,2,3\}$, where every diagonal term is a linear regression on all elements of input ρ with regression coefficients set by the unitary matrix elements $U_{ik}, k \in \{0,1,2,3\}$. We note that terms such as the $\Re(U_{i1}U^*_{i0}\rho_{10}) = U_{i0}U^*_{i1}\rho_{01} + U_{i1}U^*_{i0}\rho_{10}$ are each composed of two regressors. In particular, the dephasing suppresses some of the regressors by a factor of $(1-p)$ or $(1-p)^2$. Since the norm of each element in U and $U^\dagger$ is upper bounded by one, the norm of the regression coefficients is suppressed by these factors induced by dephasing. The suppression is stronger by a factor of $(1-p)^2$ for regressors that are anti-diagonals of the input density matrix, i.e., ρ_{30} and ρ_{21}. While the regression described above is to obtain the diagonals of the output density matrix, the regression to obtain off-diagonals of the output density matrix has a similar pattern of suppression of certain regressors.

This suppression of regression coefficients is carried over to the reduced density matrix, which can be written as

$$
\mathrm{Tr}_2(\rho') = \begin{bmatrix} \rho'_{00} + \rho'_{11} & \rho'_{02} + \rho'_{13} \\ \rho'_{20} + \rho'_{31} & \rho'_{22} + \rho'_{33} \end{bmatrix}.
\tag{4.10}
$$

When the input pair of qubits ρ is a product state of two data qubits, we have

$$
\rho = \rho^{(1)} \otimes \rho^{(2)} \equiv \begin{bmatrix} \lambda_0 & \sqrt{\lambda_0\lambda_1} \\ \sqrt{\lambda_0\lambda_1} & \lambda_1 \end{bmatrix} \otimes \begin{bmatrix} \mu_0 & \sqrt{\mu_0\mu_1} \\ \sqrt{\mu_0\mu_1} & \mu_1 \end{bmatrix},
\tag{4.11}
$$

where the λ's and μ's are defined like Eq. (4.6) for the two data qubits $\rho^{(1)}$ and $\rho^{(2)}$. Substituting Eq. (4.11) into Eq. (4.9) and (4.10), we see that all regressors containing $\sqrt{\mu_0\mu_1}$ or $\sqrt{\lambda_0\lambda_1}$ are suppressed by a factor of $(1-p)$ after the first-layer unitary, while the regressor $\sqrt{\lambda_0\lambda_1\mu_0\mu_1}$ is suppressed by a factor of $(1-p)^2$. The output density matrix elements then become the regressors for regressions performed by subsequent upper layers, as follows.

For unitary TTN without *ancillas*, Eq. (4.9) and (4.10) are carried over to the output of every layer of the network, since there is no entanglement in the input pair of qubits. However, at the upper layers, the regression onto the output density matrix element has regressors already composed of terms that were suppressed in previous layers, as described above for $\rho \to \rho'$. Viewing the regressors at the input of the last layer, the suppression on most of them by some power of $(1-p)$ resembles the concept of regularization in regressions but does not involve a penalty term on the coefficient norm in the loss function.

In cases where there can be entanglement in each of the input qubits, such as the intermediate layers in a MERA or in a unitary TTN with ancillas, the pattern of suppressing certain regressors is similar, where the coherence of the input is suppressed by some power of $(1-p)$. In particular, the regressors on the anti-diagonals are most strongly suppressed by a factor of $(1-p)^m$ where m is the number of input qubits.

4.4.4 Fully-dephased Unitary Tensor Networks

When the network is fully-dephased at every layer, all of the off-diagonal regressors are removed. Each diagonal term of the output density matrix then becomes a regression on only the diagonals of the input density matrix. In App. 4.10.2, we show that in this situation each node of the unitary tensor network U_{ij} reduces to a unitary-stochastic matrix $M_{ij} \equiv |U_{ij}|^2$. When the output of the unitary node is partially traced over, the overall operation is equivalent to a singly stochastic matrix $S_{i_Bj} \equiv \sum_{i_A} |U_{i_A i_B j}|^2$, where i_A enumerates the traced-over part of the system. The tensor network QML model then reduces to a classical Bayesian network (see App. 4.9) with the joint probability factorization Eq. (4.19) presented in App. 4.10.3 and 4.10.4.

4.5 Adding Ancillas and Increasing the Virtual Bond Dimension

The Stinespring's dilation theorem [115, 116] states that any quantum channel or completely positive and trace-preserving (CPTP) map $\Lambda : \mathcal{B}(\mathcal{H}_A) \to \mathcal{B}(\mathcal{H}_B)^3$ over finite-dimensional Hilbert spaces $\mathcal{H}_A$ and $\mathcal{H}_B$ is equivalent to a unitary operation on a higher dimensional Hilbert space $\mathcal{H}_B \otimes \mathcal{H}_E$, where $\mathcal{H}_E$ is also finite-dimensional, followed by a partial tracing over $\mathcal{H}_E$. A motivating example demonstrating directly that ancillas are necessary to allow the evolution on fully-dephased input induced by a generic unitary to be as expressive as that induced by a singly stochastic matrix is presented in App. 4.11. In particular, the dimension of the ancillary system $\mathcal{H}_E$ can be chosen such that $\dim(\mathcal{H}_E) \leq \dim(\mathcal{H}_A)\dim(\mathcal{H}_B)$ for any Λ^4 [115]. In terms of qubits, the theorem implies that there need to be at least $2n_o$ ancilla qubits to achieve an arbitrary quantum channel between n_i input qubits and n_o output qubits. This is because the total combined number of n_i input qubits and n_a ancilla qubits should equal the total combined number of n_o output qubits and the qubits that are traced out as environment degrees of freedom. Using Stinespring's dilation theorem, we can show $2^{n_i + n_a - n_o} \leq 2^{n_i} 2^{n_o}$ which leads to $n_a \leq 2n_o$.

In the scheme of adding ancillas per node in a unitary TTN, every node requires then in principle at least two ancilla qubits to achieve an arbitrary quantum channel, because there are two input qubits coming from the previous layer and one output qubit passing to the next layer.

However, we find it more expressive to add ancillas per data qubit instead and to trace out half of all output qubits per node before contracting with the node at the next layer. We call this the ancilla-per-data-qubit scheme. This scheme is able to achieve superior classification performance in the numerical experiment tasks that we conducted (described in App. 4.14),

---

[3]We denote the convex set of positive-semidefinite linear operators with unit trace, namely the set of density operators, on a complex Hilbert space $\mathcal{H}$ (thus Hermitian and bounded) as $\mathcal{B}(\mathcal{H})$.

[4]In the Stinespring's representation of such a CPTP map Λ, there exists an isometry $V : \mathcal{B}(\mathcal{H}_A) \to \mathcal{B}(\mathcal{H}_B \otimes \mathcal{H}_E)$ such that $\Lambda(\rho) = \text{Tr}_E(V\rho V^\dagger), \forall \rho \in \mathcal{B}(\mathcal{H}_A)$.
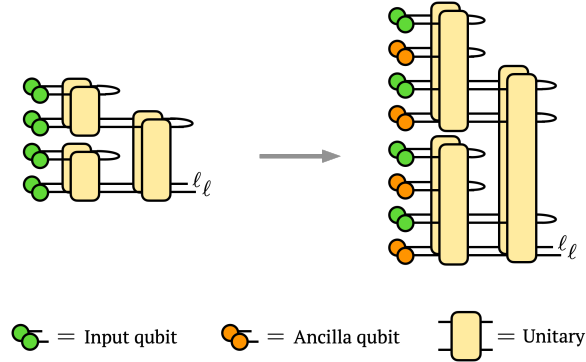
Figure 4.3: Adding one ancilla qubit, initialized to a fixed basis state, per data qubit to a unitary TTN classifying four features, with a corresponding virtual bond dimension increased to four. Only one output qubit is measured in the basis state ℓ regardless of the number of ancillas added per data qubit. We always decimate the Hilbert space by half between consecutive layers of unitary nodes.

as compared to the ancilla-per-unitary-node scheme described earlier, despite that the two schemes share the same number of trainable parameters when adding the same number of ancillas. A diagram of this ancilla scheme is shown in Fig. 4.3. This scheme effectively increases the virtual bond dimension of the network, which means that the network can represent a larger subset of unitaries on all input qubits.

Although the ancilla-per-data-qubit scheme achieves superior classification performance, it never produces arbitrary quantum channels at each node. To see this, for any unitary node in the first layer, the number of input qubits is $n_i = 2$, that of ancillas is $n_a = n_i k = 2k$ where $k \in \mathbb{Z}$ is the number of ancillas per data qubit, and that of output qubits passing to the next layer is $n_o = 1 + k$ such that $n_a < 2n_o, \forall a \in \mathbb{Z}$. As a result, the channels achievable via the first layer of unitaries constitute only a subset of all possible channels between its input and output density matrices. For any unitary node in subsequent layers, there are no longer any ancillas, whereas there is at least one output qubit observed or operated on later. Consequently, the channels achievable via each layer of unitaries then also constitute only a subset of all possible channels between its input and output density matrices.

4.6 Related Work

Dephasing or decoherence was used to connect probabilistic graphical models and TNs by Miller et al. [117]. Robeva et al. showed that the data defining a discrete undirected graphical model (UGM) is equivalent to that defining a tensor network with non-negative nodes [118]. The Born machine (BM) [117, 119] is a more general probabilistic model built from TNs that arise naturally from the probabilistic interpretation of quantum mechanics. The locally purified state (LPS) [119] adds to the BM some purification edges each of which partially

traces over a node, and represents the most general family of quantum-inspired probabilistic models. The decohered Born Machine (DBM) [117] adds to a subset of the virtual bonds in BM some decoherence edges that fully dephase the underlying density matrices. A fully-DBM, i.e., a BM all of whose virtual bonds are decohered, can be viewed as a discrete UGM [117]. Any DBM can be viewed as an LPS, and vice versa [117]. A summary of the relative expressiveness of these families of probabilistic models is given in App. 4.12.

The unitary TTN and the MERA, dephased or not, are DBMs or equivalently LPSs. Each partial tracing in them is represented by a purification edge, while each dephasing channel acting on the input of a unitary node in them can be viewed as a larger unitary node contracting with some environment node and the input node, before tracing out the environment degree of freedoms using a purification edge. Each of the tensor networks produces a normalized joint probability once the data nodes are specified with normalized quantum states and the readout node is specified with a basis state. Fully-dephasing every virtual bond in the network gives rise to a fully-DBM, which can be also viewed as a discrete UGM in the dual graphical picture. We describe in App. 4.10.3 that, by directly taking into account the effect of the partial tracing or the purification, the fully-dephased networks can also be viewed as Bayesian networks via some directed acyclic graphs (DAGs).

4.7 Numerical Experiments

To demonstrate the competing effect between dephasing and adding ancillas while accordingly increasing the bond dimension of the network, we train the unitary TTN to perform binary classification on grouped classes on three datasets of different levels of difficulty[5]. We vary both the dephasing probability p in dephasing every layer of the network, and the number of ancillas, which results in a varying bond dimension of the TTN. In the fully-dephased limit, the unitary TTN essentially becomes a Bayesian network that computes a classical joint probability distribution (see App. 4.10).

In each dataset, we use a training set of 50040 samples of 8×8-compressed images and a validation dataset of 9960 samples, and we employ the qubit encoding given in Eq. (4.5). The performance is evaluated by classifying another 10000 testing samples. The unitarity of each node is enforced by parametrizing a Hermitian matrix H and letting $U = e^{iH}$. In all of our cases where the model can be efficiently simulated[6], they can be optimized with analytic gradients using the Adam optimizer [120] with respect to a categorical cross-entropy loss function, with backpropagations through the dephasing channels. Hyperparameters in the optimizer and in initializing the unitaries are tuned [121]. The ResNet-18 model [122], serving as a benchmark of the state-of-the-art classical image recognition model, is adapted to and trained/tested on the same compressed, grayscale images.

---

[5]https://github.com/HaoranLiao/dephased_ttn_mera.git. Example images of the three datasets are shown in App. 4.15.

[6]If the model cannot be efficiently simulated, stochastic approximations such as the simultaneous perturbation stochastic approximation (SPSA) with momentum algorithm [108] can be used for training.
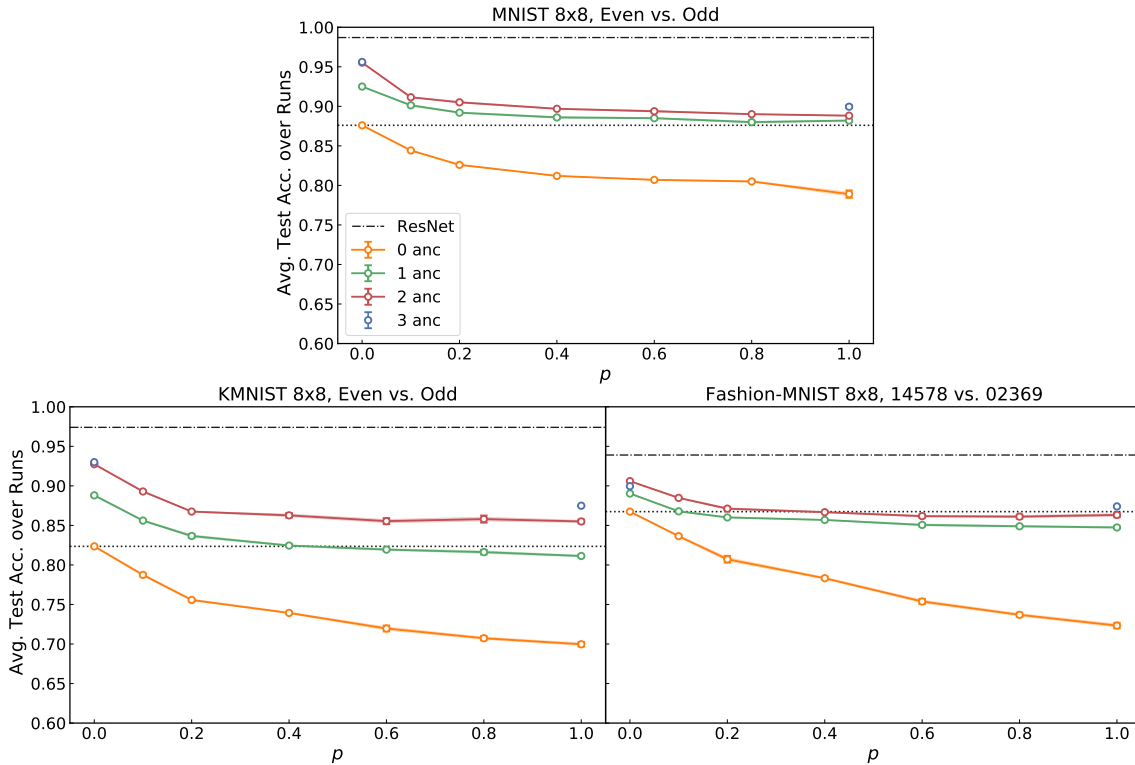
Figure 4.4: Average testing accuracy over five runs with random batching and random initialization as a function of dephasing probability p when binary-classifying 8×8 compressed MNIST, KMNIST, or Fashion-MNIST images. In each image dataset, we group the original ten classes into two, with the grouping shown in the titles. Every layer of the unitary TTN, including the data layer, is locally dephased with a probability p. Each curve represents the results from the network with a certain number of ancillas added per data qubit, with the error bars showing one standard error. The dotted reference line shows the accuracy of the non-dephased network without any ancilla.

For the first 8×8-compressed, grayscale MNIST [123] dataset, and the second 8×8-compressed, grayscale KMNIST [124] dataset, we group all even-labeled original classes into one class and group all odd-labeled original classes into another, and perform binary classification on them. For the third 8×8-compressed, grayscale Fashion-MNIST [125] dataset, we group $0, 2, 3, 6, 9$-labeled original classes into one class and the rest into another. The binary classification performance on each of the three datasets as a function of dephasing probability p and the number of ancillas is shown for the unitary TTN in Fig. 4.4. Due to high computational costs, we simulate a three-ancilla network with p values equal to 0 and 1 only. This suffices to reveal the performance trends in both the non-decohered unitary tensor network and the corresponding Bayesian network.

There are two interesting observations to make on the results in Fig. 4.4. First, the classification performance is very sensitive to small decoherence and decreases the most rapidly in the small p regime, especially in networks with at least one ancilla added. Further dephasing the network does not decrease the performance significantly, and in some cases, it does not further decrease the performance at all. A similar observation is made for the MERA (see Fig. 4.6). Second, in the strongly dephased regime where the ancillas are very noisy, adding such noisy ancillas helps the network regain performance relative to that of the non-dephased no-ancilla network. On all three datasets, the performance regained after adding two ancillas across all dephasing probabilities is comparable to the performance with the no-ancilla non-dephased network. This suggests that in implementing such unitary TTNs in the NISQ era with noisy ancillas, it is favorable to add at least two ancillas to the network and to accordingly expand the bond dimension of the unitary TTN to at least eight, regardless of the decoherence this may introduce.

However, due to the high computational costs with more than three ancillas added to the network, our experiments do not provide sufficient information about whether the corresponding Bayesian network in the fully-dephased limit will ever reach the same level of classification performance as the non-dephased unitary TTN by increasing the number of ancillas. Despite this, we note that in the KMNIST and Fashion-MNIST datasets the rate of improvement of the Bayesian network as more ancillas are added is diminishing.

Dephasing the data layer is special compared to dephasing other internal layers within the network, since the coherence in each of the product-state data qubits has not been mixed to form the next-layer features. Since the coherences are non-linear functions of the diagonals of ρ, given the linear nature of tensor networks, it is not possible to reproduce the coherence in the data qubits in subsequent layers once the input qubits are fully-dephased. To examine to what extent the observed performance decrement may be attributed to decoherence within the network as opposed to decoherence of the data qubits, we perform the same numerical experiment on the Fashion-MNIST dataset but keep the input qubits coherent without any dephasing. The result, shown in Fig. 4.5, indicates that the decoherence of the virtual bonds in the unitary TTN alone is a significant source causing the classification performance to decrease, accounting for more than half of the performance decrement.
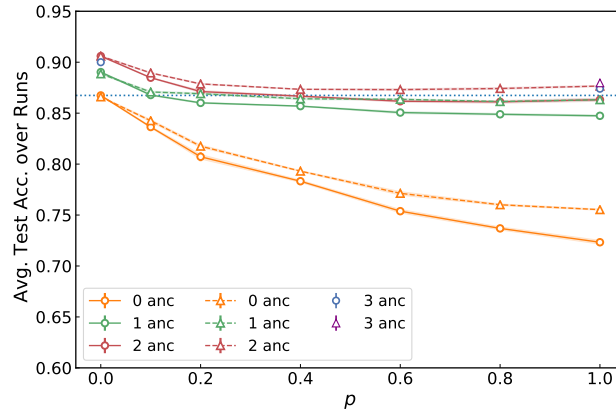
Figure 4.5: Average testing accuracy over five runs as a function of dephasing probability p when classifying 8×8 compressed Fashion-MNIST images. Each curve represents the results from the network with a certain number of ancillas added per data qubit. The circles (triangles) show the performance of the unitary TTN when every layer including (except) the data layer is locally dephased with a probability p. The dotted reference line shows the accuracy of the non-dephased network without any ancilla.
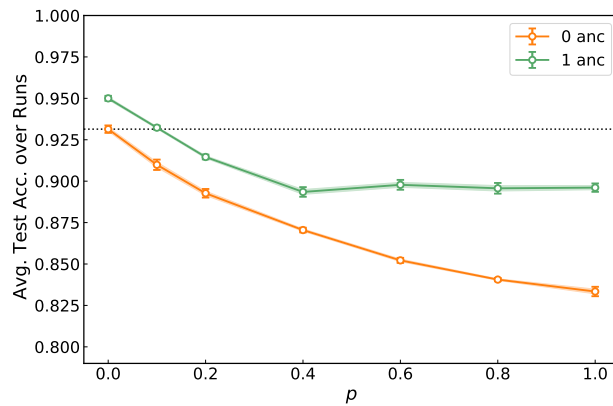
Figure 4.6: Average testing accuracy over ten runs with random batching and initialization as a function of dephasing probability p in dephasing a 1D MERA structured tensor network to classify the eight principle components of non-compressed MNIST images. Ancillas are added per data qubit.

4.8 Discussions

In this paper, we investigated the competition between dephasing tensor network QML models and adding ancillas to the networks, in an effort to investigate the advantage of coherence in QML and to provide guidance in determining the number of noisy ancillas to be included in NISQ-era implementations of these models. On one hand, as we increase the dephasing probability p of every layer of the network, every regressor associated with each layer of unitary nodes will have certain terms in it damped by some power of $(1 - p)$. The damping cannot be offset by the regression coefficients which are given in terms of the elements of the unitary matrices. The effect of this damping of the regressors under dephasing decreases the classification accuracy of the QML model. When the network is fully-dephased, these regressors are eliminated, and the tensor network QML model becomes a classical Bayesian network that is completely describable by classical probabilities and stochastic matrices. On the other hand, as we increase the number of input ancillas and accordingly increase the virtual bond dimensions of the tensor network, we allow the network to represent a larger subset of unitaries between the input and output qubits. As a result, the performance of the network improves, as demonstrated by adding up to two ancillas and a corresponding increment of the virtual bond dimension to eight in our numerical experiments. This improvement applies to all decoherence probabilities. We also find that adding more than two ancillas gives either diminishing or no improvement. The numerical experiments are insufficient to show whether the performance of the corresponding Bayesian network can match that of the non-decohered network as more than three ancillas are added, although we did find that in the KMNIST and Fashion-MNIST datasets the rate of improvement of the Bayesian network as more ancillas are added is diminishing. It remains an open question where coherence provides any quantum advantage in QML.

Most importantly, we find that the performance of the two-ancilla Bayesian network, namely the fully-dephased network, is comparable to that of the corresponding non-decohered unitary TTN with no ancilla, suggesting that when implementing the unitary TTN, it is favorable to add at least two arbitrarily noisy ancillas and to accordingly increase the virtual bond dimension to at least eight.

We also observe that the performance of both the unitary TTN and the MERA decreases most rapidly in the small decoherence regime. With ancillas added, the performance decreases and quickly levels off at around $p = 0.2$ for the unitary TTN. The MERA with one ancilla added also exhibits this level-off performance after around $p = 0.4$. However, without any ancilla added, neither the unitary TTN nor the MERA shows a level-off performance and their performance decreases all the way until the networks are fully dephased. This contrast is an interesting phenomenon to be studied in the future.

4.9 Discrete Bayesian Networks

Let a set of vertices and an edge set of ordered pairs of vertices form a directed graph $G = (V, E)$, and let $X = \{X_v\}, \forall v \in V$ be a set of discrete random variables indexed by the vertices. Let $\mathrm{pa}(v)$ or $X_{\mathrm{pa}(v)}$ denote the set of parent vertices/variables each of which has an edge directed towards v. A directed edge represents some conditional probability of the variable on its parent. We say that X is a discrete Bayesian network (a.k.a. belief network) with respect to G if G is acyclic, namely, it is a directed acyclic graph (DAG), or equivalently if the joint probability mass function of X can be written as a product of the individual probability mass functions conditioned on their parent variables, i.e., $P(X) = \prod_{v \in V} P(X_v | X_{\mathrm{pa}(v)})$.

4.10 Fully-dephased Unitary Tensor Networks

4.10.1 Fully-dephasing Qubits after Unitary Evolution

To fully dephase a quantum state, we simply choose a basis to represent the density matrix and then set all off-diagonal elements of the matrix to zero, leaving the diagonal elements unchanged. If we represent the fully-dephasing ($p = 1$) superoperator as $\mathcal{D}$, then

$$\mathcal{D}[\rho] = \sum_i \langle i | \rho | i \rangle | i \rangle \langle i | = \sum_i \rho_{ii} | i \rangle \langle i | . \tag{4.12}$$

For convenience, we adopt the notation $\lambda_i \equiv \rho_{ii}$, where the λ_i can be identified as probabilities from some discrete distribution. If we allow a generic unitary U to act on ρ before it is fully-dephased, then we have

$$\mathcal{D}[U \rho U^\dagger] = \sum_i \langle i | U \rho U^\dagger | i \rangle | i \rangle] \langle i | = \sum_{ijk} \rho_{jk} \langle i | U | j \rangle \langle k | U^\dagger | i \rangle | i \rangle \langle i | , \tag{4.13}$$

so that the new probabilities λ_i' encoded in the fully-dephased state are given by

$$\lambda_i' = \mathcal{D}[U \rho U^\dagger]_{ii} = \sum_{jk} \rho_{jk} \langle i | U | j \rangle \langle k | U^\dagger | i \rangle = \sum_{jk} \rho_{jk} U_{ij} U_{ik}^* \tag{4.14}$$

From Eq. (4.14), we can see that each probability is a function of the entire density matrix, along with the elements of U. If ρ is assumed to be fully-dephased already, then $\rho_{jk} = \lambda_j \delta_{jk}$ and therefore

$$\lambda_i' = \sum_{jk} \lambda_j \delta_{jk} U_{ij} U_{ik}^* = \sum_j \lambda_j |U_{ij}|^2 = \sum_j M_{ij} \lambda_j . \tag{4.15}$$

By the unitarity of U, $M_{ij} \equiv |U_{ij}|^2$ is doubly stochastic, i.e., $\sum_i M_{ij} = \sum_i |U_{ij}|^2 = \mathbb{1}_j$ and $\sum_j M_{ij} = \sum_j |U_{ij}|^2 = \mathbb{1}_i$, which maps the old probabilities λ to new probabilities λ' that are normalized, i.e., $\sum_i \lambda_i' = \sum_{ij} M_{ij} \lambda_j = \sum_j \mathbb{1}_j \lambda_j = 1$. Such doubly stochastic matrices M that

correspond to some unitaries are called unitary-stochastic matrices. For $N \leq 2$, all $N \times N$ doubly stochastic matrices are also unitary-stochastic. But unitary-stochastic matrices form a proper subset of doubly stochastic matrices for $N \geq 3$[7] [126, 127].

4.10.2 Fully-dephasing a Reduced Density Matrix after Unitary Evolution

In some tensor networks such as the TTN, the effective size of the feature space is reduced by tracing over some of the degrees of freedom after each layer. The combined effects of the unitary layer and partial trace produce a quantum channel, whose output is then fully-dephased. If we partition the Hilbert space of an input density matrix ρ into parts A and B, then the outputs λ'_{i_B} after tracing over part A are given by

$$
\begin{aligned}
\lambda'_{i_B} &= \left[\mathrm{Tr}_A\left(\mathcal{D}[U\rho U^\dagger]\right)\right]_{i_B i_B} \\
&= \left[\sum_{i_A i_B j k} \mathrm{Tr}_A\left(\rho_{jk}\langle i_A i_B|U|j\rangle\langle k|U^\dagger|i_A i_B\rangle|i_A\rangle\langle i_A||i_B\rangle\langle i_B|\right)\right]_{i_B i_B} \\
&= \sum_{i_A j k}\rho_{jk}\langle i_A i_B|U|j\rangle\langle k|U^\dagger|i_A i_B\rangle\,\mathrm{Tr}\left(|i_A\rangle\langle i_A|\right) \\
&= \sum_{jk}\rho_{jk}\sum_{i_A}U_{i_A i_B j}U^*_{i_A i_B k}.
\end{aligned}
\tag{4.16}
$$

We can again see that the output diagonals depend on all elements of ρ and U. If ρ is already fully dephased, then we have

$$
\lambda'_{i_B} = \sum_{jk}\lambda_j\delta_{jk}\sum_{i_A}U_{i_A i_B j}U^*_{i_A i_B k} = \sum_j\lambda_j\sum_{i_A}|U_{i_A i_B j}|^2 = \sum_j S_{i_B j}\lambda_j,
\tag{4.17}
$$

where $S_{i_B j} \equiv \sum_{i_A}|U_{i_A i_B j}|^2$ is a rectangular singly stochastic matrix with respect to index i_B only, i.e., $\sum_{i_B}S_{i_B j} = \sum_{i_A i_B}|U_{i_A i_B j}|^2 = \mathbb{1}_j$. It again maps the old probabilities λ to new probabilities λ' which are normalized, i.e., $\sum_{i_B}\lambda'_{i_B} = \sum_{i_B j}S_{i_B j}\lambda_j = \sum_j\mathbb{1}_j\lambda_j = 1$. We remark that the output index i_B runs from 1 to $\dim(B)$, while the input index j runs from 1 to $\dim(A)\cdot\dim(B)$, and the Bayesian update by this singly stochastic matrix applies only in the coarse-graining direction.

4.10.3 Fully-dephasing the Unitary TTN

Dephasing a unitary TTN is to apply local dephasing channels on each pair of output bonds before contracting with the node at the next layer, as shown in Fig. 4.1 (right). In terms

---

[7]The dimension of the parameter space for $N \times N$ unitary-stochastic matrices is $(N-1)^2$ as for doubly stochastic matrices. The parameter space covered by unitary-stochastic matrices is, however, in general, smaller than that covered by doubly stochastic matrices [126].

of the underlying density matrix, the dephasing channel is to apply Eq. (4.3) to the bonds, each of which may represent a higher-dimensional state if there are ancilla qubits added as discussed in Sec. 4.5. We note that assuming local dephasing, there is no need to dephase before partially tracing out some generally entangled qubits out of the unitary TTN node, say tracing over part A of the output system AB, since there exists a U_{AE} on $\rho_{AB} \otimes \rho_E$ by the definition of dephasing such that

$$\text{Tr}_A \left(\mathcal{E}_A \left[\rho_{AB} \right] \right) = \text{Tr}_A \left[\text{Tr}_E \left(U_{AE} \rho_{AB} \otimes \rho_E U_{AE}^\dagger \right) \right] = \text{Tr}_A(\rho_{AB}). \tag{4.18}$$

A diagram of the dephased unitary TTN is shown in Fig. 4.1 (right).

As shown in App. 4.10.2, fully decohering after partially tracing out every composite node of a unitary TTN leads to a TTN composed of nodes each of which is a rectangular singly stochastic matrix S (reduced from a unitary-stochastic matrix), acting on a vector of the diagonals of a density matrix, that only preserves the normalization in the coarsed-graining direction. The fully-dephased TTN then exhibits a chain of conditional probabilities and can be interpreted as successive Bayesian updates across layers. A diagram using the third-order copy tensors (see App. 4.13) to fully dephase the unitary TTN is shown in Fig. 4.7 (left), and the dual graphical picture as a Bayesian network is depicted in Fig. 4.7 (right).

Formally, a fully-dephased unitary TTN can be viewed as a discrete Bayesian network via a DAG with input quantum states as parent variables. In other words, the Bayesian network provides a dual graphical formulation of the fully-dephased unitary TTN, with the graph edges functioning as the tensor nodes while the graph vertices acting as the virtual bonds [117, 118]. The graph vertices in the Bayesian network, which is dual to the virtual bonds in the TTN composed of stochastic matrices, represent vector variables $\lambda^{(k,j)} \equiv \text{diag}(\rho^{(k,j)})$, where k and j denotes the j-indexed vertices at the kth layer of the network with 0 indexing the layer with parent variables, and ρ is the corresponding density matrix in the dual tensor network picture. We use the shorthand $\lambda^{(k)} \equiv \{\lambda^{(k,0)}, \ldots, \lambda^{(k,n_k)}\}$ to group all n_k vertices at the kth layer into a set. The output vertex of the Bayesian network stands for a readout variable ℓ specifying the basis state of the measurement. The Bayesian network then yields a joint probability once the parent variables are specified with normalized quantum states, i.e., the joint probability represented by the network can be written in the following factorized form

$$P(\lambda^{(0)} \ldots, \lambda^{(\log(m))}, \ell) = P(\ell|\lambda^{(\log(m))}) \prod_{k=1}^{\log(m)} P(\lambda^{(k)}|\lambda^{(k-1)}) P(\lambda^{(0)}), \tag{4.19}$$

where $m \equiv n_0$ is the number of vertices at the data layer. $P(\lambda^{(k)}|\lambda^{(k-1)})$ is the conditional probability represented by the edges between the $(k-1)$th and kth layer of the Bayesian network, or equivalently by the rectangular singly stochastic matrices at the kth layer of the dual tensor network. $P(\ell|\lambda^{(\log(m))})$ is the conditional probability of obtaining the basis vector ℓ.

When, for instance, the unitary TTN is fully dephased to become a Bayesian network, both schemes of adding ancillas, as described in Sec. 4.5, give rise to networks that share
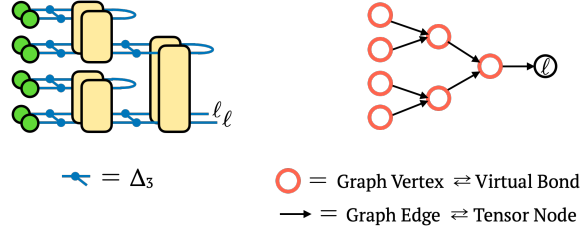
Figure 4.7: Left: Fully-dephasing a unitary TTN, where the third-order copy tensor Δ_3 is defined as $\Delta_3 = \sum_i e_i^{\otimes 3}$ with e_i the qubit basis state (see App. 4.13). Right: The dual graphical picture of the fully-dephased unitary TTN as a Bayesian network via a directed acyclic graph (DAG). The transition matrices conditioning on each pair of input vectors are rectangular singly stochastic matrices S's reduced from some unitary-stochastic matrices.

the same form of factorized conditional probabilities as shown in Eq. (4.19). The difference between the two schemes lies in that adding ancillas per node leads to $\lambda^{k,j}$ fixed at two dimensional $\forall k, j$, whereas adding ancillas per data qubit allows $\lambda^{k,j}$'s dimension to grow with the number of ancillas $\forall k \in \{1, \ldots, \log(m)\}, \forall j$, since increasing virtual bond dimension increases the number of diagonals.

4.10.4   Fully-dephasing the MERA

Similar to the fully-dephased unitary TTN, the fully-dephased MERA is shown in Fig. 4.8 (left), whose dual graphical formulation as a Bayesian network is shown in Fig. 4.8 (right), such that the joint probability yielded by the network upon specifying the input quantum states as the parent variables has the same factorized form as Eq. (4.19). An entangler with fully-dephased input and output transforms to a unitary-stochastic matrix M, and the partially-traced-over unitary, serving as the "isometry", with fully-dephased input and output transforms to a singly stochastic matrix S (reduced from a unitary-stochastic matrix) with respect to the coarse-graining direction. We note that the dimension of the vector variables dual to the output bonds of entanlgers in the tensor network picture is twice as large as other variables, since they represent correlated variables outputted by the unitary-stochastic matrices. Each of the two outgoing directed edges from these variables can be interpreted as a conditional probability conditioning on half of the support of these discrete variables.

4.11   Ancillas Are Required to Achieve Evolution by Singly Stochastic Matrices

Ancillas are necessary to allow the evolution on fully-dephased input induced by a generic unitary to be as expressive as that induced by general singly stochastic matrices. Consider
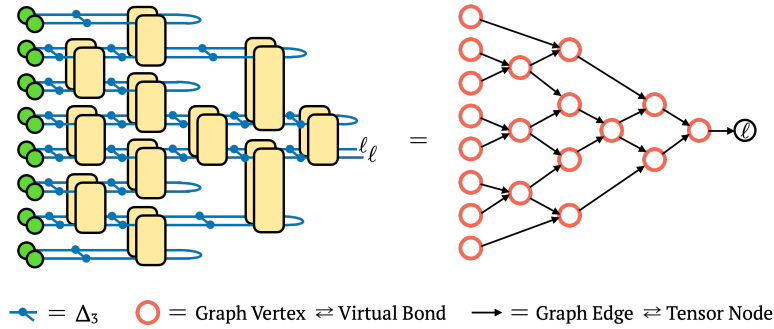
Figure 4.8: Left: Fully-dephasing a MERA. Right: Equivalently, the dual graphical picture of the fully-dephased unitary TTN as a Bayesian network via a DAG, since the fully-dephased MERA is a tensor network composed of unitary-stochastic matrices M's and rectangular singly stochastic matrices S's with respect to the coarse-graining direction, with input being the diagonals of the encoded qubits.

a singly stochastic matrix

$$\begin{bmatrix} 1 & 1 & 1 & 1 \\ 0 & 0 & 0 & 0 \end{bmatrix}, \tag{4.20}$$

which maps an input state in $\{|00\rangle, |01\rangle, |10\rangle, |11\rangle\}$ to $|0\rangle$. Note that this is naturally a mapping between fully-dephased input and fully-dephased output. But this mapping cannot be achieved by acting a unitary on the data qubit alone. To achieve that, we need to unitarily evolve a combined system including at least one ancilla. After tracing out the ancilla, it is possible to leave the data qubit in $|0\rangle$. Namely, $\{|00\rangle, |01\rangle, |10\rangle, |11\rangle\} \rightarrow |0\rangle \otimes |0\rangle_E$ or $\{|00\rangle, |01\rangle, |10\rangle, |11\rangle\} \rightarrow |0\rangle \otimes |1\rangle_E$ is achievable by a unitary on the combined system. Note that this is also a mapping between fully-dephased input and fully-dephased output naturally. Therefore, considering generic unitary evolution such as contracting with a node in the unitary TTN, it is necessary to include ancillas to achieve what can be mapped by a singly stochastic matrix between the fully-dephased input and fully-dephased output.

4.12   Probabilistic Graphical Models and Tensor Networks

It was shown by Robeva et al. [118] in Theorem 2.1 that the data defining a discrete undirected graphical model (UGM) is equivalent to that defining a tensor network (TN) with non-negative nodes, but with dual graphical notations that interchange the roles of nodes and edges. Hence, we have discrete UGM=non-negative TN, where = represents that the two classes of model can produce the same probability distribution using the same number of parameters, i.e., they are equally expressive.

The Born machine (BM) [117, 119], which models a probability mass function as the absolute value squared of a complex function, is a family of more general probabilistic models built from TNs that arise naturally from the probabilistic interpretation of quantum mechanics. The locally purified state (LPS), first discussed by Glasser et al. [119] and generalized by Miller et al. [117], adds to each node in a BM a purification edge, allowing it to represent the most general family of quantum-inspired probabilistic models. Glasser et al. [119] showed that LPS is more expressive than BM, i.e., LPS>BM.

The decohered Born Machine (DBM) was introduced by Miller et al. [117], which adds to a subset of the virtual bonds BM decoherence edges that fully dephase the underlying density matrices. A BM all of whose virtual bonds are decohered is called a fully-DBM. Miller et al. [117] showed that fully decohering a BM gives rise to a discrete UGM, and conversely any subgraph of a discrete UGM can be viewed as the fully-decohered version of some BM. Hence, we have fully-DBM=discrete UGM.

Theorem 3 and 4 by Miller et al. [117] showed that LPS=DBM, since each purification edge joining a pair of LPS cores can be expressed as a larger network of copy tensors, and each decoherence edge of a DBM can be absorbed into nearby pair of tensors and form a purification edge. Following this view of LPS=DBM and the fact that LPS>BM, one arrives at DBM>BM, which can also be understood as BM being a special case of DBM with an empty set of decohered edges added.

A summary of the relative expressiveness is given in Tab. 4.1.

Table 4.1: The relative expressiveness, defined as the probability distributions a model can produce with the same number of parameters, among the discrete graphical model (UGM), the tensor network (TN) with non-negative nodes, the Born machine (BM), the decohered Born machine (DBM), and the locally purified state (LPS).

Relative Expressiveness	Ref.
discrete UGM = non-negative TN	[118]
fully-DBM = discrete UGM	[117]
LPS > BM	[119]
LPS = DBM > BM	[117]

4.13 Copy Tensors

A copy tensor of order n is defined to be $\Delta_n = \sum_i e_i^{\otimes n}$ where e_i is the ith basis vector, whose conventional tensor diagram is given as a solid dot with n bonds [128]. An order-one copy tensor contraction can be viewed as a marginalization, while an order-three copy tensor can be used to denote conditioning on the same vector, as shown in Fig. 4.9. The contraction of two third-order copy tensors with a density matrix and with themselves while leaving two

bonds uncontracted conveniently reproduces Eq. (4.12), in which the basis vector is the basis state $|i\rangle$, as taking the diagonals of a matrix. Therefore, it is useful to denote a dephasing channel with a dephasing rate $p = 1$, as shown in Fig. 4.9.

Figure 4.9: Left: using a third-order copy tensor contracting with a basis state vector results in an outer product of the basis vector, which can be thought of as conditioning on the same basis state upon contraction with two nodes. Right: Obtaining the diagonals of a density matrix, or a matrix in general, can be done by contracting the matrix with two third-order copy tensors and contracting one bond of each of the copy tensors together.

4.14 Comparing the Two Ancilla Schemes in the Unitary TTN

As shown in Tab. 4.2, adding one ancilla per data qubit and accordingly doubling the virtual bond dimension yields superior performance to adding two ancillas per unitary node, in the task of classifying 1902 8×8-compressed MNIST images each showing a digit 3 or 5. Both ancilla-added unitary TTNs are trained on 5000 samples using the Adam optimizer and validated on 2000 samples. The two ancilla schemes share the same number of trainable parameters.

Table 4.2: Average testing accuracies over five trials between adding two ancillas per unitary node and adding one ancilla per data qubit, when the dephasing rate $p = 0$ or $p = 1$, in the same classification task.

	Per unitary node	Per data qubit
$p = 0$	0.938 ± 0.001	0.972 ± 0.001
$p = 1$	0.912 ± 0.002	0.940 ± 0.002

4.15 Datasets for the Numerical Experiments

The three datasets used are demonstrated in Fig. 4.10. The compression to the 8×8 dimension allows tractable computation and optimization when ancillas are added to the tensor network QML models. Each pixel of an image is featurized through Eq. (4.5). The
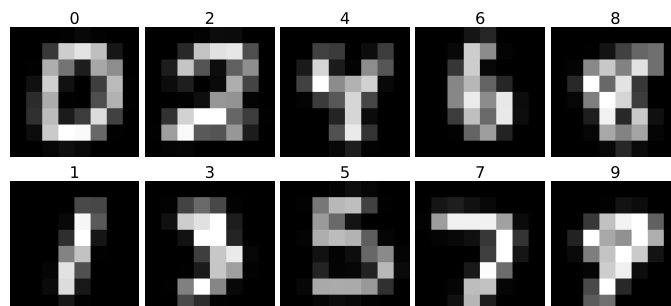
(a) 8×8-compressed MNIST images
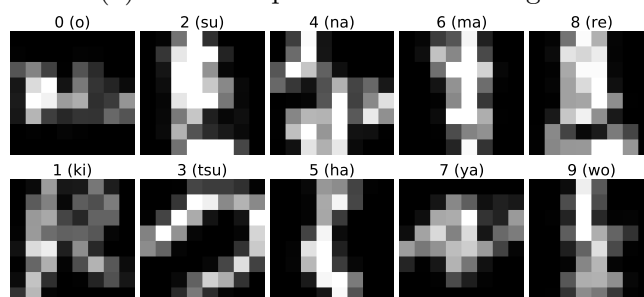
(b) 8×8-compressed KMNIST images
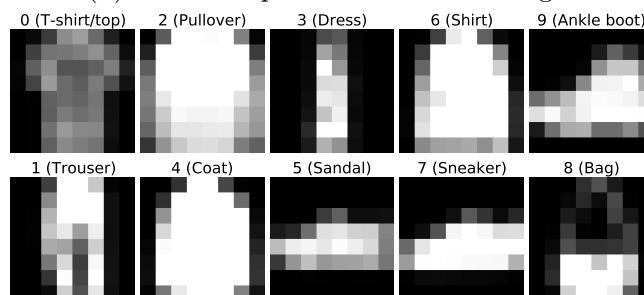
(c) 8×8-compressed Fashion-MNIST images

Figure 4.10: Example images of each original class in the three datasets, with the class label shown above each example. In each dataset, the classes in the top row are grouped into one and the classes in the bottom row are grouped into another for binary classification.

three datasets have different levels of difficulty in terms of binary classification of grouped classes, with the MNIST dataset being the easiest one while the Fashion-MNIST dataset being the most challenging.

Chapter 5

Interplay of vibration- and environment-assisted energy transfer

5.1 Preface

This chapter is taken from the previously published Ref. [129], originally appearing in New Journal of Physics. It was co-authored by Dr. Zeng-zhao Li, Liwen Ko, the author of this thesis, Dr. Mohan Sarovar and Professor K. Birgitta Whaley. This project was let by Dr. Zeng-zhao Li. Liwen Ko did the analysis on symmetry. The author of this thesis did numerical simulations with Lindblad master equation and contributed to discussions of the results. Dr. Sarovar and Professor Whaley provided high-level insights. The majority of the writing was completed by Dr. Zeng-zhao Li.

5.2 Introduction

Recent years have seen a rapid growth in understanding how underdamped vibrational degrees of freedom play a role in efficient exciton transport in photosynthetic light harvesting systems [130–138], and in the long time room-temperature coherence observed in these systems [139–143]. This phenomenon has been referred to as vibrationally-assisted energy transfer (VAET) in the literature [17]. At the same time, fluctuating environments, such as those due to overdamped vibrational modes, have also been shown to promote exciton transport under certain conditions, a phenomenon termed environment-assisted quantum transport (ENAQT) [18, 19]. In particular, the latter occurs when the excitonic degrees of freedom interact with the environment via a pure dephasing interaction, which can be understood as the direct manifestation of a quantum random walk with dephasing [144].

In this work we study the interplay between these two environment-driven exciton transport mechanisms. Earlier theoretical work has established that it is possible to observe oscillations due to excitonic-vibronic quantum coherence even in the presence of additional strong environmental noise [145]. We extend this line of study here by analyzing a dimeric

chromophore donor-acceptor system to provide a comprehensive picture of the regimes where either VAET or ENAQT dominate, as well as the effect of the interplay between these two processes on the energy transfer efficiency in intermediate regimes. VAET is modeled by explicit treatment of an underdamped vibrational mode, while the environmental effect of the overdamped modes is captured by the addition of a classical noise, pure dephasing process (the Haken-Strobl-Reineker model [146]). While all the details of the vibrational environment of natural photosynthetic systems are not captured by such a classical noise model – most importantly, thermal effects and relaxation are not captured – the phenomenon of ENAQT has been observed within such a model of environmental noise [18], and therefore it is sufficient in the first instance to study the interplay between this phenomenon and VAET.

The model we study is particularly suited to experimental validation by trapped ion quantum simulators which could also simulate other interesting physics such as Dirac dynamics [147]. This platform has been used to experimentally study VAET [17], and the addition of classical fluctuations can be easily achieved by noisy modulation of addressing lasers. We have also recently studied the effect of multiple underdamped vibrational modes on energy transfer within the context of a trapped ion simulation [148]. We expect that the predictions made below for regimes of energy transfer can also be validated on the circuit-QED platform [149].

The remainder of the paper is organized as follows. In Sec. 5.3 we summarize the model and our theoretical approach. In Sec. 5.4 we present an analysis of the symmetries in our model that explain the physical relevance of some of the parameters, especially in the trapped ion simulation of the model. In Sec. 5.5 we undertake numerical simulations to analyze various aspects of the interplay of VAET and ENAQT. Specifically, we find that the presence of additional classical dephasing noise tends to weaken the effects of vibrational assistance of energy transfer, with the VAET peaks eventually disappearing as the variance of the classical noise is increased. The optimum transfer efficiency is obtained at zero classical noise, where the only environmental effect is vibrational assistance of energy transfer from a vibration that is resonant with an excitonic energy difference. At larger values of classical noise, the energy transfer efficiency can be maximized at a finite noise variance and the resulting dephasing-enhanced energy transfer is found to occur at a given finite dimer energy gap that could be either resonant or off-resonant with the vibrational mode. Finally, in Sec. 5.6 we conclude with a brief discussion.

5.3 A dimeric noisy chromophore donor-acceptor system

A basic model for demonstrating the VAET processes is a dimeric chromophore donor-acceptor system [17]. We therefore exploit it here as a prototype for larger photosynthetic energy transfer systems to explore the interplay between quantum and classical noise. The
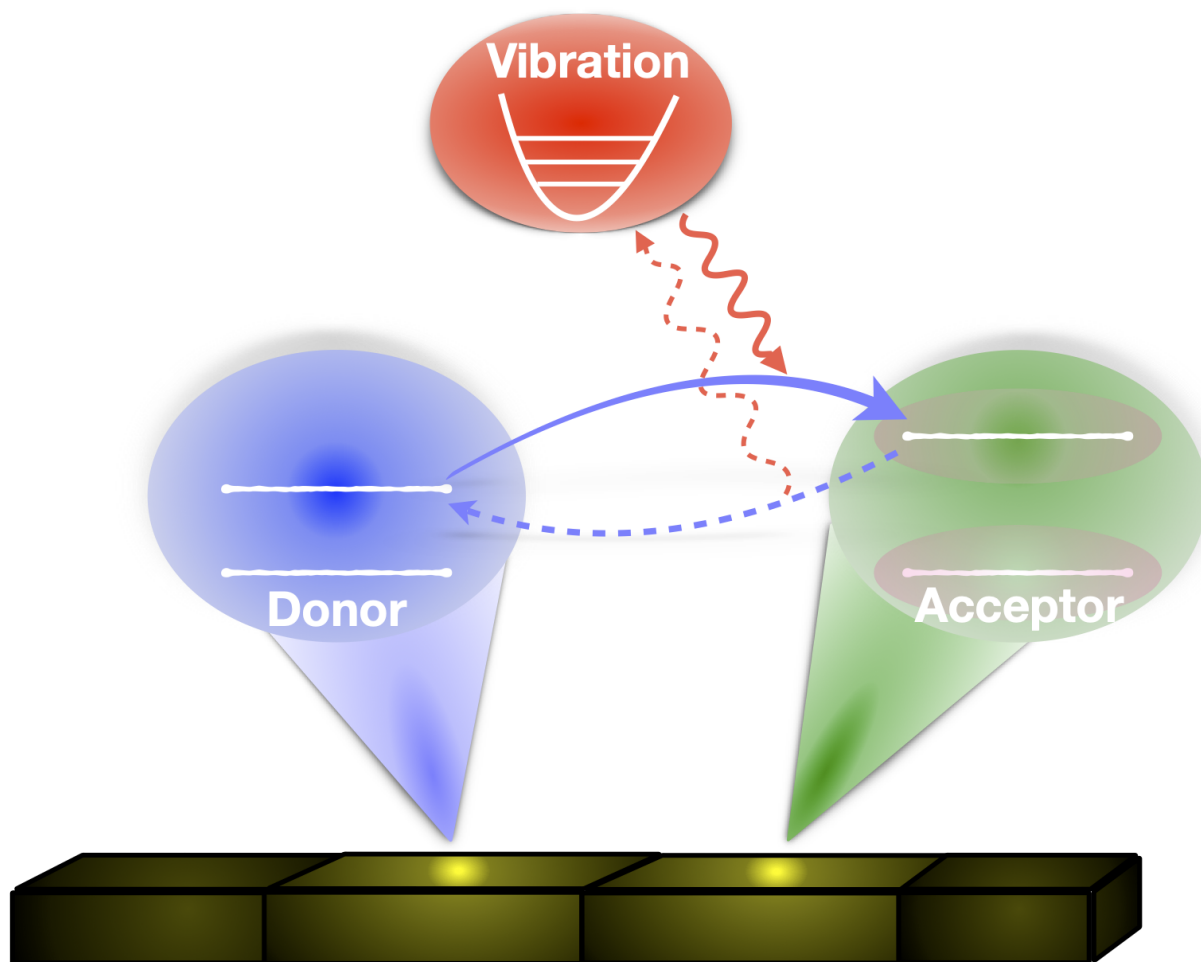
Figure 5.1: (color online) A schematic diagram of the dimeric noisy chromophore donor-acceptor system as simulated on a trapped-ion platform. The yellow ions in the chain represent the donor and acceptor species. The magenta ellipse encircling the energy levels of the acceptor indicates the energetic shifts induced by classical stochastic fluctuations of the environment. The basic mechanism of excitation energy transfer from the donor to the acceptor (blue sold arrow) may be assisted by quantum noise in a form of the single vibration (red solid arrow). Dashed arrows illustrate the inverse downhill process.

noisy VAET system is schematized in Fig. 5.1 and is described by the Hamiltonian

$$H = \frac{1}{2}\omega_d\sigma_z^{(d)} + \frac{1}{2}[\omega_a - \delta(t)]\sigma_z^{(a)} + \frac{1}{2}J\sigma_x^{(d)}\sigma_x^{(a)}$$
$$+\nu a^\dagger a + \frac{1}{2}\kappa\sigma_z^{(a)}(a + a^\dagger), \tag{5.1}$$

where $\sigma_z^{(i)} = |e\rangle_i\langle e| - |g\rangle_i\langle g|$ and $\sigma_x^{(i)} = |e\rangle_i\langle g| + |g\rangle_i\langle e|$ with $i = d, a$. Eq. (5.1) includes donor
(d) and acceptor (a) sites, each of which is modeled by a two-level system with transition
frequency ω_i, as well as the excitonic coupling J between these. The single vibration denoted
by annihilation/creation operators $a/a^\dagger$ coupled to the acceptor is a source of quantum
noise and may coherently assist the excitation energy transfer [17]. The term $\delta(t)$ added to
the site energy describes a classical Gaussian white noise source within the Haken-Strobl-
Reinker model [146, 150–152], i.e., δ at any time instant is distributed as $1/\sqrt{2\pi\sigma^2}e^{-\delta^2/(2\sigma^2)}$,
characterized by zero mean and variance σ^2. Here, we consider only diagonal fluctuations
that are typically larger than fluctuations of the inter-molecular couplings [153, 154] and the
decoherence is dominated by pure dephasing [146].

We focus here on the single-excitation manifold. This subspace is spanned by the basis
states $|eg\rangle$ and $|ge\rangle$. With the projection operator $\Pi = |eg\rangle\langle eg| + |ge\rangle\langle ge|$, we obtain an
effective Hamiltonian

$$\tilde{H} = \Pi H \Pi = \frac{1}{2}[\Delta + \delta(t)]\tilde{\sigma}_z + \frac{1}{2}J\tilde{\sigma}_x$$
$$+\nu a^\dagger a + \frac{1}{2}\kappa\tilde{\sigma}_z(a + a^\dagger). \tag{5.2}$$

Here $\Delta(= \omega_d - \omega_a)$ is the difference between the excitation energies of donor (d) and acceptor
(a). The Pauli operators in this two-dimensional single-excitation subspace are defined as
$\tilde{\sigma}_z = |eg\rangle\langle eg| - |ge\rangle\langle ge|$ and $\tilde{\sigma}_x = |eg\rangle\langle ge| + |ge\rangle\langle eg|$. In the absence of noise, negative
Δ means uphill energy transfer from the donor to the acceptor that may be accompanied
by an absorption of a phonon from the the vibrational mode to assist the transfer, while
positive Δ corresponds to downhill transfer that can be enhanced by a phonon emitted to
the vibration [17]. When the classical noise is present, the energy levels fluctuate. The form
of the coupling term $\tilde{\sigma}_z$ implies that these two excitations are anticorrelated via the noise
source [148, 155]. This means that the noise can bring the excitation levels to resonance and
thereby enhance the excitation energy transfer efficiency.

The chromophore donor-acceptor dimeric system shown in Fig. 5.1 has been experimen-
tally engineered on a trapped-ion platform [17]. The energy sites can be encoded in internal
electronic state of the ions, for example, Ca$^+$ ($|S\rangle$ ($m_j = 1/2$) and $|D\rangle$ ($m_j = 1/2$)) and
therefore the single excitation states are represented by the combined state (e.g., $|DS\rangle$ and
$|SD\rangle$). The interaction between the sites can be engineered via a bichromatic laser beam
along the axis of the trap to be a two-qubit Mølmer-Sørensen quantum interaction and the
site-vibration coupling can be achieved via a tightly focused laser beam localized to each ion.
The dephasing noise represented by $\delta(t)\sigma_z^{(a)}/2$ causing instability of the acceptor splitting in

Eq. (5.1) might be incorporated in the trapped-ion platform by either engineering fluctuations of local magnetic fields acting on internal electronic states of the ion [24] or modulating a Stark-shift generated by a laser beam. In Appendix 5.7, we present a microscopic derivation of the site-vibration coupling that allows a direct mapping between the Hamiltonian of molecular photosynthetic systems and an emulation of the Hamiltonian on platforms such as trapped ions.

To demonstrate how the VAET process is influenced by the classical noise, we consider the physical quantities

$$P_a = \frac{1}{N_r} \sum_{i=1}^{N_r} P_{a,i}, \tag{5.3}$$

$$\eta_a = \frac{1}{N_r} \sum_{i=1}^{N_r} \eta_{a,i}, \tag{5.4}$$

where $P_{a,i}(t) = Tr(\Pi_a \rho_i(t))$ and $\eta_{a,i} = \frac{1}{t_f} \int_0^{t_f} P_{a,i}(t)dt$ are the transfer probability and efficiency, where the latter is defined as the accumulated acceptor population during a given time period t_f, for each noise realization. Here $\Pi_a = |ge\rangle\langle ge|$ is the projection operator onto the excited state at acceptor site a and N_r is the number of noise realizations over which we average. The total density matrix operator for the ith noise realization is $\rho_i(t) = U\rho_s(t=0)\rho_b U^\dagger$, with $U = e^{-i\tilde{H}t}$. For the calculations shown here the initial states are $\rho_s(t=0) = |eg\rangle\langle eg|$ and $\rho_b = \sum_{n=0}^\infty \frac{n_b^n}{(n_b+1)^{n+1}}|n\rangle\langle n|$ for the donor-acceptor dimer and for the vibration, respectively. In our work the temperature of the vibration is quantified by the average phonon number n_b via the relation $n_b = \frac{1}{e^{h\nu/k_B T}-1}$ with h and k_B being the Planck and Boltzmann constants, respectively, implying more phonons at a higher temperature. The number of the noise realizations and Fock space size of the vibration are made large enough to make sure the accuracy and convergence of our results, i.e., $N_r = 800$ and $N = 24$. In the numerical simulations below we use values for parameters that are typical of trapped-ion energy scales (i.e., kHz frequencies), rather than values typical of natural photosynthetic systems. However, these can be related by a simple scaling of energies (see, e.g., Table I in Ref. [148]).

5.4 An invariance of the VAET system

In this section, we show that the effective Hamiltonian in Eq. (5.2) possesses an important symmetry implying that, for the quantities we compute here, only the difference in sign between the excitation energy difference Δ and the vibrational frequency ν is significant. This symmetry has some practical importance in the context of trapped-ion simulation of these dynamics since sweeping ν to negative values can be easier than sweeping Δ to negative values. This is because the former is defined by a difference in frequencies that can be tuned, while the latter corresponds to an energy gap, which is more difficult to tune [17].

In general we expect that the probability P_a will be different when the Hamiltonian is different (e.g., transformed by some symmetry operations). However, the acceptor population P_a, is invariant under the simultaneous sign change of the excitation energy difference Δ and the vibrational frequency ν. Consider the time traces of the transfer probability $P_a(t)$, Eq. (5.3), shown in Fig. 5.2 as an example. It is evident from these plots that for the off-resonant transition (i.e., $\nu^2 \neq \Delta^2 + J^2$), the empty circles for which $\{\Delta/2\pi, \nu/2\pi\} = \{1.2, -0.9\}$kHz give the same probability as the filled circles, for which $\{\Delta/2\pi, \nu/2\pi\} = \{-1.2, 0.9\}$kHz, i.e., with opposite signs of both Δ and ν. This is also true for the resonant transitions $\nu^2 \neq \Delta^2 + J^2$ both in the absence of classical noise, indicated by the red empty and filled squares with $\{\Delta/2\pi, \nu/2\pi\} = \{1.2, -0.9\}$kHz and $\{-1.2, 0.9\}$kHz, respectively, in Fig. 5.2, and in the presence of the classical noise source ($\delta \neq 0$, not shown here). To understand this invariance, we performed a symmetry-based analysis for both the situation in the absence of noise and the situation in the presence of noise. As detailed in Appendix 5.8, we find that if the initial state is an eigenstate of a parity operator and of the Pauli operator σ_z, and if all coefficients in the initial state have the same phase modulo π, then the probability $P_a(t)$ is invariant when simultaneously changing the sign of Δ and ν. This invariance is independent both of the value of the temperature parameter n_b and of whether or not the resonance condition ($\Delta^2 + J^2 = \nu^2$) is satisfied. This surprising independence derives fundamentally from the inherited parity symmetry and the time-reversal symmetry of the Hamiltonian that fully governs dynamical evolution under a certain initial state associated with an additional symmetry. See Appendix 5.8 for full details. We finally mention that, for more complex photosynthetic systems or trapped-ion platforms that go beyond the Hamiltonian under our consideration, one could perform similar analysis as to that in Appendix 5.8 to assess whether an invariant property exists or not.

5.5   Features of the noisy VAET

Here we demonstrate how the basic features of excitonic energy transport are influenced by the interplay between quantum and classical noise present in the dimeric chromophore donor-acceptor system of Eq. (5.1), considering in particular the effect of the classical stochastic noise on the VAET induced by the quantum noise. In Fig. 5.3 we first present a typical example of the time evolution of the transfer probability in the absence of classical noise. This shows oscillations characterized by the transition frequency $\nu \sim \sqrt{\Delta^2 + J^2}$, with a corresponding oscillatory period $2\pi/\nu \sim 0.556$ms (approximately four cycles in each period of 2.4ms). Because of the coherent coupling of the donor-acceptor dimer to the underdamped vibration, we expect additional slow oscillations at a frequency $\sim \frac{\kappa J}{\nu}\sqrt{n}$ (period ~ 6.4ms). These occur on a longer time scale than that shown here. It is also shown in Fig. 5.3 that with the increase of the average phonon number n_b, that quantifies the temperature of the vibration mentioned in Sec. 5.3, P_a first increases as expected but becomes suppressed at later times. This suppression results from a reduced period of the above-mentioned slow oscillations for an increased n_b which has a relatively higher probability (i.e., $n_b^n/(n_b+1)^{n+1}$)
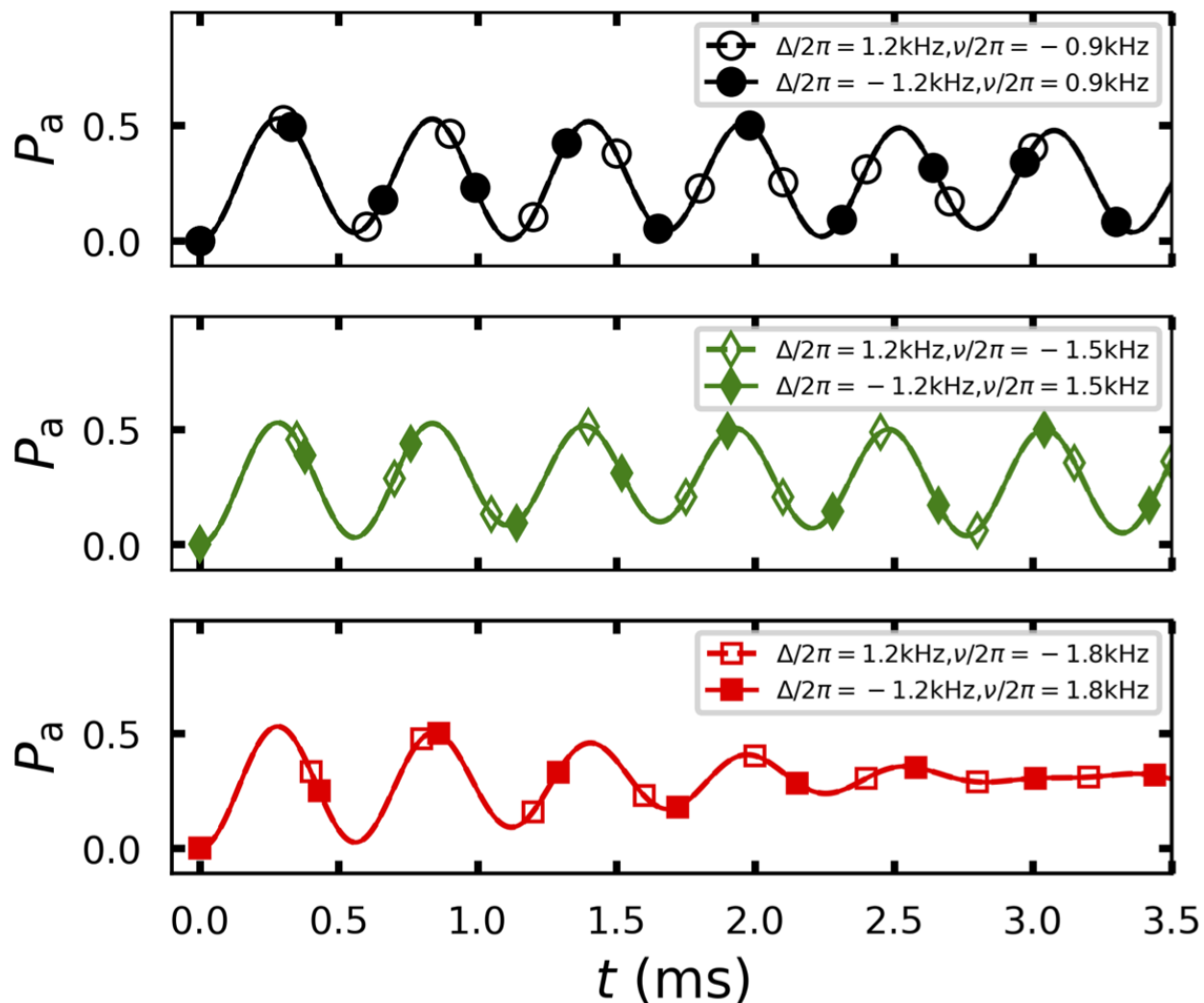
Figure 5.2: (color online) An example of the invariance of the transfer probability P_a under the simultaneous sign change of Δ and ν in the dimeric VAET system. The red curves denote the resonant case $(\Delta^2 + J^2 = \nu^2)$ while two other curves refer to off-resonant cases. We take $J/2\pi = 1.3$kHz, $\kappa/2\pi = 0.229$kHz, $n_b = 0.4$, and $N_r = 800$. The classical noise $\delta = 0$ is used in these calculations.
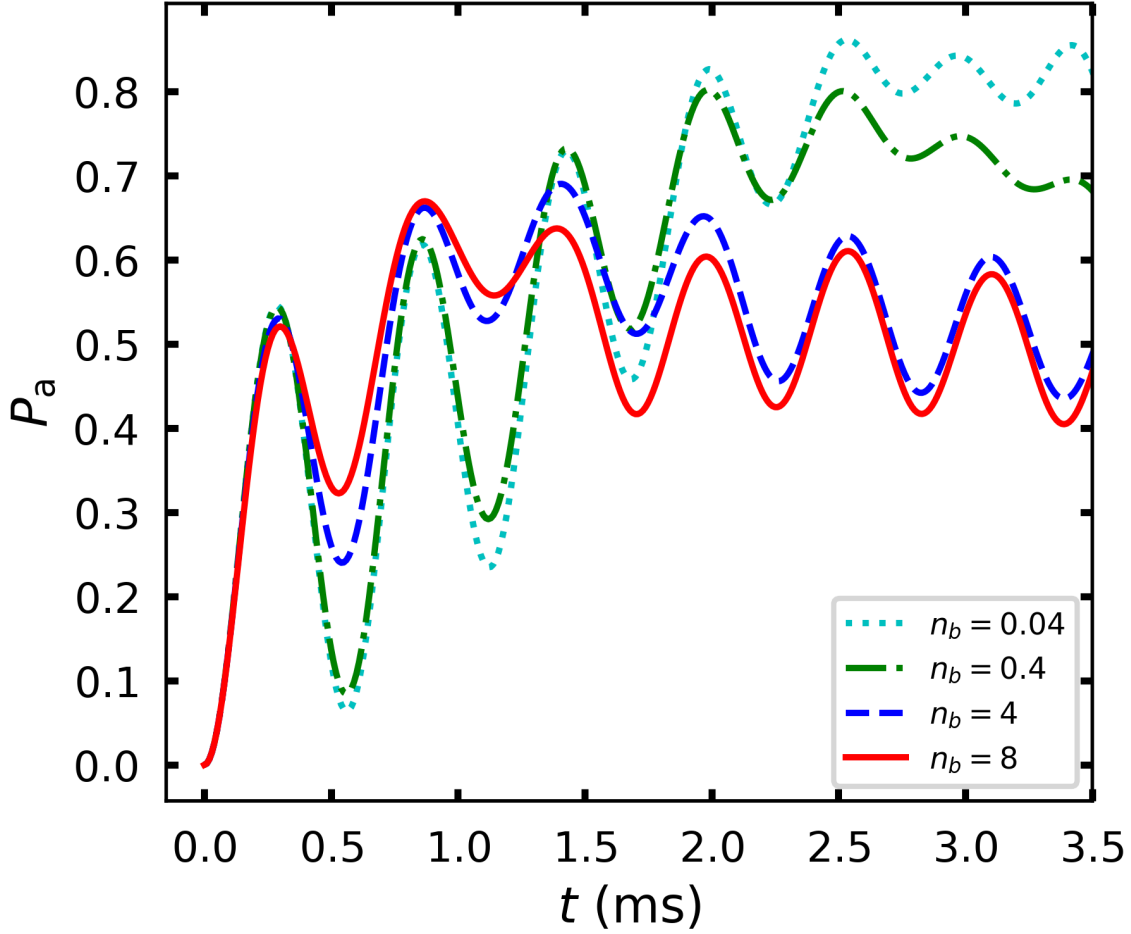
Figure 5.3: (color online) A sample time evolution of transfer probability between electronic
excited states at sites of the donor-acceptor dimer for various values of temperature ($n_b =$
$0.04, 0.4, 4, 8$) in the absence of classical noise ($\delta = 0$). The other parameters are $\Delta/2\pi =$
1.2kHz, $\nu/2\pi = 1.8$kHz, $J/2\pi = 1.3$kHz, $\kappa/2\pi = 0.229$kHz, and $N_r = 800$.

for a larger n state $|n\rangle\langle n|$. Starting from this reference behavior with no classical noise
($\delta = 0$), in the following we shall develop an understanding of the effect of finite classical
noise by sweeping the values of both the vibrational frequency (ν) and the donor-acceptor
excitation energy difference (Δ).

5.5.1 VAET in the presence of weak noise

The upper panels in Fig. 5.4 show two-dimensional plots of the acceptor population P_a as a
function of the vibrational mode frequency $\nu/2\pi$ and the classical noise variance σ^2 over the
time period $0 - t_f$, for $t_f = 2$ms and three different temperatures (panels a-c). The lower
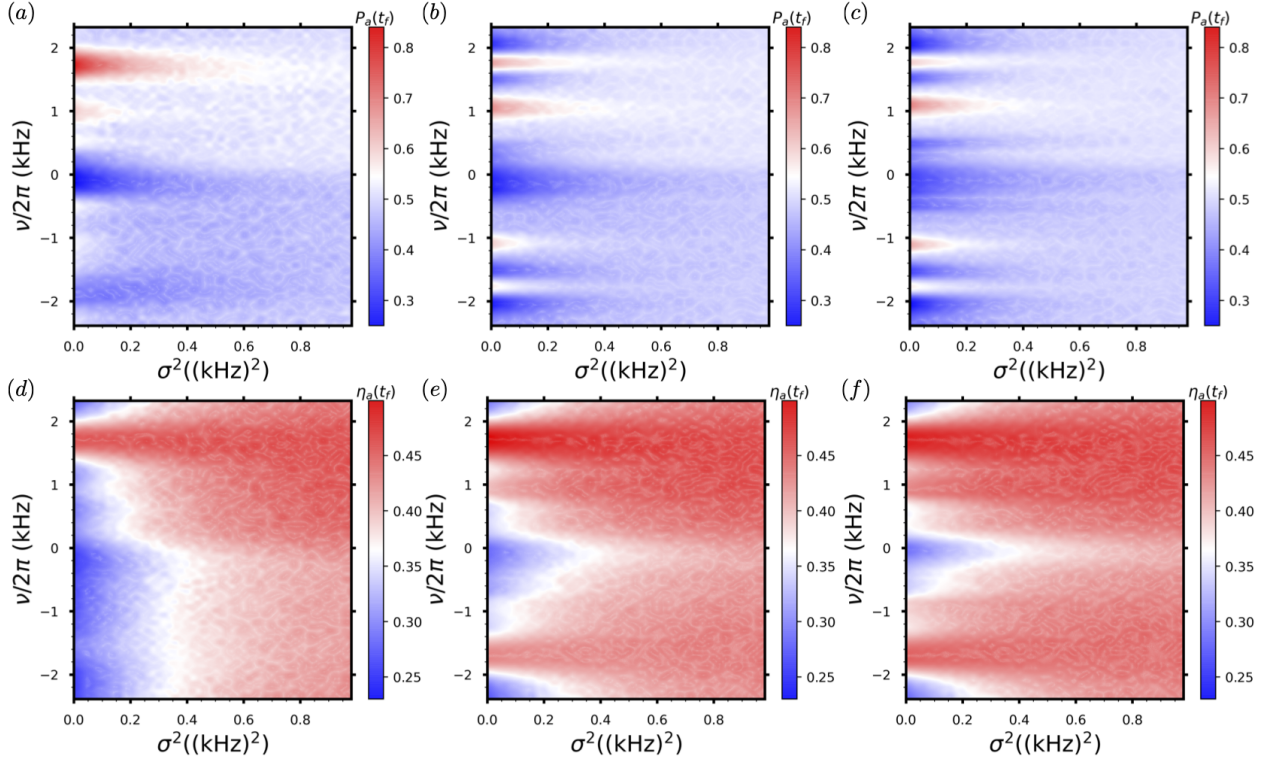
Figure 5.4: (color online) Probability $P_a(t_f)$ (upper panel a-c) and efficiency $\eta_a(t_f)$ (lower panel d-f) of energy transfer as a function of vibrational mode frequency (ν) and classical noise variance (σ^2). The detuning between donor and acceptor is $\Delta/2\pi = 1.2$kHz. The three upper/lower plots are at different temperatures with mean boson mode occupation number ranging from low ($n_b = 0.4$), intermediate ($n_b = 4$), and high ($n_b = 8$). Other parameters are $t_f = 2$ms, $J/2\pi = 1.3$kHz, $\kappa/2\pi = 0.229$kHz, and $N_r = 800$.

panels (d-f) show the corresponding efficiencies η_a (accumulated population) over same time period. These plots correspond to the weak noise (small variance) regime. The distinct horizontal bars at resonance, $\nu = \pm\sqrt{\Delta^2 + J^2} \sim 2\pi \times 1.8$kHz (here $\Delta/2\pi = 1.2$kHz, $J/2\pi = 1.3$kHz), for example, those in panels (a) and (d), are signatures of VAET corresponding to an energy transfer process assisted by one phonon from the underdamped vibration. In addition to these resonant points that show high transfer probability P_a and correspondingly high efficiency η_a, we also observe VAET processes involving more than one phonon. Specifically, the lower intensity horizontal bars at $\nu \sim \pm 2\pi \times 0.9$kHz or $\nu \sim \pm 2\pi \times 0.6$kHz indicate the two- or three-phonon absorption processes that can assist excitonic transfer in the donor-acceptor system. The plots show that classical noise injected as a random Gaussian modulation of the energy gap between excitations at the donor and acceptor sites begins to play a role as σ^2 is increased from zero. As expected, this noise is seen to gradually reduce the extent of VAET as σ^2 increases. However the extent of this reduction depends on whether the vibrational
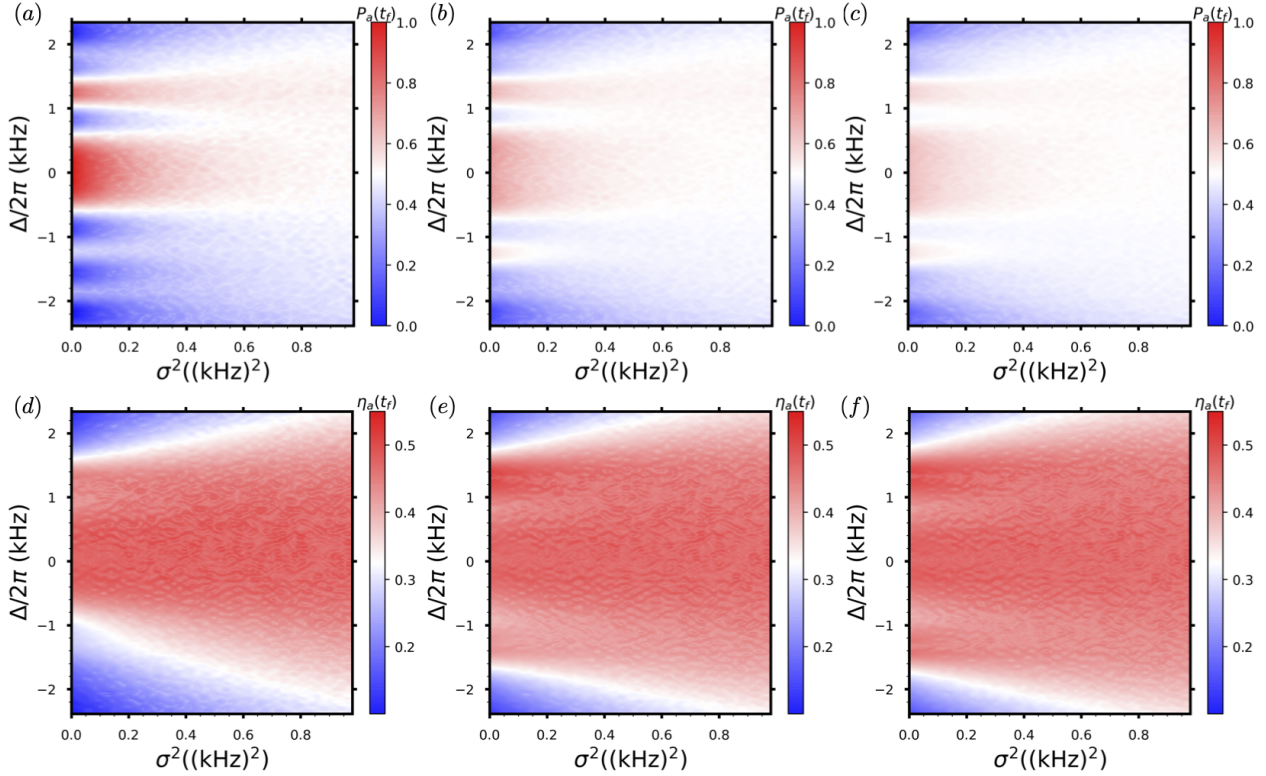
Figure 5.5: (color online) Probability $P_a(t_f)$ (upper panel a-c) and efficiency $\eta_a(t_f)$ (lower panel d-f) of energy transfer as a function of donor-acceptor energy difference (Δ) and classical noise variance (σ^2), for three different temperatures. The three upper/lower plots have mean boson mode occupation number ranging from low ($n_b = 0.4$), intermediate ($n_b = 4$), and high ($n_b = 8$), corresponding to values of temperature $T = 0.069\mu$K, 0.387μK, and 1.77μK, respectively. Here the vibrational mode frequency is $\nu/2\pi = 1.8$kHz and all other parameters are the same as in Fig 5.4. Note that a trapped-ion quantum simulator can be operated in the regime where all Hamiltonian parameters are of order a few kHz [17] that leads to low temperatures evaluated above.

frequency is positive or negative, as demonstrated in panels (a) and (b). This asymmetry in the degree of vibrational assistance for $\pm\sqrt{\Delta^2 + J^2}$ becomes less pronounced as temperature increases (see panels (b, e) ($n_b = 4$) and panels (c, f) ($n_b = 8$)). It is also evident that the effect of VAET is increasingly suppressed as the classical noise variance increases, with both P_a and η_a becoming increasingly uniform as a function of the vibrational frequency ν. The meaning of the negative vibrational frequency ($\nu < 0$) that appears in Fig. 5.4 is already mentioned in Sec. 5.4 above and will be further explained in Appendix 5.8.

In addition to sweeping the vibrational mode frequency in Fig. 5.4, we have also considered sweeping the donor-acceptor energy difference, Δ, since this may be easier to realize in experiments. Fig. 5.5 shows the transfer probability (upper panel a-c) and efficiency (lower

panel d-f) as a two-dimensional function now of $\Delta/2\pi$ and of the classical noise variance σ^2.
In this case, the optimal transfer efficiency is found at $\Delta = 0$ since the donor and acceptor
are in resonance here. There are still distinct peaks around $\Delta = \pm\sqrt{\nu^2 - J^2} \sim \pm 2\pi \times 1.2\text{kHz}$
(with $\nu/2\pi = 1.8\text{kHz}$ and $J/2\pi = 1.3\text{kHz}$), see for example panel (a). Note that a peak at
a positive value of Δ represents downhill energy transfer with emission of a phonon, so the
signatures of these features are more intense. Peaks at negative values of Δ signify uphill
VAET processes assisted by absorption of a phonon from the vibration. There are additional
peaks observable near $\Delta/2\pi \sim \pm 1.8\text{kHz}$ in Fig. 5.5(a), implying off-resonant transitions as-
sisted by the vibrational mode $\nu/2\pi = 1.8\text{kHz}$. We see again that increasing the variance
of the classical noise decreases the VAET signatures [see Fig. 5.5(b) or (c)], similar to what
was observed in Fig. 5.4.

Comparing Figs. 5.4 and 5.5 we see a clear difference in the behavior of the energy
transfer efficiency depending on which parameter is swept, i.e., ν or Δ. This difference
derives fundamentally from the different aspects of the basic relation $n\nu = \pm\sqrt{\Delta^2 + J^2}$ (with
n the number of phonons in the vibration), revealed by either fixing the donor-acceptor gap
Δ (> 0 in Fig. 5.4) and sweeping ν, or fixing the vibrational frequency ν (> 0 in Fig. 5.5)
while sweeping Δ. Sweeping ν allows the $n > 1$, multiple phonons resonances to be seen,
while sweeping Δ allows the $\Delta = 0$, donor/acceptor resonance to be seen.

5.5.2   Optimal value of the classical noise variance for energy transport efficiency

The previous plots have focused on the low noise regime. In this regime, the existence of an
optimal classical noise variance σ^2 at which the efficiency is maximized, the key prediction
of purely dephasing-enhanced energy transfer [18], is not evident. Instead, the efficiency
for a finite donor-acceptor gap ($\Delta \neq 0$) is seen to increase with increasing σ^2. In order to
see a turnover of efficiency with increasing noise variance, one has to study larger values of
σ^2. Fig. 5.6(a) shows plots of the energy transfer efficiency at larger values of the classical
noise variance σ^2. For a given finite energy detuning between donor and acceptor ($\Delta = \sqrt{\nu^2 - J^2} \sim 2\pi \times 1.2\text{kHz}$), the efficiency is seen to be low for small noise variance σ^2, to rise
as σ^2 increases, and is now seen to subsequently decrease again at the significantly higher
values of σ^2 used here. This behavior is characteristic of the turnover of quantum random
walks under dephasing [144] and has been termed an ENAQT turnover [18]. Fig. 5.6(b)
shows the corresponding probability $P_a(t_f)$, which also shows an optimal σ value but with
a weaker maximum. It is evident from these plots that the appearance of a quantum Zeno
regime at large σ^2, where the dephasing severely inhibits any amount of energy transfer, is
more easily observable for large detuning values $|\Delta| > J$.

We conclude that in the high noise regime, ENAQT dominates and VAET plays little
role in energy transfer dynamics. This is expected since vibrational assistance is a resonant
phenomenon, and noise broadening of the energy difference between donor and acceptor
eliminates a well-defined energy gap for the vibrational mode to be on resonance with.
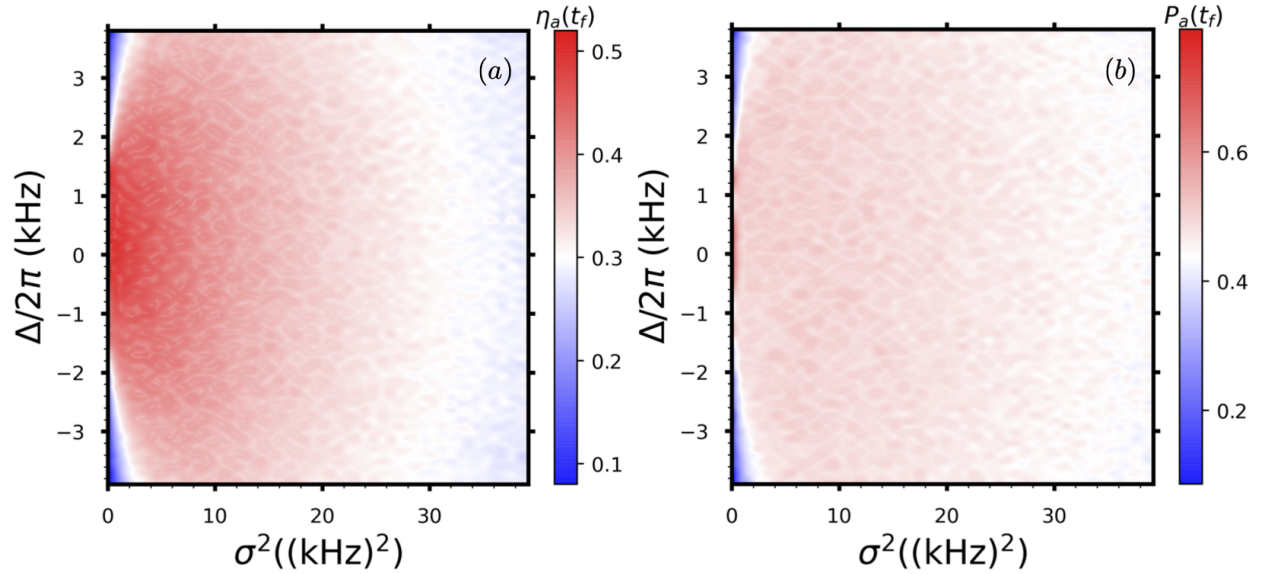
Figure 5.6: (color online) The turnover of efficiency (a) and probability (b) of the excitation energy transfer as a function of the classical noise variance σ^2 for larger values of this, with $n_b = 4$. All other parameters are the same as in Fig. 5.5.

5.6 Discussions and conclusions

We have studied the interplay between vibrationally assisted excitonic energy transfer due to coupling of electronically excited states with underdamped vibrational modes and the effect of classical dephasing that has been previously identified as enabling energy transfer in certain regimes. We illustrated the interplay between these two processes by considering a dimeric chromophore donor-acceptor dimer system, which provides the basic features of a larger light-harvesting complex that are relevant to the interaction of excitonic and vibrational degrees of freedom. We find that while addition of the classical noise weakens the VAET processes and destroys the quantum signature of this in the weak noise regime, it can nevertheless enhance the VAET when the noise becomes higher. We also established an invariance property of this dimeric VAET system and provided a symmetry-based explanation for this. We look forward to experiments, e.g., on trapped ion emulation platforms, that will demonstrate and validate the results shown here, in particular the interplay between VAET and dephasing-induced optimal values of classical noise, as well as the invariance property. We expect that the basic features of the interplay between quantum and classical noise, representing coupling with underdamped and overdamped oscillators, the latter confined to dephasing interactions, that have been demonstrated and analyzed here for a typical dimeric chromophore donor-acceptor dimeric system can be manifested also in larger and more complex photosynthetic systems. Generalization to other kinds of noise, or to noise injected as a modulation of the vibrational mode frequency or of the exciton-vibration coupling is straightforward. We expect that our

observation that weak classical noise tends to weaken VAET will generally hold for other kinds of generic noise as well. It would be interesting if this is not true for some highly structured noise with tailored spectrum.

We emphasize that the detrimental effect of the classical noise on the VAET reported in the present work is dependent on frequency of molecular vibration and difference of excitonic energies [156]. Specifically, in Fig. 5.4(a-c) with a fixed donor-acceptor gap, the detrimental effect of the classical noise manifests itself in different ways for a resonant absorption of either single or multiple phonons from the vibration. For the off-resonant cases in Fig. 5.4(a-c), the classical noise demonstrates a beneficial effect (this is because noise can bring the excitation levels to resonance and thereby enhance the energy transfer). In Fig. 5.5(a-c) with a fixed vibrational mode frequency, the detrimental effect of the classical noise truly depends on the donor-acceptor gap, e.g., downhill ($\Delta > 0$) or uphill ($\Delta < 0$), and resonant or off-resonant transfer. In addition, our observation in Fig. 5.5(a-c) is consistent with that in Ref. [156], namely the vibration plays a minor role in the region of small absorption energy difference but contributes strongly to assist the transfer in the region of large absorption energy.

We also comment on the relationship between our work and Ref. [157], which studied a similar problem of excitation energy transfer of a dimer under the influence of both a vibration and an environment. In that work, it is claimed that the transfer dynamics are dominated by the environment and the vibrational modes contribute to acceleration the energy transfer only slightly. While this conclusion is consistent with the conclusions drawn in the present work, we would like to point out a few differences between Ref. [157] and our work. The first one is the theoretical methods employed. The environment and the vibration were taken into account in Ref. [157] via relaxation functions in the form of either an exponential decay or Brownian oscillator model, respectively, which is different from the Gaussian white noise or the quantized oscillator included in a straightforward way into the Hamiltonian [i.e., Eq. (5.1)] in our work. The second difference is that Ref. [157] considered a specific case, namely, resonant downhill energy transfer affected by a vibration and an environment. In contrast, we consider the effect of finite classical noise in a more complete way by sweeping the values of the vibrational frequency, the donor-acceptor excitation energy difference, or the variance of the classical noise, as shown explicitly in the weak-noise regime in Figs. 5.4 and 5.5.

Finally, we note that in addition to the trapped-ion platform that we focus on in our work, the circuit-QED platform could also be used for the implementation of our predictions. The effects of classical noise on energy transfer have already been studied on this platform [149], where individual superconducting qubits played the role of energy sites. As in that case, the interaction between sites can be achieved by cavity-mediated, or direct, coupling between qubits. The new element, the vibrational mode, can be modeled by a mode of a transmission line resonator. A key difference in superconducting platforms, is that the usual coupling between qubits and resonator modes is of the form $\sigma^+ a + \sigma_- a^\dagger$, which is different from the usual VAET coupling considered here, $\sigma_z(a + a^\dagger)$. However, this coupling could be engineered by operating in the dispersive regime [158] and linearizing the interaction around a large classical pump.
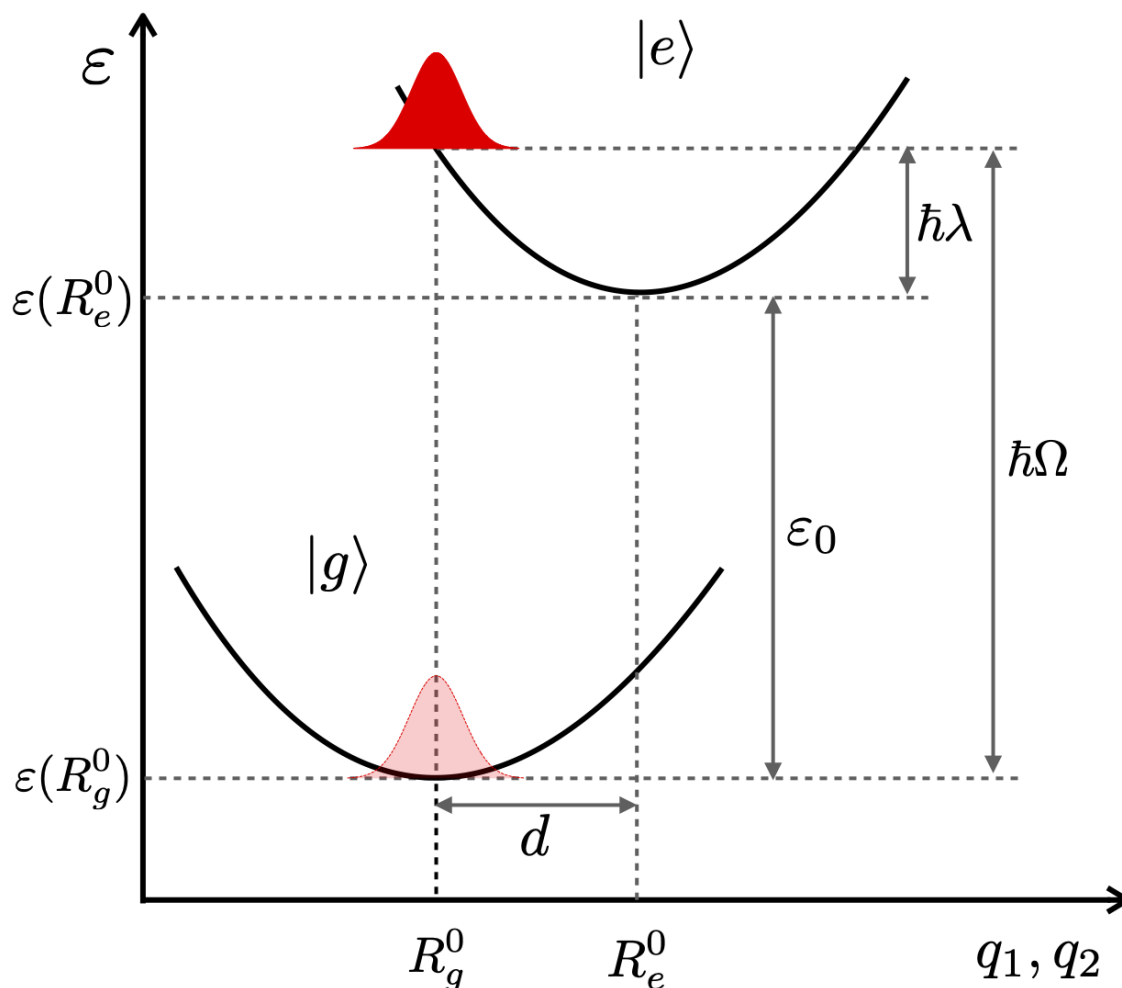
Figure 5.7: Schematic of the electronic excitation and reorganization processes with the Franck-Condon transition energy $\hbar\Omega$ and the reorganization energy $\hbar\lambda$.

5.7 Derivation of the electron-vibration interaction

In this appendix, we demonstrate how to connect the Hamiltonian for light harvesting systems that is commonly studied for the natural systems with an equivalent description derived for emulation of these by artificial systems such as trapped ions.

5.7.1 Equivalent descriptions with different coupling forms

To demonstrate in a simple manner an equivalence between two Hamiltonian descriptions that consider a coupling of a vibration to either an excited state or both ground and excited states [159], respectively, we take the molecular system shown in Fig. 5.7 as an example.

This is described by the Hamiltonian

$$
H(q_1, q_2) = (\frac{p^2}{2m} + \frac{m\omega^2}{2}q_1^2)|g\rangle\langle g|
$$
$$
+(\frac{p^2}{2m} + \frac{m\omega^2}{2}q_2^2 + \varepsilon_0)|e\rangle\langle e|. \tag{5.5}
$$

Here the zero of energy is defined to be at the minimum of the nuclear potential energy surface for the electronic ground state $|g\rangle$. According to Fig. 5.7, we define the Franck-Condon transition energy $\hbar\Omega$ and reorganization energy $\hbar\lambda$ as

$$
\hbar\Omega = \varepsilon_0 + m\omega^2 q_1 d, \tag{5.6}
$$
$$
\hbar\lambda = \frac{1}{2}m\omega^2 d^2, \tag{5.7}
$$

respectively.

Written in terms of the center of mass and difference coordinates $\bar{q}$ and d, defined as $\bar{q} = \frac{q_2 + q_1}{2}$ and $d = \frac{q_2 - q_1}{2}$ with q_1 and q_2 the potential surface coordinate of the ground and excited states, respectively, the above Hamiltonian becomes

$$
\begin{aligned}
H(\bar{q}, d) &= [\frac{p^2}{2m} + \frac{m\omega^2}{2}(\bar{q} - d)^2]|g\rangle\langle g| \\
&+ [\frac{p^2}{2m} + \frac{m\omega^2}{2}(\bar{q} + d)^2 + \varepsilon_0]|e\rangle\langle e| \\
&= (\frac{p^2}{2m} + \frac{m\omega^2}{2}\bar{q}^2)(|g\rangle\langle g| + |e\rangle\langle e|) + \frac{m\omega^2}{2}(d^2 \\
&- 2\bar{q}d)|g\rangle\langle g| + [\frac{m\omega^2}{2}(d^2 + 2\bar{q}d) + \varepsilon_0]|e\rangle\langle e| \\
&= \frac{p^2}{2m} + \frac{m\omega^2}{2}\bar{q}^2 + \frac{m\omega^2}{2}d^2 + \varepsilon_0|e\rangle\langle e| + m\omega^2\bar{q}d\sigma_z.
\end{aligned} \tag{5.8}
$$

Here $\sigma_z = |e\rangle\langle e| - |g\rangle\langle g|$. It is then obvious that both the ground and the first excited states are coupled to the vibration. An alternative equivalent form $H(q_1, d)$ is obtained by substituting $q_2 = q_1 + 2d$ into $H(q_1, q_2)$. This yields

$$
\begin{aligned}
H(q_1, d) &= (\frac{p^2}{2m} + \frac{m\omega^2}{2}q_1^2)|g\rangle\langle g| \\
&+ [\frac{p^2}{2m} + \frac{m\omega^2}{2}(q_1 + 2d)^2 + \varepsilon_0]|e\rangle\langle e| \\
&= (\frac{p^2}{2m} + \frac{m\omega^2}{2}q_1^2)(|g\rangle\langle g| + |e\rangle\langle e|) + \varepsilon_0|e\rangle\langle e| \\
&+ 2m\omega^2 q_1 d|e\rangle\langle e| + 2m\omega^2 d^2|e\rangle\langle e| \\
&= \frac{p^2}{2m} + \frac{m\omega^2}{2}q_1^2 + \varepsilon_0|e\rangle\langle e| + 2m\omega^2 q_1 d|e\rangle\langle e| \\
&+ 2m\omega^2 d^2|e\rangle\langle e|.
\end{aligned} \tag{5.9}
$$

It is evident that in this form the vibration is coupled only to the excited state.

As demonstrated, $H(\bar{q}, d)$ and $H(q_1, d)$ are both equivalent to $H(q_1, q_2)$, despite containing different forms for the coupling between the vibration and the electron. This equivalence can be also illustrated by further substituting $q_1 = \bar{q} - d$,

$$
\begin{aligned}
H(q_1, d) &= \frac{p^2}{2m} + \frac{m\omega^2}{2}(\bar{q} - d)^2 + \varepsilon_0 |e\rangle\langle e| \\
&\quad + 2m\omega^2(\bar{q} - d)d|e\rangle\langle e| + 2m\omega^2 d^2 |e\rangle\langle e| \\
&= \frac{p^2}{2m} + \frac{m\omega^2}{2}\bar{q}^2 + \frac{m\omega^2}{2}d^2 - m\omega^2 \bar{q}d + \varepsilon_0 |e\rangle\langle e| \\
&\quad + 2m\omega^2(\bar{q}d - d^2)|e\rangle\langle e| + 2m\omega^2 d^2 |e\rangle\langle e| \\
&= \frac{p^2}{2m} + \frac{m\omega^2}{2}\bar{q}^2 + \frac{m\omega^2}{2}d^2 + \varepsilon_0 |e\rangle\langle e| \\
&\quad + m\omega^2 \bar{q}d(|e\rangle\langle e| - |g\rangle\langle g|) = H(\bar{q}, d). \qquad (5.10)
\end{aligned}
$$

5.7.2 Connection to our model

The lesson that we learn from the above analysis is that two alternative forms of a Hamiltonian with coupling of the vibration to either the ground state or both excited and ground states can be appropriate for describing the system. In particular, one needs to be careful about which additional energetic terms are needed in order to establish an equivalence between the two forms.

To make the connection of the above-demonstrated equivalence with our current model more apparent, we rewrite Eqs. (5.8) and (5.9) by performing a shift of the zero of energy to the average of the minima of the two potential surfaces and further quantizing the two quadratic Hamiltonians. When the zero of energy is shifted to $\frac{\varepsilon_0}{2}$, Eq. (5.8) can be rewritten as

$$
\begin{aligned}
H(\bar{q}, d) &= \frac{p^2}{2m} + \frac{m\omega^2}{2}\bar{q}^2 + \frac{m\omega^2}{2}d^2 \\
&\quad + \frac{\varepsilon_0}{2}(|e\rangle\langle e| - |g\rangle\langle g|) + m\omega^2 \bar{q}d\sigma_z \\
&= \frac{p^2}{2m} + \frac{m\omega^2}{2}\bar{q}^2 + \frac{m\omega^2}{2}d^2 + \frac{\varepsilon_0}{2}\sigma_z + m\omega^2 \bar{q}d\sigma_z.
\end{aligned}
$$
$$(5.11)$$

A further quantization of the harmonic oscillator, i.e., $\frac{p^2}{2m} + \frac{m\omega^2}{2}\bar{q}^2 \to \hbar a^\dagger a$ and $\bar{q} \to a^\dagger + a$, yields the Hamiltonian

$$
\begin{aligned}
H &= \hbar\omega a^\dagger a + \frac{\varepsilon_0}{2}\sigma_z - \kappa(a^\dagger + a)\sigma_z + \frac{m\omega^2 d^2}{2} \\
&= \hbar\omega a^\dagger a + \frac{\varepsilon_0}{2}\sigma_z - \kappa(a^\dagger + a)\sigma_z + \frac{\kappa^2}{2m\omega^2}, \qquad (5.12)
\end{aligned}
$$

where $\kappa = -m\omega^2 d$. Similarly, Eq. (5.9) under the consideration of the same shifted zero of energy becomes

$$
\begin{aligned}
H(q_1, d) &= \frac{p^2}{2m} + \frac{m\omega^2}{2}q_1^2 + \frac{\varepsilon_0}{2}(|e\rangle\langle e| - |g\rangle\langle g|) \\
&\quad + 2m\omega^2 q_1 d|e\rangle\langle e| + 2m\omega^2 d^2|e\rangle\langle e| \\
&= \frac{p^2}{2m} + \frac{m\omega^2}{2}q_1^2 + \frac{\varepsilon_0}{2}\sigma_z \\
&\quad + 2m\omega^2 q_1 d|e\rangle\langle e| + 2m\omega^2 d^2|e\rangle\langle e|.
\end{aligned}
\tag{5.13}
$$

Quantization of Eq. (5.13) using $\frac{p^2}{2m} + \frac{m\omega^2}{2}q_1^2 \to \hbar\tilde{a}^\dagger\tilde{a}$ and $q_1 \to \tilde{a}^\dagger + \tilde{a}$ leads to

$$
\begin{aligned}
\tilde{H} &= \hbar\tilde{a}^\dagger\tilde{a} + \frac{\varepsilon_0}{2}\sigma_z - 2\kappa(\tilde{a}^\dagger + \tilde{a})|e\rangle\langle e| + \frac{2\kappa^2}{m\omega^2}|e\rangle\langle e| \\
&= \hbar\tilde{a}^\dagger\tilde{a} + (\frac{\varepsilon_0}{2} + \frac{2\kappa^2}{m\omega^2})|e\rangle\langle e| - 2\kappa(\tilde{a}^\dagger + \tilde{a})|e\rangle\langle e| \\
&\quad - \frac{\varepsilon_0}{2}|g\rangle\langle g|.
\end{aligned}
\tag{5.14}
$$

Comparison between Eq. (5.12) and Eq. (5.14) clearly shows the relationship between equivalent descriptions with different forms of the electron-vibration coupling.

Finally we illustrate the connection between the Huang-Rhys parameter in the natural systems and the site-vibration coupling of the simulation systems. The Huang-Rhys parameter D is a dimensionless factor related to the scaled mean square displacement

$$
D = \frac{d'^2 m\omega}{2\hbar},
\tag{5.15}
$$

where $d' = q_2 - q_1 = 2d$. This yields the displacement $d' = \sqrt{\frac{2\hbar D}{m\omega}}$. The interaction term between the local excitonic degree of freedom and the vibration in Eq. (5.11) has the form

$$
\begin{aligned}
&m\omega^2 \bar{q} d\sigma_z \\
&= m\omega^2 \times \frac{1}{2}\sqrt{\frac{2\hbar D}{m\omega}} \times \sqrt{\frac{\hbar}{2m\omega}}(a^\dagger + a) \times (|e\rangle\langle e| - |g\rangle\langle g|) \\
&= \frac{1}{2}\hbar\omega\sqrt{D}(a^\dagger + a)\sigma_z.
\end{aligned}
\tag{5.16}
$$

Equivalently, if we consider the alternative coupling form in Eq. (5.13), this interaction is given by

$$
\begin{aligned}
&2m\omega^2 q_1 d|e\rangle\langle e| \\
&= m\omega^2 \sqrt{\frac{2\hbar D}{m\omega}} \times \sqrt{\frac{\hbar}{2m\omega}}(a^\dagger + a) \times |e\rangle\langle e| \\
&= \hbar\omega\sqrt{D}(a^\dagger + a)|e\rangle\langle e|.
\end{aligned}
\tag{5.17}
$$

This implies the site-vibration coupling parameter $\kappa = -\sqrt{D}\hbar\omega/2$.

5.8 Symmetry analysis on the VAET system

In this appendix we present a symmetry-based analysis to support the invariance property of our VAET system both in the absence and in the presence of the classical noise.

5.8.1 Absence of classical noise

We first consider the case of the absence of classical noise, $\bar{H} = \tilde{H}(\delta = 0)$. Given the effective Hamiltonian in Eq. (5.2) and the initial state $|\phi_0\rangle (= |eg, n\rangle)$, the probability of being in the target state at time t is $P(t) = \langle \phi_0 | e^{i\bar{H}t} \Pi_a e^{-i\bar{H}t} | \phi_0 \rangle$, where the $\Pi_a = |ge\rangle\langle ge|$ is the projection onto the target state. The extension to a thermal state of the vibration $\rho_b = \sum_{n=0}^{\infty} \frac{n_b^n}{(n_b+1)^{n+1}} |n\rangle\langle n|$ is straightforward. We are going to transform the Hamiltonian by conjugating it with different symmetry operations, which corresponds to changing the signs of some subsets of the four parameters Δ, J, ν, and κ. We will show that when the initial state $|\phi_0\rangle$ is an eigenstate of the relevant symmetry operations, $P(t)$ is invariant under the corresponding sign changes.

The first symmetry is the parity corresponding to a sign change of the exciton-vibration coupling constant κ. Under this sign change the Hamiltonian $\bar{H}$ becomes $H_1 = \frac{\Delta}{2}\tilde{\sigma}_z + \frac{J}{2}\tilde{\sigma}_x + \nu a^\dagger a - \frac{\kappa}{2}\tilde{\sigma}_z(a + a^\dagger)$. The physical meaning of this sign change is to invert the coordinate of the harmonic oscillator (i.e., a parity operation). If our initial state treats both directions of the coordinate equally, then we expect that inverting the coordinate will have no effect on the system dynamics other than inverting the spatial coordinates. We define the parity operator Υ just as for the spatial coordinate of the 1D harmonic oscillator, i.e.,

$$\Upsilon|n\rangle = \begin{cases} -|n\rangle & n \text{ is odd,} \\ |n\rangle & n \text{ is even,} \end{cases} \tag{5.18}$$

so the new Hamiltonian can be written as $H_1 = \Upsilon^\dagger \bar{H} \Upsilon$. The probability of being in the target state then becomes

$$
\begin{aligned}
P_1(t) &= \langle \phi_0 | e^{iH_1 t} \Pi_a e^{-iH_1 t} | \phi_0 \rangle \\
&= \langle \phi_0 | e^{i\Upsilon^\dagger \bar{H} \Upsilon t} \Pi_a e^{-i\Upsilon^\dagger \bar{H} \Upsilon t} | \phi_0 \rangle \\
&= \langle \phi_0 | \Upsilon^\dagger e^{i\bar{H}t} \Upsilon \Pi_a \Upsilon^\dagger e^{-i\bar{H}t} \Upsilon | \phi_0 \rangle \\
&= \langle \phi_0 | \Upsilon^\dagger e^{i\bar{H}t} \Pi_a e^{-i\bar{H}t} \Upsilon | \phi_0 \rangle,
\end{aligned}
\tag{5.19}
$$

where we have used the identity $e^{i\Upsilon^\dagger \bar{H} \Upsilon t} = \Upsilon^\dagger e^{i\bar{H}t} \Upsilon$ and the fact that $\Upsilon \Pi_a \Upsilon^\dagger = \Pi_a$. Since the eigenvalue of the parity operator Υ is ± 1, $P_1(t) = P(t)$ if $|\phi_0\rangle$ is an eigenstate of Υ, i.e., $P(t)$ is invariant under the sign change of κ.

Similarly, a sign change of J leads to $H_2 = \frac{\Delta}{2}\tilde{\sigma}_z - \frac{J}{2}\tilde{\sigma}_x + \nu a^\dagger a - \frac{\kappa}{2}\tilde{\sigma}_z(a + a^\dagger)$, which corresponds to redefining the ground state with a minus sign, i.e., $-|eg\rangle$ or $-|ge\rangle$ for $\Delta < 0$ or > 0, respectively. Unless the initial state has nonzero coefficients on both $|eg\rangle$ and $|ge\rangle$,

we expect this redefinition to have no effect on the system dynamics. The Hamiltonian H_2 is obtained by conjugating $\bar{H}$ with $\tilde{\sigma}_z$ (i.e., $H_2 = \tilde{\sigma}_z^\dagger \bar{H} \tilde{\sigma}_z$). So the target state probability now becomes

$$
\begin{aligned}
P_2(t) &= \langle \phi_0 | e^{iH_2 t} \Pi_a e^{-iH_2 t} | \phi_0 \rangle \\
&= \langle \phi_0 | e^{i\tilde{\sigma}_z^\dagger \bar{H} \tilde{\sigma}_z t} \Pi_a e^{-i\tilde{\sigma}_z^\dagger \bar{H} \tilde{\sigma}_z t} | \phi_0 \rangle \\
&= \langle \phi_0 | \tilde{\sigma}_z^\dagger e^{i\bar{H} t} \tilde{\sigma}_z \Pi_a \tilde{\sigma}_z^\dagger e^{-i\bar{H} t} \tilde{\sigma}_z | \phi_0 \rangle \\
&= \langle \phi_0 | \tilde{\sigma}_z^\dagger e^{i\bar{H} t} \Pi_a e^{-i\bar{H} t} \tilde{\sigma}_z | \phi_0 \rangle.
\end{aligned}
\tag{5.20}
$$

Therefore when the initial state $|\phi_0\rangle$ is an eigenstate of $\tilde{\sigma}_z$, $P(t)$ is invariant under the sign change of J.

The last symmetry to be discussed is the time reversal symmetry. The physical meaning of the sign change of the entire Hamiltonian $\bar{H}$, namely, $H_3 = -\bar{H}$, is most apparent when we look at the time evolution operator $U_3 = e^{-iH_3 t} = e^{-iH(-t)}$. Evolving H_3 forward in time corresponds to evolving the original Hamiltonian $\bar{H}$ backward in time. Conjugating the forward time evolution operator e^{-iHt} with the time reversal operator Θ will give us the backward time evolution operator, which is the forward time evolution operator of H_3, i.e., $\Theta^\dagger e^{-i\bar{H} t} \Theta = e^{i\bar{H} t} = e^{-iH_3 t}$. In the Hilbert space of our VAET system, the effect of Θ acting on a state is to replace all the coefficients of the basis states by their complex conjugates, i.e., $\Theta \sum_{\alpha=eg,ge} \sum_n c_{\alpha,n} |\alpha, n\rangle = \sum_{\alpha=eg,ge} \sum_n c_{\alpha,n}^* |\alpha, n\rangle$. Note that Θ is an antiunitary (antilinear and unitary) operator, so one has to be careful when using this with the Dirac bracket notation. The target state probability under the time-reversed dynamics is

$$
\begin{aligned}
P_3(t) &= \langle \phi_0 | e^{iH_3 t} \Pi_a e^{-iH_3 t} | \phi_0 \rangle \\
&= \langle \phi_0 | \Theta^\dagger e^{i\bar{H} t} \Theta \Pi_a \Theta^\dagger e^{-i\bar{H} t} \Theta | \phi_0 \rangle \\
&= \langle \phi_0 | \Theta^\dagger e^{i\bar{H} t} \Pi_a e^{-i\bar{H} t} \Theta | \phi_0 \rangle.
\end{aligned}
\tag{5.21}
$$

If all the coefficients in the initial state have the same phase (mod π), then complex conjugation just adds an overall phase factor, i.e., $\Theta |\phi_0\rangle = e^{i\phi} |\phi_0\rangle$ and $\langle \phi_0 | \Theta^\dagger = \langle \phi_0 | e^{-i\phi}$. Since these two phase factors cancel each other out, we arrive at the result that $P(t)$ is invariant under sign change of the entire Hamiltonian when all coefficients in the initial state $|\phi_0\rangle$ have the same phase modulo π.

For initial states $|\phi_0\rangle = |eg, n\rangle$ we can combine the results from the above three symmetry analyses, obtaining relevant combinations of the three possible sign changes. Furthermore, the above arguments and conclusions also hold for thermal states of the vibration, $\rho_b = \sum_{n=0}^\infty \frac{n_b^n}{(n_b+1)^{n+1}} |n\rangle\langle n|$ given that a thermal states is a superposition of many Fock states (i.e., phonon number states $|n\rangle\langle n|$). In particular, it is useful to understand why putting a minus sign on the vibrational frequency ν yields the same result as putting a minus sign on excitonic detuning Δ. We can see this by realizing that a simultaneous sign change on ν and Δ in $\bar{H} = \tilde{H}(\delta = 0) = \frac{1}{2}\Delta\tilde{\sigma}_z + \frac{1}{2}J\tilde{\sigma}_x + \nu a^\dagger a + \frac{1}{2}\kappa\tilde{\sigma}_z(a + a^\dagger)$ is equivalent to first changing the sign of the entire Hamiltonian $\bar{H}$ (time-reversal operation), and then reverting the signs of both κ (parity operation) and J ($\tilde{\sigma}_z$ operation) back to their original values.

5.8.2   Presence of classical noise

To show that the invariance property also holds in the presence of classical noise, we have numerically demonstrated that the same results can be obtained via consideration of the Lindblad master equation. This demonstration supports the equivalence between the Lindblad equation and the average behavior of adding Gaussian white noise to Hamiltonian [160]. We can therefore perform the symmetry analysis on the Lindblad equation $\dot{\rho}(t) = \mathcal{L}\rho = -i[\bar{H}, \rho(t)] + \gamma[\sigma_z, [\sigma_z, \rho(t)]]$, where γ is proportional to the variance of the Gaussian white noise, and the probability of being in the target state is given by $P(t) = \text{Tr}(\Pi_a e^{-i\mathcal{L}t}\rho_0)$.

For the parity symmetry that changes the Hamiltonian to $\Upsilon^\dagger \bar{H} \Upsilon$, we have

$$
\begin{aligned}
\mathcal{L}_1\rho &= -i[\Upsilon^\dagger \bar{H} \Upsilon, \rho(t)] + \gamma[\sigma_z, [\sigma_z, \rho(t)]] \\
&= -i\Upsilon^\dagger[\bar{H}, \Upsilon\rho(t)\Upsilon^\dagger]\Upsilon - \gamma\Upsilon^\dagger[\sigma_z, [\sigma_z, \Upsilon\rho(t)\Upsilon^\dagger]]\Upsilon \\
&= \Upsilon^\dagger \mathcal{L} \Upsilon \rho.
\end{aligned} \tag{5.22}
$$

This gives rise to the time evolution

$$
\begin{aligned}
e^{-i\mathcal{L}_1 t} &= \sum_{n=0}^\infty \frac{1}{n!}(-i\mathcal{L}_1 t)^n = \sum_{n=0}^\infty \frac{1}{n!}(-i\Upsilon^\dagger \mathcal{L} \Upsilon t)^n \\
&= \Upsilon^\dagger e^{-i\mathcal{L}t}\Upsilon.
\end{aligned} \tag{5.23}
$$

Therefore $P'_1(t) = \text{Tr}(\Pi_a e^{-i\mathcal{L}_1 t}\rho_0) = \text{Tr}(\Pi_a e^{-i\mathcal{L}t}\Upsilon\rho_0\Upsilon^\dagger)$. We then arrive at an analogous conclusion to the noiseless case, namely that $P(t)$ is invariant under sign change of κ when $\Upsilon\rho(0)\Upsilon^\dagger = \rho_0$.

Similarly, for the symmetry that leads to the transformed Hamiltonian $\tilde{\sigma}_z^\dagger \bar{H} \tilde{\sigma}_z$,

$$
\begin{aligned}
\mathcal{L}_2\rho &= -i[\sigma_z^\dagger \bar{H} \sigma_z, \rho(t)] + \gamma, \sigma_z, [\sigma_z, \rho(t)]] \\
&= -i\sigma_z^\dagger[\bar{H}, \sigma_z\rho(t)\sigma_z^\dagger]\sigma_z - \gamma\sigma_z^\dagger[\sigma_z, [\sigma_z, \sigma_z\rho(t)\sigma_z^\dagger]]\sigma_z \\
&= \sigma_z^\dagger \mathcal{L} \sigma_z \rho,
\end{aligned} \tag{5.24}
$$

which leads to $P'_2(t) = \text{Tr}(\Pi_a e^{-i\mathcal{L}_2 t}\rho_0) = \text{Tr}(\Pi_a e^{-i\mathcal{L}t}\sigma_z\rho_0\sigma_z^\dagger)$. We then conclude that when $\sigma_z\rho_0\sigma_z^\dagger = \rho_0$, $P(t)$ is invariant under a sign change of J.

For the time reversal symmetry we have,

$$
\begin{aligned}
\mathcal{L}_3\rho &= -i[\Theta^\dagger \bar{H} \Theta, \rho(t)] + \gamma, \sigma_z, [\sigma_z, \rho(t)]] \\
&= -i[-\bar{H}, \rho(t)] + \gamma, \sigma_z, [\sigma_z, \rho(t)]] \\
&= -i\Theta^\dagger(-1)[\bar{H}, \Theta\rho(t)\Theta^\dagger]\Theta - \gamma\Theta^\dagger[\sigma_z, [\sigma_z, \Theta\rho(t)\Theta^\dagger]]\Theta \\
&= \Theta^\dagger \mathcal{L} \Theta \rho.
\end{aligned} \tag{5.25}
$$

Note that Θ and $\Theta^\dagger$ are both antilinear. We then have $e^{-i\mathcal{L}_3 t} = \Theta^\dagger e^{-i\mathcal{L}t}\Theta$ and $P'_3(t) = \text{Tr}(\Pi_a e^{-i\mathcal{L}_3 t}\rho_0) = \text{Tr}(\Pi_a e^{-i\mathcal{L}t}\Theta\rho_0\Theta^\dagger)$. This leads to the conclusion that $P(t)$ is invariant under a sign change of $\bar{H}$ when either $\Theta\rho_0\Theta^\dagger = \rho_0$ or ρ_0 is real.

Combining the above analyses, we find that in the presence of Gaussian white noise $P(t)$ is still invariant under a simultaneous sign change of both ν and Δ when $\Upsilon \rho_0 \Upsilon^\dagger = \sigma_z \rho_0 \sigma_z^\dagger = \rho_0$ and ρ_0 is real.

Chapter 6

Unraveling excitation energy transfer assisted by collective behaviors of vibrations

6.1 Preface

This chapter is taken from the previously published Ref. [148], originally appearing in New Journal of Physics. It was co-authored by Dr. Zeng-zhao Li, Liwen Ko, the author of this thesis, Dr. Mohan Sarovar and Professor K. Birgitta Whaley. This project was let by Dr. Zeng-zhao Li. Liwen Ko and the author of this thesis contributed to discussions of the results. Dr. Sarovar and Professor Whaley provided high-level insights. The majority of the writing was completed by Dr. Zeng-zhao Li.

6.2 Introduction

Recent experimental and theoretical studies of the molecular structures present in biological light harvesting complexes have revealed the delicate interplay of electronic and vibrational degrees of freedom, and how these come together to orchestrate efficient transfer of photoexcitations in such systems [139, 142, 161–166]. Coherent beating patterns in nonlinear spectroscopy signals initially ascribed to long-lived electronic coherence in such systems [167] are now generally agreed to be due to a combination of electronic and vibrational coherence, with a key role played by coupling of the relevant electronic degrees of freedom to long-lived, underdamped vibrational modes of molecules [168–172]. This revelation has brought to light the subtle ways in which vibrational dynamics in molecular complexes can influence electronic and excitonic properties [173–177]. In this work we draw inspiration from these studies of molecular systems and ask whether vibrational degrees of freedom can exert other subtle influences on energy transfer in such complexes. In particular, can the presence of

multiple underdamped vibrations in a molecular complex influence energy transfer dynamics in non-trivial ways?

With the recent growth of quantum technologies, controllable artificial quantum simulators have been developed to probe the underlying basic mechanism of the observed long-time coherences [17, 178, 179]. In Ref. [17], an engineered vibrationally assisted energy transfer (VAET) was experimentally demonstrated for an excitonic dimer emulated in a trapped-ion platform. In that work, not only was a one-phonon VAET process signified by a peak at the vibrational frequency being equal to the excitonic transition frequency unambiguously reported, but also unresolved peaks at smaller frequencies were found. It was suggested that the latter were due to multiphonon VAET processes. This provides further motivation for the study of multiphonon VAET processes. In this work we seek to ascertain the extent to which such multiphonon VAET can be resolved, and also the consequences of any collective behavior of the vibrations for excitonic energy transfer processes. Specifically, it is of interest to explore whether cooperative or interference effects might play a role in the vibrationally enhanced energy transfer. In addition, these systems offer the possibility of finding both the phononic analog of the well-known two-photon absorption [180–182], and the inverse phenomenon [183], in which one phonon might simultaneously excite two excitonic transitions, where the latter could be of different frequencies. The latter inverse situation offers a new twist with phonons relative to atoms, namely that in the context of VAET we can ask whether one phonon from a specific vibrational mode can simultaneously cause an excitonic transition and a vibrational transition in a different vibrational mode.

To address these questions, we consider here a donor-bridge-acceptor trimeric chromophore system coupled to two vibrational degrees of freedom. We analyze the dynamics within a single electronic excitation subspace with explicit incorporation of the vibrational states, performing full numerical simulations for the excitation energy transfer probability from donor to acceptor via the bridging chromophore under various conditions. We construct a two-dimensional spectral representation of the VAET probabilities by scanning the frequencies of the two vibrations. These two-dimensional (2D) VAET spectra allow identification of several mechanisms through which the vibrational modes can influence and/or enhance energy transfer. These mechanisms include both single mode VAET, and multi-mode VAET in which the two vibrational modes can cooperate and/or interfere. Detailed assignment of the VAET features is facilitated by calculation of the vibronic states resulting from the coupling of electronic and vibrational degrees of freedom, which shows that a number of the VAET features are correlated with the presence of avoided crossings in the vibronic energy spectra. In the weak site-vibration coupling regime we analyze the dynamical results with a perturbative analysis and use of double-sided Feynman diagrams [184]. For both weak and strong site-vibration coupling regimes we then investigate the dependence of the VAET features on exciton dissipation and vibrational temperature.

The context of this study is quantum emulation of excitonic energy transfer in ion traps and their use in elucidating the dynamic consequences of exciton-vibration coupling for energy transport in molecular excitonic systems. We focus first on the behavior when the vibrations are coupled locally to individual chromophore sites, as in the case of trapped

ions coupled to transverse modes. The model trimeric system of primary interest in this work is generalized from a dimeric system studied previously with an experimental ion trap emulator [17] and starts from a Hamiltonian in which individual vibrational modes are coupled to Frenkel excitons on specific sites. We then extend this to study of the energy transfer dynamics induced by Hamiltonian coupling to vibrations that are correlated between sites, which naturally results from coupling to the longitudinal modes of trapped ions.

The trapped ion internal states in an ion trap emulation of molecular chromophores can be regarded as pseudo-chromophores. The ability to select different states and modulate their energies with external fields allows exploration of the effects of different energetic landscapes on energy transfer. However, the Hamiltonian for interaction of such internal ionic states with the external vibrational modes of the trapped ions has some subtle differences from the form of Hamiltonian relevant to studies of excitonic energy transfer in molecular aggregates such as natural light harvesting systems [185] or J-aggregates. We show here that despite these differences, the effective Hamiltonian that results from projection to the single electronic excitation subspace maps onto the standard form for excitonic energy transfer in the presence of vibrations that are correlated between different chromophores. We study the influence of these correlations on the effectiveness of the energy transfer, focusing in particular on the role of vibrations in enabling uphill energy transport in the excitonic degrees of freedom. The role of coherence in overcoming energy barriers has motivated discussion of rectification [186], while the coherent coupling of vibrational degrees of freedom in a quantum bath to an uphill gradient of excitonic states has been demonstrated to allow quantum ratcheting of energy transfer over long distances [187]. Clearly the phenomenon of VAET [17] is a prime enabler for such uphill energy transport. In this work we shall explore in detail the ways in which VAET processes facilitate and enhance energy transport, with particular emphasis on the role of VAET with correlated vibrational modes. We shall find that not only do resonant single phonon processes play a key role in enhancing energy transport, but that multi-phonon processes can also be strong facilitators of energy transport.

The remainder of the paper is organized as follows. Sec. 6.3 introduces the model of the trimeric chromophore system with excitonic sites coupling locally to individual vibrational modes, e.g., as with a linear array of trapped ions coupled to transverse vibrational modes. In Sec. 6.4, we summarize the procedure for numerical calculations of the 2D VAET spectra and the perturbation theory for analysis of the excitation energy transfer features. Full details of the latter are presented in the Supplementary Material [188]. Sections 6.5 and 6.6 present and analyze results revealing the various VAET signatures in the weak and strong site-vibration coupling regimes, respectively. In Sec. 6.7, we present the vibronic energy spectrum and discuss the insights this offers for the VAET processes. We also discuss here the effects of the vibrational cross coupling terms induced by restriction to the single-exciton subspace of a Hamiltonian suitable for emulation of excitonic energy transfer with trapped ions. Sec. 6.8 presents 2D VAET spectra and analysis for a trimeric system realizable for linear arrays of trapped ions with coupling only to longitudinal vibrational modes, resulting in a Hamiltonian with explicit correlations in the coupling of individual sites to the vibrational modes. Sec. 6.9 provides a summary and outlook for observation of the predicted VAET

phenomena in trapped ion experiments, together with a discussion of the implications of this
VAET study for understanding excitonic energy transfer in molecular systems.

6.3 The effective model of a trimeric chromophore system

We consider a donor-bridge-acceptor trimeric chromophore system coupled to two undamped
vibrations, shown schematically in Fig. 6.1(a). The model can be described by the Hamiltonian

$$H_{tr} = H_{\text{s}} + H_{\text{v}} + H_{int}, \tag{6.1}$$

where (setting $\hbar = 1$)

$$
\begin{aligned}
H_{\text{s}} &= \omega_1\sigma_z^{(1)} + \omega_2\sigma_z^{(2)} + \omega_3\sigma_z^{(3)} \\
&\quad + J_{12}\sigma_x^{(1)}\sigma_x^{(2)} + J_{23}\sigma_x^{(2)}\sigma_x^{(3)}, \tag{6.2} \\
H_{\text{v}} &= \nu_a a^\dagger a + \nu_b b^\dagger b, \tag{6.3} \\
H_{int} &= \kappa_a\sigma_z^{(2)}(a + a^\dagger) + \kappa_b\sigma_z^{(3)}(b + b^\dagger). \tag{6.4}
\end{aligned}
$$

In the electronic Hamiltonian H_{s}, the three sites correspond to the donor, bridge, and acceptor, respectively. Each site is modelled by a two-level system, with $2\omega_i$ the transition frequency between its ground and excited states, $|g\rangle_i$ and $|e\rangle_i$, respectively. The Pauli operators $\sigma_{x,z}^{(i)}$ are given by $\sigma_x^{(i)} = |g\rangle_i\langle e| + |e\rangle_i\langle g|$ and $\sigma_z^{(i)} = |e\rangle_i\langle e| - |g\rangle_i\langle g|$. J_{ij} is the coupling strength between adjacent ith- and jth-sites. We assume that the coupling between the first and third sites is vanishingly small. The vibrational mode with creation operator $a^\dagger$ ($b^\dagger$) and frequency ν_a (ν_b) is coupled to the bridge (acceptor) site with coupling strength κ_a (κ_b). In the quantum emulation context, such local coupling of sites to individual vibrations can be realized by coupling to transverse modes of a linear chain of trapped ions, so we denote this Hamiltonian by H_{tr}. In addition to these undamped single-mode vibrations coupled to the electronic sites included in the above Hamiltonian, we shall also incorporate dissipation effects by use of non-Hermitian terms in the electronic Hamiltonian. Since the immediate context of this study is the emulation of excitonic energy transfer by trapped ions, the origin of these non-Hermitian terms will be due to optical dephasing or to spontaneous emission, rather than to the dissipation provided by an overdamped vibrational bath as is usual for natural light harvesting systems.

We focus on the excitation energy transfer in a single electronic excitation subspace. An effective Hamiltonian within this subspace is obtained using the subspace projection operator

(a)

(b)
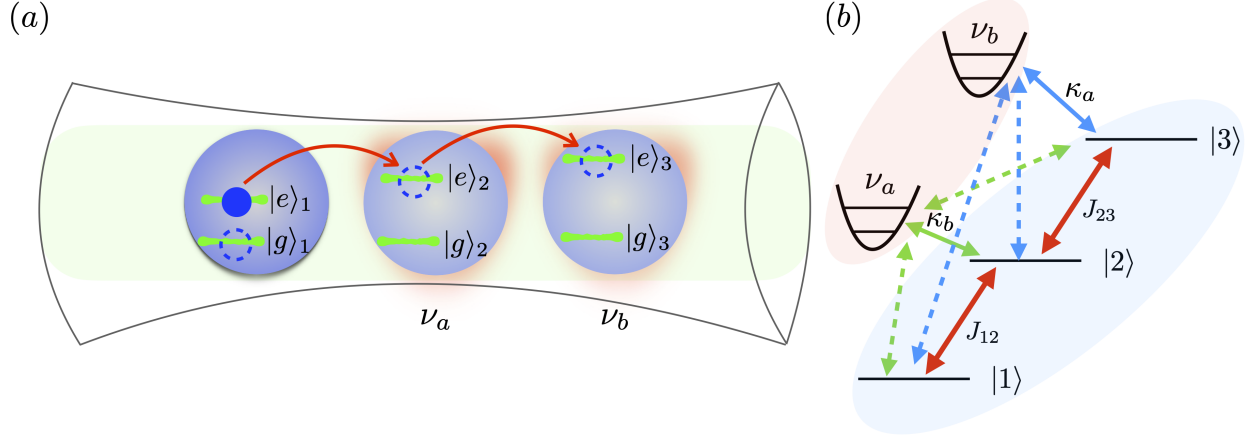
Figure 6.1: (color online) (a) Schematic of the excitation state transfer in a donor-bridge-acceptor trimeric chromophore system coupled to two vibrations. Each site is modelled by its two lowest energy levels $|e\rangle_i$ and $|g\rangle_i$. The backgrounds in light red indicate two vibrations that are individually coupled to the bridge and acceptor sites, respectively, by a σ_z type coupling (Eq. (6.4)). (b) The effective three-level model of the trimeric chromophore system coupled to two vibrations in the single electronic excitation subspace. In addition to the direct Hamiltonian couplings indicated by the green, blue, and red solid line arrows, there are also cross couplings deriving from the restriction to the single-excitation subspace (Eq. (6.5)). These are shown by the green and blue dashed line arrows.

$\Xi \equiv |egg\rangle\langle egg| + |geg\rangle\langle geg| + |gge\rangle\langle gge|$, using $\tilde{H}_{tr} = \Xi H_{tr}\Xi$. Explicitly, we find

$$
\begin{aligned}
\tilde{H}_{tr} =\ & \tilde{\omega}_1|1\rangle\langle 1| + \tilde{\omega}_2|2\rangle\langle 2| + \tilde{\omega}_3|3\rangle\langle 3| \\
& + J_{12}(|1\rangle\langle 2| + |2\rangle\langle 1|) + J_{23}(|2\rangle\langle 3| + |3\rangle\langle 2|) \\
& + \kappa_a(a^\dagger + a)(|2\rangle\langle 2| - |1\rangle\langle 1| - |3\rangle\langle 3|) \\
& + \kappa_b(b^\dagger + b)(|3\rangle\langle 3| - |1\rangle\langle 1| - |2\rangle\langle 2|) \\
& + \nu_a a^\dagger a + \nu_b b^\dagger b,
\end{aligned}
\tag{6.5}
$$

where $|1\rangle \equiv |egg\rangle, |2\rangle \equiv |geg\rangle, |3\rangle \equiv |gge\rangle$, $\tilde{\omega}_1 = \omega_1 - \omega_2 - \omega_3$, $\tilde{\omega}_2 = \omega_2 - \omega_1 - \omega_3$, and $\tilde{\omega}_3 = \omega_3 - \omega_1 - \omega_2$. The couplings in the full Hamiltonian are depicted in Fig. 6.1(a) and resulting couplings of the effective Hamiltonian in the single excitation subspace are illustrated in Fig. 6.1(b). We note that, just as for a dimer [17], assistance from vibrations for energy transport becomes unnecessary when the transition frequencies of three sites are identical, since there are then no energetic differences between spatially separated sites. Our numerical calculations in this paper will focus on electronically uphill processes, as indicated schematically in Fig. 6.1(b).

Two important remarks on the effective model in Eq. (6.5) are in order here. First, the counter-rotating terms in the XX-type interaction of Eq. (6.2) do not conserve the number

or excitations and therefore do not survive the projection into the single electronic excitation manifold (since $\Xi\sigma_+^{(1)}\sigma_+^{(2)}\Xi = \Xi\sigma_-^{(1)}\sigma_-^{(2)}\Xi = 0$). Second, it is evident that, in addition to the coupling between an electronic site and its directly connected vibrational mode [see Eq. (6.4)], the single-excitation effective model of Eq. (6.5) contains terms that couple a vibration to excited states of its unconnected sites, as indicated by dashed arrows in light green and blue in Fig. 6.1(b). These terms derive from the projection of the σ_z operators through which sites 2 and 3 couple to their individual vibrations, i.e., $\Xi\sigma_z^{(2)}\Xi = |2\rangle\langle 2| - |1\rangle\langle 1| - |3\rangle\langle 3|$ and $\Xi\sigma_z^{(3)}\Xi = |3\rangle\langle 3| - |1\rangle\langle 1| - |2\rangle\langle 2|$.

The Hamiltonian Eq. (6.1) differs formally from the common modelling of vibrational coupling of molecular chromophores, for which only coupling to excited electronic states is included, i.e., $\kappa_a\sigma_+^{(2)}\sigma_-^{(2)}(a^\dagger + a) + \kappa_b\sigma_+^{(3)}\sigma_-^{(3)}(b^\dagger + b)$ [185]. In the Born-Oppenheimer approximation, the ground electronic state of a molecular system is defined to be at the minimum of all relevant vibrational degrees of freedom and therefore there is no linear coupling to the electronic ground state. For a single chromophore, this coupling will just shift the overall energy of the system and both pictures are used for single chromophores in the literature. However, for two or more chromophores, we find that on projection to the single excitation subspace the σ_z coupling introduces cross-coupling terms between excitations on different sites that mimic correlations between vibrations at different sites in a molecular system [168, 185, 189–194]. In the following sections we shall see that these cross-couplings can give rise to enhanced collective phenomena in VAET. We note that the cross-couplings in Eq. (6.5) show both positive correlations between some sites, eg., between donor and acceptor sites for mode ν_a and negative correlations between other sites, e.g., between donor and bridge sites for mode ν_a. Consequently the overall effect of the correlations is not easily rationalized in terms of arguments for correlated dimers [185].

To illustrate the relevance of this study for understanding of natural photosynthetic systems, Table 6.1 shows typical values for the parameters considered in this work and compares them to the corresponding typical values for the Fenna-Matthews-Olson (FMO) light harvesting complex unit of green sulphur bacteria [195, 196]. The first row shows typical values from the parameter ranges employed in this work and the third row shows

Table 6.1: Comparison of typical parameters for trapped ion emulators used in this work (line 1) with values found in natural photosynthetic systems (line 3). Line 2 shows parameters scaled up from line 1 to the regime for natural systems. Note that the vibrational frequencies on line 1 are for two-phonon processes.

Parameters	$\tilde{\omega}_1$	$\tilde{\omega}_2$	$\tilde{\omega}_3$	J_{12}	J_{23}	ν_a	ν_b	κ_a	κ_b	$k_B T_a$	$k_B T_b$
values (kHz)	-0.5	0	0.5	0.1	0.1	0.52	0.52	0.1	0.1	0.72	0.72
scale-up (cm^{-1})	-138.6	0	138.6	27.72	27.72	144	144	27.72	27.72	200	200
natural system (cm^{-1})	-138.6	0	138.6	-5.9	-13.7	180	180	42.2	42.2	200	200

corresponding typical values for the FMO system. The second row shows the result of setting
our site energies $\tilde{\omega}_1$, $\tilde{\omega}_2$, and $\tilde{\omega}_3$ to the natural value and scaling up the other parameters
accordingly. It is evident that the range of parameters available in ion trap emulations scales
consistently to the natural system, suggesting that analogs of the phenomena observed here
might be present also in some natural light harvesting complexes (for more discussion of this,
see the Supplementary Material [188]). Of particular relevance here are systems that have
uphill regions in their landscape of Frenkel (site) exciton energies. This includes the FMO
monomer complex [195], as well as the purple bacterium Rhodopseudomonas viridis [197]
and the CP43 core antenna of photosystem II [198].

6.4   Excitation energy transfer probability

We calculate the probability of finding an excitation in the acceptor, i.e., the third site, given
an initial excitation localized on the donor, i.e., on the first site, as a function of time, $P_3(t)$.
Since there is no direct excitonic transfer from donor to acceptor, in the absence of coupling
to vibrations the excitation is transferred via the bridging site. $P_3(t)$ is given by

$$P_3(t) \quad = \quad Tr[|3\rangle\langle 3|U|1\rangle\langle 1|\rho_a\rho_b U^\dagger]. \tag{6.6}$$

Here the unitary time evolution is for the whole system, i.e., $U|1\rangle\langle 1|\rho_a\rho_b U^\dagger$, where $|1\rangle\langle 1|$,
ρ_a, and ρ_b are initial states of the chromophoric trimer and two vibrational modes, re-
spectively, and $U = e^{-i\tilde{H}_{tr}t}$ is an evolution operator with $\tilde{H}_{tr}$ given by Eq. (6.5). Trac-
ing over the vibrational degrees of freedom leads to the reduced excitonic system dynam-
ics and then further taking the quantum average of the site number operator $|3\rangle\langle 3|$ gives
the population at the acceptor site, $P_3(t)$. Numerical calculations of the transfer probabil-
ity in Eq. (6.6) are performed assuming thermal initial states for the two vibrations, i.e.,
$\rho_a = e^{-\nu_a a^\dagger a/k_B T_a}/Tr_a[e^{-\nu_a a^\dagger a/k_B T_a}]$ and $\rho_b = e^{-\nu_b b^\dagger b/k_B T_b}/Tr_b[e^{-\nu_b b^\dagger b/k_B T_b}]$, where $k_B T_a$ and
$k_B T_b$ are individual temperatures of each vibration. We shall use $Max[P_3(t)]$ $(0 \leq t \leq t_f)$ and
$\int_0^{t_f} P_3(t)dt$, which measure the maximum and accumulated population during a given time
period t_f, respectively, as quantitative measures of the excitonic energy transfer efficiency.

In order to assist in interpreting and understanding the results from these numerical
calculations, we also develop an analytic perturbation theory approach. Our analytical
treatment focuses on a symmetric version of the effective three-level model, namely, $J_{12} =
J_{23} = J$ and $\tilde{\omega}_3 - \tilde{\omega}_2 = \tilde{\omega}_2 - \tilde{\omega}_1 = \Delta$ in Eq. (6.5). The excitonic Hamiltonian in Eq. (6.5)
then becomes $H_0^{(e)} = \sum_{j=1}^3 \lambda_j |e_j\rangle\langle e_j|$, with eigenergies $\lambda_j = 0, \pm\Omega$ $(\Omega = \sqrt{2J^2 + \Delta^2})$ and
eigenstates $|e_j\rangle$.

Transforming to the interaction picture with respect to the free Hamiltonian [i.e., in-
cluding only $H_0^{(e)}$ and the vibrational part (i.e., $H_0^{(\nu)} = \nu_a a^\dagger a + \nu_b b^\dagger b$)], the site-vibration

Hamiltonian becomes (see [188])

$$H_I(t) = \sum_{j,k} \kappa_a A_{jk}[a^\dagger e^{i(\Delta_{jk}+\nu_a)t} + a e^{i(\Delta_{jk}-\nu_a)t}]|e_j\rangle\langle e_k| \tag{6.7}$$

$$+ \sum_{j,k} \kappa_b B_{jk}[b^\dagger e^{i(\Delta_{jk}+\nu_b)t} + b e^{i(\Delta_{jk}-\nu_b)t}]|e_j\rangle\langle e_k|,$$

where $\Delta_{jk} = \lambda_j - \lambda_k$ is the transition frequency between eigenstates and the forms for the coefficients A_{jk}, B_{jk} are given in Appendix 6.10. We use fourth-order perturbation theory with respect to the site-vibration coupling to expand the evolution operator as

$$U_I(t) = \mathcal{T}e^{-i\int_0^t ds H_I(s)} \approx 1 + \sum_{i=1}^4 U_I^{(i)}, \tag{6.8}$$

and correspondingly obtain the transition probability

$$P_3(t) = P_3^{(0)} + P_3^{(1)} + P_3^{(2)}, \tag{6.9}$$

with

$$P_3^{(0)} = Tr_{a,b}[(\mathcal{A}^{(0)})^\dagger \mathcal{A}^{(0)} \rho_a \rho_b],$$
$$P_3^{(1)} = Tr_{a,b}\{[(\mathcal{A}^{(1)})^\dagger \mathcal{A}^{(1)} + (\mathcal{A}^{(0)})^\dagger \mathcal{A}^{(2)} + (\mathcal{A}^{(2)})^\dagger \mathcal{A}^{(0)}] \rho_a \rho_b\},$$

and

$$P_3^{(2)} = Tr_{a,b}\{[(\mathcal{A}^{(2)})^\dagger \mathcal{A}^{(2)} + (\mathcal{A}^{(1)})^\dagger \mathcal{A}^{(3)}$$
$$+ (\mathcal{A}^{(3)})^\dagger \mathcal{A}^{(1)} + (\mathcal{A}^{(0)})^\dagger \mathcal{A}^{(4)} + (\mathcal{A}^{(4)})^\dagger \mathcal{A}^{(0)}] \rho_a \rho_b\},$$

where the transition amplitudes are given by $\mathcal{A}^{(0)} = \langle 3|U_0|1\rangle$ and $\mathcal{A}^{(i)} = \langle 3|U_0 U_I^{(i)}|1\rangle$, with $U_0 = e^{-i(H_0^{(e)}+H_0^{(\nu)})t}$.

Unless otherwise stated, in the numerical calculations and perturbative analysis of these in the following two sections we shall study the maximum probability $Max[P_3(t)]$ during a given time period ($0 \le t \le t_f = 400$ms), for a symmetric trimeric system with $J_{12} = J_{23} = J$ and $\tilde{\omega}_3 - \tilde{\omega}_2 = \tilde{\omega}_2 - \tilde{\omega}_1 = \Delta$ in Eq. (6.5), coupled to two vibrations at a temperature larger (by a factor of $\simeq 10$) than these energies. This choice of parameters represents an energetically uphill process in the single excitation subspace. We shall present 2D VAET spectra obtained by evaluating $Max[P_3(t)]$ over the given time period as a function of the two vibrational frequencies ν_a and ν_b. These frequencies are given in units of the energy difference Δ_{31} between the eigenstates $|e_3\rangle$ and $|e_1\rangle$ of the electronic Hamiltonian $H_0^{(e)}|e_j\rangle = \lambda_j|e_j\rangle$. A full description of the perturbative analysis is given together with explicit expressions for the eigenstates of the symmetric model in the Supplementary Material [188]. The numerical calculations typically employ a vibrational basis of $N = 15$ Fock states, which is sufficient for convergence of the VAET spectra over a broad range of parameters, as described in Appendix 6.11.

6.5 VAET signatures in the weak site-vibration coupling regime

When the site-vibration coupling is weak, e.g., $\kappa_a, \kappa_b < \Delta, J$, the electronic states of the trimeric chromophore system are only weakly perturbed and do not gain substantial vibronic character. In this situation the energy transfer processes are primarily excitonic in origin but assistance by vibrations that are coupled to the excitonic states can be still expected. Fig. 6.2(a) presents a 2D VAET spectrum in this regime and Fig. 6.2(b) presents a corresponding schematic diagram summarizing the energy transfer processes responsible for each of the main features of the 2D VAET spectrum. The perturbative analysis of these features is then summarized in Fig. 6.3. We now discuss the 2D VAET spectral features, starting with those due to single-mode VAET processes and then proceeding to the multi-mode VAET processes.

6.5.1 Single-mode VAET

The main features due to single modes in the weak site-vibration coupling regime are represented by the three vertical lines at $\nu_a/\Delta_{31} = 1, 0.5, 0.25$ and the horizontal lines at $\nu_b/\Delta_{31} = 1, 0.5, 0.25$. These signify resonant one-, two-, and four-phonon VAET processes, respectively, assisted by either the vibration ν_a which is coupled to the bridging site 2 (vertical lines) or the vibration ν_b which is coupled to the terminal, acceptor site (horizontal lines). For a given number of phonons, e.g., one, two or four, the vertical line is more intense than the corresponding horizontal line, indicating a stronger impact of the bridging vibration ν_a in assisting the energy transfer.

This can be confirmed by our perturbative analysis as follows. For the resonant one-phonon VAET, perturbative expansion of the transfer probability (see Ref. [188] for full details) shows that the first order term, which is second order in the interaction Hamiltonian, is proportional to $\alpha^4(W_{31}^{-a})^* W_{31}^{-a} \sim t^2 \kappa_a^2 A_{13}^2$ for transitions along the line $\nu_a/\Delta_{31} = 1$, and to $\alpha^4(W_{31}^{-b})^* W_{31}^{-b} \sim t^2 \kappa_b^2 B_{13}^2$ along the line $\nu_b/\Delta_{31} = 1$. Here $\alpha \sim 1$ for the weak coupling regime and the coefficients A_{13}, B_{13} are given by Eqs. (6.17) and (6.18) of Appendix 6.10, respectively. This VAET process is illustrated schematically by the Feynman diagrams in Fig. 6.3(a). Averaging this transfer probability over the thermal distributions of vibrational states for modes ν_a and ν_b [188], shows that even under conditions of identical site-vibration couplings ($\kappa_a = \kappa_b$) and identical vibrational temperatures ($k_B T_a = k_B T_b$), there will nevertheless be a higher probability for excitations along the vertical line than along the horizontal line, confirming the stronger impact of the vibration ν_a that is coupled to the bridge site. This effect is clearly visible in the 1-dimensional top and right slices of Fig. 6.2(a), where it can be seen that the probability at the one-phonon VAET peak $\nu_a/\Delta_{31} = 1$ (top slice) is almost four times as large as that of the one-phonon VAET $\nu_b/\Delta_{31} = 1$ (right slice). Closer examination of the perturbative couplings shows that this difference arises from the factor of 2 in A_{13} relative to B_{13} (see Eqs. (6.17) and

(6.18)). A_{13} is the matrix element of the electronic coupling to the bridge vibrational mode ν_a, between the lowest excitonic state $|e_1\rangle$ and the highest excitonic state $|e_3\rangle$ [188], i.e., $A_{13} = \langle e_1|(|2\rangle\langle 2| - |1\rangle\langle 1| - |3\rangle\langle 3|)|e_3\rangle$. B_{13} is the corresponding matrix element of the terminal vibrationa mode, i.e., $B_{13} = \langle e_1|(|3\rangle\langle 3| - |1\rangle\langle 1| - |2\rangle\langle 2|)|e_3\rangle$. For the symmetric Hamiltonian we have $\langle e_1|1\rangle\langle 1|e_3\rangle = -\langle e_1|2\rangle\langle 2|e_3\rangle = J^2/2\Omega^2$ and $\langle e_1|3\rangle\langle 3|e_3\rangle = J^2/\Omega^2$, resulting in a larger value for A_{13}, the coupling to the bridge vibrational mode.

When either vibrational frequency, ν_a or ν_b, is equal to half of an excitonic transition frequency, the transition from $|e_1\rangle$ to $|e_3\rangle$ is still accessible but only via the intermediate state $|e_2\rangle$. The excitonic transition is then accompanied by an absorption of two phonons. This single-mode two-phonon VAET appears in Fig. 6.2(a) at the vertical line $\nu_a/\Delta_{31} = 0.5$ and at the horizontal line $\nu_b/\Delta_{31} = 0.5$. We denote these processes as single mode two-phonon absorption (TPhonA) in Fig. 6.3(b). The corresponding transfer probabilities in the weak site-site coupling limit ($J < \Delta$) are given by $\alpha^4(W_{32,21}^{-a-a})^* W_{32,21}^{-a-a} \sim \alpha^4 t^4 \kappa_a^4 A_{12} A_{23} A_{32} A_{21}$ and $\alpha^4(W_{32,21}^{-b-b})^* W_{32,21}^{-b-b} \sim \alpha^4 t^4 \kappa_b^4 B_{12} B_{23} B_{32} B_{21}$, with $\alpha \sim 1$ for weak coupling as before, and A_{ij} and B_{ij} given in Eqs. (6.13)-(6.16). Further perturbative analysis with respect to J/Δ reveals that the transition $|e_1\rangle \to |e_2\rangle \to |e_3\rangle$ is a second-order process when the absorbed phonons are both borrowed from the bridging vibration ν_a (since $A_{12} \propto \frac{J}{\Delta}$ and $A_{23} \propto \frac{J}{\Delta}$, see Appendix 6.10 and Ref. [188]), but becomes a third-order process when the two phonons are provided by the terminal mode ν_b (since $B_{21} \propto (\frac{J}{\Delta})^3$ and $B_{23} \propto \frac{J}{\Delta}$). Therefore, by a similar argument to the one-phonon VAET above, i.e., multiplying the above transfer probability by a prefactor $2n_a^2$ or $2n_b^2$ [188] to account for thermal averaging over the vibrational modes, it is then evident that just as in the one-phonon VAET process, the vibration (ν_a) coupled to the bridge site has a stronger impact on the two-phonon VAET processes than the vibration ν_b connected to the terminal, i.e., acceptor site. This stronger impact of the bridge site vibration results from the form of its interaction with the excitonic states in the single excitation manifold as described by Eq. (6.5). This shows that the bridging ν_a mode couples to the neighboring excitonic states $|1\rangle$ and $|2\rangle$ in a spatially anticorrelated manner, while the ν_b vibrational mode couples to the $|1\rangle$ and $|2\rangle$ states in a positively correlated manner. (Note that both modes have spatially anticorrelated coupling with regard to states $|2\rangle$ and $|3\rangle$.) In a simple semiclassical dynamical picture, anticorrelated couplings bring the localized excitonic states into resonance and thus promote energy transfer, while correlated couplings preserve the non-resonant relationship and suppress energy transfer. Thus the bridging ν_a mode enhances the energy transfer from $|1\rangle$ to $|2\rangle$ and thereby promotes the overall transfer from donor to acceptor. The stronger role of coupling to a spatially anticorrelated vibrational mode rather than a spatially correlated mode is also seen with spatially anti-correlated classical noise, see e.g., [194].

Another observable feature of the single-mode VAET in Fig. 6.2(a) is the four-phonon process at $\nu_a/\Delta_{31} = 0.25$ or $\nu_b/\Delta_{31} = 0.25$, which is described by the Feynman diagrams in Fig. 6.3(c). Comparison between the corresponding vertical and horizontal lines in Fig. 6.2(a) supports the conclusion above that the vibration ν_a which is coupled to the bridge site has a stronger impact on the energy transfer than the vibration coupled to the terminal site. Since
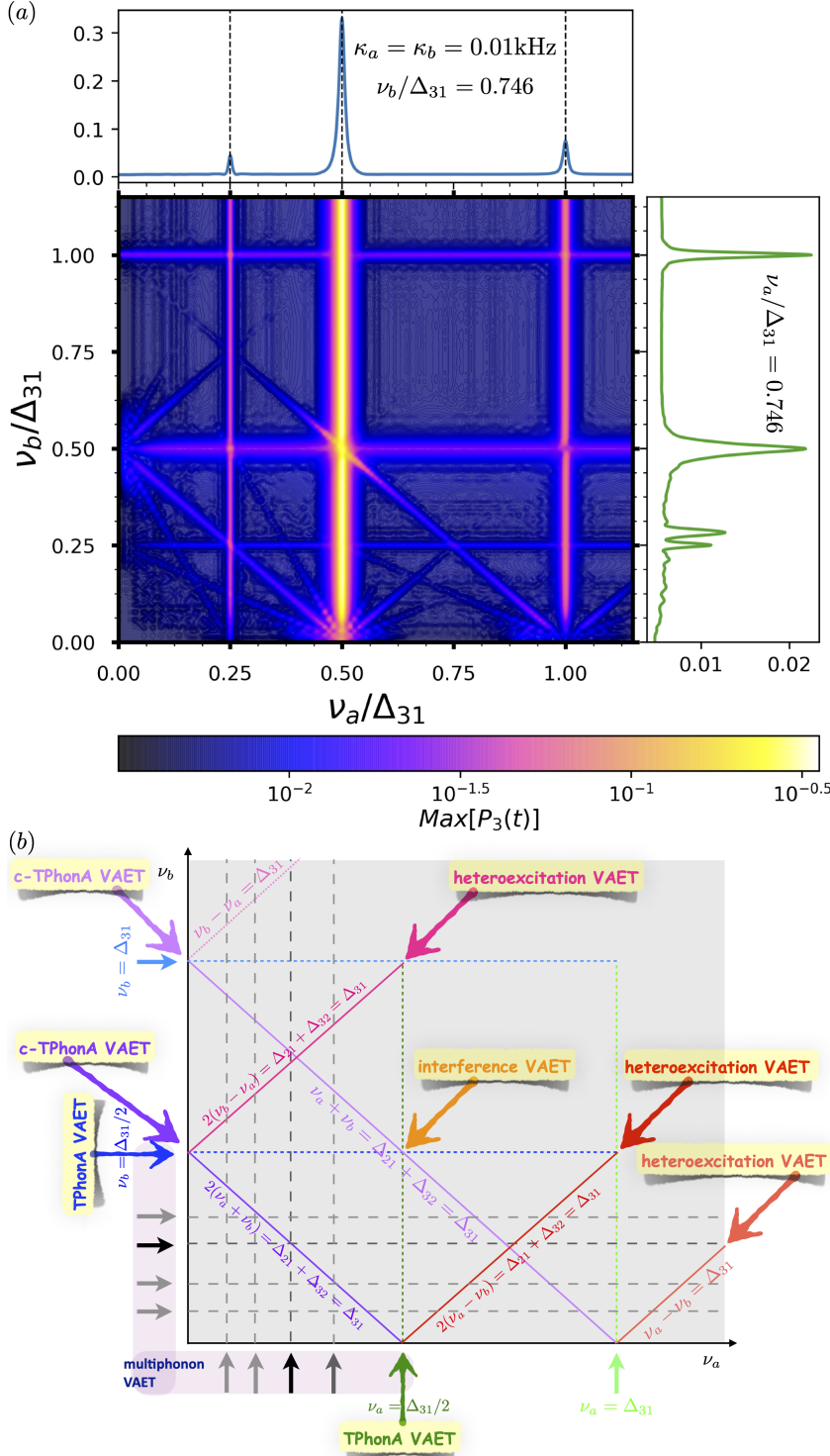
Figure 6.2: (color online) (a) 2D VAET spectrum of a symmetric trimeric chromophore system coupled to two non-interacting vibrations in the weak site-vibration coupling regime $\kappa_a = \kappa_b = 0.01$kHz. The maximum transfer probability $\mathrm{Max}[P_3(t)]$ is taken during a time period $t \in [0, 400]$ms. Δ_{ij} is the energy difference between eigenstates $|e_i\rangle$ and $|e_j\rangle$ of the electronic part in Eq. (6.5) with $\{\tilde{\omega}_1, \tilde{\omega}_2, \tilde{\omega}_3, J_{12}, J_{23}\} = \{-0.5, 0, 0.5, 0.1, 0.1\}$kHz, satisfying $\Delta_{31} = 2\Delta_{21}$ [188]. We consider two vibrations with identical temperatures $k_B T_a = k_B T_b = 1.5$kHz. The truncation number of each vibrational Fock space is $N = 15$. The 1-dimensional slices on the top and right of the 2-dimensional contour plot are taken at $\nu_b/\Delta_{31} = 0.746$ and $\nu_a/\Delta_{31} = 0.746$, respectively. (b) Schematic diagram identifying the different single- and multi-mode VAET features of the 2D VAET plot for the trimeric chromophore system shown in (a).
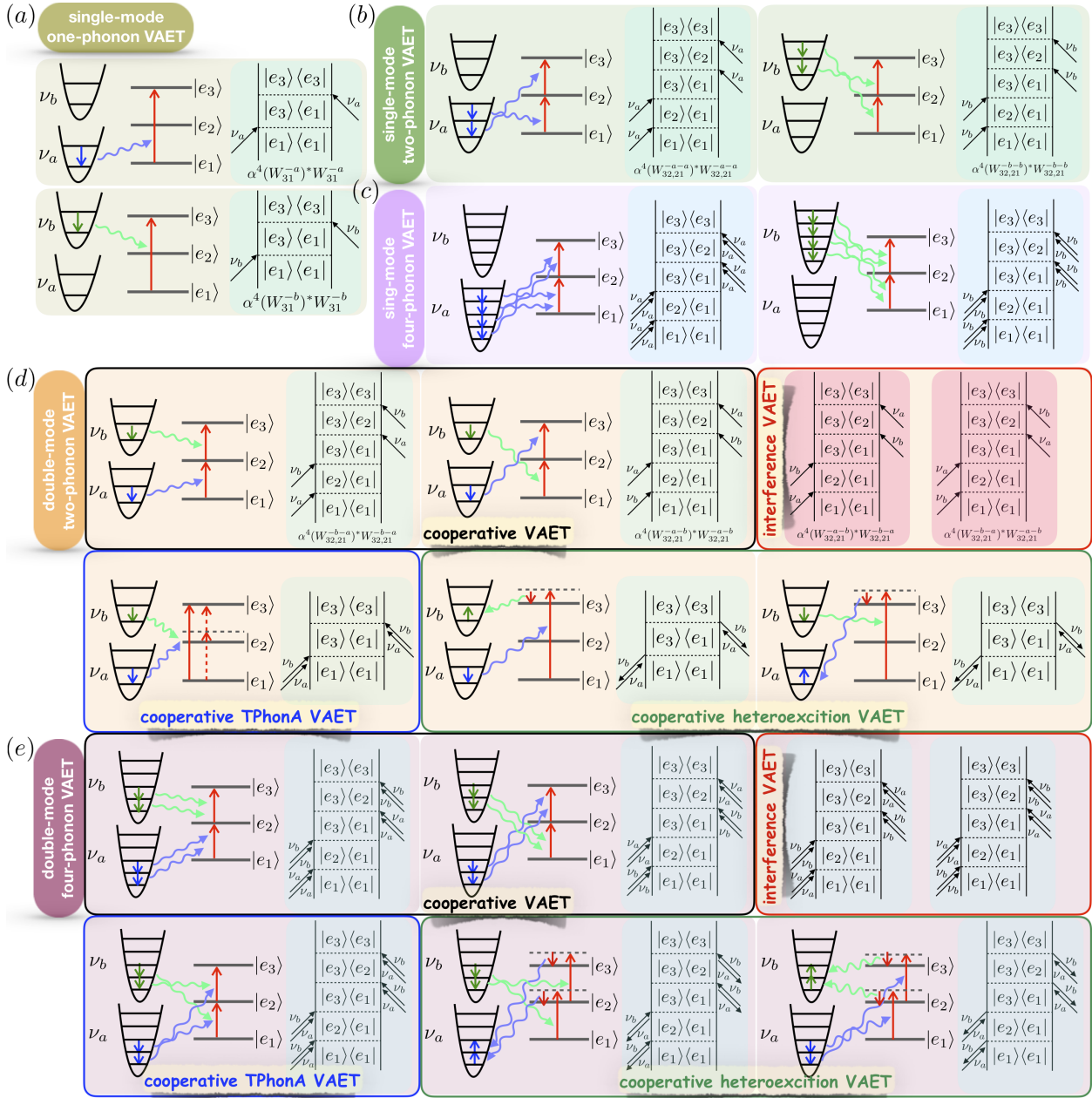
Figure 6.3: (color online) Schematics of the various VAET processes contributing to the 2D VAET specrum of Fig. 6.2. Panels (a) - (c) show single-mode VAET and panels (d) - (e) show multimode VAET. Depicted are schematics of one-, two-, and four-phonon transfer processes, together with the corresponding Feynman diagrams connecting the initial state $|e_1\rangle$ and final state $|e_3\rangle$. The interaction amplitudes $W_{jk}^{q_1 x_1}$ and $W_{jk,kk'}^{q_1 x_1, q_2 x_2}$ with $x_i \in \{a, b\}$, and $q_i \in \{+, -\}$ appearing below some of the Feynman diagrams are defined in the Supplementary Material [188].

this four-phonon VAET is a higher order process than that considered in our perturbation theory, we do not provide an analytical expression for the transfer probability here.

We also find that the two-phonon VAET at $\nu_{a(b)}/\Delta_{31} = 0.5$ is dominant over the one-phonon VAET at $\nu_{a(b)}/\Delta_{31} = 1$. This is particularly marked for the single-mode VAET enabled by the vibration ν_a that is coupled to the bridge site. This is evident from the vertical lines in Fig. 6.2(a) and the 1-dimensional slice located above this. While the dominance of TPhonA VAET is clearly visible for the bridging site vibration, it is also manifested to a lesser degree for the terminal site vibration (see 1-dimensional slice to the right of Fig. 6.2(a) where the integrated strength of TPhonA VAET is clearly stronger [188], despite a slightly lower maximal value). This dominance of the two-phonon VAET over one-phonon VAET is particularly marked in the weak coupling regime (recall $\kappa_a = \kappa_b = 0.01$kHz for Fig. 6.2), but will also be evident in the strong coupling regime results presented in Sec. 6.6 below. The reason for this dominance is the relatively high temperature considered here, i.e., $k_B T_{a(b)} = 1.5$kHz, which ensures availability of the required number of phonons for both one- and two-phonon VAET, while the probability of energy transfer increases with average phonon number. Thus, for the one-phonon VAET, the average phonon numbers are $n_{a(b)} \sim 1$ when $\nu_{a(b)}/\Delta_{31} = 1$, while for the two-phonon VAET, the average phonon numbers are $n_{a(b)} \sim 2.4$ when $\nu_{a(b)}/\Delta_{31} = 0.5$. In the latter situation there is a higher than required average phonon number for $\nu_a(b)$, implying that the two-phonon processes are more likely ($1 < 2.4/2 = 120\%$). This analysis also holds when the temperature becomes so low that the necessary number of phonons cannot be taken from the thermal state, e.g., for $k_B T_{a(b)} = 0.5$kHz, where the two-phonon VAET is still dominant relative to one-phonon VAET. Here the average phonon number is $n_{a(b)} \sim 0.143$ when $\nu_{a(b)}/\Delta_{31} = 1$, and $n_{a(b)} \sim 0.548$ when $\nu_{a(b)}/\Delta_{31} = 0.5$. Since $14.3\% < 0.548/2 = 27.4\%$, the two-phonon VAET is still dominant at this lower temperature (see also Section 6.5.3 below).

Finally, we note that the single-mode two- and four-phonon VAET features seen in Fig. 6.2 are in good agreement with the additional partially-resolved peaks observed in the recent experimental study of single-mode VAET in a dimer system emulated with trapped ions [17].

6.5.2   Multimode VAET

The collective behaviors of multiple vibrations enable unique signatures of VAET arising in our trimeric system, relative to those due to individual ones of single vibrations presented above. Such signatures are represented by the diagonal and anti-diagonal lines in Figs. 6.2(a) and (b). They include cooperativity and interference of the two vibrations. Of particular interest for the former is the manifestation of the phononic analog of Göppert-Mayer's two-photon absorption [180], constituting the anti-diagonal lines, and the inverse of this that combines vibrational and excitonic transitions, which we refer to as heteroexcitation, and which constitute the diagonal lines.

6.5.2.1   Cooperative Two-Phonon Absorption VAET

The anti-diagonal lines in Fig. 6.2(a) signify cooperative processes in which phonons from
both modes are involved in a VAET process. For example, the line $\nu_a/\Delta_{31} + \nu_b/\Delta_{31} = 1$
signifies a double-mode two-phonon cooperative VAET process. We designate this as a
cooperative TPhonA process (c-TPhonA) in Fig. 6.2(b). This cooperative process with a
simultaneous absorption of phonons from two vibrations in assisting the energy transfer
constitutes a phononic analogue of two-photon absorption [180].

At the symmetric lattice point $\{\nu_a/\Delta_{31}, \nu_b/\Delta_{31}\} = \{0.5, 0.5\}$ satisfying the resonance
condition $\nu_a = \nu_b = \Delta_{21} = \Delta_{32}$, the transition from $|e_1\rangle$ to $|e_3\rangle$ proceeds via the bridge
state $|e_2\rangle$ and is assisted by two strongly cooperative processes consisting of absorption of a
single phonon from one mode, followed by a second phonon from the other mode, with per-
turbative transfer probability $\alpha^4 (W_{32,21}^{-b-a})^* W_{32,21}^{-b-a}$ or $\alpha^4 (W_{32,21}^{-a-b})^* W_{32,21}^{-a-b}$ [188], as illustrated
in Fig. 6.3(d). The two transfer processes having absorption of two phonons from distinct
vibrational modes in different orders can interfere with each other, giving rise to a double-
mode two-phonon interference VAET. The Feynman pathways for this interference are shown
in the right hand (red) subpanel of Fig. 6.3(d) and the associated perturbative expression
for the probability is $\alpha^4 (W_{32,21}^{-a-b})^* W_{32,21}^{-b-a} + \alpha^4 (W_{32,21}^{-b-a})^* W_{32,21}^{-a-b}$ [188]. Fig. 6.4 shows the time
dependence of $P_3(t)$ at $(0.5, 0.5)$ (solid green line) together with corresponding time traces
for nearby points along the $(0.5, \nu_b/\Delta_{31})$ (dashed blue and yellow lines). This shows that
the symmetric point (green line) is a point of destructive interference along the ν_b axis, since
it has a smaller maximal probability than the time traces of the nearby points. Similarly
comparing the time traces of $P_3(t)$ for points along the $(\nu_a/\Delta_{31}, 0.5)$ line shows that the point
$(0.5, 0.5)$ is a point of constructive interference along the ν_a axis, since here the green curve
has a higher maximal value than those of nearby points (red and cyan dot-dashed curves).

At all points away from the symmetric lattice point, i.e., along the rest of the anti-
diagonal line $\nu_a/\Delta_{31} + \nu_b/\Delta_{31} = 1$ with $\nu_a \neq \nu_b$, the transition from $|e_1\rangle$ to $|e_3\rangle$ involves a
virtual intermediate state, i.e., $|e_2'\rangle$ rather than $|e_2\rangle$ as illustrated in the lower left subpanel of
Fig. 6.3(d). These points therefore show relatively small transfer probability in Fig. 6.2. We
point out that the upper portion of the anti-diagonal with $\nu_b > \nu_a$ is noticeably less intense
than the lower part where $\nu_b < \nu_a$. This is once again a consequence of the stronger impact
of the vibration ν_a that is coupled to the bridge site in assisting the energy transfer, relative
to that of the vibration coupled to the terminal site. In situations for which the impact of
the vibration ν_b becomes dominant in the energy transfer, for example the Hamiltonian with
site-correlated vibrational modes analyzed in Sec. 6.8, this effect is reversed.

Similarly, the second anti-diagonal line visible in Fig. 6.2(a), i.e., $\nu_a/\Delta_{31} + \nu_b/\Delta_{31} = 0.5$
at the bottom left, signifies a double-mode, four-phonon cooperative VAET involving two
processes of two-phonon absorption each. Here the lattice point, i.e., $\{\nu_a/\Delta_{31}, \nu_b/\Delta_{31}\} =
\{0.25, 0.25\}$, can host an interference between two transfer pathways involving different or-
dering of the two-phonon absorptions, while the rest of this anti-diagonal line, i.e., $\nu_a \neq \nu_b$,
shows a relatively low transfer probability due to the off-resonant nature of the intermediate
virtual state. This constitutes a higher-order phononic analogue of two-photon absorption,
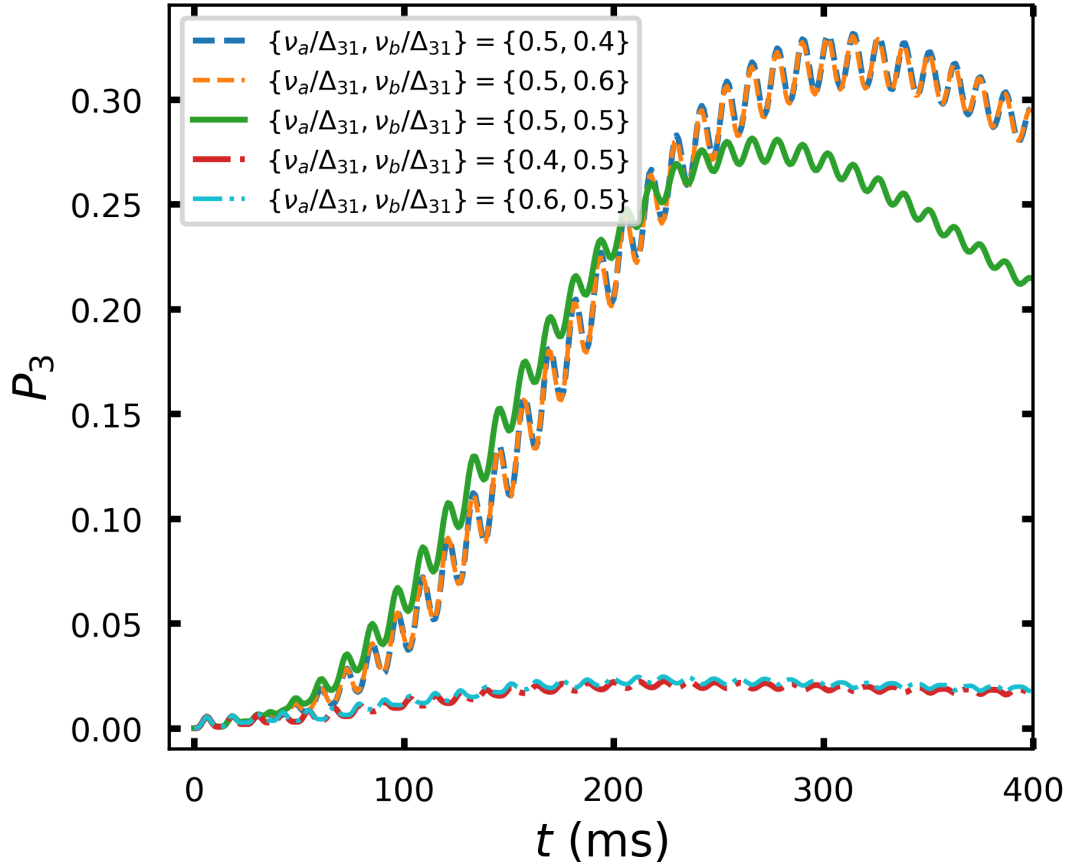
Figure 6.4: (color online) Time evolution of the probability P_3 of the acceptor at the symmetric point $\{\nu_a/\Delta_{31}, \nu_b/\Delta_{31}\} = \{0.5, 0.5\}$ and nearby points along the $\nu_a/\Delta 31 = 0.5$ and $\nu_a/\Delta 31 = 0.5$ lines in Fig. 6.2. All other parameters are the same as in Fig. 6.2(a).

which is illustrated in Fig. 6.3(e).

6.5.2.2   Heteroexcitation VAET

In addition to these cooperative VAET processes for which both vibrations contribute phonons to assist excitonic energy transfer, we also find evidence of VAET processes in which a phonon from one vibrational mode can simultaneously excite not only the electronic system but also the other vibrational mode. This is a new kind of cooperative mechanism of VAET, which we shall refer to as "heteroexcitation". It is evidenced by the diagonal lines in Fig. 6.2(a), which are also shown with their assignments as solid diagonal lines in Fig. 6.2(b). For example, the line $\nu_a/\Delta_{31} - \nu_b/\Delta_{31} = 1$ indicates that one phonon of vibrational mode ν_a generates an electronic transition from site 1 to 3, together with absorption of a single phonon in mode ν_b. The line $\nu_a/\Delta_{31} - \nu_b/\Delta_{31} = 0.5$ represents processes in which two

phonons of vibrational mode ν_a generate the same electronic transition, but now together
with absorption of two phonons in mode ν_b. An analogous interpretation applies to the line
$\nu_b/\Delta_{31} - \nu_a/\Delta_{31} = 0.5$.

We note that the alternative heteroexcitation associated with the diagonal line $\nu_b/\Delta_{31} -
\nu_a/\Delta_{31} = 1$, shown as the dotted diagonal line at the top left of Fig. 6.2(b), in which one
phonon from vibrational mode ν_b generates an excitonic transition together with absorption
of a phonon of vibrational mode ν_a is not observable in Fig. 6.2(a). This is because of the
weaker impact of the vibration coupled to the terminal site. This vibration now has to
provide one phonon to be absorbed by both the timer and the other vibration, which is a
significantly weaker process at this temperature. However this transition would appear on
further increasing the temperature of mode b ($k_B T_b$), so we also show the relevant Feynman
diagrams for this process in Fig. 6.3(e).

We note that while the reverse of two photon absorption, namely one photon exciting two
atoms, has been discussed previously, it was assumed there that atoms of identical frequency
are excited by a single photon [183], consistent with the larger wavelength of optical photons
relative to atoms. The heteroexcitations seen here constitute a generalized phononic analog
of that optical phenomenon, where now not only the energies, but also the nature of the two
degrees of freedom being excited can be different. Another interesting interpretation of this
process is that of redistribution of energy from one phonon reservoir to another, mediated
by the electronic degrees of freedom.

6.5.3 Vibrational temperature effects

One interesting capability of artificial energy transport as studied with emulations using e.g.,
trapped ions, that is not possible in real molecular systems, is the ability to individually
vary the effective temperature of different vibrational modes. Here we assess the effects of
these temperatures on VAET features. Fig. 6.5 presents 2D VAET spectra at three different
temperatures from that in Fig. 6.2, including also the presence of a temperature bias between
the two vibrations in panels (b) and (c).

In the absence of a temperature bias, i.e, when the vibrational temperatures are equal
(panel (a)), comparison with the higher vibrational temperature spectrum of Fig. 6.2 ($k_B T_a =
k_B T_b = 1.5$kHz) shows that collective VAET features such as the cooperative behavior ev-
idenced by the anti-diagonal and diagonal lines in the 2D spectrum become weaker as the
vibrational temperature decreases, indicating a suppression of vibrationally assisted energy
transfer processes. However the two-phonon VAET is still dominant over the one-phonon
VAET, as discussed in Section 6.5.1.

When a temperature bias between the two vibrations is present, as in panels (b) and (c),
we find that increasing either $k_B T_a$ [Fig. 6.5(b)] or $k_B T_b$ [Fig. 6.5(c)] will enhance the transfer
processes assisted by either of the vibrations coupled to the bridge or to the acceptor. This
suggests that the weaker impact of the vibration coupled to the acceptor seen above could
be enhanced by selectively raising the temperature of this mode in an emulation experiment.
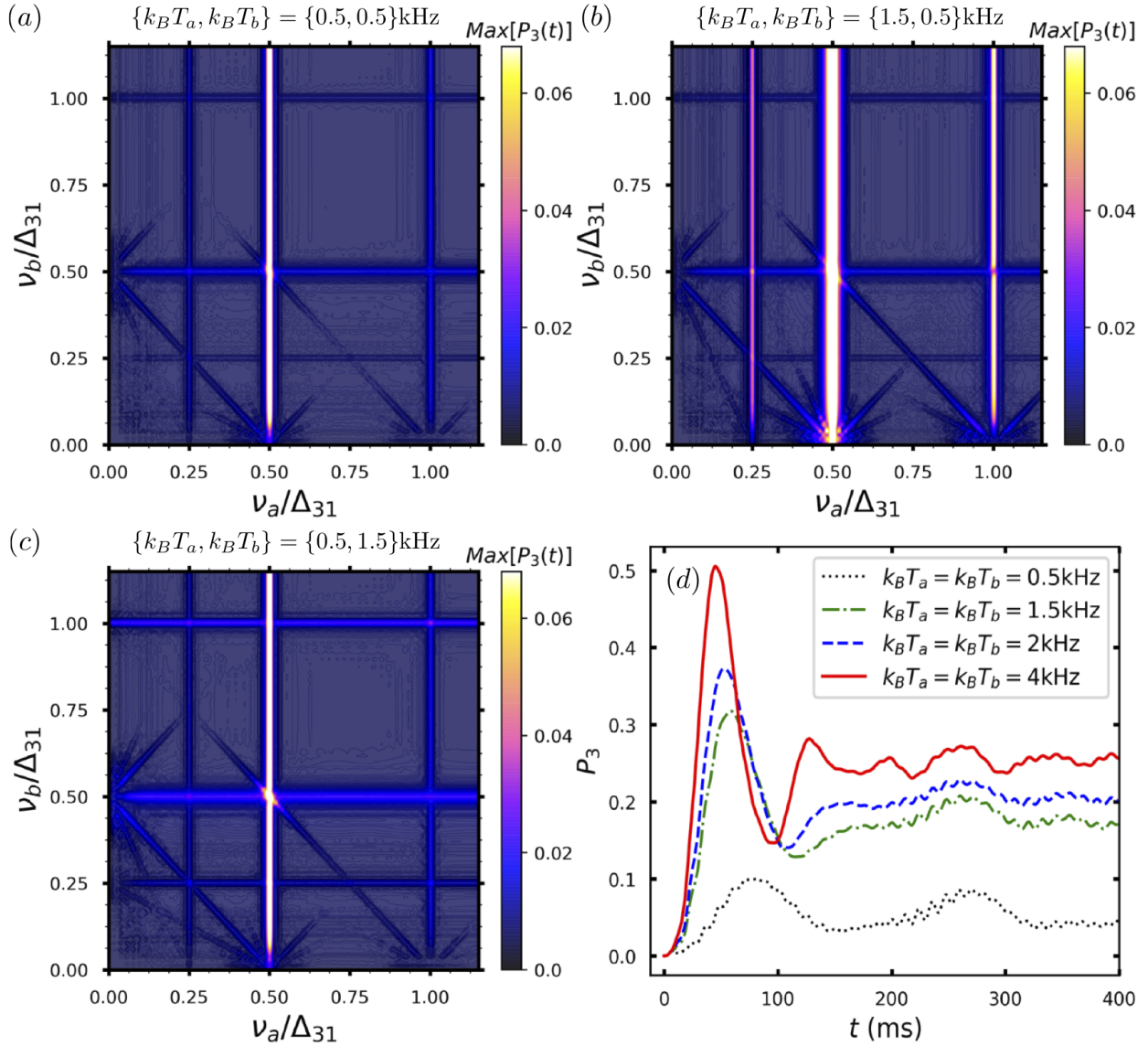
Figure 6.5: (color online) 2D VAET spectra showing $\text{Max}[P_3(t)]$ in a time period $t \in [0, 400]$ms for different vibrational temperatures $\{k_B T_a, k_B T_b\}$ in the weak coupling regime. (a) $\{k_B T_a, k_B T_b\} = \{0.5, 0.5\}$, (b) $\{k_B T_a, k_B T_b\} = \{1.5, 0.5\}$, and (c) $\{k_B T_a, k_B T_b\} = \{0.5, 1.5\}$. All calculations employed phonon truncation at $N = 15$ and site-vibration coupling strength $\kappa_a = \kappa_b = 0.01$kHz. (d) Time trace of the transfer probability $P_3(t)$ at the resonance points $(\nu_a/\Delta_{31}, \nu_b/\Delta_{31}) = (0.5, 0.5)$ and $(\nu_a, \nu_b) = (0.52, 0.52)$ kHz, for temperatures $k_B T_a = k_B T_b = 0.5$kHz, 1.5kHz, 2kHz, 4kHz, with $N = 40$ phonon truncation and site-vibration couplings $\kappa_a = \kappa_b = 0.05$kHz. All other parameters are the same as in Fig. 6.2.

Panels (b) and (c) of Fig. 6.5 show that the presence of a temperature bias across the two vibrations can also enhance heteroexcitations at $|\nu_a - \nu_b| = \Delta_{31}, \Delta_{31}/2$, relative to that seen for equal temperatures in Fig. 6.5(a). Such enhancement of heteroexcitations would increase with further increase of the temperature bias.

The time dependence of energy transfer probability in VAET processes is also strongly dependent on the vibrational temperatures. Fig. 6.5(d) shows the time evolution of the transfer probability at the resonance points $(\nu_a/\Delta_{31}, \nu_b/\Delta_{31}) = (0.5, 0.5)$ and $(\nu_a, \nu_b) = (0.52, 0.52)$kHz in Figs. 6.2 and 6.5(a). We see that increasing the temperature generically enhances the energy transfer, with the maximum probability reaching values up to ~ 0.5 when $k_B T_a = k_B T_b = 4$kHz.

6.5.4   Dissipative effects

In contrast to the assistance provided by undamped vibrations for excitation energy transfer discussed above, the decay of an electronic excitation at each site, resulting from e.g., spontaneous emission or coupling to damped vibrational environments, is expected to suppress energy transfer processes. Here we study the effect of such relaxation processes, using a non-Hermitian approach that in the single excitation subspace is equivalent to use of the Lindblad master equation with a relaxation operator [199] (see detailed analysis in the Supplementary Material [188]).

Including a non-Hermitian Hamiltonian term, the system under such dissipation is described by $H_{eff} = H_{tr} - \frac{i}{2} \sum_{j=1}^{3} \gamma_j |e_j\rangle\langle e_j|$ where $H_{tr} = H_s + H_v + H_{int}$ given by Eq. (6.1). The effective Hamiltonian in the single electronic excitation subspace is then obtained as $\tilde{H}_{eff} = \Xi H_{eff} \Xi = \tilde{H}_{tr} - \frac{i}{2}(\gamma_1 |1\rangle\langle 1| + \gamma_2 |2\rangle\langle 2| + \gamma_3 |3\rangle\langle 3|)$, where $\tilde{H}_{tr}$ is given by Eq. (6.5) [188]. The average effect of dissipation on the excitation energy transfer is then obtained by repeating the 2D VAET spectral calculations with $\tilde{H}_{tr}$ replaced by $\tilde{H}_{eff}$.

Fig. 6.6 shows the 2D VAET spectrum with dissipation given by parameters $\gamma_1 = \gamma_2 = \gamma_3 = \gamma = 0.001$kHz. We see suppression of all energy transfer processes, particularly those along the anti-diagonal and diagonal lines, relative to the dissipation-free results in Fig. 6.2(a). As expected, the single-mode two-phonon VAET is the most pronounced VAET process in Fig. 6.6.

Fig. 6.7(a) shows that for a specific VAET transfer process, e.g., the single mode TPhonA VAET at the resonant position $\nu_a/\Delta_{31} = \nu_b/\Delta 31 = 0.5$, the time-dependent probability of finding an excitation at the acceptor, $P_3(t)$, is increasingly suppressed for all t as γ increases. To analyze which sites contribute to this suppression, Fig. 6.7(b) shows calculations with different dissipative parameters γ_i at each site. Only small variations are seen, within the general trend that a strong dissipation at the donor site provides the greatest suppression (red dotted line), followed by having the strongest dissipation at the acceptor site (blue solid line). Interestingly, when the strongest dissipation is at the bridge site, the energy transport is most robust to the dissipation (yellow and green dashed lines).
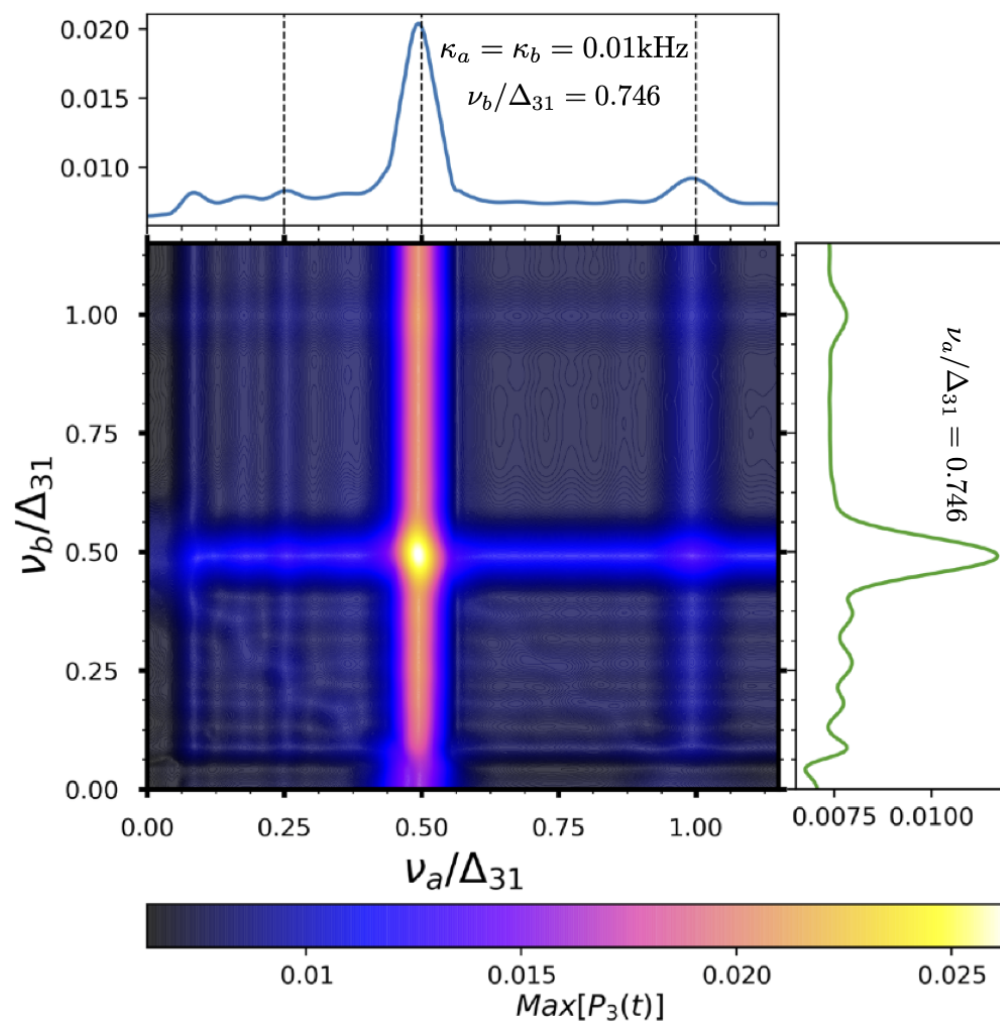
Figure 6.6: (color online) 2D VAET spectrum for a trimeric chromophore system coupled to two non-interacting vibrations in the weak site-vibration coupling regime, $\kappa_a = \kappa_b = 0.01$kHz, with dissipative parameters $\gamma_1 = \gamma_2 = \gamma_3 = 0.001$kHz. Here the truncation number of each vibrational Fock space is $N = 10$ and other parameters are same as in Fig. 6.2.
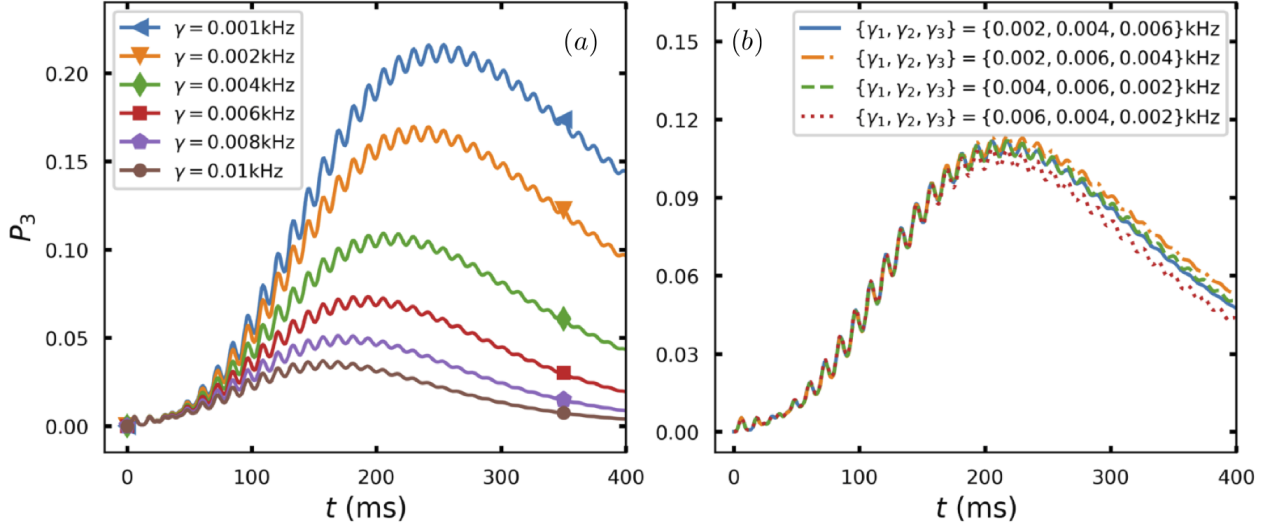
Figure 6.7: (color online) Energy transfer probability $P_3(t)$ as a function of time for (a) identical ($\gamma_1 = \gamma_2 = \gamma_3 = \gamma$) and (b) different values of site dissipation rates. Here we take the site-vibrational coupling $\kappa_a = \kappa_b = 0.01$kHz, the vibrational frequency $\nu_a/\Delta_{31} = \nu_b/\Delta_{31} = 0.5$, and the temperature $k_B T_a = k_B T_b = 1.5$kHz. All other parameters are the same as in Fig. 6.2.

6.6   VAET signatures in the presence of strong site-vibration coupling

As the site-vibration coupling strength increases, different VAET features emerge and the balance between single- and multi-phonon VAET processes changes. We explore these changes by considering larger coupling strengths $\kappa_a = \kappa_b = 0.03$kHz and 0.1kHz, summarized in Figs. 6.8(a) and 6.8(b), respectively. The top and right side slices in each of these plots are taken at $\nu_a/\Delta_{31} = 0.746$ (right slice) and $\nu_b/\Delta_{31} = 0.746$ (top slice). In addition to the basic VAET features from Fig. 6.2(a) (where $\kappa_a = \kappa_b = 0.01$kHz), we now observe additional multiphonon VAET processes in Fig. 6.8(a) that involve three, five, and six phonons, indicated by vertical lines at $\nu_a/\Delta_{31} = 1/3$, $1/5$, and $1/6$, respectively. For the larger site-vibration coupling strength $\kappa_a = \kappa_b = 0.1$kHz shown Fig. 6.8(b), these vertical lines become more distinct and also start to shift noticeably away from the excitonic resonant transition frequencies. We also see that in the strong coupling regime, not only do the one-phonon (e.g., $\nu_a/\Delta_{31} = 1$) and two-phonon (e.g., $\nu_a/\Delta_{31} = 0.5$) VAET processes become more comparable in intensity, but also the impact of the vibration coupled to the acceptor, ν_b, becomes comparable to that of the bridging vibration ν_a. Thus, we now see local maxima at $\nu_a/\Delta_{31}, \nu_b/\Delta_{31} = 1$ and 0.25, in both the right and top slices of Fig. 6.8(a) and (b). The greater structure in these intensity patterns contrasts with the simpler structure obtained for weak site-vibration coupling in Fig. 6.2(a).
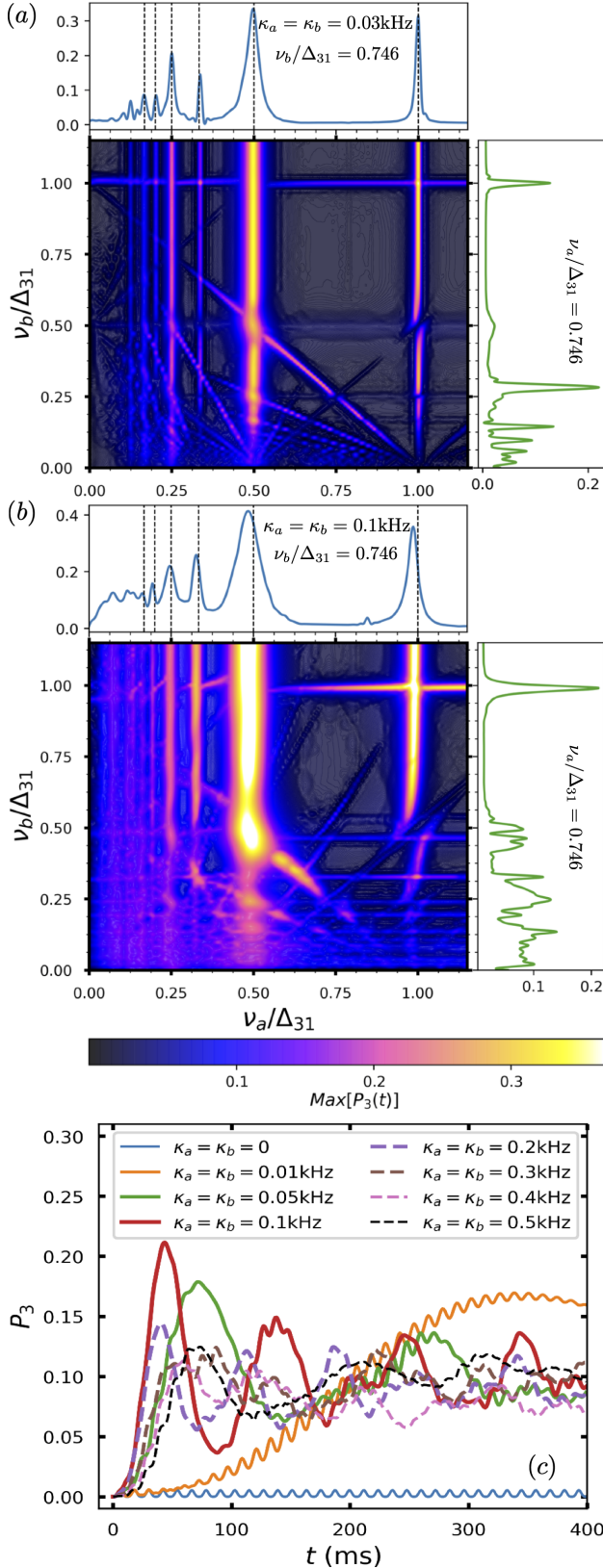
Figure 6.8: (color online) 2D VAET spectra for the trimeric chromophore system coupled to two non-interacting vibrations in the strong site-vibration coupling regime. Panels (a) - (b) show the maximum transfer probability $Max[P_3(t)]$ in a time period $t \in [0, 400]$ms for two values of the site-vibration coupling $\kappa_a = \kappa_b = \kappa$: (a) $\kappa = 0.03$kHz and (b) $\kappa = 0.1$kHz. The slices on the top and right side of each contour plot are taken at $\nu_b/\Delta_{31} = 0.746$ and $\nu_a/\Delta_{31} = 0.746$, respectively. (c) Time trace of the energy transfer probability $P_3(t)$ for several combinations of κ_a, κ_b at the resonance points $(\nu_a/\Delta_{31}, \nu_b/\Delta_{31}) = (0.5, 0.5)$ and $(\nu_a, \nu_b) = (0.52, 0.52)$kHz). The vibrational temperatures are $k_B T_a = k_B T_b = 1.5$kHz. All other parameters are the same as in Fig. 6.2.

To further demonstrate the effects of strong site-vibration coupling on the VAET, we plot in Fig. 6.8(c) the time evolution of the $P_3(t)$ at the resonance point $(\nu_a/\Delta_{31}, \nu_b/\Delta_{31}) = (0.5, 0.5)$ for a two-phonon VAET process at various values of the coupling strength $\kappa = \kappa_a = \kappa_b$. When the electronic sites are decoupled from the vibrations, i.e., $\kappa_a = \kappa_b = 0$, the blue reference curve in Fig. 6.8(c) shows Rabi oscillations characterized by the transition frequency $\nu_a = \Omega = \sqrt{\Delta^2 + 2J^2} = 0.52$kHz, with corresponding oscillatory period $2\pi/\nu_a \sim$ 12ms (approx. eight cycles in each period of 100ms). When the coupling is nonzero, we observe modulated Rabi-like oscillations that show slow oscillations superimposed on the fast oscillations with the frequency Ω. See, for example, the solid orange curve in Fig. 6.8(c), for which $\kappa_a = \kappa_b = 0.01$kHz. As κ increases to 0.05kHz (green curve) and beyond to 0.1kHz (red curve), the initial rise of $P_3(t)$ is faster and the first maximum higher. However, further increase of the site-vibration coupling strength beyond 0.1kHz reverses this trend. In the next section we shall see that this is a result of the formation of vibronic states with strong mixing of excitonic and vibrational degrees of freedom, giving rise to very different transition frequencies.

6.7 Vibronic spectral analysis of VAET and role of cross-coupling terms in the effective Hamiltonian

6.7.1 Vibronic states

In order to better understand the origin of the VAET features, we have calculated the energy spectrum for the trimer excitonic system coupled to the two vibrational modes including three vibrational levels [Eq. (6.5)] as a function of the scaled frequencies $(\nu_a/\Delta_{31}, \nu_b/\Delta_{31})$, for specific values of the coupling strengths. This reveals the energies of the vibronic states formed as a consequence of the two exciton-vibration couplings. Fig. 6.9 shows the corresponding two dimensional vibronic spectrum for the case of coupling strengths $\kappa_a = \kappa_b = 0.03$kHz. The figure clearly shows the presence of avoided crossings that derive from the exciton-vibration coupling. For example, along the horizontal line $\nu_b/\Delta_{31} = 0.5$, whenever ν_a/Δ_{31} approaches a resonant transition frequency of the trimer excitonic system (i.e., zero detuning at $\nu_a/\Delta_{31} = 0.25, 0.5, 1$ as shown in Fig. 6.2), this gives rise to an avoided crossing due to the site-vibration coupling. Each avoided crossing in the spectrum shown in Fig. 6.9 indicates a vibronic state, i.e., a mixing of the electronic and vibrational degrees of freedom [161].

Some of the avoided crossings in the vibronic energy spectrum correspond to VAET features discussed above. A perturbative analysis of the vibronic energies predicts the presence of avoided crossings at the degenerate states. Thus the specific avoided crossings magnified in Figs. 6.9(b) and (c) indicate the hybridized vibronic states ($\cong |110\rangle \pm |300\rangle$ and $|111\rangle \pm |301\rangle$ (i, j, k in $|ijk\rangle$ represent the excitonic state $|e_i\rangle$, and vibrational occupation states $|j\rangle$ and $|k\rangle$, respectively) that give rise to the one-phonon VAET feature along the vertical line $\nu_a/\Delta_{31} = 1$) in Fig. 6.2(a). Similarly, the states $\cong |121\rangle \pm |301\rangle$ at the avoided crossing in Fig. 6.9(d) are associated with the single-mode two-phonon VAET indicated by
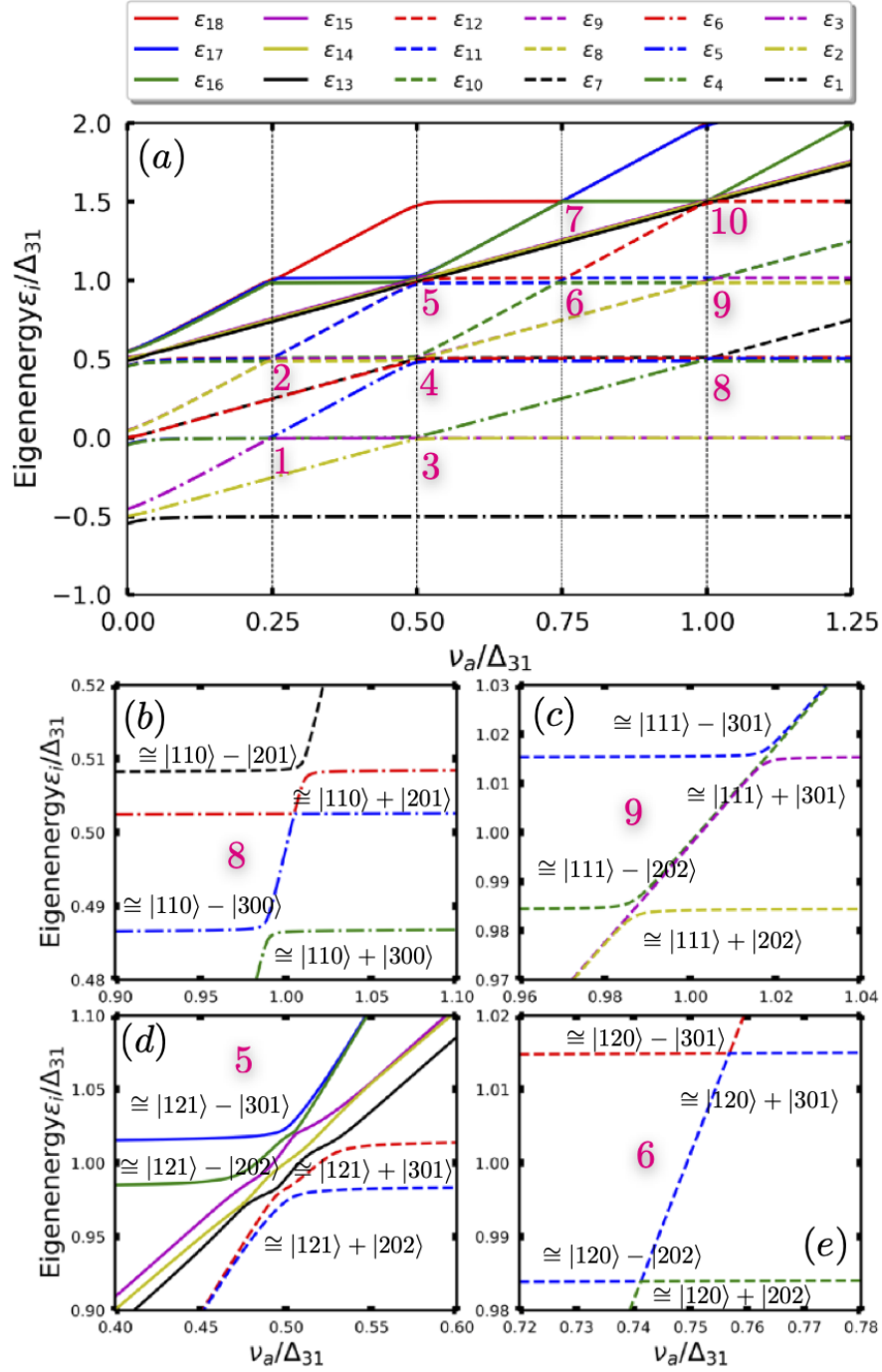
Figure 6.9: (color online) Vibronic energy spectrum of the effective excitonic levels $|e_i\rangle$ coupled to two vibrational modes $|j\rangle$ and $|k\rangle$ with $N = 3$ levels each, as a function of ν_a/Δ_{31}. Here only eighteen of the twenty seven lowest energy levels are shown. Panels (b)-(e) show enlarged views of each avoided crossing in panel (a). The parameters are $\{\tilde{\omega}_1, \tilde{\omega}_2, \tilde{\omega}_3, J_{12}, J_{23}\} = \{-0.5, 0, 0.5, 0.1, 0.1\}$kHz and $\nu_b = \Delta_{21} = \Delta_{32} = 0.52$kHz and $\kappa_a = \kappa_b = 0.03$kHz.

the vertical line, i.e., $\nu_a/\Delta_{31} = 0.5$, in Fig. 6.2. We also see vibronic states associated with the cooperative VAET features. In Fig. 6.9(e), the avoided crossing of states $\cong |120\rangle \pm |301\rangle$ corresponds to an intersection of the horizontal line $\nu_b/\Delta_{31} = 0.5$ and the off-diagonal line $2\nu_a - \nu_b = \Delta_{31}$ in Fig. 6.2 that indicates the double-mode cooperative VAET.

We note that the avoided crossings in the vibronic spectrum become more pronounced as the coupling strength κ_a or κ_b increases, consistent with the perturbative analysis. This means that not only does the gap between the two adjacent levels increase, but also the shift from the excitonic resonant transition frequencies (e.g., $\nu_a/\Delta_{31} = 1, 0.5, 0.25$) will be larger. This trend is also visible in the cross-sectional slices in Fig. 6.8(a) and (b). Consequently, for given frequencies ν_a, ν_b, increasing either κ_a or κ_b to values so large that they are comparable with the excitonic energy differences will be expected to suppress energy transfer processes below the values seen for smaller coupling. Indeed, this is consistent with the decrease in $P_3(t)$ seen for large $\kappa_a = \kappa_b$ values in Fig. 6.8(c).

6.7.2 Effect of cross couplings in single excitation subspace

The VAET features presented above are based on the consideration of the effective Hamiltonian Eq. (6.5) derived as the single electronic excitation restriction of the model in Eq. (6.1) for the trimeric chromophore system. This trimeric model, generalized from an experimentally investigated dimer for an artifical excitonic system realized in a trapped ion system [17], contains interaction of the vibrations with both excited and the ground states, i.e., $\kappa_a\sigma_z^{(2)}(a^\dagger + a) + \kappa_b\sigma_z^{(3)}(b^\dagger + b)$. We saw that the resulting effective model in the single electronic excitation manifold has cross coupling terms, i.e., an interaction of a vibration with the excited states of unconnected sites.

Here we analyze the effects of the cross coupling terms on the excitation energy transfer. To isolate the effects resulting from these terms, we rewrite the effective Hamiltonian in Eq. (6.5) as

$$
\begin{aligned}
\bar{H}_{tr}(\zeta) = {} & \tilde{\omega}_1|1\rangle\langle 1| + \tilde{\omega}_2|2\rangle\langle 2| + \tilde{\omega}_3|3\rangle\langle 3| \\
& + J_{12}(|1\rangle\langle 2| + |2\rangle\langle 1|) + J_{23}(|2\rangle\langle 3| + |3\rangle\langle 2|) \\
& + \kappa_a(a^\dagger + a)(-\zeta|1\rangle\langle 1| + |2\rangle\langle 2| - \zeta|3\rangle\langle 3|) \\
& + \kappa_b(b^\dagger + b)(-\zeta|1\rangle\langle 1| - \zeta|2\rangle\langle 2| + |3\rangle\langle 3|) \\
& + \nu_a a^\dagger a + \nu_b b^\dagger b,
\end{aligned}
\tag{6.10}
$$

with variable parameter ζ which interpolates between Eq. (6.5) for $\zeta = 1$ and the usual single excitation manifold effective Hamiltonian for molecular excitons without cross coupling terms for $\zeta = 0$. The latter case corresponds to the full Hamiltonian, Eq. (6.1), with the site-vibration coupling in Eq. (6.4) replaced by $\kappa_a\sigma_+^{(2)}\sigma_-^{(2)}(a^\dagger + a) + \kappa_b\sigma_+^{(3)}\sigma_-^{(3)}(b^\dagger + b)$.

Fig. 6.10 shows the two-dimensional VAET spectra for two symmetric trimeric systems with identical energy gaps (i.e., $\Delta_{21} = \Delta_{32}$) that allow interference VAET to appear. Comparison of either the two left panels (a) and (c) with $\Delta_{21} = \Delta_{32} = 0.332\text{kHz}$,

Figure 6.10: (color online) Comparison of 2D VAET spectra of symmetric trimeric chromophore systems described by the effective Hamiltonian $\bar{H}(\zeta)$, Eq. (6.5) with $\zeta = 1$ (upper row) and $\zeta = 0$ (lower row). The parameter values $\{\tilde{\omega}_1, \tilde{\omega}_2, \tilde{\omega}_3\}$ specified above the panels give excitonic energy differences $\{\Delta_{21}, \Delta_{32}\} = \{0.332, 0.332\}$kHz in (a), (c) and $\{0.52, 0.52\}$kHz in (b), (d) with $\Delta_{31} = \Delta_{21} + \Delta_{32}$. The other parameters are $J_{12} = J_{23} = 0.1$kHz, $\kappa_a = \kappa_b = 0.01$kHz, $k_B T_a = k_B T_b = 0.749$kHz, and $N = 10$.

or the two right panels with $\Delta_{21} = \Delta_{32} = 0.52$kHz, shows that the cross coupling terms in $\tilde{H} = \bar{H}_{tr}(\zeta = 1)$ significantly enhance the energy transfer. For example, the one-phonon VAET at $\nu_b = \Delta_{31} = 1.04$kHz, which shows high intensity for $\bar{H}_{tr}(\zeta = 1)$ (panel (b)), is considerably less intense $\bar{H}_{tr}(\zeta = 0)$ (panel (d)).

Comparing now the left and right panels of either the upper ($\zeta = 1$) or lower ($\zeta = 0$) row shows the effect of modifying the energy barrier for both Hamiltonians. Thus the higher probabilities for the two-phonon VAET processes seen in panel (a) are due to the lower excitonic energy barrier $\tilde{\omega}_3 - \tilde{\omega}_2 = \tilde{\omega}_2 - \tilde{\omega}_1 = 0.3$kHz which is more similar to the excitonic coupling $J = 0.1$kHz, than that of panel (b) for which $\tilde{\omega}_3 - \tilde{\omega}_2 = \tilde{\omega}_2 - \tilde{\omega}_1 = 0.5$kHz.

The appearance of an interference VAET requires a specific condition, i.e., $\Delta_{21} = \Delta_{32}$. To isolate the interference VAET features we therefore present in Fig. 6.11 2D VAET spectra for two asymmetric systems that do not host any interferences. The upper row of Fig. 6.11 shows spectra with $\{\tilde{\omega}_1, \tilde{\omega}_2, \tilde{\omega}_3\}$ equal to $\{-0.5, 0, 0.3\}$kHz (a) and $\{-0.3, 0, 0.5\}$kHz (b), implying different energy gaps of $\{\Delta_{21}, \Delta_{32}\} = \{0.508, 0.343\}$kHz. We see that the double-mode two-phonon cooperative VAET, located at the lattice point $[\{\nu_a, \nu_b\} = \{\Delta_{21}, \Delta_{32}\}$ in panel (a) and at $\{\nu_a, \nu_b\} = \{\Delta_{32}, \Delta_{21}\}$ in panel (b) is now the only dominant process. The corresponding time traces are shown in Fig. 6.12 where it is evident that they have a maximal value intermediate between those of symmetrically distributed neighboring points, implying an absence of interference at the symmetric points $\nu_a = \nu_b = \Delta_{21} = \Delta_{32}$. This is in contrast to the 2D VAET spectra for systems with identical energy gaps $\Delta_{21} = \Delta_{32}$ in Fig. 6.10, where the interferences at the crossing point of vertical ($\nu_a = 0.332$kHz) and horizontal ($\nu_b = 0.332$kHz) lines in panel (a) and at the crossing point of $\nu_a = 0.52$kHz and $\nu_b = 0.52$kHz in panel (b) are clearly visible. The corresponding time traces (not shown), show destructive interference along the vertical lines $[\nu_a = 0.332$kHz (Fig.10 (a)) and $\nu_a = 0.52$kHz (Fig.10 (b)], and constructive interference along the horizontal lines $[\nu_b = 0.332$kHz (Fig.10 (a)) and $\nu_b = 0.52$kHz (Fig.10 (b)]. We also present the corresponding results for the effective Hamiltonian $\bar{H}_{tr}(\zeta = 0)$ in the lower row of Fig. 6.11, to emphasize the key role of the cross coupling terms in amplifying these cooperative VAET processes. The interference features are no longer visible here, confirming the critical role of the cross-correlated vibrations in enabling these quantum features.

6.8   VAET with explicitly correlated vibrational modes

The energy transfer in the trimeric chromophore system discussed in Sections 6.3-6.7 relies on the assistance of two independent vibrational modes that are coupled to the bridge and acceptor sites, respectively [see Eq. (6.4)]. Experimental realization of this ideal Hamiltonian with the local and independent control of the site-vibration interaction for a trapped-ion quantum simulator requires that the ionic states be coupled to transverse vibrational modes. This is more challenging than coupling to the longitudinal vibrations, requiring stabilization
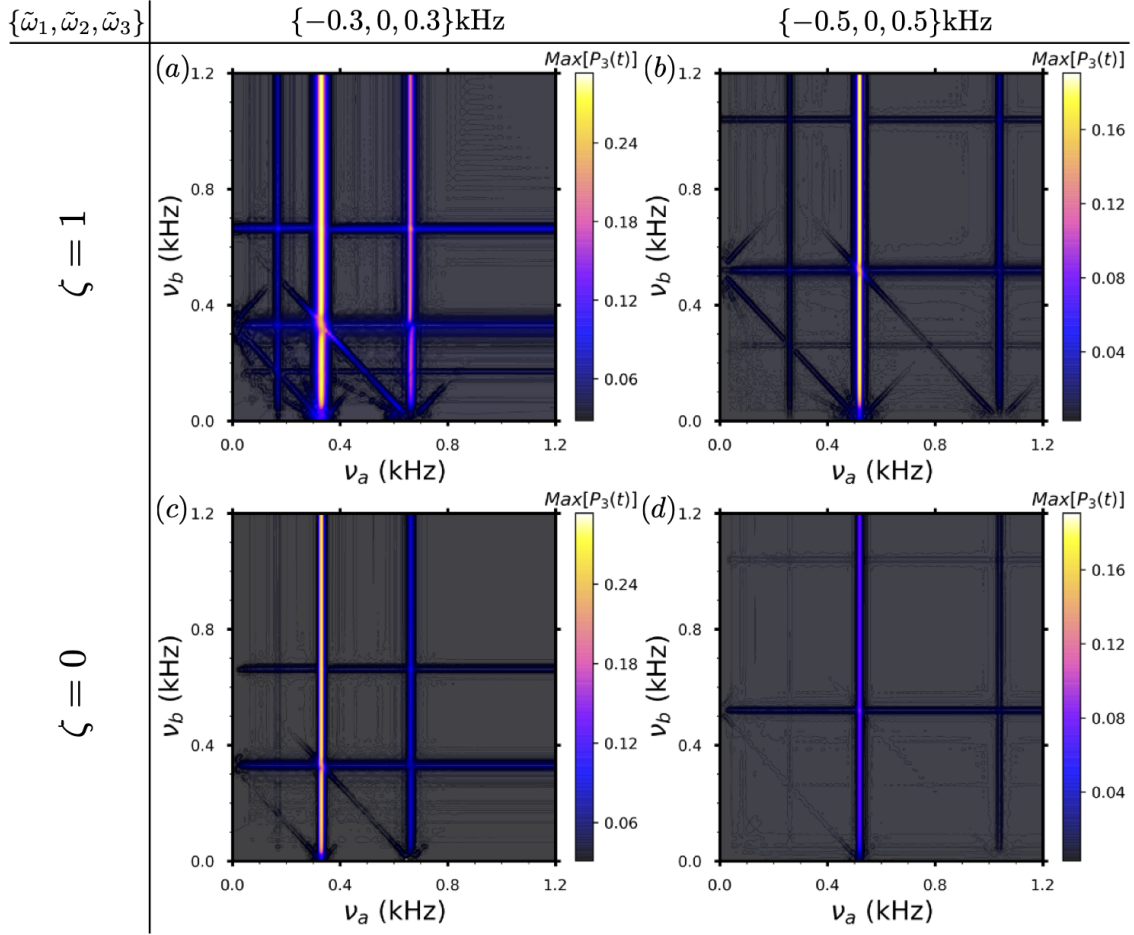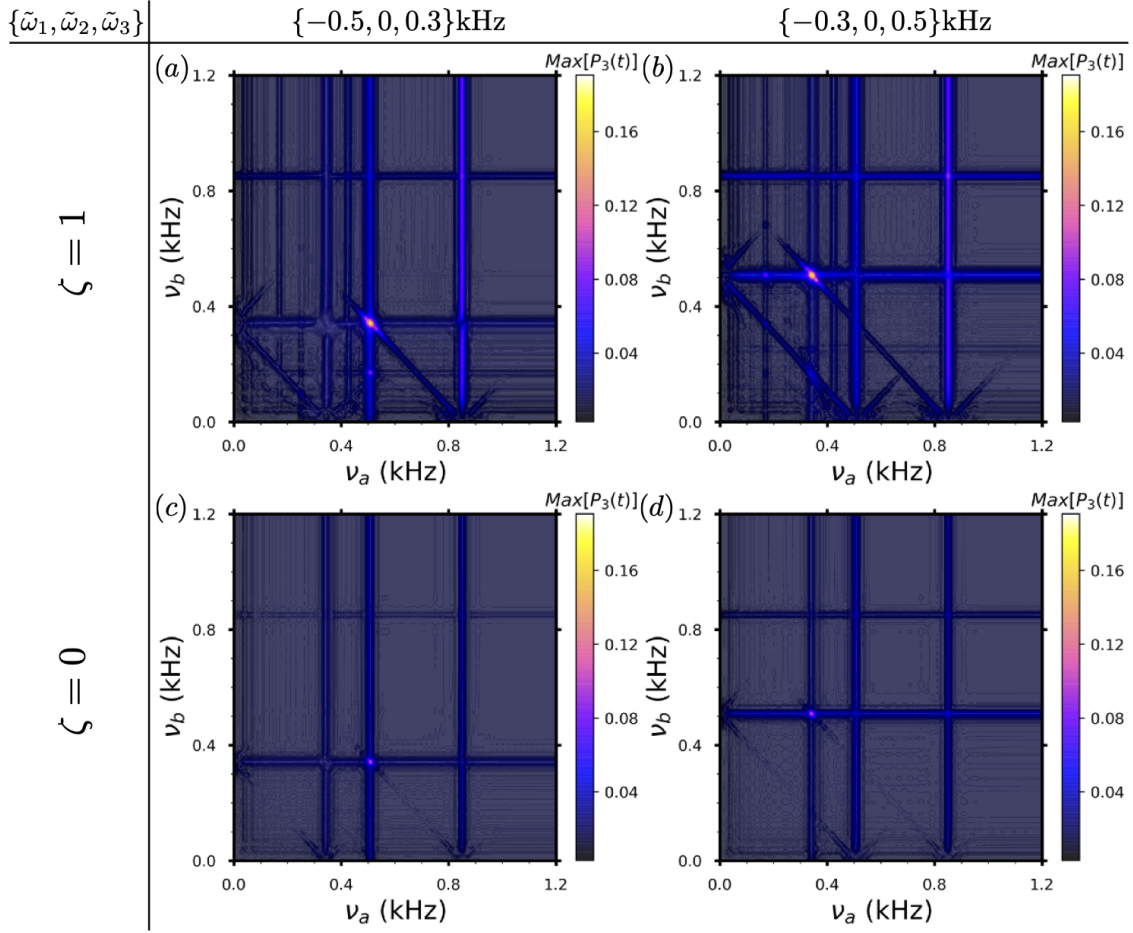
Figure 6.11: (color online) 2D VAET spectra of an asymmetric trimeric chromophore system described the effective Hamiltonian $\bar{H}(\zeta)$, Eq. (6.5) with $\zeta = 1$ (upper row) and $\zeta = 0$ (lower row). The parameter values $\{\tilde{\omega}_1, \tilde{\omega}_2, \tilde{\omega}_3\}$ specified above the panels give excitonic energy differences $\{\Delta_{21}, \Delta_{32}\} = \{0.508, 0.343\}$ (panels (a), (c)), $\{0.343, 0.508\}$kHz (panels (b), (d)), with $\Delta_{31} = \Delta_{21} + \Delta_{32}$ in all cases. The other parameters are $J_{12} = J_{23} = 0.1$kHz, $\kappa_a = \kappa_b = 0.01$kHz, $k_B T_a = k_B T_b = 0.749$kHz, and $N = 10$.
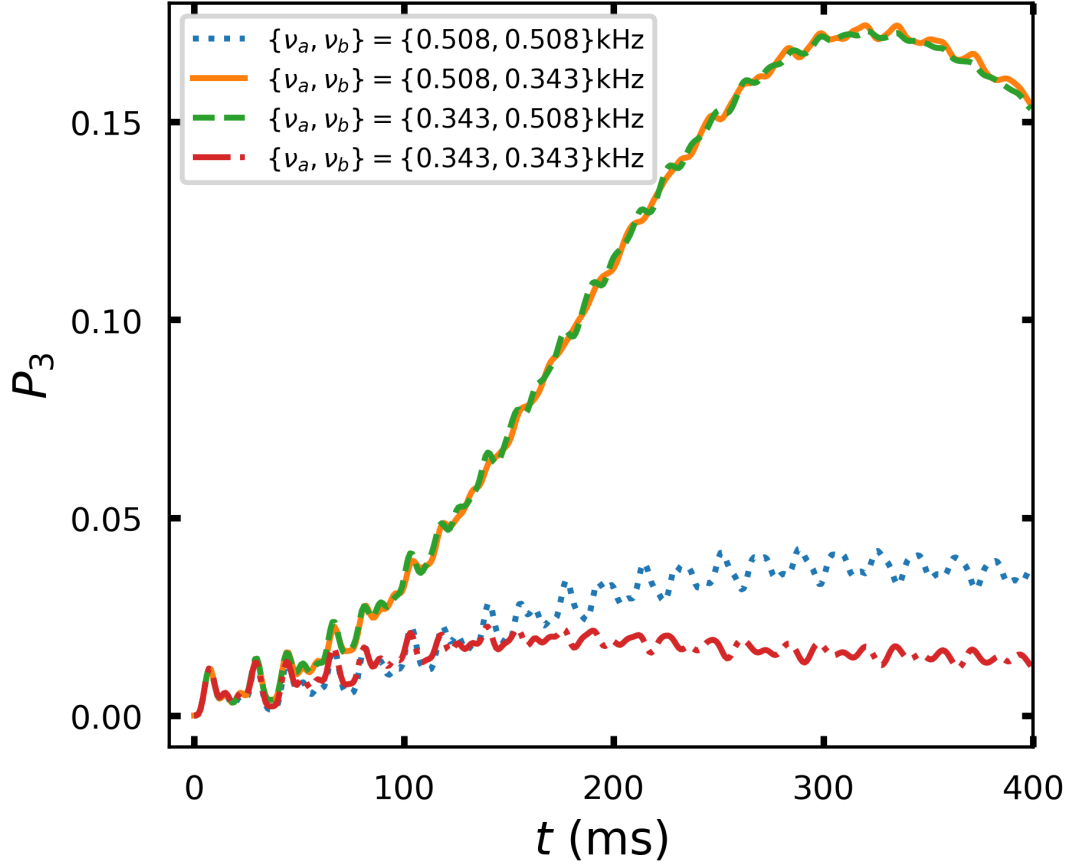
Figure 6.12: (color online) Time evolution of the probability P_3 of the acceptor at the asymmetric point $\{\nu_a, \nu_b\} = \{0.508, 0.343\}$kHz in Fig. 6.11(a) and $\{\nu_a, \nu_b\} = \{0.343, 0.508\}$kHz in Fig. 6.11(b), together with nearby symmetric points $\{\nu_a, \nu_b\} = \{0.508, 0.508\}$kHz, $\{0.343, 0.343\}$kHz. All other parameters are the same as in Fig. 6.11.

with regard to the trapping frequency. Coupling to longitudinal modes allows instead access to normal modes that are linear combinations of local vibrations, exemplified for a three-ion system by the following Hamiltonian [200]:

$$
\begin{aligned}
H_{\ln g} &= \frac{\omega_1'}{2}\sigma_z^{(1)} + \frac{\omega_2'}{2}\sigma_z^{(2)} + \frac{\omega_3'}{2}\sigma_z^{(3)} \\
&+ J_{12}'\sigma_x^{(1)}\sigma_x^{(2)} + J_{23}'\sigma_x^{(2)}\sigma_x^{(3)} + J_{13}'\sigma_x^{(1)}\sigma_x^{(3)} \\
&+ \nu_c c^\dagger c + \nu_d d^\dagger d + \kappa_c'(\sigma_z^{(1)} - \sigma_z^{(3)})(c + c^\dagger) \\
&+ \kappa_d'(\sigma_z^{(1)} - 2\sigma_z^{(2)} + \sigma_z^{(3)})(d + d^\dagger).
\end{aligned} \tag{6.11}
$$

Note that here we have also included a direct excitonic coupling J_{13}' between donor and acceptor sites. This Hamiltonian describes the coupling of the trimeric system to the symmetric and asymmetric normal modes of vibration along the longitudinal axis of a linear
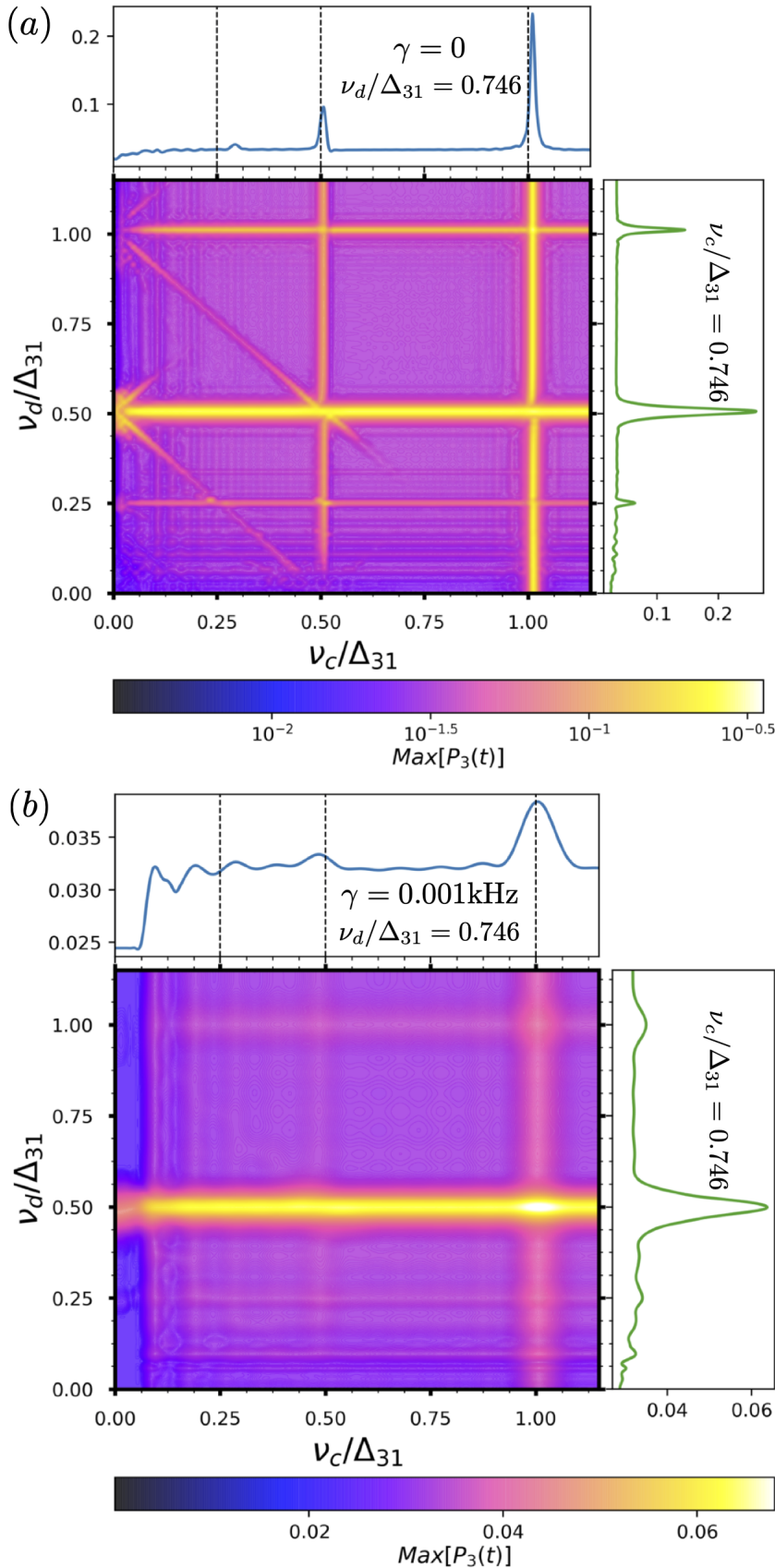
Figure 6.13: (color online) The VAET features of the trimeric chromophore system weakly coupled to correlated and anti-correlated vibrational models described by the effective Hamiltonian Eq. (6.12) for the cases of (a) without ($\gamma = 0$) and (b) with ($\gamma = 0.001\text{kHz}$) dissipation. The color bar in (a) is same as in Fig. 6.2(a) for comparison, but note the change in scale of panel (b) relative to panel (a). The parameters are $\{\tilde{\omega}'_1, \tilde{\omega}'_2, \tilde{\omega}'_3\} = \{-1, 0, 1\}$, $\{J'_{12}, J'_{23}, J'_{13}\} = \{0.1, 0.1, 0.08\}$, $\{\kappa'_c, \kappa'_d\} = \{0.005, 0.005\}$, $\{k_B T_c, k_B T_d\} = \{1.5, 1.5\}$ kHz, which are equivalent to those in Fig. 6.2(a).

chain of three ions. In contrast to the transverse coupling Hamiltonian of Eq. (6.4), we now have one vibrational mode, ν_c (the symmetric stretch) that shows anti-correlated coupling to the donor and the acceptor and a second vibrational mode ν_d (the asymmetric stretch) that shows a more complex correlated coupling with all three sites. Anti-correlated vibrations have been claimed to drive non-adiabatic electronic energy transfer in photosynthetic light-harvesting systems [168]. It is thus of interest to analyze the possibility of VAET processes in such a Hamiltonian possessing both correlated and anti-correlated site-vibration couplings.

Following the procedure outlined in Section 6.3 to project the Hamiltonian onto the single electronic excitation subspace, we obtain the following effective Hamiltonian:

$$
\begin{aligned}
\tilde{H}_{\mathrm{lng}} &= \frac{\tilde{\omega}_1'}{2}|1\rangle\langle 1| + \frac{\tilde{\omega}_2'}{2}|2\rangle\langle 2| + \frac{\tilde{\omega}_3'}{2}|3\rangle\langle 3| + J_{12}'(|1\rangle\langle 2| + |2\rangle\langle 1|) \\
&\quad + J_{23}'(|2\rangle\langle 3| + |3\rangle\langle 2|) + J_{13}'(|1\rangle\langle 3| + |3\rangle\langle 1|) \\
&\quad + \nu_c c^\dagger c + \nu_d d^\dagger d + 2\kappa_c'(c + c^\dagger)(|1\rangle\langle 1| - |3\rangle\langle 3|) \\
&\quad + 2\kappa_d'(d + d^\dagger)(|1\rangle\langle 1| - 2|2\rangle\langle 2| + |3\rangle\langle 3|),
\end{aligned}
\tag{6.12}
$$

with $\tilde{\omega}_1' = \omega_1' - \omega_2' - \omega_3'$, $\tilde{\omega}_2' = \omega_2' - \omega_1' - \omega_3'$, $\tilde{\omega}_3' = \omega_3' - \omega_1' - \omega_2'$. We then perform the numerical simulations to evaluate the maximum energy transfer probability $\mathrm{Max}[P_3(t)]$ for the effective model $\tilde{H}'_{eff} = \tilde{H}_{\mathrm{lng}} - \frac{i\gamma}{2}(|1\rangle\langle 1| + |2\rangle\langle 2| + |3\rangle\langle 3|)$, where we also include the effects of dissipation via non-Hermitian decay of chromophore excitations with parameter γ. The resulting 2D VAET spectra for the dynamics with and without dissipation in the weak coupling regime are presented in Fig. 6.13(a) and (b), respectively.

It is notable that the values of $\mathrm{Max}[P_3(t)]$ in Fig. 6.13(a) are systematically larger than the corresponding values in Fig. 6.2(a). This difference is due to two specific differences in the Hamiltonian of Eq. (6.12) relative to that of Eqs. (6.1) - (6.4). Firstly, in Eq. (6.12) the donor and acceptor are directly coupled through a Coulomb term (J_{13}'). This promotes direct transfer from donor to acceptor, without involvement from the bridge site. Secondly, the vibrational mode ν_c serves to vibrationally assist this direct transfer process. This additional transfer mechanism and its vibrational enhancement lead to the larger $\mathrm{Max}[P_3(t)]$. Fig. 6.13(a) shows that this system with explicitly correlated couplings to the longitudinal vibrational modes generates a very different relative impact of the symmetric stretch ν_c and the asymmetric stretch vibration ν_d on the VAET spectra from that seen for the local transverse couplings in Sections 6.3-6.7. This is evident both in the ratios of single mode two-phonon to one-phonon VAET processes (horizontal and vertical lines), and in the variable intensities of the two-mode two-phonon VAET processes (antidiagonal lines). As we explain in detail below, this different impact reflects the fact that with the longitudinal modes, the asymmetric stretch ν_d couples more strongly to the bridge site than to the donor and acceptor sites, while the symmetric stretch ν_c couples only to the latter. This is true both in the full Hamiltonian $\tilde{H}_{\mathrm{lng}}$ and in the corresponding effective Hamiltonian, Eq. (6.12).

The single mode one-phonon VAET line for the symmetric stretch (vertical line $\nu_c/\Delta_{31} = 1$) is more intense than that for the asymmetric stretch (horizontal line $\nu_d/\Delta_{31} = 1$). We note that since $J_{13}' \neq 0$, this one-phonon process between states $|e_1\rangle$ and $|e_3\rangle$, which become

approximately $|1\rangle$ and $|3\rangle$ in the weak site-site coupling regime, does not necessarily require a coupling to the bridge site. Furthermore, mode ν_c promotes this transfer directly and does so efficiently, because it dynamically reduces the energy gap between donor and acceptor due to the anticorrelated displacements of site energies resulting from coupling to this mode, as noted above. In contrast, mode ν_d causes correlated displacements of the energies of $|1\rangle$ and $|3\rangle$ [see Eq. (6.12)], and thus is less effective at promoting this transfer with a single phonon VAET process. This is in direct analogy to the effects of anti-correlated versus correlated classical fluctuations on energy transfer studied in [190, 191, 194].

The two-phonon lines $\nu_d/\Delta_{31} = 0.5$ and $\nu_c/\Delta_{31} = 0.5$ show an even greater disparity, to the extent that the two-phonon VAET for the symmetric stretch ($\nu_c/\Delta_{31} = 0.5$) is not dominant over the corresponding one-phonon process. The strongest feature in the VAET spectrum is now the single mode two-phonon absorption in ν_d, i.e., the horizontal line $\nu_d/\Delta_{31} = 0.5$. This parallels the analogous dominance of the single mode two-phonon absorption for the mode coupled to the bridge site in the VAET spectrum of Fig. 6.2(a) (vertical line at $\nu_a/\Delta_{31} = 0.5$). The anomalous observation of the one-phonon symmetric stretch VAET for ν_c being more intense than the two-phonon process results from the fact that this mode is completely decoupled from the excited state of the bridge site in both Eq. 6.11 and Eq. 6.12. This is quite different from not only the interaction of mode ν_d in Eq. (6.12), but also that of modes ν_a and ν_b in Eq. 6.5, all of which include some coupling to the excited state of the bridge site in the effective Hamiltonian for the single excitation subspace.

More marked is the behavior in the anti-diagonal lines representing multi-mode VAET (corresponding to TPhonA in Fig. 6.2(b)). For example, the anti-diagonal line $\nu_c/\Delta_{31} + \nu_d/\Delta_{31} = 1$ shows significant intensity in the sector $\nu_d > \nu_c$ but negligible intensity in the sector $\nu_d < \nu_c$. When dissipation is taken into account, Fig. 6.13(b) shows that all transfer processes are suppressed, similar to what is seen for the uncorrelated trimeric system above (see Fig. 6.6).

We have additionally considered a vanishing value of the direct donor-acceptor coupling J'_{13} to characterize the impact of this coupling on the enhancements derived from the correlated vibrational modes [188]. As expected, this leads to smaller values of $\mathrm{M}ax[P(t)]$ due to the removal of the direct excitonic coupling between donor and acceptor. In addition, we find that the one-phonon transition from $|e_1\rangle$ to $|e_3\rangle$, which is approximated by $|1\rangle$ and $|3\rangle$, respectively, in the weak site-site coupling regime, can now no longer be assisted by the symmetric stretch. Thus, in this case there is no vertical line at $\nu_c/\Delta_{31} = 1$ representing a one-phonon VAET process. This is because while the symmetric stretch mode ν_c undergoes anticorrelated coupling with the donor and acceptor sites (i.e., with their exciton states $|1\rangle$ and $|3\rangle$), in the absence of direct excitonic coupling it cannot enhance energy transfer from site 1 to site 3.

6.9   Discussion and conclusions

We have systematically studied the phenomenon of vibrationally assisted energy transfer,
VAET, in a donor-bridge-acceptor trimeric chromophore system coupled to two vibrations
over a range of coupling strengths. In this work we focused on two types of systems. The
first derives from a Hamiltonian with uncorrelated local coupling, as would be obtained by
coupling to transverse modes in a trapped ion quantum emulator. The second derives from
explicitly correlated non-local coupling, as would be obtained by coupling to normal modes
of longitudinal motion in a trapped ion quantum emulator. The parameters considered in
this work are within the regime of current trapped-ion experiments [17] and in all cases
we considered a parameter set ensuring energetically uphill transitions from both donor to
bridge chromophores and bridge to acceptor chromophores.

In the case of local site-vibration couplings, we found a rich array of VAET phenomena
going beyond the one-phonon VAET observed previously with a trapped ion quantum emula-
tor [17]. In particular, we also find clearly resolved signatures of two- and even four-phonon
absorption processes in the 2D VAET spectrum at weak site-vibration coupling strength,
while increasing the coupling strength introduces up to to six-phonon VAET processes. The
two-phonon VAET processes constitute a phononic analogue of the well-known two-photon
absorption [180] and we refer to them as TPhonA. They are found to be dominant for
all coupling strengths, although the relative contributions of both one- and greater than
two-phonon VAET processes do increase with coupling strength, gaining intensity from off-
resonant contributions in the strong coupling regime. At all values of coupling strength,
we find that for every VAET process the vibration coupled to the bridge has a significantly
stronger impact than the terminal vibration, consistent with its central spatial location for
energy transport across the chain of sites.

We also found that the two vibrations can give rise to multi-mode VAET processes in
which they behave collectively, specifically via cooperation and interference that enhance the
efficiency of energy transfer relative to that obtained from VAET with a single vibrational
mode. This includes cooperative TPhonA in which the two phonons derive from different
modes, possibly with different frequencies. We also observe an interesting phenomenon that
is formally related to the reverse of this, namely processes in which a phonon from one vi-
brational mode simultaneously excites both the excitonic states of the trimeric chromophore
system and the other vibrational mode. We term this process "heteroexcitation". A vibronic
spectral analysis of the VAET features allowed detailed assignment and rationalization of
the spectra, revealing the constructive effects of cross coupling terms in our derived effective
model. Detailed analysis of transfer processes showing quantum interference was arrived at
by considering a generalized asymmetric trimeric analog of the symmetric model for which
the bulk of the numerical calculations were made.

The collective VAET features were found to be reduced but not completely suppressed by
dissipative effects. We showed that they can however be enhanced by raising the temperature
of the vibrational modes, as well as by increasing the strength of the site-vibration coupling.

In the case of explicitly correlated non-local site-vibration couplings, as would be obtained

by coupling ions to longitudinal modes, we found generically similar VAET features but with
quite different relative strengths. The most important parameter determining the integrated
strength of excitonic energy transfer was seen to be the vibrational coupling to the bridge
site of the chromophore system.

Our projection of the full Hamiltonian onto a single excitation subspace generates an
effective Hamiltonian with induced cross-correlations in the effective site-vibration coupling
that can be mapped onto excitonic energy transport for molecular chromophores coupled
to correlated vibrational modes. The richness of the VAET spectra found here raises the
intriguing question as to whether some of these VAET processes may be operating in natural
systems. In particular, the results show the important role played by resonant vibrations
in enhancing uphill energy transport. Such modes provide sharp features in the 2D VAET
spectra, indicating a significant enhancement of the generic quantum ratcheting of energy
transport that is derived from coherent coupling to a quantum vibrational bath [187]. As
illustrated in Table 6.1, the parameters considered in our study are scaled versions of param-
eters found in natural photosynthetic systems. This motivates further analysis of whether
examples of the more complex VAET phenomena such as two-phonon absorption and het-
eroexcitations are present in any natural systems.

For trapped-ion simulations of molecular excitation energy transfer between interacting
pigment molecules modeled as two-level systems that are coupled to vibrational modes, the
quantum simulator would consist of a chain of ions, e.g., Ca^+, confined in a radio-frequency
Paul trap with well defined sites determined by the trap geometry and the Coulomb inter-
action between the ions [17]. Each ion in this "ion crystal" represents the site of single
pigment molecule, with two internal electronic states of the ions encoding the two relevant
molecular energy levels at that site. The lower energy level represents the ground state and
the higher energy level the molecular (Frenkel) exciton state. It is convenient to use the
internal ionic states that are commonly employed as qubit states for quantum computation
with the particular trapped ion species. For example, with Ca^+ the two magnetic substates
$|S\rangle$ ($m_j = 1/2$) and $|D\rangle$ ($m_j = 1/2$) are used, which can be addressed by an optical transi-
tion [17]. The quantum states representing a single excitation localized on one molecular site
correspond then to the combined three-ion states $|DSS\rangle$, $|SDS\rangle$, and $|SSD\rangle$. The exciton-
exciton interaction between individual sites can be engineered by the use of a (global) laser
beam incident on all sites with tones detuned from the qubit transition by the axial vibra-
tional frequencies of the ion chain. Selecting a specific normal vibrational mode allows that
mode of the ion crystal to act as a bus that can transfer excitation between distinct sites
via the two-qubit Mølmer-Sørensen quantum interaction [32]. This inter-site exciton-exciton
interaction is complemented by site-vibration couplings that are achieved with the use of
tightly focused laser beams that are localized on individual ions.

We emphasize that the cooperative behavior of multiple vibrations seen in this work act
not only to enhance the excitation energy transfer but also demonstrate a rich set of VAET
phenomena. Following the experimental observation of single-mode one-phonon VAET for a
dimeric system in a trapped-ion quantum emulator [17], generalization of such experiments
to three and more ions [179], as well as to other emulation platforms [178] appears feasible.

We look forward to experimental verification of the predictions of VAET signatures for two-phonon absorption and for heteroexcitations in emulations of a trimeric chromophore system.

6.10 Key results of perturbative analysis of energy transfer

Here we summarize some key results from the analytical perturbative calculations provided in the Supplementary Material [188] that are used in the main text. In the interaction picture, the coefficients A_{jk}, B_{jk} that determine the perturbative factors discussed in Section 6.5 are given explicitly as functions of J, Δ and Ω as

$$A_{12} = A_{21} = \frac{2\Delta J(\Delta + \Omega)}{\Omega^2 \sqrt{2[J^2 + \Delta(\Delta + \Omega)]}}, \tag{6.13}$$

$$A_{23} = A_{32} = \frac{2\Delta J(\Delta - \Omega)}{\Omega^2 \sqrt{2[J^2 + \Delta(\Delta - \Omega)]}}, \tag{6.14}$$

$$B_{12} = B_{21} = \frac{2J^3}{\Omega^2 \sqrt{2[J^2 + \Delta(\Delta + \Omega)]}}, \tag{6.15}$$

$$B_{23} = B_{32} = \frac{2J^3}{\Omega^2 \sqrt{2[J^2 + \Delta(\Delta - \Omega)]}}, \tag{6.16}$$

$$A_{13} = A_{31} = -\frac{2J^2}{\Omega^2}, \tag{6.17}$$

$$B_{13} = B_{31} = \frac{J^2}{\Omega^2}, \tag{6.18}$$

with $\Delta = \tilde{\omega}_2 - \tilde{\omega}_1 = \tilde{\omega}_3 - \tilde{\omega}_2$ and $\Omega = \sqrt{\Delta^2 + 2J^2}$. The energy transfer probability at the acceptor can be written as $P_3(t) = Tr[U_0^\dagger |3\rangle\langle 3| U_0 U_I(t)|1\rangle\langle 1|\rho_a\rho_b U_I^\dagger(t)]$, where $U_0 = e^{-i(H_0^{(e)} + H_0^{(\nu)})t}$ and the evolution operator in the interaction picture is $U_I(t) = \mathcal{T} e^{-i\int_0^t ds H_I(s)}$, with $\mathcal{T}$ the time-ordering operator. To calculate the probability $P_3(t)$, we write the donor and acceptor states in the site basis in terms of eigenstates, giving $|1\rangle = \alpha|e_1\rangle - \beta|e_2\rangle + \gamma|e_3\rangle$ and $|3\rangle = \gamma|e_1\rangle + \beta|e_2\rangle + \alpha|e_3\rangle$, where $\alpha = \frac{\sqrt{J^2 + \Delta(\Delta + \Omega)}}{\sqrt{2}\Omega}$, $\beta = \frac{J}{\Omega}$, and $\gamma = \frac{\sqrt{J^2 + \Delta(\Delta - \Omega)}}{\sqrt{2}\Omega}$. Note that in the weak site-site coupling limit, i.e., $J \ll \Delta$, we have $\alpha \to 1$ and $\beta, \gamma \to 0$ and the excitonic eigenstates $|e_3\rangle$ and $|e_1\rangle$ can then be approximated by $|3\rangle$ and $|1\rangle$, respectively [188].

6.11 Convergence

As demonstrated in the main text, a large transfer probability can be realized by increasing either the vibrational temperatures $k_B T_a$ and $k_B T_b$, or the site-vibration coupling strengths
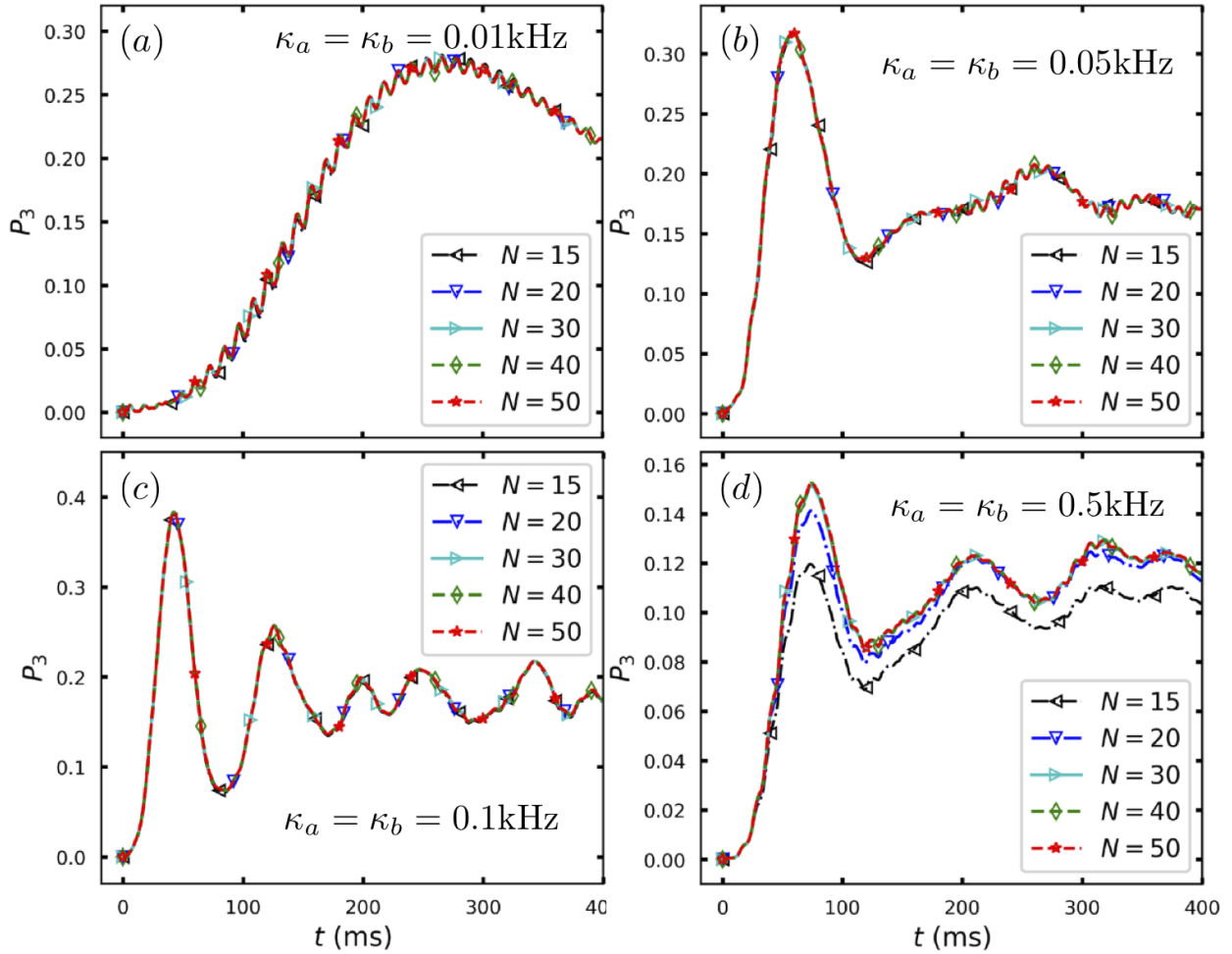
Figure 6.14: (color online) Convergence of the transfer probability for several values of site-vibration coupling (a) $\kappa_a = \kappa_b = 0.01$kHz, (b) $\kappa_a = \kappa_b = 0.05$kHz, (c) $\kappa_a = \kappa_b = 0.1$kHz, and (d) $\kappa_a = \kappa_b = 0.5$kHz. Here we consider $k_B T_a = k_B T_b = 1.5$kHz, $\nu_a/\Delta_{31} = \nu_b/\Delta_{31} = 0.5$, and other parameters are same as in Fig. 6.2.

κ_a, κ_b. However higher values of temperature or site-vibration coupling might cause convergence issues if the truncation number N of each vibrational Fock space is not large enough. To address this issue and confirm convergence of the numerical results, we show in Fig. 6.14 the transfer probability for various values of N, at vibrational temperatures $k_B T_a = k_B T_b = 1.5$kHz for several values of the site-vibration coupling. When the coupling strength is weak, e.g., $\kappa_a = \kappa_b = 0.01$kHz in Fig. 6.14(a), and when it is increased to 0.05kHz and 0.1kHz as in Fig. 6.14(b) and (c), respectively, the results are already convergent for $N = 15$. This provides evidence for the accuracy of our results in Fig. 6.2(a). Increasing the coupling strength to an ultra-strong regime [201], e.g., to $\kappa_a = \kappa_b = 0.5$kHz, which is comparable to the excitonic transition frequency, requires a value as large as $N = 30$ to achieve a good convergence, as shown in Fig. 6.14(d). Similarly, convergence of the spectra in the very low vibrational frequency regime (i.e., smaller $\nu_{a(b)}/\Delta_{31}$) might be expected to require a larger value of N. However, the general form of the spectra in this region is already converged at $N = 15$, as shown explicitly in the Supplemental Material [188].

Chapter 7

Conclusion

This thesis has focused on the impact of environmental interactions on both digital quantum computing and analogue quantum emulation. We started in Chapter 2 with an overview on the modeling of qubits in open quantum systems, especially the types of environmental interactions in superconducting and trapped-ion quantum devices. These two types of hardware are two major platforms of interest in the main body of this thesis.

In Chapter 3, we introduced a novel Hamiltonian switching control technique aimed at counteracting environmental noise in superconducting quantum systems. The key idea of this method is alternating between two time-constant Hamiltonians as the control ansatz and optimizing the duration allocated to each Hamiltonian through classical optimization. This approach enables the execution of quantum logic gates with high fidelity. We demonstrated the efficacy of this method on qubits coupled to both a TLS (Two-Level System) bath and a Lindblad bath, achieving high fidelity in each scenario. Notably, for a qubit entangled with a TLS bath, gate fidelity was enhanced to surpass $1 - 10^{-4}$, and secondary optimization using GRAPE improved it to beyond $1 - 10^{-8}$. This fidelity surpasses the thresholds of the majority of quantum error correction codes. Moreover, we revealed properties of the control like critical time and critical depth and their dependence on system parameters, providing guidelines for the design of efficient control protocols. Our findings suggest that this Hamiltonian switching control method offers a straightforward and effective strategy for mitigating environmental noise in NISQ devices.

In Chapter 4, we focused on the potential of tensor network quantum machine learning (QML) models as viable applications on near-term quantum hardware. We benchmarked two types of QML networks, TTN and MERA on image classification datasets MNIST, Fashion-MNIST and KMNIST As expected, the classification accuracy decrease with increasing dephasing probability p. A detailed regression analysis shows that in the limit of full-dephasing, the network becomes a classical Bayesian network. By expanding the virtual bond dimension through the addition of ancillas, we can make the network more expressive and consequently improving the classification accuracy. A decohered network with two ancilla on each input bond can achieve similar performance as a fully-coherent network with no ancilla, suggesting the benefit of adding ancilla for near-term implementations. How-

ever, although we found adding more than two ancilla has the trend of diminishing return, we didn't achieve a conclusion for a general number of ancilla as the simulations becomes intractable for more than three ancilla.

In Chapter 5, we studied the interplay between two types of environmental effect, namely vibration modes and dephasing, on energy transfer between two qubits, emulating the energy transfer between two chromophores in light-harvesting complexes. As shown in a prior work [17], coupling to a vibrational mode can assist transfer between two qubits by compensating for the energy gap, a phenomenon called VAET. We have shown that the additional dephasing noise destroys VAET signatures in the low-noise regime and decreases energy transfer efficiency. However, we also observed further increasing dephasing noise level will first increase and then decrease energy transfer efficiency and this turnover is named ENAQT. And VAET effect is not significant in the high-noise ENAQT regime.

In Chapter 6, we extended the study of the VAET effect in a trimeric system coupled to two vibration modes. We first focused on the scenario where two independent vibration modes coupled to the bridging and the terminal qubit respectively, and analyzed the simulated energy transfer spectra, finding a rich array of transfer processes involving varying numbers of photons. Among them, two phonon processes were found to contribute the most significantly to energy transfers and the mode coupled to the bridging site has stronger impact than that coupled to the terminal site. By adjusting environmental parameters, we found dephasing reduces VAET features and raising temperature enhance these features. Moreover, for a more experimentally feasible model with two coupled vibration modes, the VAET spectra have similar pattern but different relative strengths. In general, our studies of VAET in Chapters 5 and 6 are all conducted with models that are feasible for a trapped-ion quantum emulator and relative parameters strength that are comparable to biological light-harvesting complexes, which motives future experimental reproduction of these findings.

In this thesis, we studied the various scenarios of qubits within open quantum systems, with a special emphasis on understanding environmental effects relevant to the near-term hardware. Recognizing the pivotal role these types of hardware play in the foreseeable future, our investigation sheds light on practical approaches to mitigate environmental noise—a pressing concern for near-term quantum devices. Specifically, we introduced strategies for robust control in logic gate implementation and demonstrated the utility of ancillary qubits in QML to counteract noise impacts. Furthermore, we explored the emulation of energy transfer processes, highlighting the significant influence of environmental vibrational modes. Our findings, grounded in experimentally relevant models, not only advance our theoretical understanding but also offer insights for enhancing the performance of near-term quantum hardware.

Bibliography

[1] S. McArdle, S. Endo, A. Aspuru-Guzik, S. C. Benjamin, and X. Yuan, "Quantum computational chemistry", Rev. Mod. Phys. **92**, 015003 (2020).

[2] D. S. Abrams and S. Lloyd, "Simulation of Many-Body Fermi Systems on a Universal Quantum Computer", en, Physical Review Letters **79**, 2586 (1997).

[3] P. Shor, "Algorithms for quantum computation: discrete logarithms and factoring", in Proceedings 35th annual symposium on foundations of computer science (1994), pp. 124–134.

[4] J. Biamonte, P. Wittek, N. Pancotti, P. Rebentrost, N. Wiebe, and S. Lloyd, "Quantum machine learning", en, Nature **549**, Publisher: Nature Publishing Group, 195 (2017).

[5] D. Herman, C. Googin, X. Liu, Y. Sun, A. Galda, I. Safro, M. Pistoia, and Y. Alexeev, "Quantum computing for finance", Nature Reviews Physics **5**, 450 (2023).

[6] M. A. Nielsen and I. L. Chuang, *Quantum computation and quantum information: 10th anniversary edition* (Cambridge University Press, 2010).

[7] H. Bernien, S. Schwartz, A. Keesling, H. Levine, A. Omran, H. Pichler, S. Choi, A. S. Zibrov, M. Endres, M. Greiner, V. Vuletić, and M. D. Lukin, "Probing many-body dynamics on a 51-atom quantum simulator", Nature **551**, 579 (2017).

[8] D. Hangleiter, J. Carolan, and K. P. Y. Thébault, *Analogue quantum simulation: a new instrument for scientific understanding* (Springer International Publishing, 2022).

[9] J. Preskill, "Quantum computing in the NISQ era and beyond", Quantum **2**, 79 (2018).

[10] A. Peruzzo, J. McClean, P. Shadbolt, M. H. Yung, X. Q. Zhou, P. J. Love, A. Aspuru-Guzik, and J. L. O'Brien, "A variational eigenvalue solver on a photonic quantum processor", Nature Communications **5**, `10.1038/ncomms5213` (2014).

[11] E. Farhi, J. Goldstone, and S. Gutmann, *A quantum approximate optimization algorithm*, 2014.

[12] M. Cerezo, A. Arrasmith, R. Babbush, S. C. Benjamin, S. Endo, K. Fujii, J. R. McClean, K. Mitarai, X. Yuan, L. Cincio, and P. J. Coles, "Variational quantum algorithms", Nature Reviews Physics **3**, 625 (2021).

[13] P. W. Shor, "Scheme for reducing decoherence in quantum computer memory", Phys. Rev. A **52**, R2493 (1995).

[14] B. M. Terhal, "Quantum error correction for quantum memories", Reviews of Modern Physics **87**, 307 (2015).

[15] P. Aliferis, D. Gottesman, and J. Preskill, "Accuracy threshold for postselected quantum computation", arXiv preprint quant-ph/0703264 (2007).

[16] E. T. Campbell, B. M. Terhal, and C. Vuillot, "Roads towards fault-tolerant universal quantum computation", Nature **549**, 172 (2017).

[17] D. J. Gorman, B. Hemmerling, E. Megidish, S. A. Moeller, P. Schindler, M. Sarovar, and H. Haeffner, "Engineering vibrationally assisted energy transfer in a trapped-ion quantum simulator", Phys. Rev. X **8**, 011038 (2018).

[18] P. Rebentrost, M. Mohseni, I. Kassal, S. Lloyd, and A. Aspuru-Guzik, "Environment-assisted quantum transport", New J. Phys. **11**, 033003 (2009).

[19] L. Chen, P. Shenai, F. Zheng, A. Somoza, and Y. Zhao, "Optimal energy transfer in light-harvesting systems", Molecules **20**, 15224 (2015).

[20] A. Blais, A. L. Grimsmo, S. M. Girvin, and A. Wallraff, *Circuit Quantum Electrodynamics*, en, May 2020.

[21] P. Krantz, M. Kjaergaard, F. Yan, T. P. Orlando, S. Gustavsson, and W. D. Oliver, "A quantum engineer's guide to superconducting qubits", Applied Physics Reviews **6**, `10.1063/1.5089550` (2019).

[22] C. D. Bruzewicz, J. Chiaverini, R. McConnell, and J. M. Sage, "Trapped-ion quantum computing: Progress and challenges", Applied Physics Reviews **6**, 021314 (2019).

[23] K. Wintersperger, F. Dommert, T. Ehmer, A. Hoursanov, J. Klepsch, W. Mauerer, G. Reuber, T. Strohm, M. Yin, and S. Luber, "Neutral atom quantum computing hardware: performance and end-user perspective", EPJ Quantum Technology **10**, `10.1140/epjqt/s40507-023-00190-1` (2023).

[24] P. Schindler, D. Nigg, T. Monz, J. T. Barreiro, E. Martinez, S. X. Wang, S. Quint, M. F. Brandl, V. Nebendahl, C. F. Roos, M. Chwalla, M. Hennrich, and R. Blatt, "A quantum information processor with trapped ions", New J. Phys. **15**, 123012 (2013).

[25] H.-P. Breuer and F. Petruccione, *The Theory of Open Quantum Systems* (Oxford University Press, Jan. 2007).

[26] M. A. Rol, F. Battistel, F. K. Malinowski, C. C. Bultink, B. M. Tarasinski, R. Vollmer, N. Haider, N. Muthusubramanian, A. Bruno, B. M. Terhal, and L. DiCarlo, "Fast, high-fidelity conditional-phase gate exploiting leakage interference in weakly anharmonic superconducting qubits", Physical Review Letters **123**, `10.1103/physrevlett.123.120502` (2019).

[27] R. W. Simmonds, K. M. Lang, D. A. Hite, S. Nam, D. P. Pappas, and J. M. Martinis, "Decoherence in josephson phase qubits from junction resonators", Physical Review Letters **93**, 1 (2004).

[28] M. Neeley, M. Ansmann, R. C. Bialczak, M. Hofheinz, N. Katz, E. Lucero, A. O'Connell, H. Wang, A. N. Cleland, and J. M. Martinis, "Process tomography of quantum memory in a Josephson-phase qubit coupled to a two-level state", Nature Physics **4**, 523 (2008).

[29] J. H. Cole, C. Müller, P. Bushev, G. J. Grabovskij, J. Lisenfeld, A. Lukashenko, A. V. Ustinov, and A. Shnirman, "Quantitative evaluation of defect-models in superconducting phase qubits", Applied Physics Letters **97**, 10.1063/1.3529457 (2010).

[30] H. P. Breuer, D. Burgarth, and F. Petruccione, "Non-Markovian dynamics in a spin star system: Exact solution and approximation techniques", Physical Review B - Condensed Matter and Materials Physics **70**, 1 (2004).

[31] J. I. Cirac and P. Zoller, "Quantum computations with cold trapped ions", Phys. Rev. Lett. **74**, 4091 (1995).

[32] A. Sørensen and K. Mølmer, "Quantum computation with ions in thermal motion", Physical review letters **82**, 1971 (1999).

[33] Z. Yang, R. L. Kosut, and K. B. Whaley, "Hamiltonian switching control of noisy bipartite qubit systems", New Journal of Physics (2024).

[34] J. Preskill, "Quantum Computing in the NISQ era and beyond", Quantum **2**, 79 (2018).

[35] C. P. Koch, "Controlling open quantum systems: Tools, achievements, and limitations", Journal of Physics Condensed Matter **28**, 10.1088/0953-8984/28/21/213001 (2016).

[36] M. Bukov, A. G. Day, D. Sels, P. Weinberg, A. Polkovnikov, and P. Mehta, "Reinforcement Learning in Different Phases of Quantum Control", Physical Review X **8**, 10.1103/PhysRevX.8.031086 (2018).

[37] M. Y. Niu, S. Boixo, V. N. Smelyanskiy, and H. Neven, "Universal quantum control through deep reinforcement learning", npj Quantum Information **5**, 10.1038/s41534-019-0141-3 (2019).

[38] R. L. Kosut, M. D. Grace, and C. Brif, "Robust control of quantum gates via sequential convex programming", Phys. Rev. A **88**, 052326 (2013).

[39] Y. Dong, X. Meng, L. Lin, R. Kosut, and K. B. Whaley, *Robust control optimization for quantum approximate optimization algorithm*, 2019.

[40] J. Yao, M. Bukov, and L. Lin, *Policy gradient based quantum approximate optimization algorithm*, 2020.

[41] J. Yao, P. Köttering, H. Gundlach, L. Lin, and M. Bukov, *Noise-robust end-to-end quantum control using deep autoregressive policy networks*, 2020.

[42] J. Yao, L. Lin, and M. Bukov, *Reinforcement Learning for Many-Body Ground State Preparation based on Counter-Diabatic Driving*, Oct. 2020.

[43] J. Schliemann, A. Khaetskii, and D. Loss, "Electron spin dynamics in quantum dots and related nanostructures due to hyperfine interaction with nuclei", Journal of Physics: Condensed Matter **15**, R1809 (2003).

[44] L. Ratschbacher, C. Sias, L. Carcagni, J. M. Silver, C. Zipkes, and M. Köhl, "Decoherence of a single-ion qubit immersed in a spin-polarized atomic bath", Physical Review Letters **110**, 1 (2013).

[45] M. Warner, S. Din, I. S. Tupitsyn, G. W. Morley, A. M. Stoneham, J. A. Gardener, Z. Wu, A. J. Fisher, S. Heutz, C. W. M. Kay, and G. Aeppli, "Potential for spin-based information processing in a thin-film molecular semiconductor", Nature **503**, 504 (2013).

[46] C. Arenz, G. Gualdi, and D. Burgarth, "Control of open quantum systems: Case study of the central spin model", New Journal of Physics **16**, `10.1088/1367-2630/16/6/065023` (2014).

[47] J. Fischer and H. P. Breuer, "Correlated projection operator approach to non-Markovian dynamics in spin baths", Physical Review A - Atomic, Molecular, and Optical Physics **76**, 1 (2007).

[48] S. Bhattacharya, A. Misra, C. Mukhopadhyay, and A. K. Pati, "Exact master equation for a spin interacting with a spin bath: Non-Markovianity and negative entropy production rate", Physical Review A **95**, 1 (2017).

[49] J. Jing and L. A. Wu, "Decoherence and control of a qubit in spin baths: An exact master equation study", Scientific Reports **8**, 1 (2018).

[50] N. Shenvi, R. De Sousa, and K. B. Whaley, "Nonperturbative bounds on electron spin coherence times induced by hyperfine interactions", Physical Review B - Condensed Matter and Materials Physics **71**, 1 (2005).

[51] N. Shenvi, R. de Sousa, and K. B. Whaley, "Universal scaling of hyperfine-induced electron spin echo decay", Phys. Rev. B **71**, 224411 (2005).

[52] R. de Sousa, N. Shenvi, and K. B. Whaley, "Qubit coherence control in a nuclear spin bath", Phys. Rev. B **72**, 045330 (2005).

[53] M. Grace, C. Brif, H. Rabitz, I. A. Walmsley, R. L. Kosut, and D. A. Lidar, "Optimal control of quantum gates and suppression of decoherence in a system of interacting two-level particles", Journal of Physics B: Atomic, Molecular and Optical Physics **40**, `10.1088/0953-4075/40/9/S06` (2007).

[54] M. D. Grace, C. Brif, H. Rabitz, D. A. Lidar, I. A. Walmsley, and R. L. Kosut, "Fidelity of optimally controlled quantum gates with randomly coupled multiparticle environments", Journal of Modern Optics **54**, 2339 (2007).

[55] M. D. Grace, J. Dominy, R. L. Kosut, C. Brif, and H. Rabitz, "Environment-invariant measure of distance between evolutions of an open quantum system", New Journal of Physics **12**, 0 (2010).

[56] R. L. Kosut, C. Arenz, and H. Rabitz, "Quantum control landscape of bipartite systems", Journal of Physics A: Mathematical and Theoretical **52**, 165305 (2019).

[57] M. Gaudin, "Diagonalisation d'une classe d'hamiltoniens de spin", Journal de Physique **37**, 1087 (1976).

[58] A. Hutton and S. Bose, "Mediated entanglement and correlations in a star network of interacting spins", Phys. Rev. A **69**, 042312 (2004).

[59] C. Müller, J. H. Cole, and J. Lisenfeld, "Towards understanding two-level-systems in amorphous solids: Insights from quantum circuits", Reports on Progress in Physics **82**, 1 (2019).

[60] F. Arute, K. Arya, R. Babbush, D. Bacon, J. C. Bardin, R. Barends, R. Biswas, S. Boixo, F. G. Brandao, D. A. Buell, B. Burkett, Y. Chen, Z. Chen, B. Chiaro, R. Collins, W. Courtney, A. Dunsworth, E. Farhi, B. Foxen, A. Fowler, C. Gidney, M. Giustina, R. Graff, K. Guerin, S. Habegger, M. P. Harrigan, M. J. Hartmann, A. Ho, M. Hoffmann, T. Huang, T. S. Humble, S. V. Isakov, E. Jeffrey, Z. Jiang, D. Kafri, K. Kechedzhi, J. Kelly, P. V. Klimov, S. Knysh, A. Korotkov, F. Kostritsa, D. Landhuis, M. Lindmark, E. Lucero, D. Lyakh, S. Mandrà, J. R. McClean, M. McEwen, A. Megrant, X. Mi, K. Michielsen, M. Mohseni, J. Mutus, O. Naaman, M. Neeley, C. Neill, M. Y. Niu, E. Ostby, A. Petukhov, J. C. Platt, C. Quintana, E. G. Rieffel, P. Roushan, N. C. Rubin, D. Sank, K. J. Satzinger, V. Smelyanskiy, K. J. Sung, M. D. Trevithick, A. Vainsencher, B. Villalonga, T. White, Z. J. Yao, P. Yeh, A. Zalcman, H. Neven, and J. M. Martinis, "Quantum supremacy using a programmable superconducting processor", Nature **574**, 505 (2019).

[61] D. M. Reich, N. Katz, and C. P. Koch, "Exploiting non-markovianity for quantum control", Scientific Reports **5**, `10.1038/srep12430` (2015).

[62] N. Khaneja, T. Reiss, C. Kehlet, T. Schulte-Herbrüggen, and S. J. Glaser, "Optimal control of coupled spin dynamics: Design of NMR pulse sequences by gradient ascent algorithms", Journal of Magnetic Resonance **172**, 296 (2005).

[63] A. V. Khaetskii, D. Loss, and L. Glazman, "Electron spin decoherence in quantum dots due to interaction with nuclei", Physical review letters **88**, 186802 (2002).

[64] F. Poggiali, P. Cappellaro, and N. Fabbri, "Optimal Control for One-Qubit Quantum Sensing", Physical Review X **8**, Publisher: American Physical Society, 021059 (2018).

[65] D. Stefanatos and E. Paspalakis, "Rapid biexciton-state preparation in a quantum dot using on-off pulse sequences", Physical Review A **102**, Publisher: American Physical Society, 052618 (2020).

[66] F. Mazzoncini, V. Cavina, G. M. Andolina, P. A. Erdman, and V. Giovannetti, "Optimal control methods for quantum batteries", Physical Review A **107**, 032218 (2023).

[67] M. G. Bason, M. Viteau, N. Malossi, P. Huillery, E. Arimondo, D. Ciampini, R. Fazio, V. Giovannetti, R. Mannella, and O. Morsch, "High-fidelity quantum driving", Nature Physics **8**, 147 (2012).

[68] G. C. Hegerfeldt, "Driving at the quantum speed limit: Optimal control of a two-level system", Physical Review Letters **111**, 1 (2013).

[69] S. Lloyd, *Quantum approximate optimization is computationally universal*, 2018.

[70] M. E. Morales, J. D. Biamonte, and Z. Zimborás, "On the universality of the quantum approximate optimization algorithm", Quantum Information Processing **19**, 1 (2020).

[71] D. Gottesman, "Theory of fault-tolerant quantum computation", Phys. Rev. A **57**, 127 (1998).

[72] J. Johansson, P. Nation, and F. Nori, "Qutip 2: a python framework for the dynamics of open quantum systems", Computer Physics Communications **184**, 1234 (2013).

[73] M. H. Goerz, D. M. Reich, and C. P. Koch, "Optimal control theory for a unitary operation under dissipative evolution", New Journal of Physics **16**, 055012 (2014).

[74] C. R. Harris, K. J. Millman, S. J. van der Walt, R. Gommers, P. Virtanen, D. Cournapeau, E. Wieser, J. Taylor, S. Berg, N. J. Smith, R. Kern, M. Picus, S. Hoyer, M. H. van Kerkwijk, M. Brett, A. Haldane, J. F. del Río, M. Wiebe, P. Peterson, P. Gérard-Marchant, K. Sheppard, T. Reddy, W. Weckesser, H. Abbasi, C. Gohlke, and T. E. Oliphant, "Array programming with NumPy", Nature **585**, 357 (2020).

[75] P. Weinberg and M. Bukov, "Quspin: a python package for dynamics and exact diagonalisation of quantum many body systems part i: spin chains", SciPost Physics **2**, `10.21468/scipostphys.2.1.003` (2017).

[76] F. F. Floether, P. de Fouquieres, and S. G. Schirmer, "Robust quantum gates for open systems via optimal control: markovian versus non-markovian dynamics", New Journal of Physics **14**, 073023 (2012).

[77] P. Virtanen, R. Gommers, T. E. Oliphant, M. Haberland, T. Reddy, D. Cournapeau, E. Burovski, P. Peterson, W. Weckesser, J. Bright, S. J. van der Walt, M. Brett, J. Wilson, K. J. Millman, N. Mayorov, A. R. J. Nelson, E. Jones, R. Kern, E. Larson, C. J. Carey, İ. Polat, Y. Feng, E. W. Moore, J. VanderPlas, D. Laxalde, J. Perktold, R. Cimrman, I. Henriksen, E. A. Quintero, C. R. Harris, A. M. Archibald, A. H. Ribeiro, F. Pedregosa, P. van Mulbregt, and SciPy 1.0 Contributors, "SciPy 1.0: Fundamental Algorithms for Scientific Computing in Python", Nature Methods **17**, 261 (2020).

[78] R. L. Kosut, G. Bhole, and H. Rabitz, *Robust quantum control: analysis & synthesis via averaging*, 2022.

[79] Z. Chen, J. Kelly, C. Quintana, R. Barends, B. Campbell, Y. Chen, B. Chiaro, A. Dunsworth, A. G. Fowler, E. Lucero, E. Jeffrey, A. Megrant, J. Mutus, M. Neeley, C. Neill, P. J. J. O'Malley, P. Roushan, D. Sank, A. Vainsencher, J. Wenner, T. C. White, A. N. Korotkov, and J. M. Martinis, "Measuring and Suppressing Quantum State Leakage in a Superconducting Qubit", Physical Review Letters **116**, Publisher: American Physical Society, 020501 (2016).

[80] E. Lucero, J. Kelly, R. C. Bialczak, M. Lenander, M. Mariantoni, M. Neeley, A. D. O'Connell, D. Sank, H. Wang, M. Weides, J. Wenner, T. Yamamoto, A. N. Cleland, and J. M. Martinis, "Reduced phase error through optimized control of a superconducting qubit", Phys. Rev. A **82**, 042339 (2010).

[81] J. M. Chow, J. M. Gambetta, A. W. Cross, S. T. Merkel, C. Rigetti, and M. Steffen, "Microwave-activated conditional-phase gate for superconducting qubits", New Journal of Physics **15**, Publisher: IOP Publishing, 115012 (2013).

[82] Z. Li, P. Liu, P. Zhao, Z. Mi, H. Xu, X. Liang, T. Su, W. Sun, G. Xue, J.-N. Zhang, W. Liu, Y. Jin, and H. Yu, *Error per single-qubit gate below 10^{-4} in a superconducting qubit*, Feb. 2023.

[83] J. L. Allen, R. Kosut, J. Joo, P. Leek, and E. Ginossar, "Optimal control of two qubits via a single cavity drive in circuit quantum electrodynamics", Physical Review A **95**, 042325 (2017).

[84] J.-L. Brylinski and R. Brylinski, *Universal quantum gates*, 2001.

[85] N. Margolus and L. B. Levitin, "The maximum speed of dynamical evolution", Physica D: Nonlinear Phenomena **120**, 188 (1998).

[86] S. Deffner and E. Lutz, "Energy–time uncertainty relation for driven quantum systems", Journal of Physics A: Mathematical and Theoretical **46**, 335302 (2013).

[87] K. Bhattacharyya, "Quantum decay and the mandelstam-tamm-energy inequality", Journal of Physics A: Mathematical and General **16**, 2993 (1983).

[88] L. Mandelstam and I. Tamm, in *Selected Papers*, edited by B. M. Bolotovskii, V. Y. Frenkel, and R. Peierls (Springer Berlin Heidelberg, 1991), pp. 115–123.

[89] T. Caneva, M. Murphy, T. Calarco, R. Fazio, S. Montangero, V. Giovannetti, and G. E. Santoro, "Optimal Control at the Quantum Speed Limit", Physical Review Letters **103**, Publisher: American Physical Society, 240501 (2009).

[90] S. Deffner and E. Lutz, "Quantum speed limit for non-markovian dynamics", Phys. Rev. Lett. **111**, 010402 (2013).

[91] D. Burgarth, S. Bose, C. Bruder, and V. Giovannetti, "Local controllability of quantum networks", Phys. Rev. A **79**, 060305 (2009).

[92] L. T. Brady, C. L. Baldwin, A. Bapat, Y. Kharkov, and A. V. Gorshkov, "Optimal protocols in quantum annealing and quantum approximate optimization algorithm problems", Phys. Rev. Lett. **126**, 070505 (2021).

[93] H. Liao, I. Convy, Z. Yang, and K. B. Whaley, "Decohering tensor network quantum machine learning models", Quantum Machine Intelligence **5**, 7 (2023).

[94] G. Evenbly and G. Vidal, "Tensor network states and geometry", Journal of Statistical Physics **145**, 891 (2011).

[95] J. Eisert, in *Emergent phenomena in correlated matter modeling and simulation*, Vol. 3, edited by E. Pavarini, E. Koch, and U. Schollwöck (Verlag des Forschungszentrum Jülich, 2013) Chap. 17.

[96] I. Convy, W. J. Huggins, H. Liao, and K. B. Whaley, "Mutual information scaling for tensor network machine learning", Machine Learning: Science and Technology **3**, 015017 (2022).

[97] S. Lu, M. Kanász-Nagy, I. Kukuljan, and J. I. Cirac, "Tensor networks and efficient descriptions of classical data", arXiv:2103.06872 (2021).

[98] G. Evenbly and G. Vidal, "Algorithms for entanglement renormalization", Physical Review B **79** (2009).

[99] J. C. Bridgeman and C. T. Chubb, "Hand-waving and interpretive dance: an introductory course on tensor networks", Journal of Physics A: Mathematical and Theoretical **50** (2017).

[100] Y. Levine, D. Yakira, N. Cohen, and A. Shashua, "Deep learning and quantum entanglement: fundamental connections with implications to network design", in Proceedings of ICLR (2018).

[101] N. Cohen and A. Shashua, "Convolutional rectifier networks as generalized tensor decompositions", in Proceedings of ICML (2016), pp. 955–963.

[102] Y. Shi, L. Duan, and G. Vidal, "Classical simulation of quantum many-body systems with a tree tensor network", Physical Review A **74**, 022320 (2006).

[103] G. Vidal, "Entanglement renormalization", Physical Review Letters **99**, 1 (2007).

[104] E. M. Stoudenmire, "Learning relevant features of data with multi-scale tensor networks", Quantum Science and Technology **3**, 034003 (2018).

[105] J. A. Reyes and E. M. Stoudenmire, "Multi-scale tensor network architecture for machine learning", Machine Learning: Science and Technology **2**, 035036 (2021).

[106] M. L. Wall and G. D'Aguanno, "Tree-tensor-network classifiers for machine learning: from quantum inspired to quantum assisted", Physical Review A **104**, 042408 (2021).

[107] E. Grant, M. Benedetti, S. Cao, A. Hallam, J. Lockhart, V. Stojevic, A. G. Green, and S. Severini, "Hierarchical quantum classifiers", npj Quantum Information **4**, 65 (2018).

[108] W. J. Huggins, P. Patil, B. Mitchell, K. B. Whaley, and E. M. Stoudenmire, "Towards quantum machine learning with tensor networks", Quantum Science and Technology **4**, 024001 (2019).

[109] K. Mitarai, M. Negoro, M. Kitagawa, and K. Fujii, "Quantum circuit learning", Physical Review A **98**, 032309 (2018).

[110] M. Benedetti, E. Lloyd, S. Sack, and M. Fiorentini, "Parameterized quantum circuits as machine learning models", Quantum Science and Technology **4**, 043001 (2019).

[111] V. Havlíček, A. D. Córcoles, K. Temme, A. W. Harrow, A. Kandala, J. M. Chow, and J. M. Gambetta, "Supervised learning with quantum-enhanced feature spaces", Nature **567**, 209 (2019).

[112] E. M. Stoudenmire and D. J. Schwab, "Supervised learning with quantum-inspired tensor networks", in Proceedings of NIPS (2016), pp. 4799–4807.

[113] R. Larose and B. Coyle, "Robust data encodings for quantum classifiers", Physical Review A **102**, 032420 (2020).

[114] H. Liao, I. Convy, W. J. Huggins, and K. B. Whaley, "Robust in practice: adversarial attacks on quantum machine learning", Physical Review A **103**, 042427 (2021).

[115] D. Kretschmann, D. Schlingemann, and R. F. Werner, "The information-disturbance tradeoff and the continuity of Stinespring's representation", IEEE Transactions on Information Theory **54**, 1708 (2008).

[116] J. Watrous, *The theory of quantum information* (Cambridge University Press, 2018).

[117] J. Miller, G. Roeder, and T.-D. Bradley, "Probabilistic graphical models and tensor networks: a hybrid framework", arXiv:2106.15666 (2021).

[118] E. Robeva and A. Seigal, "Duality of graphical models and tensor networks", Information and Inference **8**, 273 (2019).

[119] I. Glasser, R. Sweke, N. Pancotti, J. Eisert, and J. I. Cirac, "Expressive power of tensor-network factorizations for probabilistic modeling, with applications from hidden markov models to quantum machine learning", in Proceedings of NIPS (2019), pp. 1498–1510.

[120] D. P. Kingma and J. Ba, "Adam: a method for stochastic optimization", arXiv:1412.6980 (2015).

[121] R. Liaw, E. Liang, R. Nishihara, P. Moritz, J. E. Gonzalez, and I. Stoica, "Tune: a research platform for distributed model selection and training", arXiv:1807.05118 (2018).

[122] K. He, X. Zhang, S. Ren, and J. Sun, "Deep residual learning for image recognition", in Proceedings of CVPR (2016), pp. 770–778.

[123] Y. LeCun, C. Cortes, and C. J. Burges, *MNIST handwritten digit database*, 2010.

[124] T. Clanuwat, M. Bober-Irizar, A. Kitamoto, A. Lamb, K. Yamamoto, and D. Ha, "Deep learning for classical Japanese literature", arXiv:1812.01718 (2018).

[125] H. Xiao, K. Rasul, and R. Vollgraf, "Fashion-MNIST: a novel image dataset for benchmarking machine learning algorithms", arXiv:1708.07747 (2017).

[126] G. Tanner, "Unitary-stochastic matrix ensembles and spectral statistics", Journal of Physics A: Mathematical and General **34**, 8485 (2001).

[127] K. Zyczkowski, M. Kus, W. Slomczynski, and H.-J. Sommers, "Random unistochastic matrices", Journal of Physics A: Mathematical and General **36**, 3425 (2003).

[128] J. Biamonte and V. Bergholm, "Tensor networks in a nutshell", arXiv:1708.00006 (2017).

[129] Z.-Z. Li, L. Ko, Z. Yang, M. Sarovar, and K. B. Whaley, "Interplay of vibration- and environment-assisted energy transfer", New Journal of Physics **24**, 033032 (2022).

[130] A. W. Chin, J. Prior, R. Rosenbach, F. Caycedo-Soler, S. F. Huelga, and M. B. Plenio, "The role of non-equilibrium vibrational structures in electronic coherence and recoherence in pigment-protein complexes", Nat. Phys. **9**, 113 (2013).

[131] E. K. Irish, R. Gómez-Bombarelli, and B. W. Lovett, "Vibration-assisted resonance in photosynthetic excitation-energy transfer", Phys. Rev. A **90**, 012510 (2014).

[132] Y. Sato and B. Doolittle, "Influence of intra-pigment vibrations on dynamics of photosynthetic exciton", J. Chem. Phys. **141**, 185102 (2014).

[133] N. Killoran, S. F. Huelga, and M. B. Plenio, "Enhancing light-harvesting power with coherent vibrational interactions: a quantum heat engine picture", J. Chem. Phys. **143**, 155102 (2015).

[134] M. H. Lee and A. Troisi, "Vibronic enhancement of excitation energy transport: interplay between local and non-local exciton-phonon interactions", J. Chem. Phys. **146**, 075101 (2017).

[135] A. Kolli, E. J. O'Reilly, G. D. Scholes, and A. Olaya-Castro, "The fundamental role of quantized vibrations in coherent light harvesting by cryptophyte algae", J. Chem. Phys. **137**, 174109 (2012).

[136] I. B. Juhász and Á. I. Csurgay, "Impact of undamped and damped intramolecular vibrations on the efficiency of photosynthetic exciton energy transfer", AIP Advances **8**, 045318 (2018).

[137] P. Nalbach, C. A. Mujica-Martinez, and M. Thorwart, "Vibronically coherent speed-up of the excitation energy transfer in the fenna-matthews-olson complex", Phys. Rev. E **91**, 022706 (2015).

[138] E. O'Reilly and A. Olaya-Castro, "Non-classicality of the molecular vibrations assisting exciton energy transfer at room temperature", Nat. Commun. **5**, 3012 (2014).

[139] J. A. Cina and G. R. Fleming, "Vibrational coherence transfer and trapping as sources for long-lived quantum beats in polarized emission from energy transfer complexes", J. Phys. Chem. A **108**, 11196 (2004).

[140] N. Christensson, H. F. Kauffmann, T. Pullerits, and T. Mancăl, "Origin of long-lived coherences in light-harvesting complexes", J. Phys. Chem. B **116**, 7449 (2012).

[141] M. B. Plenio, J. Almeida, and S. F. Huelga, "Origin of long-lived oscillations in 2d-spectra of a quantum vibronic model: electronic versus vibrational coherence", J. Chem. Phys. **139**, 235102 (2013).

[142] G. D. e. Scholes, "Using coherence to enhance function in chemical and biophysical systems", Nature **543**, 647 (2017).

[143] L. Wang, M. A. Allodi, and G. S. Engel, "Quantum coherences reveal excited-state dynamics in biophysical systems", Nat. Rev. Chem. **3**, 477 (2019).

[144] V. Kendon, "Decoherence in quantum walks - a review", Mathematical Structures in Computer Science **17**, `10.1017/S0960129507006354` (2007).

[145] A. G. Dijkstra, C. Wang, J. Cao, and G. R. Fleming, "Coherent exciton dynamics in the presence of underdamped vibrations", J. Phys. Chem. Lett. **6**, 627 (2015).

[146] V. Capek, "Haken-strobl-reineker model: its limits of validity and a possible extension", Chem. Phys. **171**, 79 (1993).

[147] X.-K. Song, F.-G. Deng, L. Lamata, and J. G. Muga, "Robust state preparation in quantum simulations of dirac dynamics", Phys. Rev. A **95**, 022332 (2006).

[148] Z.-Z. Li, L. Ko, Z. Yang, M. Sarovar, and K. B. Whaley, "Unraveling excitation energy transfer assisted by collective behaviors of vibrations", New J. Phys **23**, 073012 (2021).

[149] A. Potocnik, A. Bargerbos, F. A. Y. N. Schröder, S. A. Khan, M. C. Collodo, S. Gasparinetti, Y. Salathe, C. Creatore, C. Eichler, H. E. Türeci, and et al., "Studying light-harvesting models with superconducting circuits", Nat. Commun. **9**, 904 (2018).

[150] S. Hoyer, M. Sarovar, and K. B. Whaley, "Limits of quantum speedup in photosynthetic light harvesting", New J. Phys. **12**, 065041 (2010).

[151] M. Sarovar, Y.-C. Cheng, and K. B. Whaley, "Environmental correlation effects on excitation energy transfer in photosynthetic light harvesting", Phys. Rev. E **83**, 011906 (2011).

[152] T. Fujita, J. Huh, and A. Aspuru-Guzik, "A stochastic reorganizational bath model for electronic energy transfer", J. Chem. Phys. **140**, 244103 (2014).

[153] M. Cho, H. M. Vaswani, T. Brixner, J. Stenger, and G. R. Fleming, "Exciton analysis in 2d electronic spectroscopy", J. Phys. Chem. B **109**, 10542 (2005).

[154] J. Adolphs and T. Renger, "How proteins trigger excitation energy transfer in the fmo complex of green sulfur bacteria", Biophys J. **91**, 2778 (2006).

[155] C. Uchiyama, W. J. Munro, and K. Nemoto, "Environmental engineering for quantum energy transport", npj Quanttum Inf. **4**, 011038 (2018).

[156] A. Ishizaki and G. R. Fleming, "Insights into photosynthetic energy transfer gained from free-energy structure: coherent transport, incoherent hopping, and vibrational assistance revisited", J. Phys. Chem. B **125**, 3286 (2021).

[157] Y. Fujihashi, G. R. Fleming, and A. Ishizaki, "Impact of environmentally induced fluctuations on quantum mechanically mixed electronic and vibrational pigment states in photosynthetic energy transfer and 2d electronic spectra", J. Chem. Phys. **142**, 212403 (2015).

[158] A. Blais, R.-S. Huang, A. Wallraff, S. M. Girvin, and R. J. Schoelkopf, "Cavity quantum electrodynamics for superconducting electrical circuits: an architecture for quantum computation", Phys. Rev. A **69**, 062320 (2004).

[159] A. Ishizaki, T. R. Calhoun, G. S. Schlau-Cohen, and G. R. Fleming, "Quantum coherence and its interplay with protein environments in photosynthetic electronic energy transfer", Phys. Chem. Chem. Phys. **12**, 7319 (2010).

[160] M. Ban, S. Kitajima, and F. Shibata, "Reduced dynamics and the master equation of open quantum systems", Phys. Lett. A **374**, 2324 (2010).

[161] L. Wang, M. A. Allodi, and G. S. Engel, "Quantum coherences reveal excited- state dynamics in biophysical systems", Nat. Rev. Chem. **3**, 477 (2019).

[162] E. Collini, C. Y. Wong, K. E. Wilk, P. M. G. Curmi, P. Brumer, and G. D. Scholes, "Coherently wired light-harvesting in photosynthetic marine algae at ambient temperature", Nature **463**, 644 (2010).

[163] D. Abramavicius and S. Mukamel, "Quantum oscillatory exciton migration in photosynthetic reaction centers", J. Chem. Phys. **133**, 064510 (2010).

[164] N. Christensson, H. F. Kauffmann, T. Pullerits, and T. Mančal, "Origin of long-lived coherences in light-harvesting complexes", J. Phys. Chem. B **116**, 7449 (2012).

[165] M. B. Plenio, J. Almeida, and S. F. Huelga, "Origin of long-lived oscillations in 2d-spectra of a quantum vibronic model: electronic versus vibrational coherence", J. Chem. Phys. **139**, 235102 (2013).

[166] S. H. Yeh, R. D. Hoehn, M. A. Allodi, G. S. Engel, and S. Kais, "Elucidation of near- resonance vibronic coherence lifetimes by nonadiabatic electronic-vibrational state character mixing", Proc. Natl. Acad. Sci. **116**, 18263 (2018).

[167] G. S. Engel, T. R. Calhoun, E. L. Read, T. K. Ahn, T. Mančal, Y. C. Cheng, R. E. Blankenship, and G. R. Fleming, "Evidence for wavelike energy transfer through quantum coherence in photosynthetic systems", Nature **446**, 782 (2007).

[168] V. Tiwari, W. K. Peters, and D. M. Jonas, "Electronic resonance with anti-correlated pigment vibrations drives photosynthetic energy transfer outside the adiabatic framework", PNAS **110**, 1203 (2012).

[169] A. W. Chin, J. Prior, R. Rosenbach, F. Caycedo-Soler, S. F. Huelga, and M. B. Plenio, "The role of non-equilibrium vibrational structures in electronic coherence and recoherence in pigment-protein complexes", Nat. Phys. **9**, 113 (2013).

[170] S. F. Huelga and M. B. Plenio, "Vibrations, quanta and biology", Contemporary Physics **54**, 181 (2013).

[171] S. F. Huelga and M. B. Plenio, "A vibrant environment", Nat. Phys. **10**, 621 (2014).

[172] E. Romero, R. Augulis, V. I. Novoderezhkin, M. Ferretti, J. Thieme, D. Zigmantas, and R. van Grondelle, "Quantum coherence in photosynthesis for efficient solar-energy conversion", Nat. Phys. **10**, 678 (2014).

[173] F. D. Fuller, J. Pan, A. Gelzinis, V. Butkus, S. S. Senlik, D. E. Wilcox, C. F. Yocum, L. Valkunas, D. Abramavicius, and J. P. Ogilvie, "Vibronic coherence in oxygenic photosynthesis", Nat. Chem. **6**, 706 (2014).

[174] E. J. O'Reilly and A. Olaya-Castro, "Non-classicality of the molecular vibrations assisting exciton energy transfer at room temperature", Nat. Comms. **5**, 3012 (2014).

[175] J. C. Dean, T. Mirkovic, Z. S. Toa, D. G. Oblinsky, and G. D. Scholes, "Vibronic enhancement of algae light harvesting", Chem **1**, 858 (2016).

[176] H. G. Duan, V. I. Prokhorenko, R. J. Cogdell, K. Ashraf, A. L. Stevens, M. Thorwart, and R. J. D. Miller, "Nature does not rely on long-lived electronic quantum coherence for photosynthetic energy transfer", PNAS **8**, 8493 (2017).

[177] P. Bhattacharyya and G. R. Fleming, "The role of resonant nuclear modes in vibrationally assisted energy transport: the lhcii complex", J. Chem. Phys. **153**, 044119 (2020).

[178] A. Potočnik, A. Bargerbos, F. A. Y. N. Schröder, S. A. Khan, M. C. Collodo, S. Gasparinetti, Y. Salathé, C. Creatore, C. Eichler, H. E. Türeci, A. W. Chin, and A. Wallraff, "Studying light-harvesting models with superconducting circuits", Nat. Comms. **9**, 904 (2018).

[179] C. Maier, T. Brydges, P. Jurcevic, N. Trautmann, C. Hempel, B. P. Lanyon, P. Hauke, R. Blatt, and C. F. Roos, "Environment-assisted quantum transport in a 10-qubit network", Phys. Rev. Lett. **122**, 050501 (2019).

[180] M. G. Göppert-Mayer, "Über elementarakte mit zwei quantensprüngen", Ann of Phys. **9**, 273 (1931).

[181] W. Kaiser and C. G. B. Garrett, "Two-photon excitation in $CaF_2 : Eu^{2+}$", Phys. Rev. Lett. **7**, 229 (1961).

[182] I. D. Abella, "Optical double-photon absorption in cesium vapor", Phys. Rev. Lett. **9**, 453 (1962).

[183] L. Garziano, V. Macri, R. Stassi, O. D. Stefano, F. Nori, and S. Savasta, "One photon can simultaneously excite two or more atoms", Phys. Rev. Lett. **117**, 043601 (2016).

[184] S. Mukamel, *Principles of nonlinear optical spectroscopy* (Oxford University Press, New York, United States, 1995).

[185] A. Ishizaki, T. R. Calhoun, G. S. Schlau-Cohenab, and G. R. Fleming, "Quantum coherence and its interplay with protein environments in photosynthetic electronic energy transfer", Phys. Chem. Chem. Phys. **12**, 7319 (2010).

[186] A. Ishizaki and G. R. Fleming, "Theoretical examination of quantum coherence in a photosynthetic system at physiological temperature", PNAS **13**, 17255 (2009).

[187] S. Hoyer, A. Ishizaki, and K. B. Whaley, "Spatial propagation of excitonic coherence enables ratcheted energy transfer", Physical Review E **86**, 041911 (2012).

[188] See Supplemental Material.

[189] H. Lee, Y.-C. Cheng, and G. R. Fleming, "Coherence dynamics in photosynthesis: protein protection of excitonic coherence", Science **316**, 1462 (2007).

[190] F. Fassioli, A. Nazir, and A. Olaya-Castro, "Environmental engineering for quantum energy transport", J. Phys. Chem. Lett **1**, 2139 (2010).

[191] M. Sarovar, Y.-C. Cheng, and K. B. Whaley, "Environmental correlation effects on excitation energy transfer in photosynthetic light harvesting", Physical Review E **83**, 011906 (2011).

[192] D. Abramavicius and S. Mukamel, "Exciton dynamics in chromophore aggregates with correlated environment fluctuations", The Journal of chemical physics **134**, 05B602 (2011).

[193] B. S. Rolczynski, H. Zheng, V. P. Singh, P. Navotnaya, A. R. Ginzburg, J. R. Caram, K. Ashraf, A. T. Gardiner, S.-H. Yeh, S. Kais, R. J. Cogdell, and G. S. Engel, "Correlated protein environments drive quantum coherence lifetimes in photosynthetic pigment-protein complexes", Chem **4**, 138 (2018).

[194] C. Uchiyama, W. J. Munro, and K. Nemoto, "Environmental engineering for quantum energy transport", npj Quant. Inf **4**, 33 (2018).

[195] J. Adolphs and T. Renger, "How proteins trigger excitation energy transfer in the fmo complex of green sulfur bacteria", Biophys. J. **91**, 2778 (2006).

[196] P. Nalbach, D. Braun, and M. Thorwart, "Exciton transfer dynamics and quantumness of energy transfer in the fenna-matthews-olson complex", Phys. Rev. E **84**, 041926 (2011).

[197] K. Timpmann, A. Freiberg, and V. Sundström, "Energy trapping and detrapping in the photosynthetic bacterium rhodopseudomonas viridis: transfer-to-trap-limited dynamics", Chemical physics **194**, 275 (1995).

[198] F. Müh, M. E.-A. Madjet, and T. Renger, "Structure-based simulation of linear optical spectra of the cp43 core antenna of photosystem ii", Photosynthesis research **111**, 87 (2012).

[199] R. A. Bertlmann, W. Grimus, and B. C. Hiesmayr, "Open-quantum-system formulation of particle decay", Phys. Rev. A **73**, 054101 (2006).

[200] The three-ion system realizable in the current experimental setup is from the communication with Joseph Broz and Hartmut Häffner.

[201]   A. F. Kockum, A. Miranowicz, S. D. Liberato, S. Savasta, and F. Nori, "Ultrastrong coupling between light and matter", Nat. Rev. Phys. **1**, 19 (2019).